ASSESSMENT OF THE PERFORMANCE OF LOW-COST GNSS RECEIVERS FOR DEFORMATION MONITORING APPLICATION

Chenyu Xue

BEng., MSc.

Thesis submitted to the University of Nottingham for the Degree of Doctor of Philosophy

Abstract

Current deformation monitoring applications adopting GNSS technology are usually conducted with high-grade GNSS sensors, consisting of both geodetic receiver and geodetic antenna. However, the high-cost feature of the equipment constrains its broader application. With the development of state-of-art low-cost GNSS receivers/antennas in recent years, especially those with multi-GNSS precise carrier phase measurement, the potential for its application in deformation monitoring is expected. However, compared to conventionally adopted survey-grade equipment, most low-cost receivers have the major drawback of single-frequency and larger background noise in the signal processing phase, and the patch antennas have the major disadvantage of the less gain, less multipath suppression, etc. Despite the comparatively poorer quality, empirical research has demonstrated its feasibility in landslide monitoring within centimetre level of accuracy. To test the feasibility and accuracy of the low-cost equipment in other deformation applications, a systematic approach is adopted by carrying out several experiments. Experiments are conducted sequentially from zero-baseline test for internal receiver noise evaluation, short baseline static test to identify and mitigate the practical GNSS monitoring errors majorly consisted of multipath, short baseline dynamic test to determine the precision of low-cost equipment in dynamic monitoring scenario, and finally, the low-cost equipment is tested on a real bridge monitoring project to assess its feasibility and evaluate its accuracy. It is concluded that the modal frequencies from deformation monitoring could be revealed from measurements of a single low-cost rover, and with proper multipath mitigation technique, displacement amplitude could be obtained within centimetre accuracy by a closely-spaced dual low-cost system. The difference of low-cost rover measurement is quantified to be within around 3mm compared to geodetic GNSS sensors. This finding is quite promising for low-cost GNSS deformation monitoring applications. However, future investigation still needs to be carried out with a calibrated patch antenna or with a geodetic antenna to examine further improvement and possibly explore the potential of applying it in real-time.

Acknowledgments

This research was carried at Nottingham Geospatial Institute(NGI), a research group at the University of Nottingham. The research was fully sponsored by a 3-year research scholarship awarded by the Faculty of Engineering, University of Nottingham.

In completion of this research paper, firstly, I would like to express my sincere appreciation and thanks to Dr. Panos Psimoulis and Professor Xiaolin Meng for their supervision and guidance throughout my Ph.D. journey. They have provided invaluable suggestions and recommendations. Their expertise in this field helped me tremendously in experiment design, data processing, and analysis. During each supervision meeting, constructive feedback was given to me, leading to a deeper understanding of the research carried out. I would also like to thank Dr. Chris Hill to be my internal examiner. His feedback after the annual review meeting is very conducive and inspires me to get a comprehensive understanding of the problem.

I would also like to thank Dr. Lukasz K Bonenberg and Sean Ince for their technical and software support. Dr. Lukasz helped a lot in the experiment arrangement, equipment preparation, and testing. Sean also provided support in equipment preparation and administration to facilitate my experiment.

Thanks also go to my colleagues in NGI, postgraduate research student Xinao Wang for provision of technical help, postgraduate research student Vivek Agarwal, Ioulia Peppa, Mohammed Habboub, and visiting scholar Ayse Giz Gulnerman, Fangchao Li, and other postgraduate taught students for their continuous accompaniment and support.

Last but not least, I would like to express my utmost gratitude and respect to my parents. They always stand by me and keep in touch with me when in lock down, relieve my loneliness and encourage me to stay strong and healthy. Their love, understanding, and care throughout the years of my study are essential for me to carry on with my research.

I would also to extend my special thanks and appreciation to my internal examiner Dr. James Pinchin, external examiner Dr. Qiuzhao Zhang and independent chair Professor Stuart Marsh for their valuable time taken to assess my thesis and Viva-voce examination. Their expertise and research in relevant subjects lead to many useful suggestions and recommendations to improve and perfect my thesis.

Table of Contents

List of Figures

List of Tables

List of Equations

List of Abbreviations

AI	Artificial Intelligence
APC	Antenna Phase Centre
ARP	Antenna Reference Point
BCS	Bridge Coordinate System
C/A	Coarse Acquisition
CDDIS	Crustal Dynamics Data Information System
CDMA	Code Division Multiple Access
CME	Common Mode Error
DD	Double Difference
DFT	Discrete Fourier Transform
DLL	Delay Lock Loop
DOP	Dilution of Precision
E, N, U	Easting, Northing, and Up coordinate components
ECEF	Earth Centred Earth-Fixed
EKF	Extended Kalman Filter
ESA	European Space Agency
FCB	Fractional Cycle Bias
FDMA	Frequency Division Multiple Access
FEM	Finite Elements Models
FFT	Fast Fourier Transform
FIR	Finite Impulse Response
G, R, E	GPS, GLONASS, Galileo
GDOP	Geometric Dilution of Precision
GEO	Geostationary Earth Orbit
GNSS	Global Navigation Satellite System
GPS	Global Positioning System
GLONASS	Globalnaya Navigazionnaya Sputnikovaya Sistema
HDOP	Horizontal Dilution of Precision
IFB	Inter-Frequency Bias (GLONASS)
IGS	International GNSS Service
IGSO	Inclined Geosynchronous Satellite Orbit
(D)InSAR	(Differential) Interferometric Synthetic Aperture Radar
ILS	Integer Least Squares
IRNSS	Indian Regional Navigation Satellite System
ITRF	International Terrestrial Reference Frame
LAMBDA	Least-Squares Ambiguity Decorrelation Adjustment
LIDAR	Light Detection and Ranging
LNA	Low Noise Amplifier
MEO	Medium Earth Orbits
MRMS	Moving Root Mean Square
MSTD	Moving Standard Deviation
NASA	National Aeronautics and Space Administration
NDE	Non-Destructive Evaluation
NGS	National Geodetic Survey
OTF	On the Fly

OEM	Original Equipment Manufacture
PCO	Phase Centre Offset
PCV	Phase Centre Variation
PDOP	Position Dilution of Precision
PLL	Phase-Locked Loop
PPK	Postprocessing Kinematic
PPM	Parts per million
PSD	Power Spectral Density
QZSS	Quasi-Zenith Satellite System
RINEX	The Receiver Independent Exchange Format
RMS/rms	Root Mean Square
RMSD	Root Mean Square Difference
RTK	Real-Time Kinematic
RTS	Robotic Total Station
SBAS	Satellite-based Augmentation System
SBL	Short Baseline
SD	Single Difference
SHM	Structural Health Monitoring
SNR	Signal to Noise Ratio
STD	Standard Deviation
TDOP	Time Dilution of Precision
TEC	Total Electron Content
TOA	Time of Arrival
TTFF	Time To First Fix
UTC	Universal Time Coordinate
VDOP	Vertical Dilution of Precision
WGS84	Word Geodetic System 1984
ZBL	Zero-baseline

List of Publications

Based on Chapter 7 and Chapter 8, we published a Journal paper in *Applied Geomatics*

Xue, C., Psimoulis, P., Zhang, Q., & Meng, X. (2021). Analysis of the performance of closely-spaced low-cost multi-GNSS receivers. *Applied Geomatics*, 1-21.

Based on Chapter 9 and Chapter 10, we submitted the manuscript to the 5th Joint International Symposium on Deformation Monitoring JISDM 2022 with the title

Assessment of the accuracy of low-cost multi-GNSS receivers in monitoring bridge response

and currently is under peer review.

Based on Chapter 9, the manuscript is to be submitted to '*Measurement*' with the title

Feasibility analysis of dynamic displacement monitoring with closely-spaced low-cost GNSS receivers

Based on Chapter 10, a manuscript was drafted and will be submitted with the title

Evaluation of low-cost GNSS dynamic displacement monitoring from a short-span pedestrian bridge

Chapter 1 Introduction

1.1 Motivation and significance for deformation monitoring

Deformation monitoring or deformation survey is a systematic approach to measure the change in dimensions or positions of an object due to different loading factors. In civil engineering, it is generally known for monitoring the movement of different types of structures which gains high interest over the last decades (Uren and Price, 1994). The reason for deformation monitoring is mainly to monitor the condition of the structures, assess its stability and ascertain its safety based on the process of i) logging its horizontal or vertical movement with measuring device, ii) computation and analysis, iii) predicting its future behaviour for alarming, and iv) further action (maintenance) against the possible consequences.

To ensure the structural health and safety, it is extremely important and necessary to conduct deformation monitoring in civil engineering structures, such as dams, tunnels, bridges, high-rise and historical buildings, mining areas, etc. The cause of the deformation of these infrastructures could vary. For instance, dam walls could be shaped due to high water pressure in contact; buildings could deform due to changes in ground conditions and foundation; landslides could occur due to deteriorating embankment; bridges could deform due to wind loading and aging, etc. Apart from deformation monitoring in civil engineering infrastructures, some are also applied to monitoring the geological phenomenon and geohazards such as ground settlements, landslides, volcanoes, earthquakes for better understanding their impact and study their mechanism.

By monitoring corresponding structural responses (magnitude and pattern of deformation) from various loads, structural health can be inferred. Any structural degradation will be directly reflected by the abnormality of displacement of the structure, which further exerts a potential risk in structural safety. Therefore, monitoring the structure forms an early alarming mechanism before any anomalies and faults in the structures could propagate and lead to catastrophes. On the other hand, with periodic or continuous monitoring of the structure, any deviations from the designed standard would be detected and warned against. If the measured displacement is significant and beyond the specified limit, measures could be undertaken at an early stage and even if it is within the threshold, potential risks could also be checked and reviewed.

1.2 GPS deformation monitoring and the potential drawbacks

The deformation monitoring mainly features by measuring the vertical and horizontal displacement of the structure periodically and precisely. The accuracy of deformation monitoring required is mainly based on the type and size of the structure, environmental or loading factors, and the need to understand the deformation.

Many measuring approaches and equipment have been established and implemented for monitoring purposes and can generally be classified as, geodetic sensors such as RTS, levels, GPS, InSAR, theodolites, and geotechnic devices such as extensometers, accelerometers, tiltmeters, etc. Among these techniques, GPS technology is used and studied widely in deformation monitoring applications over the last decades due to its advantage of ubiquity and autonomy, with high precision and accuracy to millimetre level. Many researchers have successfully implemented the GPS techniques in deformation monitoring and achieved promising results even with an accuracy of millimetre level both in postprocessing and real-time kinematic mode.

However, the commonly adopted GPS technology applied in deformation monitoring normally requires high-end survey-grade equipment to achieve higher performance, for example, quick time to first fix (TTFF), good multipath suppression, precise carrier phase measurement, low system noise, etc. One major drawback is that the cost of deployment and implementation of such monitoring stations is too high and less suitable for industrial applications. This confined its usage in deformation monitoring applications which could require several stations deployed at different monitoring points.

1.3 Potentials of recently developed low-cost receivers and contribution to knowledge

Until recent years, some low-cost GNSS receivers are developed and manufactured with advanced features. Compared to the cheap chipset and navigation grade receivers, it has advanced functions such as up to 10 Hz sampling rate, multi-GNSS constellation support, and precise carrier phase observations. These features indicate its potential in precise positioning and deformation monitoring with lower cost. However, most of the recently developed low-cost receivers are single-frequency receivers, which means firstly, forming of the ionospheric free linear combination is not applicable, secondly, the ambiguity resolution time is greatly elongated in real-time processing, the time taken to resolve integer ambiguities in an on the fly (OTF) manner is in the order of 15 minutes (Cosser et al., 2003). These two major drawbacks of single-frequency receiver limit its performance in obtaining fixed and more accurate solutions especially for long baselines, dynamic environments which could result in multiple cycle slips and real-time applications.

Considering the underlying potential of low-cost receivers, and high deployment cost associated with conventional deformation monitoring accomplished by high-end survey-grade multi-frequency multi-GNSS GNSS receivers/antennas (Meng et al., 2007; Roberts et al., 2004; Msaewe et al., 2021), this study motivates to explore the possibility of applying the low-cost monitoring system in deformation monitoring applications, so that GNSS deformation monitoring could be widely implemented in a more economical manner. The single-frequency receiver for bridge monitoring is shown to have a potential by Cosser et al. (2003), where it is believed the 'best' solution by evaluation between price and accuracy is to use single-frequency receiver as the rover and dual-frequency receiver as the base. However, such set-up also indicates the ambiguity resolution can be poor compared with a geodetic rover especially at the beginning of observation or after a cycle slip. As the prices of GNSS receiver and antenna suggest the deployment cost of the deformation monitoring system is majorly attributed to the receiver instead of the antenna. Studies have shown that there are multiple benefits of using a geodetic antenna instead of a low-cost patch antenna (Cina and Piras, 2015; Zhang and Schwieger, 2013; Odolinski and

Teunissen, 2016), for example, better performance in reducing phase and code multipath, and possibly faster TTFF (Takasu and Yasuda, 2008). On the contrary, no large differences could be found between low-cost and geodetic grade receivers in carrier phase multipath level despite the huge price difference (Takasu and Yasuda, 2008). Therefore, by considering both the economic aspect as well as performance aspect, a cost-effective receiver and antenna combination for structural health monitoring would include a low-cost GNSS receiver with an external geodetic antenna, this might not be the utmost low-cost solution, but it allows to achieve a better accuracy (Cina and Piras, 2015). For the base station configuration, an ideal receiver and antenna combination would be a geodetic antenna connected with a geodetic receiver. Another option could be to take advantage of the pre-established continuous operating reference stations (CORS) for the base (Wisniewski et al., 2013). In this study, the combination of a low-cost single-frequency receiver and patch antenna is majorly adopted as the rover to examine the best achievable precision and accuracy from low-cost instruments. The performance improvement by an external geodetic antenna could be investigated further in the future.

The recent research in low-cost monitoring has mainly proven that by using low-cost single-frequency receivers with a short baseline, landslide and crustal deformation monitoring are feasible with sub-centimetre accuracy providing continuous observation, optimum observation environment with minimum cycle slip and low multipath (Cina and Piras, 2015; Bellone et al., 2016; Biagi et al., 2016; Takasu and Yasuda, 2009). However, only a few research has studied the approaches to improve the performance of low-cost single-frequency receivers, such as adopting multi-constellation (Verhagen et al., 2010; Odolinski and Teunissen, 2019) and use of multi-monitoring sensors (Zhang and Schwieger, 2016; Jo et al., 2013). Very few research applies and tests the low-cost GNSS equipment on civil engineering structural health monitoring applications (Manzini et al., 2020). The low-cost GNSS monitoring system is also generally perceived as less precise and accurate, with relatively low availability due to poor ambiguity resolution than high-end survey-grade receivers. To achieve better performance with the low-cost receiver in deformation monitoring applications, the poor ambiguity resolution by single-frequency low-cost receivers is accounted for by using a short baseline and with multi-GNSS constellations in this study. Since for solutions with short baselines, the TTFF, fix rate, accuracy will outperform solutions adopting a longer baseline (Takasu and Yasuda, 2009).

For this research, the following **hypotheses** are made,

1. The effect of different GNSS receiver grade on carrier phase performance is limited (Takasu and Yasuda, 2008). This hypothesis or finding is the foundation of this study, it indicates the potential of using a low-cost receiver to achieve the similar performance of a survey-grade receiver. It is hypothesized that the receiver-antenna positioning performance is more affected by the antenna grade instead of receiver grade for DD kinematic positioning (Takasu and Yasuda, 2008; Zhang and Schwieger, 2013; Cina and Piras, 2015; Odolinski and Teunissen, 2016).

2. The experiment results would be enhanced by taking advantage of the spatio-temporal correlation of multiple closely adjoined antennas (Zhang and Schwieger, 2016). The spatial correlation of the carrier phase multipath between the closely-spaced antennas is also indicated according to Ray et al. (2001). They found that generally the closer the antenna, the larger correlation between their carrier phase multipath. This leads to the establishment of CME filtering used in the study based on the assumption that the errors between two closely-spaced stations are partially the same. Therefore, the adoption of CME would be beneficial for precision enhancement by mitigation of the partially similar error between the closely-spaced stations.

3. High-precision displacement estimates with reduced noise levels could be achieved by averaging the measurements from a dense array of closely-spaced low-cost C/A chip-set receivers (Jo et al., 2013). Based on that, it is hypothesized that the same approach could also be implemented for noise mitigation by averaging carrier phase measurement results.

The 2nd and 3rd hypotheses are both related to using a second station or multiple stations in the near-field to enhance the performance of the current monitoring station. Therefore, a second low-cost station is adopted, and approaches are attempted for the precision enhancement according to the hypotheses.

Although the recently developed low-cost GPS receivers show the advanced features which is a prerequisite for deformation applications, and empirical research shows in certain applications, low-cost receivers have comparable performance with single-frequency geodetic receivers (Takasu and Yasuda, 2009; Odolinski and Teunissen, 2016). A comprehensive feasibility evaluation is still needed for the adoption of low-cost GNSS sensors in the deformation monitoring application. Therefore, the **aim** of the study is to determine if it is feasible to monitor the frequency and amplitude response of relatively rigid infrastructures with the use of low-cost GNSS receivers/antennas.

To achieve the aim and evaluate the full potential of low-cost receivers, the low-cost receiver and antenna are evaluated based on different scenarios and different experimental setups. The data is post-processed and experiments are set up on a very short baseline basis. In the journey to achieve the specified aim, the following **objectives** are proposed.

1) To gain an overview of the level of accuracy/precision to be obtained with low-cost receivers/antennas from various lab measurements, possibly with comparison to geodetic GNSS equipment.

In the preliminary lab test, zero-baseline test and short baseline test are proposed. The zero-baseline test is used for preliminary analysis of the noise and examines the impact of different parameters, such as receiver grade, constellation, DOP, antenna grade, etc on the residuals. Then short baseline tests are conducted for different situations, static rover, and moving rover. In the short baseline static test, the system noise in the practical case is examined for the low-cost receivers. One of the main contributors of the error such as the multipath effect is evaluated and mitigated. In the short baseline dynamic test, the precision of low-cost GNSS measurement is studied under dynamic displacement.

2) To test the deformation monitoring potentials using a set of two closely-spaced low-cost GNSS equipment in a real monitoring project.

In the final stage, to verify the results derived from the lab experiment, the low-cost monitoring system is applied in a real monitoring scenario, where the dynamic response of a relatively rigid suspension bridge is examined under different loading events.

3) To explore the possibility of results' improvement by introducing a second low-cost station or possibly a cluster of low-cost stations in the nearfield.

For both short baseline tests and the final monitoring project, another low-cost station is configured in the nearfield with the same antenna orientation and a novel method of Common Mode Error (CME) filtering is implemented to the two low-cost receiver measurements. The method of average combination of low-cost receiver results is also examined.

Therefore, the outcome of this study would indicate the accuracy/precision of low-cost receivers in different measurement scenarios, evaluate possible improvement by incorporation of a closely-spaced dual low-cost system and determine the feasibility of it for certain applications. If the accuracy requirement could be met with low-cost receiver measurement, the high-end survey-grade receivers could be potentially replaced by low-cost receivers. This will hugely reduce the monitoring cost and prosper the deformation monitoring industry, which further leads to easier access to hazard risk alerting, safety assurance, and a better understanding of structure health.

1.4 Outline of the thesis

The main body of the thesis would be divided into several chapters. In Chapter 2, the application of deformation monitoring such as SHM and landslide monitoring would be briefly reviewed, with a focus on the accuracy obtained from empirical GNSS monitoring. In Chapter 3, the GNSS techniques will be shortly discussed for deformation monitoring, with the algorithm of double-difference (DD) explained, the error sources would also be determined and discussed. In Chapter 4, Different grades of receivers and antennas are compared based on empirical studies on their architecture and performance, the equipment used in this study is also described according to their manual. In Chapter5, the applications of low-cost GNSS receivers will be reviewed with a focus on its application on deformation monitoring, several studies with low-cost GNSS monitoring and positioning will be briefly concluded in this chapter. In Chapter 6, the detailed experimental and processing approach is discussed. In Chapter 7, the zero-baseline experiment is carried out with results analysed. In Chapter 8, the short baseline static test result is studied and analysed. In Chapter 9, the dynamic test for displacement detection and frequency determination is analysed. In Chapter 10, the results from the field experiment with respect to the Wilford bridge are discussed.

In this chapter, based on the limitations of current GNSS deformation monitoring applications, the potentials, and limits of adopting low-cost GNSS are examined. The aims and objectives of the study are specified. In the next chapter, a more detailed literature review of using GNSS technology for deformation monitoring is presented.

Chapter 2 Deformation monitoring with GNSS

2.1 Purpose of SHM and geo-hazards monitoring

In recent years, deformation monitoring of large civil engineering infrastructures has attracted more and more attention globally due to the decreasing serviceability caused by the deformation of the structures (Zhou et al., 2018). Some excessive deformation cases have even resulted in fatal damage and innumerable economic losses, for instance, structural deformation induced by a high magnitude earthquake or structural failure due to a lack of timely inspection or maintenance. The deformation response of the structure, which could lead to negative and severe consequences, is closely related to and may be a dominant factor responsible for its structural behaviour (Yi et al., 2010). Studies have shown a rapidly increasing research trend of structural health monitoring (SHM) for past decades which indicates the necessity and recognition regarding SHM (Farrar and Worden, 2007). This phenomenon may attribute to the increasing awareness of the social and economic impact civil infrastructure imposes on, while they malfunction or even collapse due to multiple-factor induced deformation (Chang et al., 2003).

Empirical studies on SHM have suggested that by implementing SHM on civil infrastructures, incipient abnormalities could be detected and identified based on the analysis of key parameters derived from in-situ measured continuous time-dependent data, offering the possibility for timely maintenance, and improvement of future design (Brownjohn, 2007; Yi et al., 2010). On the other hand, due to the frequent occurrence of natural geohazards (earthquakes, tsunamis, volcanic eruptions, glacial movement, etc.), landslides, subsidence, rockfalls, debris flow, and surface flow always occur. With the acceleration of urbanisation and industrialisation, this consequently could cause serious impacts for communities and infrastructures, especially when it happens in urban areas. Therefore, the impact resultant from geohazards should be carefully monitored and mitigated. The monitoring of geohazards aims to understand the mechanism of the disruptive process, thus countermeasures to mitigate the effect of the geohazards could be devised accordingly. Among all geohazard monitoring projects, landslide monitoring is one of the most popular and important subjects for constant surveillance due to its socio-economic significance (Angeli et al., 2000).

2.2 SHM

SHM, in the context of civil infrastructure monitoring, generally refers to the process of identifying damage within structures by analysis of modal properties, from which the deformation shape and dynamics parameters could be inferred(Farrar and Worden, 2007). SHM has evolved from the simplest visual inspection, tap test to an optimal overall statistical approach nowadays, including several phases of data acquisition, integration, analysis, etc. (Brownjohn, 2007) The modern way of SHM mainly aims at an in-situ continuous time-dependent measurement. It is expected structural problems could be identified when comparing parametrical analysis of the output timeseries signal with the predicted parameters from the established model in the design phase. With its ability to monitor both dynamic and quasi-static long-period displacement, the state-of-art SHM could be the optimal 'global health monitoring' approach which guarantees thorough analysis of the structure in operation (Brownjohn, 2007; Chang et al., 2003).

Many research has shown the SHM is preferably applied to particular types of civil infrastructures, such as high-rise buildings, historical buildings, viaducts, tunnels, dams, bridges, slender structures as towers and chimneys, etc., since they play an important role in daily life, or may cause devastating impact while they collapse or fail to function. The deformation of civil infrastructures is a result of different loading activities, which could be from various factors and majorly classified as environmental-related; such as seismic ground motion, wind, thermal changes (Yi et al., 2013b), or human activity induced, such as mining, water or oil extraction, excavation, piling, tunnelling, and service loading, etc. The empirical studies show the response variables to be measured from the SHM are displacement, accelerations, velocities, strain, etc. Based on these onsite measured parameters, the as-built properties of the constructed structure could be analysed and compared against that being conceived at the design phase, consequently giving feedback to the performance-based design, making the evaluation and prediction of structures behaviour under extreme loads possible (Chang et al., 2003).

2.2.1 Techniques related to SHM

To achieve SHM of civil engineering structures, various techniques could be adopted, some aiming to determine whether the damage is present at the entire structure, which is defined as the global health monitoring, and some aiming at the pinpoint of the location of the damage, defined as non-destructive evaluation (NDE) (Chang et al., 2003). The NDE technique could be done after the global health monitoring when damage is found in the structure to examine the exact location and extent of the damage. In this research, the NDE related aspect is not mentioned, and the interest is mainly focused on global health monitoring to detect the existence of damage in the structure.

Most of the global health monitoring is sensor-based, when implementing the SHM system, the critical issue to take into consideration is the decision on optimal sensors to employ (Yi et al., 2011). SHM could be carried out by geodetic surveys, such as the use of space-borne GNSS technique, pseudolite, adoption of remote sensing technology, like DInSAR interferometry, digital photogrammetry, and LIDAR (laser scanner), or use of conventional geodetic equipment such as levelling, theodolites and EDM, robotic total stations (RTS), etc., or with non-geodetic technique, such as inclinometer, fibre optic strain sensors, extensometer, and accelerometer, etc. (Kalkan, 2014; Erol et al., 2004). These techniques can be used either separately or as a combination. Lots of research has covered the usage of one single technique for deformation monitoring and discussed the integration of techniques to achieve better accuracy. However, when considering the deformation monitoring of civil engineering structures, remote sensing technologies such as DinSAR, photogrammetry, etc. are rarely adopted by most empirical research. The application of these technologies is mostly used for monitoring of large-scale areas, such as subsidence monitoring, landslide monitoring, surface deformation monitoring, mining area monitoring, etc., and over long period observations which normally take a longer period (up to several years) to monitor. Furthermore, these methods provide a dense array of displacement vectors for each point cloud characterised by low temporal resolution and normally has relatively lower accuracy. (Benoit et al., 2015)

The results of SHM from analysis of the in-situ measurement are normally compared with the FEM analysis for verification purposes. However, problems arise with the FEM analysis because the FEM is an analytical method, not many models could be easily constructed for the as-built building or bridges considering the aging conditions (Chang et al., 2003), therefore the FEM model based on theories and assumptions may not give true response prediction. This implies the necessity of doing SHM for the real-time health check of the structure.

2.2.2 Comparison between commonly used SHM geodetic methods

The most commonly adopted geodetic methods for civil infrastructure deformation monitoring nowadays are GNSS related, robotic total station/electronic theodolite based, or with alternative aiding of some accelerometers, inclination sensors, strainmeters, LVDT displacement transducer, etc. Comparing the space-based GNSS monitoring and ground-based terrestrial monitoring, they both have limitations and merits. As with GNSS, the major drawback is with regard to the height components of the solutions where less accurate results can be obtained compared to Eastings and Northings (Quan et al., 2016). This is largely owing to the biased satellite geometry for the height coordinate computation. The other drawback is mainly due to the sampling frequency of the GNSS receiver, the maximum sampling frequency is up to 10-20Hz, which puts a limit on the maximum oscillation frequency it can detect. GNSS error sources could also be a problem, as the inaccurate and imprecise measurement could be resulted from various factors, such as receiver noise, receiver/satellite clock offset, satellite orbit error, ionospheric and tropospheric bias, multipath, etc. Precision could also degrade indicated by poor DOP caused by bad satellite geometry or low satellite number in track. Sometimes cycle slips could also occur due to worse measuring conditions. Nevertheless, most of the errors could be mitigated by various techniques.

For the conventional terrestrial surveys, it can also be seen many disadvantages. Firstly, the sampling rate of the RTS is unstable and varies during the measurement (Psimoulis and Stiros, 2007). Secondly, RTS measurements could be easily influenced by weather, such as direct sunlight, rainy weather, etc. Equipment could also be influenced by temperature variations. Thirdly, the measurement could suffer drifting problems caused by systematic errors. Fourthly, the terrestrial measurement usually requires a line of sight aiming and tracking with no obstruction of views. It is also noted the level of automation of terrestrial surveys cannot be compared to GNSS, as GNSS signals are ubiquitous due to the established constellations and less likely to be influenced by ambient conditions.

In summary, the major advantages of GNSS monitoring over terrestrial monitoring techniques are; 1) high autonomy and continuity of the measurement with no requirement of line of sight, 2) accurate GNSS time stamp and constant sampling rate, 3) No long-period drift, instead, accuracy could improve with continuous measurement, 4) low influence from weather condition or human related errors,5) developed network of GNSS constellations, reference stations, etc. (Yi et al., 2013a; Hyzak et al., 1997; Yi et al., 2010; Brown et al., 2006)

2.2.3 Empirical studies for deformation monitoring of civil engineering structures

Considering the advantages of GNSS monitoring technique, it could be one of the most promising and state-of-art techniques used in deformation monitoring. GNSS technologies have already been adopted and developed for deformation monitoring applications over the past decade (Figure 2.1). Table 2.1 shows several examples of GNSS-based SHM in a chronological order. With the development of higher sampling rate GNSS receivers, it is shown that motions with larger modal frequency even up to 10Hz, could be detected.

Table 2. 1 *Empirical research, examples of SHM by geodetic receivers. The deformation monitoring using GNSS technologies includes but is not limited to those cases. (The table only includes some popular research which gains a considerable amount of research interest).*

Research object & Author	Excitation	Sampling rate	Methods	Displacement amplitude/accuracy	Modal Frequency (Hz)
Calgary tower (Lovse et al.,1995)	Wind	10Hz	PPK	More than ±16mm amplitude (N-S)	0.3
Humber bridge (Ashkenazi and Roberts, 1997)	Wind	N/A	RTK	Average vertical displacement around 15cm with mm accuracy	
Suspension bridge (Nakamura, 2000)	Wind	1Hz	RTK	max 20cm displacement with an error of 1.6 cm horizontally and 2.1 cm vertically	0.1-0.3
Tall building (Celebi and Sanli, 2002)	Wind	10Hz	RTK	N/A	0.24-0.25
Steel tower (Tamura et al., 2002)	Wind	10Hz	RTK	More than ±2cm displacement	0.57
Motion simulation table (Chan et al., 2006)	Wind	20Hz	PPK	Around 10mm vertical amplitude	0.17
Wilford bridge (Meng et al., 2007)	Human, wind	10Hz	PPK	8 cm vertical distance	1.73-4.80
Oscillator test (Psimoulis et al., 2008)	Imposed load	20 Hz	PPK	0.5-3.4cm amplitude	0.05-4Hz
Train bridge (Psimoulis et al., 2008)	Train	10 Hz	PPK	N/A	0.46Hz, ~3Hz
Suspension bridge (Yi et al., 2013a)	Wind, Traffic	50Hz 100Hz	RTK	33 mm vertical amplitude	0.68Hz-10.04Hz

Figure 2. 1 *Bridge monitoring with GNSS (Meng et al., 2007)*

2.3 Landslide monitoring

Landslide monitoring is the most studied area for geohazard monitoring applications due to potentially severe human casualties, property losses, and environmental degradation. Landslides are defined as the downslope movements of rocks, debris, or earth with gravity loading. The landslide ranges both spatially and temporally and could be triggered by earthquakes, volcanic activity, heavy rainfalls, and changes in groundwater level. These factors would weaken the rock or soil and destabilize the slope and consequently trigger the landslide. In landslide monitoring, the surface displacements of a slope are normally monitored where the magnitude, direction, velocity, and acceleration of displacements can indicate slope stability, thus the dynamics of the landslide could be inferred. Moreover, if the surface movement is detected early enough, the impending slope mass failure could be predicted.

2.3.1 Different geotechnical and geodetic techniques for landslide monitoring

Similar to SHM, there can be various approaches used in landslide monitoring to determine the deformation of structures and ground surface displacements, which can be classified into different categories (Savvaidis,2003); 1) Remote sensing technique by using satellites to obtain space derived information (InSAR); 2) Photogrammetric technique by using aerial photograph; 3) Ground-based geodetic technique and sensors (total stations, EDM instruments); 4) Satellite-based positioning technique adopting GNSS; 5) Geotechnic technique and sensors. Among these techniques, the GNSS is proved to guarantee high accuracy, continuous and reliable results with high flexibility in equipment deployment and measurement autonomy.

2.3.2 Landslide monitoring using GPS technology

For landslide monitoring using GPS, the measurement is with regard to the discrete points on the sliding surface where the GPS sensors are deployed, and reference (fiducial) stations are established outside of the deformation zone forming baselines (Figure 2.2). Currently, the positioning techniques used for monitoring applications are either episodic techniques for small-scale projects or continuous monitoring for regional-scale projects. These techniques differ in system installation, maintenance costs, and the quality of the resulting coordinate timeseries. For episodic GPS deformation monitoring, repeated GPS surveys are conducted every few weeks or months using static, rapid-static, or real-time kinematic GPS surveying techniques. The variations between the current coordinate and the initial value indicate the movement of the target, although discontinuous in time, the cumulative displacement of surface points could be measured (Gili et al., 2000). On the other hand, continuous monitoring GPS systems can be used for the detailed study of landslide motions on a local scale, where few GPS stations are established outside the landslide area as the reference, and monitoring stations are established in the critical point of the landslide zone, the data measured at the monitoring station and from reference stations are transmitted to a master control station, where data processing is made. The resultant timeseries of monitoring stations are continuously obtained, hence providing continuous monitoring and tracking of the landslide movement.

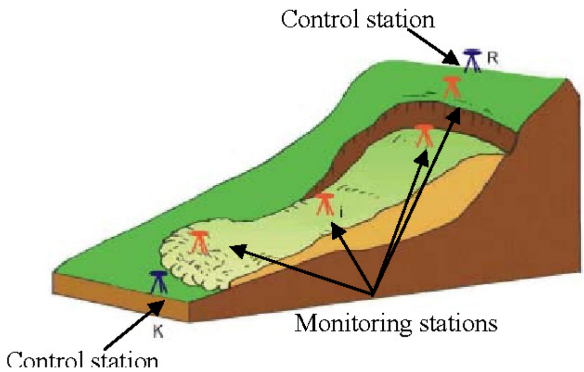

Figure 2. 2 *The concept of landslide monitoring using GPS Technology (Othman et al., 2011)*

The required accuracy for landslide monitoring according to Gili et al. (2000) should be at least in the order of centimetres in many cases. Therefore, the measurement from the GPS receiver is required to attain an accuracy of less than a centimetre for landslide monitoring application. According to Savvaidis (2003), the typical accuracy for GPS landslide monitoring by DD static mode is 5 mm ± 2 ppm with a baseline up to 50km, a more accurate result (1-3 mm ± 2ppm) could be achieved for a shorter baseline of 1-2km. On the other hand, the accuracy is claimed to be 5 mm ± 2 ppm for the RTK DGPS and ± 2 – 3 mm for continuous operating GPS. Gili et al. (2000) also reported that the precision of GPS in measuring surface displacement is normally 5–10 mm+1–2 ppm. In a GPS based landslide deformation survey, several features and capabilities of the receivers must be fulfilled (Savvaidis, 2003); 1) geodetic quality with multichannel, dual-frequency 2) carrier phase, receiver clock and signal strength measurement 3) no less than 1Hz sampling rate. Despite the conventional employment of dual-frequency geodetic receivers in empirical landslide monitoring research (Savvaidis, 2003; Gili et al., 2000), the recently developed mass-market single-frequency receivers have proven similar performance in landslide monitoring by many recent studies (Cina and Piras, 2015; Glabsch et al., 2009).

2.3.3 Empirical studies for landslide monitoring using GPS technology

The empirical studies regarding GPS-based landslide monitoring are summarised in Table 2.2 demonstrating the GNSS techniques adopted and the derived accuracy. The accuracies are determined per experimentation, which could be influenced by various factors, such as baseline length, satellite number, geometry of available satellites, monitoring environment, receiver/antenna quality, observation procedure & duration, processing software, and techniques used, etc. For other deformation monitoring applications, such as subsidence monitoring, volcano monitoring, earthquake monitoring, coastal monitoring, etc. Lots of research has also been carried out (Janssen et al., 2002), but it is beyond the scope of the study, and not focused on.

Table 2. 2 *Examples of empirical studies of GPS based landslide monitoring*

Study	Technique	Accuracy
(Gili et al.,2000)	Real-time Kinematic (RTK) and Fast static (FS)	12 to 16 mm in the horizontal plane, 18 to 24 mm in elevation
(Wang, 2011)	Post-processing with Local CORS network	accuracy under 5 mm horizontally and 15 mm vertically are often expected
(Heunecke et al., 2011)	Near real-time (NRTK)	Sub-centimetre accuracy
(Wang and Soler, 2012)	Online Positioning User Service / NOAA	Sub-centimetre accuracy
(Wang, 2013)	Precise Point Positioning with Single Receiver Phase Ambiguity (PPP-SRPA)	accuracy under 5 mm in the horizontal components and 2 cm in the vertical component
(Benoit et al., 2015)	Post-processing kinematic	a sub-centimetre level accuracy
(Cina and Piras, 2015)	NRTK	millimetre accuracy

2.4 Background and issues faced with some GNSS applications

With the maturation of GNSS technologies and the development of GNSS equipment over the last decades, most applications can be achieved with expected performance. Geodetic GNSS receivers, which are commonly employed to realize these activities, are usually expensive. For instance, empirical research has demonstrated that the use of GNSS technologies is extremely popular and beneficial in deformation monitoring and most traditional GNSS monitoring is by the employment of the geodetic dual-frequency receivers. Although millimetre accuracy can be achieved, one of the drawbacks is that deployment of a GNSS-based monitoring network requires huge investment which is majorly attributed to high-cost geodetic sensors used. This high-cost feature of the GNSS deformation monitoring approach restricted its extensive use by organizations that cannot afford it, reducing the efficiency of the monitoring system and consequently making the broad implementation of GNSS deformation monitoring unrealistic (Caldera et al., 2016).

The high expenses of a monitoring project are mainly reflected in three categories; 1) in the initial setup of the control network, where multiple locations of the structure may need to be monitored resulting in the requirement of deployment of many geodetic receivers, 2) GNSS receiver could be at risk of damage or missing especially in natural hazard monitoring, therefore the need for disposable characteristic is also a motivation for the low-cost GNSS monitoring system (Biagi et al., 2016), 3) unattended equipment with little protection may be subject to lightning, vandalism, or theft (Brown et al., 2006)

The drawbacks of the high-cost sensors used in monitoring applications all lead to the potential introduction of low-cost GNSS monitoring equipment, which should be expected to have similar functionality and performance to fulfil certain applications. Recently, the employment of low-cost receivers in various applications is gaining more and more research interest, particularly in deformation monitoring. This trend of emerging popularity in low-cost GNSS receiver study is largely related to the recent development of low-cost receivers. The evolution of GPS receiver hardware and signal processing software has boosted the ability of most low-cost GPS receivers for high-quality carrier phase measurement. This improved GPS positioning feature makes more accurate carrier phase measurement realistic and has drawn the attention of many researchers.

One of the most advantageous properties of low-cost receivers is their low cost. From an economical perspective, the low-cost feature has made the extensive use of the equipment applicable since the geodetic-grade receiver is far from affordable by most organisations, the adoption of the low-cost receiver will hugely decrease the budget and is designed to be affordable. This low-cost feature also indicates the equipment is disposable when monitoring under extreme environments and in the cases of monitoring of natural disasters (for instance landslides etc), reducing the economic impact of its possible loss or damage. Another major advantage of the low-cost property is that it permits greater sampling of cheap sensors in the area of interest so that the whole situation can be studied and described instead of data analysis of a few sensors constrained at specific locations (Poluzzi et al., 2019)

The other advantage of the modern low-cost receivers is the ability to have the high precision carrier phase measurement, offering the possibility for achieving a similar level of results compared to geodetic receivers. The low-cost receivers can also allow multi-constellation (GPS, GLONASS, Galileo, BeiDou, SBAS, etc.) observations. This indicate that an improved satellite geometry is possible by a combination of various constellations, which could also be a potential for monitoring with higher accuracy. Compared to the geodetic receiver, another advantage is owing to its simplicity. With only single-frequency observation, and few tracking channels, low-cost GNSS receivers are normally energy efficient, compact, and of smaller equipment size, which indicates less power consumption and makes it easier to carry.

The disadvantages arising from the low-cost monitoring system are also obvious. Firstly, due to single-frequency observation, much less information is available for solving the carrier phase ambiguity and creating ionospheric free observables. Secondly, low-cost GNSS receivers are characterised by is their poor multipath mitigation capability, less stable oscillators, and low SNR. The nature of the low-cost components used in the receiver also implies larger noise, poorer performance regarding accuracy and functionality.

In this Chapter, it is studied that the method adopted for GNSS deformation monitoring by most researchers over the past decades is using survey-grade receivers with differential processing between rover and reference receiver. Nevertheless, very few research has been carried out to study whether the low-cost GNSS receiver could be implemented to fulfil this objective. The empirical research with geodetic GNSS receivers shows results with millimetre accuracy (Yu et al., 2019), with less accurate and precise results from low-cost receivers. Before reviewing the empirical research on low-cost GNSS receivers, the theory, concept, and algorithms of GNSS specifically on short baseline deformation applications are introduced in the next chapter.

Chapter 3 An introduction to GNSS and DD algorithms

3.1 An Overview to GNSS

A global navigation system usually contains four major segments, the ground segment, control segment, space segment, and user segment. The space segment refers to the satellites transmitting signals, the user segment refers to the user receivers for GNSS signal tracking, and the control segment consists of operational control stations (OCS) to monitor the satellite and update the satellite information, more specifically, for GPS constellation, inverted code pseudoranges are used to calculate the satellite coordinate for broadcast ephemeris. The ground segment facilitates the user segments by providing reference control and precise ephemeris in real-time. The basic concept of GNSS is through trilateration, the unknown position could be determined by measuring distances from a known coordinate. It is normally perceived that observations from at least 4 satellites are needed for locating the unknown point.

The signal transmitted to the receiver from the satellite is encoded with navigation message including broadcast ephemeris for the receiver to compute satellite orbit coordinate and the almanac containing satellite time, satellite clock error and satellite status information, etc. Apart from the navigation message, the pseudorange is also measured by observing and processing signals within receivers. The pseudorange is a direct measurement of the one-way range (distance) from a satellite to a receiver. The receiver acquires incoming signal from the satellite, by creating internal replica signal and comparing them with the incoming signal, the travel time can be measured by the time of delay between the replica signal and incoming signal. To calculate the time delay, the technique of autocorrelation of the incoming signal from its replica signals is adopted. The pseudo distance between the satellite and receiver is formed by Equation 3.1 where the time difference is the difference between the time of transmission from the satellite atomic clock and time of reception from the receiver atomic clock.

$$Pseudorange = \ (time\ difference) \ * \ speed\ of\ light$$

Equation 3. 1 *Pseudorange equation*

The error budget within the time difference could originate from satellite clock error which can be modelled by information in the navigation message as a polynomial and the receiver clock error which could be estimated based on calculation. The pseudorange measurement is measured by the receiver and expressed in two forms, code pseudorange and carrier phase.

There are several Global Navigation Satellite Systems (GNSS), such as GPS, GLONASS, Galileo, BeiDou, and some regional navigation satellite systems such as QZSS and IRNSS and several regional augmentation systems. Table 3.1 compares several parameters and configurations of GPS, GLONASS, Galileo constellation. Apart from the GNSS from Table 3.1, BeiDou is another GNSS offering global coverage. The constellation consists of 35 satellites, including 5 geostationary orbits (GEO) satellites, 27 MEO orbits, and 3 Inclined Geosynchronous Orbit (IGSO), The signals are based on CDMA technique classified as B1 1575.42 MHz, B2 1191.795 MHz, and B3

1268.52 MHz. Currently, there are 31 GPS satellites, 24 GLONASS satellites, 22 Galileo satellites, 35 BeiDou satellites in orbit, the additional satellites provide redundant measurement improving accuracy, reliability, and availability of the system.

Table 3. 1 *Comparison between GPS, GLONASS, Galileo systems*

	GPS	GLONASS	Galileo
Initial design	24 nominal satellites in 6 planes for global coverage	24 satellites in 3 planes for global coverage	30 nominal satellites in 3 orbital planes
Plane inclination	55° inclination to the equator	64.8°inclination to equator	56° inclination to the equator
Orbit height	MEO (~20,200km altitude above the Earth)	MEO(~19100km altitude above the Earth)	MEO(~23222km altitude above the Earth)
Orbital Period	half of a sidereal day (around 11 hours and 58 minutes)	Around 11 hours and 15 minutes	Around 14hr 04min 45sec
Constellation Repeatability	~1 sidereal day	~8 sidereal days	~10 sidereal days
Signal frequency	same frequency among satellites adopting CDMA	different carrier frequency signal for different satellites adopting FDMA	same frequency among satellites adopting CDMA
Carrier signals Frequency and wavelength	L1 carrier (1575.42MHz,19cm) L2 carrier (1227.60MHz,24.4cm) L5 carrier (1176.45MHz,25.48cm)	L1 band (1597MHz-1617MHz) L2 band (1240-1260MHz)	E1 carrier (1575.42MHz) E5a (1176.45MHz) E5b (1207.14MHz,) E6 (1278.75 MHz)
Phase modulation on carrier signals	C/A code (L1), P code (L1, L2), and Navigation message (L1)	N/A	N/A
Highlights		suitable for high latitude measurement due to satellite orbits	

3.2 Coordinate frame and time frame

3.2.1 Coordinate frame

The Terrestrial Reference System (TRS) is a spatial reference system following the diurnal motion of the earth. In this geometric framework, unique coordinates of specific points can be defined. However, due to geophysical effects (tectonic or tidal deformations), points on the solid surface of the Earth regarding TRS usually have small variations with time. For GNSS, a TRS defines origin, orientation, and scale. It also includes the introduction of ellipsoidal parameter semi-major axis (a), and either flattening (1/f) or eccentricity (e^2) and various fundamental constants, c, GM, etc. A Terrestrial Reference Frame (TRF), on the other hand, determines the precise coordinate of positions on a TRS in a specific coordinate system (Cartesian, geographic, mapping). Therefore, the TRF is a realization and materialization of TRS, by setting precise coordinates physically to each point in the earth's solid surface.

The conventional TRS is defined as a tri-dimensional reference frame co-rotating with rotation of the earth with origin defined as the Earth mass geocentre, equatorial plane perpendicular to the axis of rotation of the Earth and passing through the mass geocentre of the Earth. The axes are defined with the Z-axis aiming at conventional mean pole perpendicular to the equatorial plane, X-axis directing at conventional zero meridian, and Y-axis mutually perpendicular to X and Z axis based on the right-handed system.

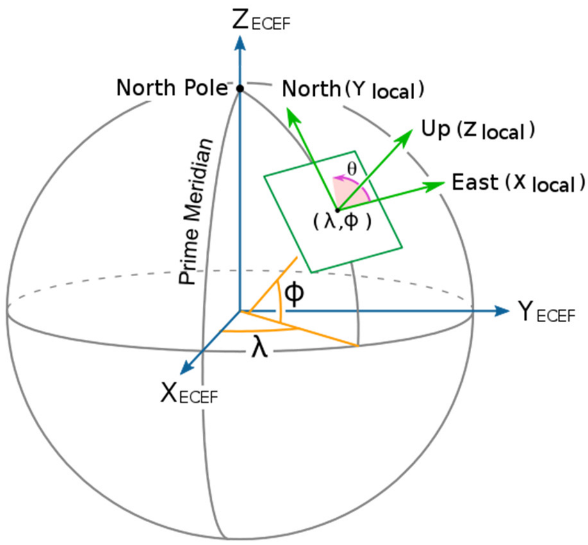

Figure 3. 1 *Sketch of different TRFs; ECEF, E/N/U and Longitude/Latitude (reprinted from 'ECEF ENU Longitude Latitude relationship in right-hand rule' by Kkddkkdd, 2017 (https://commons.wikimedia.org/wiki/File:ECEF_ENU_Longitude_Latitude_right-hand-rule.svg) CC-BY-SA-4.0*

In GNSS, a particular TRF so-called Earth-Centred, Earth-Fixed reference frame (ECEF) is adopted, where the equatorial plane, international reference pole (IRP) are fixed; international reference meridian (IRM), X, Y, Z Cartesian coordinate axes are fixed and rotate with the Earth, however 'reference' points on the solid Earth are allowed to move within the TRF due to plate tectonics. Therefore, the realisation of ECEF needs to account for the coordinates and velocity of plate tectonics and needs refinement with time to improve the coordinates and velocities. In Figure 3.1, it can be shown that a point on the earth could be represented in three ways. Firstly, in the ECEF cartesian coordinate by (X, Y, Z). This representation is widely used for scientific applications but not convenient for end-users. For geographic and geodetic purposes, a second way of representing the positions is adopted by defining the location with explicit geodetic coordinate, namely by using latitude, longitude, and ellipsoidal height. In the geodetic coordinate representation, the ellipsoidal parameters are defined with semi-major axis (a), flattening (1/f) and eccentricity (e^2) to model the earth as the best fit ellipsoid. The reference ellipsoid is defined and used as a preferred surface, where the latitude, longitude, and height calculations are with regard to. The latitude is defined as the angle between the ellipsoidal equator plane and a line passing the measured point that is normal to the reference ellipsoid. The longitude is the angle between zero meridian and plane containing the normal and minor axis of the ellipsoid which measures the rotational angle between the zero meridian and the measured point. The ellipsoidal height is the distance above the ellipsoid along normal, positive if above the ellipsoid and negative if below. A third way of representing the location is through the local cartesian coordinate system. The local coordinate system assumes the flat earth surface in a small area (less than 4km) where the earth curvature is not taken into account and uses E/N/U coordinate to represent the geo-location of elements. Easting is the eastward-measured distance and Northing is the northward-measured distance most commonly associated with Universal Transverse Mercator (UTM) coordinate system. It is a convenient coordinate where Euclidean geometry is applicable. The relationship between ECEF, E/N/U, and geodetic coordinate can be described using equations, where the coordinates are interchangeable by coordinate transformation matrices.

There are several global TRF and TRS, such as International Terrestrial Reference System (ITRS) and International Terrestrial Reference Frame (ITRF), World Geodetic System 1984 (WGS84), and European Terrestrial Reference System (ETRS) and European Terrestrial Reference Frame (ETRF). The ITRF combines space geodetic stations around the world forming a polyhedron network based on several space geodesy techniques such as VLBI (Very Long Baseline Interferometry), GPS (Global Positioning System), SLR (Satellite Laser Ranging), and DORIS (Doppler Orbitography and Radiopositioning Integrated by Satellite). As a result, global terrestrial reference frames are established with station positions and velocities. The reference ellipsoid used in ITRF is the Geodetic Reference System of 1980 (GRS80) ellipsoid (with a=6378137 m, 1/f=298.257). ITRF is the most accurate (a few centimetres) and is realised over the years with improved accuracy. Each improvement includes more stations and longer observation periods leading to more confidence in positions and velocities determination.

The world geodetic system WGS84 is an initially defined world geodetic system in 1984 where the TRS adopts WGS84 ellipsoid, gravity field, and geoid model. The WGS84 ellipsoid model (a=6378137 m, 1/f=298.257223563) is said to be identical with the GRS80 ellipsoid at a millimetre level. The initial realisation of the TRF of WGS84 is based on positions computed from the transit satellite system with an accuracy of one-to-two-meter level assuming coordinates of the control station are fixed in time. However, with the improvement of either TRS (gravity field and geoid model) or re-realisations of TRF over the last decades with some IGS stations fixed to ITRF coordinates, the WGS is refined with station coordinates of control segment sites reaching ~1cm accuracy with the inclusion of station velocities. Consequently, for most practical applications, the most recent WGS84 and ITRS are closely consistent and coincident which makes no difference.

The ETRS89 is the TRS adopted by European Reference Frame (EUREF). The EUREF decides to freeze and fix the reference coordinates where the European plate was on 1 January 1989. This leads to ETRS89 coinciding with ITRS at the epoch 1989.0 and fixed to the stable part of the Eurasian Plate. The ETRS89 is realized several times over Europe and nationally to take full benefit of successively improved realizations of the ITRS. The realization includes the first computation of station coordinates in current ITRF at the epoch of observation, then transformed to ETRF at the epoch of 1989.

3.2.2 Time Frame

In geodesy, the rate of change of hour angle defines time. With time reference point set as the passage of an object (sun or star) across the meridian. The hour angle is measured positive after mid-day when the sun goes to the west. Apparent solar time describes the hour angle of the passage of the real sun across the meridian based on the position of the sun in the sky. On the other hand, mean solar time is based on the hour angle of the mean sun, which assumes that the sun travels at a uniform speed throughout the year. Due to the ellipticity of the earth's orbit around the sun and obliquity of the ecliptic, the equation of time remains, which results in a discrepancy of around ±15 min between apparent solar time and mean solar time. The local mean time (LMT) is defined by the local hour angle of mean sun +12h and the Greenwich Mean Time GMT is specifically for the Greenwich hour angle of the mean sun, the GMT is used as a universal time reference. Another way of time definition is by sidereal time, based on Earth's rate of rotation measured relative to the fixed stars instead of using the sun as the reference since Earth completes one more rotation with respect to stars than it appears to with respect to the sun. Similarly, the Local sidereal time (LST) and the Greenwich sidereal time (GST) can be defined.

The universal time (UT) is a time standard based on Earth's rotation relative to distant celestial objects (stars and quasars), but with a scaling factor and other adjustments to make them closer to solar time. UT0 is a universal time determined at a specific observatory by observing the diurnal motion of stars or extragalactic radio sources, without considering the polar motion. UT1, on the other hand, is scaled by a factor of (one mean solar day)/(one sidereal day) to represent mean solar time at 0° longitude, with small adjustments for polar motions, which is a principal form of Universal Time. UT2 is a smoothed version of UT1 by filtering out periodic seasonal variations. UTC is a primary time standard universally used to regulate time based on International Atomic Time (TAI), the UTC usually has 86400s each day, however, leap seconds are also introduced occasionally to keep it within 0.9 seconds of UT1. Up till now, the TAI is ahead of UTC by 37 seconds, indicating the Earth's rotation speed slowing down. Time related to all GNSS is realised with atomic timescales linked to UTC. GPS Time (GPST) is defined by the GPS Control segment based on atomic clocks at the monitor stations and onboard the satellites. The GPST started in 1980, the epoch when the TAI leads UTC by 19s, and with no leap seconds introduced, this results in the current GPST ahead of UTC by 18 seconds. GPS time is synchronised with UTC and kept within 25ns level. GLONASS time (GLONSST) is defined by GLONASS ground segment by Central Synchronizer using a high precision atomic clock with leap seconds implementation, and the difference between the UTC and GLONASST is kept within 1 ms plus three hours. Galileo system time (GST) is defined by Galileo Central Segment in synchronisation with TAI within 50ns offset without the inclusion of leap seconds. BeiDou System Time (BDT) is defined by a composite clock based on the clock ensembles of the master control station and monitor station. BDT starts at 2006 based on UTC, the epoch when UTC is behind TAI by 33s, without the inclusion of leap seconds and synchronised to UTC within 100ns offset.

3.3 Pseudorange observation equations and error sources

3.3.1 Code pseudorange and carrier-phase observation model

The code pseudorange can be represented by observation Equation 3.2

$$PR_u^e = \rho_u^e\,(T^e, T_u)\ +\ c\,(\delta\,\tau_u -\ \delta\,t^e\,) + dion_u^e + dtrop_u^e + v_u^e$$

Equation 3. 2 *Code pseudorange observation equation*

Where

- $PR^e{}_u$ is the code pseudo-range observable reflecting the one-way distance between satellite e and user receiver u measured by user receiver u in units of metres, which can be calculated by the difference between the time of transmission t^e and the time of reception τ_u scaled by the speed of light in vacuum c.
- $\rho^e{}_u$ is the geometric range in units of meters between satellite e and user receiver u which is related to GPS time T and can be calculated by $\rho_u^e(T^e, T_u) = \sqrt{(X^e - X_u)^2 + (Y^e - Y_u)^2 + (Z^e - Z_u)^2}$, where (X^e, Y^e, Z^e) are known coordinates and (X_u, Y_u, Z_u) are unknown coordinates
- $\delta\,\tau_u$ is the receiver clock offset of user receiver u at the time of reception in unit of seconds due to receiver quartz clock offset from the GPS time.
- $\delta\,t^e$ is the satellite clock offset of satellite e from GPS time at the time of transmission.
- $dion^e{}_u$ represents the ionospheric bias between satellite e and user receiver u as a delaying impact on the measurement.
- $dtrop^e{}_u$ represents the delaying impact of tropospheric bias on measurement
- $v^e{}_u$ is an observation residual

The carrier phase pseudorange observation can be formulated by Equation 3.3

$$\varphi_u^e = \frac{f}{c}\,\rho_u^e\,(T^e, T_u) + f(\delta\,\tau_u -\ \delta\,t^e)\ -\ N_u^e\ -\ fcb^e - \frac{f}{c}\,dion_u^e + \frac{f}{c}\,dtrop_u^e\ + v_u^e$$

Equation 3. 3 *Carrier phase pseudo-range observation equation*

Where

- $\varphi^e{}_u$ is the carrier phase observable measured in units of cycles between satellite e and user receiver u and is comprised of an approximate initial phase ambiguity to be resolved at the lock on, a direct measurement of change in the integer number of wavelengths since lock-on, and a combination of the satellite and receiver's fractional parts of wavelength.
- $N^e{}_u$ is the correction to the approximate initial phase ambiguity between satellite e and user receiver u at lock-on in units of cycles which can be calculated as the difference between the receiver's approximate and the true initial phase ambiguity
- fcb^e is the fractional cycle bias of satellite e at the time of transmission t^e in unit of cycles, equal to the error in the satellite fractional part of the wavelength.

- $dion^e_u$ represents the ionospheric bias between satellite e and user receiver u as advancing impact (negative delay) on the measurement
- $dtrop^e_u$ represent the delaying impact of tropospheric bias on measurement.

3.3.2 Measurement Errors

GNSS systematic biases and errors are usually categorised into satellite, atmospheric, and station related errors. Satellite related errors include satellite coordinates (X_e, Y_e, Z_e) error and satellite clock offset error ($\delta\ t^e$) given in ephemeris and errors in satellite antenna phase centre (APC) model. The error in satellite coordinates is around 1m, and 5ns for satellite clock offset for broadcast ephemeris which uses inverted code pseudo-ranges with few limited operational control segments (OCS); The error in satellite coordinates is 0.025-0.05m and 0.075ns-3ns for satellite clock offset for precise ephemeris determining the precise ephemerides based on a global network of stations with the use of DD phase pseudoranges. The satellite APC is determined by phase centre offset (PCO) and phase centre variation (PCV), where the mean satellite APC is offset from the centre of mass of the satellite by a constant PCO of about 1 to 2.5m, the point of transmission varies about the mean APC due to PCV of several millimetres.

Atmosphere related errors include ionospheric bias and tropospheric bias. The ionosphere acts as a dispersive medium to GPS signals. It delays the code pseudorange but advances the phase pseudorange by the same amount. The magnitude of this delay/advance is a function of total electron content, frequency, and elevation angle and can be represented by Equation 3.4,

$$dion_u^e = \frac{1}{sin\ (elev^e{}_u)} * \frac{40.3}{f^2} * VETC_u$$

Equation 3. 4 *Magnitude of ionosphere delay/advance*

Where

- $\frac{1}{\sin\ (elev^e{}_u)}$ is referred to as the mapping function (MF^e_u) with $elev^e_u$ representing the elevation angle of satellite e with respect to a user receiver u.
- $VETC_u$ is a model of the vertical TEC at user receiver u.

The troposphere delays both the code and phase pseudorange by the same amount. The magnitude of the delay is comprised of hydrostatic components accounting for more than 90% of total tropospheric bias which can be expressed as a function of atmospheric pressure, temperature, and elevation angle; and <10% of the total tropospheric bias is related to the distribution of water vapour in the atmosphere and elevation angle classified as wet components. The hydrostatic components could be modelled using Equation 3.5 and could generally be rewritten as Equation 3.6.

$$dtrop_u^e = \frac{1}{sin\ (elev^e{}_u)} * 0.002274 * \ P_u$$

Equation 3. 5 *Hydrostatic components calculation with Hopfield model*

$$dtrop_u^e = MF_u^e * ZHD_u$$

Equation 3. 6 *Hydrostatic components general calculation equation*

Where

- *(0.002274*P_u)* is a model (Hopfield model) for the zenith hydrostatic delay *ZHD_u* at user receiver u
- P_u is the atmospheric pressure at receiver u

Station related errors include receiver clock error, receiver error, cycle slip, multipath bias, receiver APC model error, errors in models for solid earth tides and ocean tide loading, etc. The cause for receiver clock errors originates that the receivers use quartz crystal clock, which is less stable than satellite atomic clocks. However, receiver clock error can be eliminated by comparing the TOA of signals from two satellites. Receiver errors include receiver noise and receiver internal delay. Receiver noise refers to the position error caused by the GNSS receiver hardware and software. Usually higher receiver noise could be detected from low-cost receivers and lower receiver noise from high-end receivers. Receiver internal delay is caused by receivers' filter and processing delay due to different signal path lengths for each channel. Cycle slips could cause accuracy degradation due to the reestablishment of integer ambiguity resolution. The multipath bias is the major source of interference and is caused by mixed measurements of direct and non-direct signals. The signals from the satellite propagating to the receiver are reflected resulting in the receiver acquiring signals from multiple paths of transmission. The multipath errors are a function of the wavelength which is larger for code pseudorange than phase pseudorange. The receiver APC error is due to that the antenna reference point (ARP) is not coincident with the point of reception where the signal is received. It is proved that dependent on antenna type and signal frequency, a constant PCO of several centimetres is observed between the mean APC and the ARP. However, the point of reception also varies from the mean APC and is defined as PCV. The PCV errors are normally of several millimetre magnitude and are related to azimuth, the antenna type, and the frequency of the signal.

The errors aforementioned are also referred to as user equivalent range errors (UERE) which are errors associated with satellite/receiver clocks, satellite orbit, atmosphere, multipath, etc. Despite the UERE, the accuracy of GNSS positioning is also related to the arrangement of satellites in the sky. Dilution of precision (DOP) would occur if the satellite is clustered and close to each other. DOP is a term that multiplies the uncertainty associated with User Equivalent Range Errors based on the error propagation and defines the relationship between satellite geometry and the achieved precision. The DOP value normally ranges between 1 and above 20, with 1 indicating ideal case and 20 indicating poor. The DOP can be expressed by several components; GDOP, PDOP, VDOP, HDOP, TDOP, which describe the DOP value in geometry, position, vertical component, horizontal components, and time respectively.

3.3.3 Cycle slips

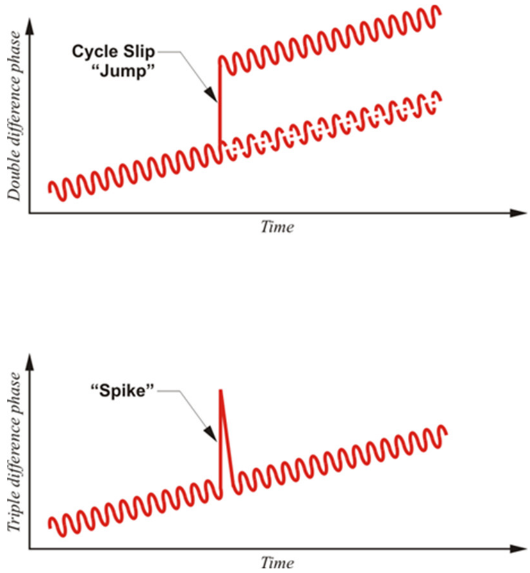

Figure 3. 2 *Cycle slip in DD and triple difference (Van Sickle, 2008)*

A cycle slip is a discontinuity in a receiver's phase lock on a satellite's signal. After convergence from the float solution, the initial phase ambiguity should be fixed for each satellite/ receiver combination since lock on. Whereas in practice, the receiver sometimes loses lock on satellites, due to i) power loss, ii) a very low signal-to-noise ratio caused by multipath, interference, high receiver dynamics, low satellite elevation, etc iii) a failure of the receiver software such as internal receiver tracking problems iv) malfunctioning of satellite oscillator v) severe ionospheric conditions vi) obstructions (buildings; trees; terrain) blocking satellite signals transmitted to receivers.

After the receiver regains tracking and locks on the satellite, a new phase ambiguity is created. The cycle slip occurs when the receiver temporarily loses lock on the satellite and when a lock on reinitiates, a new integer ambiguity is resolved. The cycle slip is usually shown as a jump in DD and a spike in a triple difference (Figure 3.2). Cycle slips usually affect more on carrier phase measurements where high precision measurement is needed. The cycle slip causes a problem of reinitiating the ambiguity resolution N^e_u where the previous resolve integer ambiguity becomes instantly unavailable. Consequently, carrier phase positioning accuracy is highly degraded if cycle slips are not detected and repaired.

In RTKLIB, the software uses the loss-of-lock indicator (LLI), lock-time, and the linear geometry jump (LG Jump) for cycle slip detection (Takasu, 2013). The LLI and lock time can be provided from the receiver in the RINEX observation file and geometry-free LC (linear combination) phase jumps can be monitored if the dual-frequency L1 and L2 carrier-phase measurements are available. To resolve cycle slips, RTKLIB adopts the following approach, if a cycle slip is detected in the measurement data beyond a specified cycle slip threshold, the state of the corresponding SD carrier minus phase bias is reset to the initial value (Takasu, 2013).

3.4 Double Difference algorithms for short baseline kinematic technique

3.4.1 Formation of DD observables

There are different techniques adopted for positioning using GNSS either with the use of code pseudorange or carrier phase, for code pseudo-range, methods exist such as code pseudorange single point positioning, code pseudorange differential positioning. For phase pseudo-range, there are methods such as phase pseudo-range static, and kinematic double-differenced positioning. There is also precise point positioning which uses code and phase pseudo-ranges.

For deformation monitoring, the most frequently adopted method is phase pseudorange kinematic DD over short baselines. Figure 3.3 illustrates the setup of the DD process.

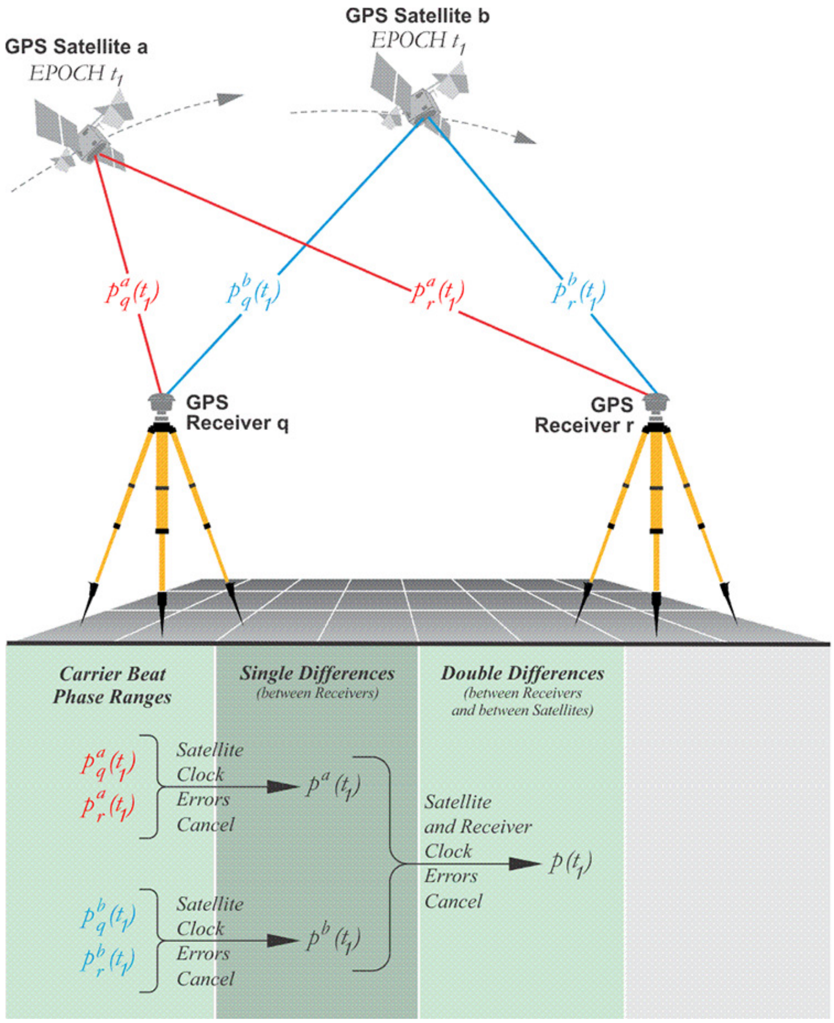

Figure 3. 3 *DD schematic illustration (Van Sickle, 2008)*

In the DD kinematic process with a short baseline, the reference receiver r is assumed static, while the rover receiver q is assumed kinematic with varying positions. For phase pseudo-range kinematic double-differenced positioning, coordinates of user receiver u are computed based on the single epoch of measurement, using broadcast ephemeris satellite coordinates and satellite clock offsets along with its phase pseudo-range observations and the phase pseudo-range observations from a reference receiver. From Figure 3.3, with SD between receivers, where the receivers receive the signal from the same satellite at the same epoch of transmission, the satellite clock and orbit errors cancel. With SD between satellites with respect to the same receiver, the receiver clock offset cancels. If the two SDs are combined, DD is formed which cancels the satellite orbit errors, satellite APC errors, satellite clock offset, and receiver clock offset. Furthermore, if the baseline between the rover receiver and reference receiver is short (<4km), the ionospheric and tropospheric error would largely be mitigated through differencing. Through the formation of double-differenced phase pseudo-range observation equations, the DD kinematic positioning first attempts to resolve the corrections to approximate initial ambiguities based on the first multiple epochs of measurement, so-called convergence, then the coordinate can be calculated after convergence. For satellite e and n, and receiver u and r, the undifferenced carrier phase pseudorange observation equations can be formed in Equation 3.7, with upper-script representing satellite and lower-script representing receiver.

$$\varphi_u^e = \frac{f}{c}\,\rho_u^e\,(T^e, T_u) + f(\delta\,\tau_u - \delta\,t^e) - N_u^e - fcb^e - \frac{f}{c}\,dion_u^e + \frac{f}{c}\,dtrop_u^e + v_u^e$$

$$\varphi_r^e = \frac{f}{c}\,\rho_r^e\,(T^e, T_r) + f(\delta\,\tau_r - \delta\,t^e) - N_r^e - fcb^e - \frac{f}{c}\,dion_r^e + \frac{f}{c}\,dtrop_r^e + v_r^e$$

$$\varphi_u^n = \frac{f}{c}\,\rho_u^n\,(T^n, T_u) + f(\delta\,\tau_u - \delta\,t^n) - N_u^n - fcb^n - \frac{f}{c}\,dion_u^n + \frac{f}{c}\,dtrop_u^n + v_u^n$$

$$\varphi_r^n = \frac{f}{c}\,\rho_r^n\,(T^n, T_r) + f(\delta\,\tau_r - \delta\,t^n) - N_r^n - fcb^n - \frac{f}{c}\,dion_r^n + \frac{f}{c}\,dtrop_r^n + v_r^n$$

Equation 3. 7 *Undifferenced carrier phase pseudorange measurement equations from satellite e, n to receiver u, r*

The DD observation equations can be formed by first difference between receivers, i.e. $\varphi_u^e - \varphi_r^e$ & $\varphi_u^n - \varphi_r^n$. Then the results can be further differenced as $(\varphi_u^n - \varphi_r^n) - (\varphi_u^e - \varphi_r^e)$ between satellites as DD. We use φ_{ru}^{en} to notate the DD phase pseudorange observable, therefore $\varphi_{ru}^{en} = (\varphi_u^n - \varphi_r^n) - (\varphi_u^e - \varphi_r^e)$ and by substitution,

$$\varphi_{ru}^{en} = \frac{f}{c}\,\rho_{ru}^{en}\,(T^e, T^n, T_r, T_u) - N_{ru}^{en} - \frac{f}{c}\,dion_{ru}^{en} + \frac{f}{c}\,dtrop_{ru}^{en} + v_{ru}^{en}\,,$$

Equation 3. 8 *DD carrier phase equations between satellite e, n and receiver r, u*

Where

- $\rho_{ru}^{en}\,(T^e, T^n, T_r, T_u) = [\,\rho_u^n\,(T^n, T_u) - \rho_r^n\,(T^n, T_r)] - [\,\rho_u^e\,(T^e, T_u) - \rho_r^e\,(T^e, T_r)]$
- $N_{ru}^{en} = (N_u^n - N_r^n) - (N_u^e - N_r^e)$
- $dion_{ru}^{en} = (dion_u^n - dion_r^n) - (dion_u^e - dion_r^e)$
- $dtrop_{ru}^{en} = (dtrop_u^n - dtrop_r^n) - (dtrop_u^e - dtrop_r^e)$
- $v_{ru}^{en} = (v_u^n - v_r^n) - (v_u^e - v_r^e)$

For a short baseline (few kilometres) and similar altitude between two receivers, it is assumed that the ionospheric and tropospheric biases will affect the observations at each receiver by approximately the same amount: $dion^n{}_u \approx dion^n{}_r$, $dion^e{}_u \approx dion^e{}_r$,

$dtrop^{n}_{u} \approx dtrop^{n}_{r}$, $dtrop^{e}_{u} \approx dtrop^{e}_{r}$, with resulting $dion^{en}_{ru}=0$, and $dtrop^{en}_{ru}=0$. Therefore, substituting $dion^{en}_{ru}=0$ and $dtrop^{en}_{ru}=0$ into Equation 3.8, it can be rewritten as,

$$\varphi_{ru}^{en} = \frac{f}{c}\, \rho_{ru}^{en}\,(T^e, T^n, T_r, T_u) - N_{ru}^{en} + v_{ru}^{en}$$

Equation 3. 9 *DD carrier phase equations between satellite e, n and receiver r, u for a short baseline after removing the ionospheric and tropospheric biases*

3.4.2 Least squares adjustment

A typical notation for GNSS observation in least square is

$$Ax = b + v,$$

Equation 3. 10 *Measurement model for least square equation formation*

Where

- A is a matrix containing the coefficient of observation equation as partial differentials
- x is a vector containing the corrections to the unknown parameters in the observation equation
- b is a vector containing the (observed-computed) values
- v is a vector containing the residuals

When solving for the receiver coordinates and corrections to the approximate initial phase ambiguity, the least-squares can be formed as

$$\frac{\partial \Phi_{ru}^{en}}{\partial X_u}\Delta X_u + \frac{\partial \Phi_{ru}^{en}}{\partial Y_u}\Delta Y_u + \frac{\partial \Phi_{ru}^{en}}{\partial Z_u}\Delta Z_u + \frac{\partial \Phi_{ru}^{en}}{\partial N_{ru}^{en}}\Delta N_{ru}^{en} = [observed\Phi_{ru}^{en} - computed\Phi_{ru}^{en}] + v_{ru}^{en}$$

Equation 3. 11 *Least square formation for a DD phase observable between satellite e, n and receiver r, u*

Where

- $\frac{\partial \Phi_{ru}^{en}}{\partial X_u} = \frac{f}{c}[-\frac{(X^n - X_u)}{\rho_u^n} + \frac{(X^e - X_u)}{\rho_u^e}]$
- $\frac{\partial \Phi_{ru}^{en}}{\partial Y_u} = \frac{f}{c}[-\frac{(Y^n - Y_u)}{\rho_u^n} + \frac{(Y^e - Y_u)}{\rho_u^e}]$
- $\frac{\partial \Phi_{ru}^{en}}{\partial Z_u} = \frac{f}{c}[-\frac{(Z^n - Z_u)}{\rho_u^n} + \frac{(Z^e - Z_u)}{\rho_u^e}]$
- $\frac{\partial \Phi_{ru}^{en}}{\partial N_{ru}^{en}} = -1$

For a four-satellite phase pseudorange double-differenced observation equation with a short baseline (Figure 3.4), three least squares can be formed as,

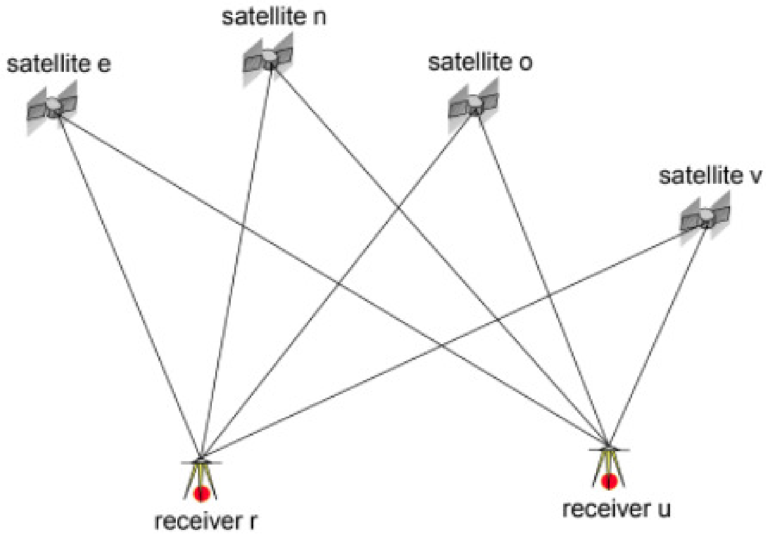

Figure 3. 4 *DD formation of baseline between reference receiver r and user receiver u when four satellites are tracked*

$$\frac{\partial\Phi_{ru}^{en}}{\partial X_u}\Delta X_u+\frac{\partial\Phi_{ru}^{en}}{\partial Y_u}\Delta Y_u+\frac{\partial\Phi_{ru}^{en}}{\partial Z_u}\Delta Z_u+\frac{\partial\Phi_{ru}^{en}}{\partial N_{ru}^{en}}\Delta N_{ru}^{en}=[observed\Phi_{ru}^{en}-computed\Phi_{ru}^{en}]+v_{ru}^{en}$$

$$\frac{\partial\Phi_{ru}^{eo}}{\partial X_u}\Delta X_u+\frac{\partial\Phi_{ru}^{eo}}{\partial Y_u}\Delta Y_u+\frac{\partial\Phi_{ru}^{eo}}{\partial Z_u}\Delta Z_u+\frac{\partial\Phi_{ru}^{eo}}{\partial N_{ru}^{eo}}\Delta N_{ru}^{eo}=[observed\Phi_{ru}^{eo}-computed\Phi_{ru}^{eo}]+v_{ru}^{eo}$$

$$\frac{\partial\Phi_{ru}^{ev}}{\partial X_u}\Delta X_u+\frac{\partial\Phi_{ru}^{ev}}{\partial Y_u}\Delta Y_u+\frac{\partial\Phi_{ru}^{ev}}{\partial Z_u}\Delta Z_u+\frac{\partial\Phi_{ru}^{ev}}{\partial N_{ru}^{ev}}\Delta N_{ru}^{ev}=[observed\Phi_{ru}^{ev}-computed\Phi_{ru}^{ev}]+v_{ru}^{ev}$$

Equation 3. 12 *Least squares formation for the DD between satellite e and satellite n, satellite e and satellite o, satellite e and satellite v with respect to user receiver u and reference receiver r respectively*

The DD partial derivative coefficient formed from other satellites o, satellite v with respect to e could also be derived similarly to the satellite with respect to e and n. Analogous to the least square notation in Equation 3.10, it is derived the representation for each vector A, x, b, and v.

$$A=\begin{matrix}\frac{\partial\Phi_{ru}^{en}}{\partial X_u} & \frac{\partial\Phi_{ru}^{en}}{\partial Y_u} & \frac{\partial\Phi_{ru}^{en}}{\partial Z_u} & -1 & 0 & 0\\ \frac{\partial\Phi_{ru}^{eo}}{\partial X_u} & \frac{\partial\Phi_{ru}^{eo}}{\partial Y_u} & \frac{\partial\Phi_{ru}^{eo}}{\partial Z_u} & 0 & -1 & 0\\ \frac{\partial\Phi_{ru}^{ev}}{\partial X_u} & \frac{\partial\Phi_{ru}^{ev}}{\partial Y_u} & \frac{\partial\Phi_{ru}^{ev}}{\partial Z_u} & 0 & 0 & -1\end{matrix}\qquad x=\begin{matrix}\Delta X_u\\ \Delta Y_u\\ \Delta Z_u\\ \Delta N_{ru}^{en}\\ \Delta N_{ru}^{eo}\\ \Delta N_{ru}^{ev}\end{matrix}$$

$$b=\begin{matrix}observed\Phi_{ru}^{en}-computed\Phi_{ru}^{en}\\ observed\Phi_{ru}^{eo}-computed\Phi_{ru}^{eo}\\ observed\Phi_{ru}^{ev}-computed\Phi_{ru}^{ev}\end{matrix}=\begin{matrix}observed\Phi_{ru}^{en}-(\frac{f}{c}\rho_{ru}^{en}-N_{ru}^{en})\\ observed\Phi_{ru}^{eo}-(\frac{f}{c}\rho_{ru}^{eo}-N_{ru}^{eo})\\ observed\Phi_{ru}^{ev}-(\frac{f}{c}\rho_{ru}^{ev}-N_{ru}^{ev})\end{matrix}\qquad v=\begin{matrix}v_{ru}^{en}\\ v_{ru}^{eo}\\ v_{ru}^{ev}\end{matrix}$$

The computation of the above least-squares leads to the float solutions where the $\Delta\mathrm{N}_{\mathrm{ru}}^{\mathrm{en}}$, $\Delta\mathrm{N}_{\mathrm{ru}}^{\mathrm{eo}}$, $\Delta\mathrm{N}_{\mathrm{ru}}^{\mathrm{ev}}$ are treated as unknowns and calculated, once the corrections to the approximate initial ambiguity are calculated and treated as known values, the fixed solutions are derived, with new matrices of

$$A = \begin{matrix} \frac{\partial\Phi_{ru}^{en}}{\partial X_u} & \frac{\partial\Phi_{ru}^{en}}{\partial Y_u} & \frac{\partial\Phi_{ru}^{en}}{\partial Z_u} \\ \frac{\partial\Phi_{ru}^{eo}}{\partial X_u} & \frac{\partial\Phi_{ru}^{eo}}{\partial Y_u} & \frac{\partial\Phi_{ru}^{eo}}{\partial Z_u} \\ \frac{\partial\Phi_{ru}^{ev}}{\partial X_u} & \frac{\partial\Phi_{ru}^{ev}}{\partial Y_u} & \frac{\partial\Phi_{ru}^{ev}}{\partial Z_u} \end{matrix} \quad x = \begin{matrix} \Delta X_u \\ \Delta Y_u \\ \Delta Z_u \end{matrix} \quad b = \begin{matrix} observed\Phi_{ru}^{en} - (\frac{f}{c}\rho_{ru}^{en} - N_{ru}^{en}) \\ observed\Phi_{ru}^{eo} - (\frac{f}{c}\rho_{ru}^{eo} - N_{ru}^{eo}) \\ observed\Phi_{ru}^{ev} - (\frac{f}{c}\rho_{ru}^{ev} - N_{ru}^{ev}) \end{matrix} \quad v = \begin{matrix} v_{ru}^{en} \\ v_{ru}^{eo} \\ v_{ru}^{ev} \end{matrix}$$

The solution of the least-squares (Equation 3.10) can be solved as,

$$x = N^{-1}d$$

Equation 3. 13 *Least squares solution*

Where

- $N = A^T A \ or \ A^T P_1 A$
- $d = A^T b \ or \ A^T P_1 b$
- P_1 are the a-priori weights of the observations, with each of the double-differenced phase pseudo-range observations being given equal weight or being weighted with respect to elevation angle.

The least-squares solution is an iterative process, where the estimation of unknown parameters of the current epoch is formed by the unknown parameter estimation of the previous iteration with adjustment for corrections at the current epoch and can be represented by X = X*+ x, where X* is the estimate of unknown parameters at the previous iteration, x is the adjustment to the unknown parameters, and X is the estimate of unknown parameters at the current iteration. In the iteration, the estimates of the unknown parameters at the previous iteration (X*) are also input to the b vector at the current iteration, and the iterations are continued until the adjustments to the unknown parameters in the x vector are considered minimal or negligible. The assessment of the quality could be obtained through the covariance matrix (C_x), where $C_x=N^{-1}$

The processing strategy for a single-frequency could be summarised as follows, firstly, the DD pseudoranges are pre-processed and the float solutions are derived using L1 phase pseudorange observables, then cycle slips could be detected and corrected by using the jumps in the L1 DD phase pseudorange residuals. Secondly, the float solutions could be produced with the L1 corrections to the approximate initial phase ambiguities solved as real values (NR_{L1}). And the real values could be estimated with integer values given as the integer ambiguity resolution (NI_{L1}) where $NI_{L1} \approx NR_{L1}$. Finally, the fixed solutions can be produced with the L1 corrections to the approximate initial phase ambiguities (NI_{L1}) treated as integer known parameters. In practice, the processing of the final results also depends on whether broadcast or precise ephemeris is used, the receiver APCs, techniques used for approximate initial phase ambiguity resolution, and tropospheric bias models.

3.4.3 Kalman Filtering

The most commonly adopted method for positioning is based on Kalman filtering although some use the least square estimation algorithm as aforementioned. The difference between the two methods is minor, with least-squares based on minimising measurement residuals, whereas the Kalman filter is derived by minimizing the mean square of the solution. The Kalman Filter also uses the measurement model, similar to Equation 3.10,

$$a(x) = b + v$$

Where

- b is the vector of GNSS pseudorange measurements
- x is the state vector containing unknown parameters to be estimated, such as position, velocity, and time
- 'a' relates to measurement to the states

It is assumed a(x) is non-linear and linearization is applied to a(x).

$$a(x_0) + \frac{\partial a(x)}{\partial x}|_{x=x0} * \Delta x = b + v$$

$$\frac{\partial a(x)}{\partial x}|_{x=x0} * \Delta x = b - a(x_0) + v$$

$$A * \Delta x = \Delta b + v$$

Equation 3. 14 *Process of linearization of a(x)*

Where

- x_0 is the current estimate of the state vector,
- $\Delta x, \Delta b$ is the respective error in the following term,
- A is the design matrix; also known as the jacobian of the measurement model

The least-square solution of the error in the current estimation of state vector at the time (t) is given as

$$\Delta x = K_t \Delta b = K_t(b_t - A_t x_t)$$

Equation 3. 15 *Calculation of corrections to the original state vector*

Where

- $K_t = Q_{x_t} * {A_t}^T * (Q_{b_t} + A_t Q_{x_t} {A_t}^T)^{-1}$
- Q_{b_t} is the covariance matrix of the observations at epoch t and can be calculated by $Q_{b_t} = \frac{1}{\sigma_0^2} * \sum$, where σ_0^2 is a-prior variance and $\sum$ is the covariance matrix of the vector of observation
- The weight matrix is defined by P and is equal to the inverse of Q_{b_t}, $P = {Q_{b_t}}^{-1}$ which also contains the a-prior knowledge of the state.

- Q_{x_t} is the covariance of the unknown parameters at time t, and can be equated to $Q_{x_t} = (A_t{}^T P A_t)^{-1}$

The estimate is updated by adding Δx to the original state vector for corrections,

$$x_t^* = x_t + \Delta x$$

Equation 3. 16 *Measurement update of the state vector*

The covariance of the unknown parameter could be updated similarly by

$$Q_{x_t}^* = (I - K_t A_t)\, Q_{x_t}$$

Equation 3. 17 *Measurement update of the covariance of the unknown parameter*

It can be shown that the Kalman filter equations are the same as the least square equations indicating they incorporate the information from measurement in the same way. The difference between them is the way of obtaining a-prior information from the two estimators, the least-squares obtain this information from external means such as by occupying a known point, while the Kalman filter predicts a prior information using the most recent estimate of the state vector. The predicted state vector is updated and uses some assumed model to describe how the state vector evolved with time based on a system Equation 3.18

$$x_{t+1} = \Phi_{(t+1,t)} * x_t{}^*$$

Equation 3. 18 *Time update of the state vector by the formation of system equation*

Where

- $\Phi_{(t+1,t)}$ is the transition matrix based on the physics of the system that propagates the state from epoch t to epoch t+1

The covariance is updated using the Equation 3.19.

$$Q_{x_{t+1}} = \Phi_{(t+1,t)} * Q_{x_t}^* * \Phi_{(t+1,t)}{}^T + Q_{w_t}$$

Equation 3. 19 *Time update of the covariance matrix*

Where

- Q_{w_t} is the process noise matrix, accounting for the noise in the system equations.

The benefit of the Kalman filter is, 1) through the formation of system equations, additional information about the system is provided by assuming how the state vector changes with time. The Kalman filter will generate smoother or more accurate result if the deviation from assumption using system equation can be accommodated, 2) Kalman filter makes the update of state vector possible using fewer measurements from fewer satellites if the uncertainty in the a-prior estimate is not infinite, whereas, for the least-squares update, it will be impossible due to insufficient measurement without a-prior information. 3) parameters such as position, velocity could be estimated in the Kalman filter based on successive position estimates, whereas for least square, only the position can be estimated.

Adopting a similar concept, the more detailed processing algorithm and procedure used in RTKLIB for short baseline DD technique could be found in Appendix B where the extended Kalman filtering (EKF) is adopted for time update and measurement update of the state vectors from the previous epochs. The strategy for integer ambiguity resolution is also briefly discussed.

3.5 Error identification in the short baseline results

3.5.1 Multipath

In the short baseline DD results, due to differencing, most errors would cancel or be largely mitigated. The remaining errors which cannot be mitigated through the differencing process are due to multipath, antenna PCV, measurement noise, etc. Multipath is solely dependent on the rover's location and its surroundings and resulting to be the major remaining errors within the measurement. This type of error is highly variable, typically uncorrelated between rover and base receivers even with very short baselines and is therefore difficult to mitigate by differencing.

Carrier phase multipath is a major source of error for high accuracy differential carrier phase positioning (Ray and Cannon, 1999). It is caused by contaminated signals which not only contain the direct signal received from the satellite but also include signals coming from various paths and finally reach the antenna by reflections or diffractions from the ground, building, or another object (Braasch, 1996) (Figure 3.5). These reflected signals can interfere with the signal that reaches the receiver directly from the satellite and cause the correlation peak to become skewed which both affects its amplitude and phase. The range delay caused by the reflection of signals is influenced by a lot of factors; i) the reflection coefficient, ii) the antenna to reflector distance, iii) the azimuth and elevation of the reflected signal iv) the existence of multiple reflectors, and v) satellite dynamics (Ray and Cannon, 1999). Multipath should be considered especially when the signal comes from the satellite with low elevation since multipath tends to have a larger influence in this case.

The multipath error impact both the code and carrier phase measurement. The effect of multipath on pseudorange solutions is orders of magnitude larger than it is in carrier phase solutions. The code multipath is relative to the chipping rate, which could result in biases of several meters, and has been successfully mitigated and calibrated based on empirical research (for example, design of the correlators and correlation algorithms (Weill, 1997). The techniques used for code multipath mitigation in the design of correlator include Narrow correlator, Multipath mitigation technique (MET), MEDLL, Edge correlator technique, Strobe correlator, and enhanced strobe correlator. The code multipath could also be mitigated through carrier smoothing. The carrier multipath examines the difference between the composite carrier phase and direct carrier phase signal. Therefore, the magnitude of the multipath carrier phase error is a function of the ratio of the direct signal power to the main reflected one. The stronger the reflected signal is, the larger the multipath error. The carrier phase multipath is based on a fraction of the carrier wavelength, with the maximum multipath bias of one-quarter of the wavelength, i.e. for L1 frequency 4.8cm. and is much harder to mitigate.

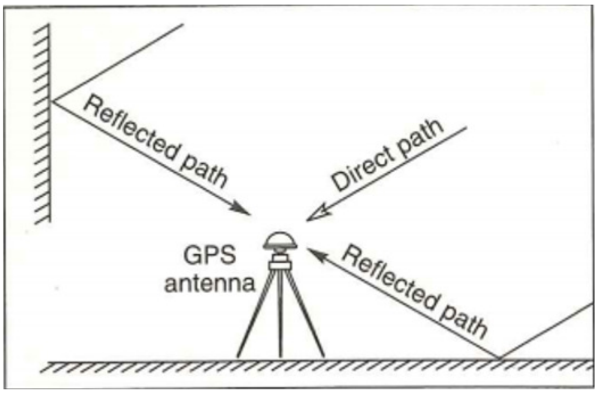

Figure 3. 5 *Multipath illustration (direct path and reflected paths). GPS signals can be reflected from nearby structures or the ground. Ground bounce is a dominant scenario in practice.*

In the phase lock loop, where the carrier phase tracking process happens, the superimposed, composite signal which contains the direct signal as well as the reflected signals by the surroundings induced multipath, could lead to inaccurate measurement of the carrier phase. The secondary signals tend to have a longer propagation time, and when interfered with the signal of interest, would change its amplitude as well as its phase, this error would detriment the integer ambiguity resolution and finally limits the performance of the high-end receiver for the precise surveying. Some GNSS receiver manufacturers have made vague claims on the mitigation of the carrier phase multipath, indicating the difference in the carrier phase multipath mitigation strategy for receivers from different manufacturers. More specifically, different designs and technologies (receiver-internal correlation technique) on the receiver correlator are adopted for the carrier phase multipath mitigation for different manufacturers. The narrow-correlator and MEDLL Technology has been devised by the NovAtel Communications Ltd. Enhanced Strobe correlator has been developed by Ashtec Inc. Other parties (e.g. Trimble) develop the improved navigation satellite receiver with a digital channel processor, which could mitigate the multipath based on the development of the hardware (Lennen, 1996). However, the hardware (correlator) based multipath mitigation strategy is only effective for high-frequency code and carrier phase multipath mitigation, and generally the correlator based multipath mitigation removes multipath due to distant reflectors, the mitigation of low-frequency multipath due to reflectors in the near field still presents a problem.

Apart from multipath mitigation from receiver internal design, there are several other methods for multipath mitigation, on the hardware side, antenna design can be made to suppress the multipath effect, such as with the ground plane and design of choke-ring or special antennas with sharp cut-off elevation angle. On the observation aspect, the multipath could also be limited by careful selection of the measurement site such as keeping antenna away from reflecting sources and by the exclusion of low elevation angle satellite observations (normally cut-off angle of 15 degree is used). Long term signal observations could also be adopted for multipath mitigation by SDF due to the periodicity of the satellite orbit. On the experiment design aspect, multiple closely-spaced antennas could be used, and multipath could be mitigated by multi-antenna spatial processing. On the data processing aspect, the approaches of adaptive filtering, wavelet filter, SNR-based model, band-pass finite impulse response (FIR) filters, Bayesian approach, etc could be used.

3.5.2 Antenna phase centre variations

The APC is supposed to be a point indicating the geometrical centre of the antenna where the measurement is with respect to. In reality, the APC varies based on the received signal direction. With different azimuths and elevation of the incoming signal, the APC changes. Dependent on the antenna type, the PCVs are different even with the same incoming signal. The PCVs result in an error range within 3-4mm, which could not be ignored in high-precision applications, the PCV biases also have repetition every day for several years based on constellation (Schmid et al., 2005).

There are three methods for the PCV determination. The first one is from the relative PCV calibration. In this method, two receivers with two ground plane antennas will be adopted, with one receiver and one antenna as the reference, the outcome would be the difference between the two antennas' PCV with the assumption of knowing the reference receiver's PCV information. The two receivers will be subjected to the same external oscillator, the errors such as atmospheric bias and cable loss are mitigated, the remaining errors are the PCV and receiver noise, and the final PCV is obtained by filtering the white noise. The second method is from the absolute PCV determination, this is performed by using a high precision robot and two antennas. The robot rotates and tilts the antenna while the reference antenna is kept fixed. The third method is from the anechoic chamber measurements. PCVs are obtained by measuring how the phase of an artificial GPS signal is changed when the antenna is rotated and tilted.

The PCV could cause problems since the measurement is with regard to the distance between the satellite and the receiver APC. The PCV effect can have an amplitude of several millimetres to centimetres in baseline error. When the same type of antenna is used in relative measurement, the PCVs could be eliminated, particularly over short baselines (Dawidowicz, 2011). However, ignoring PCVs can lead to serious vertical errors if different antennas are used (Rothacher et al., 1995).

3.5.3 Receiver and antenna measurement noise (GNSS system noise)

The GNSS system noise includes the receiver noise and antenna noise, also known as the receiver equivalent noise temperature and antenna noise temperature. The receiver equivalent noise temperature is a combination of cable loss and receiver internal noise. The receiver internal noise includes the accumulated noise originated from each processing stage of the receiver, with the most dominant contribution of the preamplifier (LNA) and is classified as code phase pseudorange noise and carrier pseudorange noise. The noise in code measurement in DLL majorly consists of thermal noise jitter and dynamic stress error. The thermal noise jitter can be suppressed by lower loop noise bandwidth and narrower correlation peaks. The noise in the carrier phase tracking loop is comprised of phase lock loop (PLL) thermal noise, oscillator jitter, and dynamic stress which is generated in the receiver hardware and behaves largely as white noise. The carrier phase noise is positively correlated to the loop bandwidth but inversely proportional to the carrier to noise ratio and integration time. It is shown that without multipath and PCV, the performance of different grades of receivers is similar, the noise within the carrier tracking loop is small when not influenced by the receiver dynamics, reaching up to 2mm (Odolinski and Teunissen, 2017a).

Receiver noise is an independent error only held intrinsic within the receiver. The amplitude of which relates to the wavelength of the signal. In code solutions, it is related to chip width. For example, 3m receiver noise error is expected in a C/A code solution and about 3cm in a P code solution. For carrier phase solutions, the receiver noise error contributes several millimetres to the overall error. It is inevitable for high-precise measurements with the use of carrier phase observables. But in most cases, it is a relatively small contributor to the GNSS error budget. It is an uncorrelated error independent of the length of the baseline between GNSS receivers.

The GNSS antenna noise comes from natural electromagnetic radiation which could be from the sky, the ground, and objects in the antenna's vicinity, the amount of noise power intercepted by the antenna depends on the direction the electromagnetic wave arrives in and the gain of the antenna in that direction, the noise power of the antenna can be represented by antenna noise temperature.

By examining the GNSS system noise, the precision of pseudoranges and carrier phases measurement can be inferred. The antenna noise is mostly influenced by natural factors, therefore, to minimize GNSS system noise, the receiver noise can be reduced by ensuring the antenna preamplifier is acceptably small. The internal measurement noise of a GNSS receiver is conventionally assessed by zero-baseline measurement. However, one drawback of such arrangement is the differencing process would eliminate most of GNSS system noise, such as preamplifier, sky, and ground noise, resulting in an overly optimistic assessment of receiver performance.

3.5.4 Dilution of Precision (DOP)

Dilution of precision (DOP), in general, is a term describing the effect of satellite geometry on measurement precisions. To better illustrate the concept and influence of DOP, Figure 3.6 shows an example in which a receiver measures the distance to two transmitters to determine its coordinate by the intersection of two circular curves. Due to measurement uncertainty, the shaded region indicates the resultant uncertainty in the computed position. It can be seen that the receiver-transmitter geometry would influence the position precision, in Figure 3.6 a, when two transmitters are further apart, the uncertainty only includes a small region with low DOP, however in Figure 3.6 b when two transmitters are closer, it is shown the uncertainty area increases resulting in high DOP.

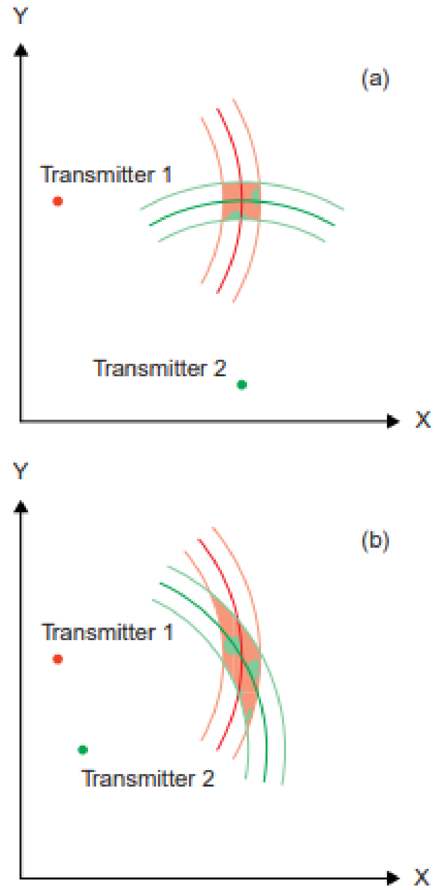

Figure 3. 6 *Uncertainty in the receiver's location is affected by the transmitters' geometry (Langley, 1999)*

With regard to GNSS, to calculate the DOP values, an error propagation model is constructed based on the observation models and pseudorange measurement, the covariance of the estimated parameters is computed to account for its behaviour as a function of satellite configuration. The covariance law estimates the overall quality of the solution by multiplying a matrix only related to satellite-receiver geometry (DOP) to total user equivalent range error (UERE) including satellite and receiver clock, the atmosphere, satellite orbits, and multipath errors (Langley, 1999).

The geometric dilution of precision (GDOP) is given by Equation 3.20 (Langley, 1999)

$$GDOP = \sqrt{D_{11} + D_{22} + D_{33} + D_{44}} = \frac{\sqrt{\sigma_E^2 + \sigma_N^2 + \sigma_U^2 + \sigma_T^2}}{\sigma}$$

Equation 3. 20 *GDOP equation*

Where

- $\sigma_E^2, \sigma_N^2, \sigma_U^2, \sigma_T^2$ are the variance of the east, north, up receiver position estimate and receiver clock offset estimate
- σ is equal to UERE.

- The scaling factor $\sqrt{D_{11}+D_{22}+D_{33}+D_{44}}$ equal to the square root of the trace matrix D is the GDOP.

Similarly, to examine a specific component on the precision dilution, position (PDOP), horizontal (HDOP), vertical (VDOP) and time (TDOP) dilution of precision could be calculated by Equation 3.21. The $PDOP$ indicates the effect of constellation geometry in 3D position accuracy, HDOP and VDOP represent the effect of constellation geometry in 2D horizontal position and vertical position, respectively. TDOP represents the receiver geometry influence on receiver clock offset estimate.

$$PDOP = \sqrt{D_{11}+D_{22}+D_{33}} = \frac{\sqrt{\sigma_E^2+\sigma_N^2+\sigma_U^2}}{\sigma}$$

$$HDOP = \sqrt{D_{11}+D_{22}} = \frac{\sqrt{\sigma_E^2+\sigma_N^2}}{\sigma}$$

$$VDOP = \sqrt{D_{33}} = \frac{\sqrt{\sigma_U^2}}{\sigma}$$

$$TDOP = \sqrt{D_{44}} = \frac{\sqrt{\sigma_T^2}}{\sigma}$$

Equation 3. 21 *PDOP, HDOP, VDOP, and TDOP equations*

For a four-satellite observation, the DOP can be visualised as a tetrahedron formed of receiver-satellite unit vectors. And the volume of the constructed tetrahedron can be shown related to the DOP, with a larger volume indicating a smaller DOP. However, with the addition of more observed satellites, for example, the inclusion of multi-constellation, DOP is likely to decrease and the effect of DOP tends to minimise (Langely, 1999; Msaewe et al., 2017). And it is normally perceived that a poor geometry is formed when satellites clustered together indicated by high DOP, on the other hand, a good geometry can be achieved with satellites evenly distributed across the sky (low DOP value).

As examined in Equation 3.20 and Equation 3.21, the DOP values are positively correlated to the variances of east, north, up receiver position estimate and receiver clock offset estimate. This indicated that lower DOP would normally imply high measurement accuracy and precision. And high DOP would normally indicate poor accuracy. Considering the relationship between DOP and geometry, DOP and expected accuracy, it is concluded that the geometry of satellite and receiver would influence the precision estimate and DOP is a useful parameter to quantify and characterise the geometrical influence.

In this Chapter, the concept, coordinate system, algorithm, and error sources associated with GNSS for short baseline deformation monitoring are mainly studied. As a cornerstone of GNSS short baseline deformation monitoring, it is crucial to study the fundamental concept of achieving the derived results. In the next chapter, the differences between different grades of GNSS receiver and antennas are reviewed.

Chapter 4 Grades of GNSS receivers and antennas

4.1 Emergence of low-cost GNSS receivers

In the 1970s, the receivers are designed as bulky equipment with privilege only for military use. Nowadays, with the technology development, GNSS receivers have been widely expanded to various platforms for different applications such as geodetic surveying, military use, car navigation, location-based service, precise agriculture, etc. And the sizes of the receiver also vary, some low-cost receivers, for example, smartphone grade, could be small enough to be integrated into a chip. The choice of employing between different receivers results from a trade-off of parameters such as receiver performance, cost, power consumption, and autonomy.

Although various grades of receivers can be found in the market, the price, application, and performance differ largely from receiver to receiver. Table 4.1 shows the comparison between typical parameters of geodetic-grade and navigation-grade receivers in the aspect of accuracy, cost, frequency, and applications. It indicates the geodetic receiver is much more expensive than the navigation grade receiver but with better performance. The low-cost navigation-use receivers can only use the code, or phase-smoothed code single-frequency satellite signals, indicating its less capable of obtaining accurate results, while the geodetic receiver can achieve more accurate results using code as well as carrier phase with multi-frequency signal (L1, L2, L5) receiving capability. This is because the maximum resolution which could be obtained by the C/A code is 3 meters, while with the use of the carrier phase, the maximum resolution that can be obtained is approximately 2mm. Therefore, due to the low level of precision of C/A code, navigation-grade receivers are rarely used in surveys that require high precision and accuracy.

Table 4. 1 *Property comparison between navigation grade and geodetic receivers (Weston and Schwieger, 2014)*

Type of receiver	accuracy	costs	Signals property	constellations	Frequency	Application
Navigation	1-10m	£5-100	Code Phase-smoothed code	Limited constellations, GPS	Single frequency (L1)	Car, location-based service, sailing, mass-market
Geodetic	1mm to 10cm	£10,000–30,000	Code carrier phase	Multi-constellations GPS GLONASS Galileo BeiDou, etc.	Dual or multi frequency (L1, L2, L5)	Surveying & geodesy geodynamics

Apart from the navigation-type cheap receivers, the recent development in low-cost receivers' design is devoted to gaining more features like carrier phase observations, use of multi constellations, more channels, at a slightly higher cost than normal navigation grade receivers, such as the u-blox receiver models with around 200 pounds and cheap receivers produced from NVS, NS-RAW from NavSpark, GNSS OEM boards, Emlid Reach, Skytraq, SwiftNavi, etc.

Table 4.2 shows the advanced features of two types of the recently developed new generation of low-cost receivers which differentiate from the conventional navigation grade receivers in terms of additional carrier phase measurement, higher quality oscillators, channel numbers, the ability for multi-constellation measurement, etc. These features have made higher accuracy results possible.

Table 4. 2 *Different properties of the newly emerged low-cost receiver capable of carrier phase measurement (Wouters and Marais, 2019)*

	NVS Technologies NV08C	u-blox NEO M8T
Frequency and constellation	L1 GPS, GLONASS, Galileo	L1 GPS, GLONASS, Galileo, BeiDou
Channels	32 channels	72 channels
oscillator accuracy	1 pps accuracy 15 ns	1 pps accuracy 20 ns
ports	2 x RS232 serial ports	1 x RS232, 1 x USB serial ports
Data format	NMEA and proprietary binary format data streams	NMEA and proprietary binary format data streams
Measurement type	code and carrier phase measurements	code and carrier phase measurements

In the recent research of low-cost receivers' application for positioning and monitoring purposes, the most popular low-cost model is mostly from u-blox. The u-blox receivers were tested both in RTK (Takasu and Yasuda, 2009; Skoglund et al., 2016; Odolinski and Teunissen, 2016; Bellone et al., 2016; Hamza, et al., 2020) and post-processing applications (Realini et al., 2013; Biagi et al., 2016; Cina and Piras, 2015). Other researchers tested the performance of low-cost receivers formed of OEM board (Alkan and Saka, 2009; Jackson et al., 2020). Some even investigated the performance of smartphone grade receivers integrated into a chip (Jo et al., 2013; Odolinski and Teunissen, 2019). Their research all attained promising results with some of the studies concluding that the performance from certain low-cost receivers was comparable to single-frequency geodetic grade receivers under certain circumstances (Takasu and Yasuda, 2009; Garrido-Carretero et al., 2019; Cina and Piras, 2015). However, the modern low-cost receivers still cannot match the performance of survey-grade receivers in terms of functionality, measurement accuracy, and precision. This is probably due to their differences in receiver software and hardware, such as circuitry design, internal memory, CPU, LNA, digital interference mitigation, digital signal processing (DSP) baseband, channels, clocks, and oscillators, GNSS engine, algorithms, etc. The different quality and design used in the hardware and software also lead to a different cost of different receivers. Despite most low-cost GNSS receivers only allowing single-frequency measurement, some multi-frequency low-cost receivers are also emerging in the market, such as Piksi Multi, and u-blox ZED-F9P. The multi-frequency low-cost receivers offer the possibility of ionospheric mitigation and faster ambiguity resolutions. Some studies have also been carried out using them (Hamza et al., 2020).

4.2 Comparison between different grades of receivers

4.2.1 Dual-frequency vs Single-frequency

One receiver-wise uniqueness of geodetic receiver compared to the low-cost receiver is that most geodetic receivers can allow for dual-frequency L1, L2, or triple frequency L1, L2, L5 measurement while most low-cost receivers are restricted to single-frequency measurement. The dual-frequency feature of the geodetic receiver makes the measurement more accurate as ionospheric-free LC condition can be created with additional L2 measurement, indicating mitigation of the ionospheric error could be possible and the integer ambiguity resolution could also be resolved faster with dual-frequency by creating the wide lane observables (Cosser et al., 2003). However, most low-cost receivers only have the capability of single-frequency measurement, which could lead to a less efficient and longer period of ambiguity resolution during the initial stage or after a cycle slip, up to tens of minutes compared to up to few minutes for dual-frequency receivers (Cina and Piras, 2015). The difference in single or dual-frequency observation is a major factor affecting its functionality thus leading to performance differences.

Over the past few years, lots of researchers investigated this type of low-cost receiver and antennas that can have carrier phase measurement for positioning analysis both in post-processing and RTK modes (Sioulis et al., 2015). For example, the survey-grade dual-frequency receivers could normally fulfil RTK-GPS functionality with expected performance, while RTK for the low-cost consumer suffers from high receiver noise, poor ambiguity resolution, and worse multipath resistance. Results from Takasu and Yasuda (2009) showed RTK for the consumer-grade receiver is feasible, but not applicable in circumstances with the mobile environment, since many cycle-slips would occur. Due to the single-frequency observation, the fix rate is greatly reduced, and the fix time is much elongated for low-cost receivers under mobile and multipath environments.

4.2.2 Comparison of receiver internal structure (receiver internal noise)

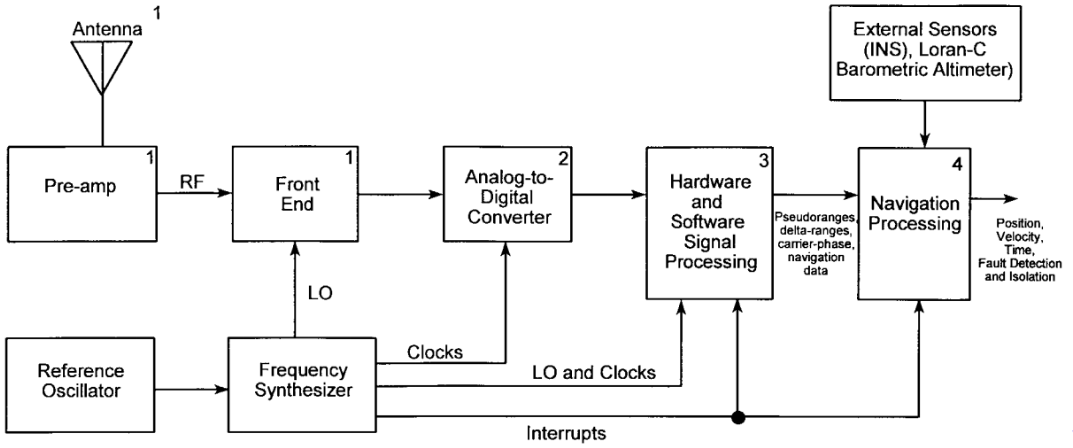

Figure 4. 1 *Generic GPS receiver block diagram (Braasch and Van Dierendonck, 1999)*

Figure 4.1 illustrates the architecture of the GPS receivers. Various grades of receivers may adopt different designs resulting in a quality difference in different modules. The as-built modules such as pre-amp noise, front end noise, the A/D converter speed (single-bit or multi-bit), the oscillator and clocks stability, channels (single or multi-channel), and DSP design quality, etc could vary from receiver to receiver leading to different performances and functionality.

In each component of the receiver architecture, the level of the noise in some way indicates the precision of pseudoranges and carrier phases being measured which is an indicator of the performance of the GPS receiver (Langley, 1997). To quantify overall internal receiver noise in comparison to GPS signal, the C/N_0 (the carrier signal to noise density ratio) is introduced and could be calculated by dividing the power level of the signal carrier by the noise power in a 1-Hz bandwidth. The C/N_0 is believed to be a key parameter for the precision determination of code and carrier measurement since the performance of the receiver's signal tracking loops (code and carrier) are correlated to C/N_0 as can be shown in the jitter modelling equations for both code and carrier correlators (Appendix E).

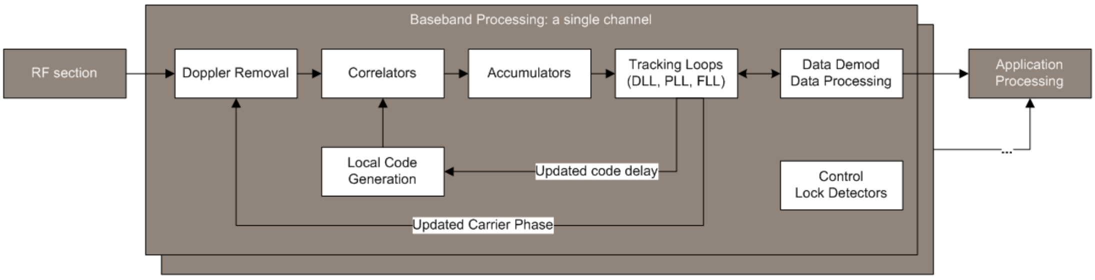

Figure 4. 2 *Baseband processing components (Navipedia, 2014a)*

In the receiver design, the most important unit is the hardware and software for digital signal processing (DSP), where pseudorange and carrier phase measurements are generated. Different designs in the DSP unit would result in different quality of measurement observed and acquired by each receiver. Inside the signal processing unit, tracking loops within the baseband processing (Figure 4.2) are accountable for the precision of the code and phase measurement. By replicating and adjusting the PRN code, tracking loops are constructed to follow and update the estimation of the code delay and the carrier phase of the incoming signal. The design of the tracking loops is of major importance to the overall performance of the receiver since it dictates the ability to correctly track the signal, hence influencing its accuracy. It is also noticed that most high-performance GPS receivers tend to use narrow correlators for noise reduction. (Langley, 1997) Therefore, the difference in LNA quality, correlator design could be the reasons for different precision of code and carrier phase measurement between consumer-grade and survey-grade receivers.

Receiver clock error is another discrepancy between different grades of receivers. The behaviour of the clock bias makes the major difference between the low-cost consumer-grade receivers with high-end geodetic receivers in the aspect of timekeeping. The clock used for survey-grade receivers is more accurate and precise compared to the low-cost navigation grade receivers with reference to GPS time, probably owing to its high-performance timing unit (more stable oscillators). This makes the clock offset more precisely predictable and more reliable (Misra, 1996). In contrast, the clock for the low-cost receiver both have larger clock offset, jittering, and drifting due to oscillator quality, with frequent time steering and adjustment during the measurement, leading to unpredictable clock bias and further influencing the positioning output. The receiver clock is considered precise and stable if the clock bias from GPS time is with smooth variations since it can be modelled and estimated. It is shown the parameter of clock offset doesn't simply reflect the calculation from the equation, but the result of the calculated undulating, instantaneous clock bias could worsen the positioning accuracy (Misra, 1996).

To evaluate the performance of the pseudorange and carrier measurement from different receivers, Figure 4.3 shows precisions measured by a low-cost receiver (u-blox M8T) and survey-grade receivers. From Figure 4.3, as for code measurement, it is shown the precision largely varies between the survey-grade receiver and low-cost receiver as well as between survey-grade and patch antenna. However, there was no large difference between carrier-phase performances between them as a result of low noise characteristics for carrier phase measurement compared to code measurement. This different level of precision will influence ambiguity resolution and consequently the positioning accuracy and precision (Odolinski and Teunissen, 2017b).

Receiver/ antenna	System	Frequency	STD code (cm)	STD phase (mm)
Survey-grade/ survey-grade	GPS	L1 L2	18 20	2 2
Low-cost/ survey-grade	GPS BDS	L1 B1	31 30	2 2
Low-cost/patch	GPS BDS	L1 B1	49 49	2 2

Figure 4. 3 *Zenith-referenced undifferenced code and phase STDs estimated by least-squares variance component estimation.(Odolinski and Teunissen, 2017a)*

4.2.3 Positioning accuracy

The accuracy also varies between these two different grades of receivers. For geodetic receivers, cm-level accuracy could be achieved with RTK-GPS, sub-centimetre accuracy could be achieved by post-processing the carrier phase with network adjustment (Takasu and Yasuda, 2008; Dabove and Manzino, 2014). According to Dabove and Manzino (2014), for low-cost receivers such as u-blox, 4-6cm of accuracy in RTK could be achieved with a CORS network, and 2-5cm accuracy could be obtained for the post-processing by considering VRS.

Table 4. 3 *Accuracy of consumer-grade receivers using different processing techniques*

	SPP	DGPS	DD/RTK	DD/PPK	PPP
Consumer grade (low-cost)	level of meter to dozen of meters(Wisniewski et al., 2013)	level of meters (Wisniewski et al., 2013)	4-6cm (Dabove and Manzino, 2014)	2-5cm (Dabove and Manzino, 2014)	0.5-3m (Rademakers et al., 2016)
Geodetic survey-grade	~5m (Meng et al., 2017)	~25cm (Leica Geosystems, 2012)	8mm horizontal and 15mm vertical (Leica Geosystems, 2012)	3mm horizontal and 3.5mm vertical (Leica Geosystems, 2012)	20mm (Guo et al., 2018)

Table 4.3 shows the summary of the positioning accuracy obtained for low-cost u-blox and survey-grade Leica GS10 receivers in various positioning modes. It is

concluded that results from the consumer-grade receivers are less accurate than that from the geodetic receivers, which is in agreement with the assumption that the low-cost receiver has worse accuracy than the survey-grade receiver.

The development of the receiver over the last decades has made a great impact on modern GPS technology applications. Nowadays, there are various grades and qualities of the receivers in the market with different prices ranging from £100-£20000, providing different accuracy and precisions suited for various applications. In general, the cost of the receiver and the performance are positively correlated., The cost would normally be higher for high-end receivers. The accuracy of the measurement is also comparatively better. Compared to low-cost receivers, survey-grade receivers usually adopt high-quality designs for noise, multipath, and interference reduction. For example, for survey-grade receivers, generally

- Front ends are characterised by the lower noise
- The A/D (analog to digital) converters are multi-bit instead of single-bit
- The DSPs are high speed with more channels available
- Dual frequencies observations are tracked
- Low and narrow bandwidths are adopted in the carrier phase tracking loop(Braasch and Van Dierendonck, 1999).

In summary, the receiver noise could come from various sources (nature noise or receiver hardware noise). To be more specific, the receiver hardware noise could originate from receiver inner circuitry geometry, antenna pre-amplifier, front end, signal correlators, signal processing segments, etc. For these modules where raw observations are processed and generated. The quality of the design may be different for different grades of receivers which further leads to different performances. In general, the major differences between low-cost and geodetic receivers are single or dual-frequency observation, clock bias, receiver noise, etc.

4.3 Antenna comparison

4.3.1 Characteristics of Different antennas

The measurement quality of GNSS receivers is also related to different grades of antennas connected to them. In general, due to patch antennas' design, they are usually less effective in multipath mitigation compared to geodetic antennas, as a result, more noise could be introduced by adopting a patch antenna (Odolinski and Teunissen, 2017b).

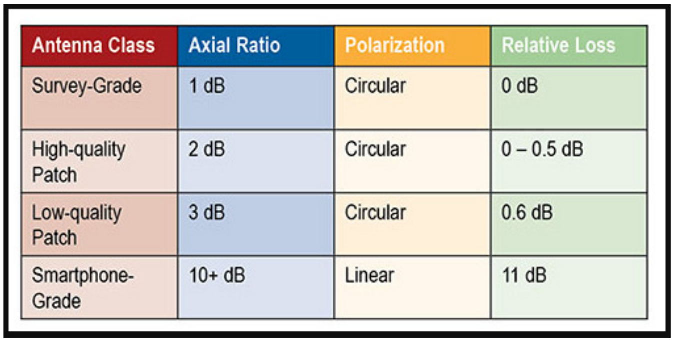

Antenna Class	Axial Ratio	Polarization	Relative Loss
Survey-Grade	1 dB	Circular	0 dB
High-quality Patch	2 dB	Circular	0 – 0.5 dB
Low-quality Patch	3 dB	Circular	0.6 dB
Smartphone-Grade	10+ dB	Linear	11 dB

Figure 4. 4 *Different antenna comparison in axial ratio, polarization, and relative loss (Pesyna et al., 2014)*

Figure 4.4 shows the property of different grades of antennas in axial ratio, polarization, and relative loss in gain with respect to survey-grade receivers. The most desirable property of an antenna is to have a stable APC, a low axial ratio, uniform quasi-hemispherical gain pattern, right-hand circular polarization, etc. These properties require the size of the antenna to be larger. This implies the larger the antenna, the performance would normally be better. (Pesyna et al., 2014)

The axial ratio (AR) is defined as the ratio of major axes length of polarization ellipse to the minor axes, for circular polarizations it should be 1 or 0 dB. If the axial ratio is greater than 1-2 dB, the polarization is often referred to as elliptical. For linear polarization, the AR should be infinite. The circular polarization has the advantage over the linear polarization in coping with Faraday Effect in the ionosphere and is more resistant to atmosphere degradation, etc. Therefore, a low axial ratio is a preferred feature for error mitigation. It is shown in Figure 4.4, with survey-grade antenna as the reference, patch antenna has a smaller relative loss in gain than that of the smartphone-grade. The large loss in gain (11dB) for the smartphone grade could result in a loose lock to the signal, and the linear polarization would also increase the multipath effect, making it less suitable for surveys. Therefore, the axial ratio, polarization, gain pattern, and APC could be factors differentiating the antenna performance.

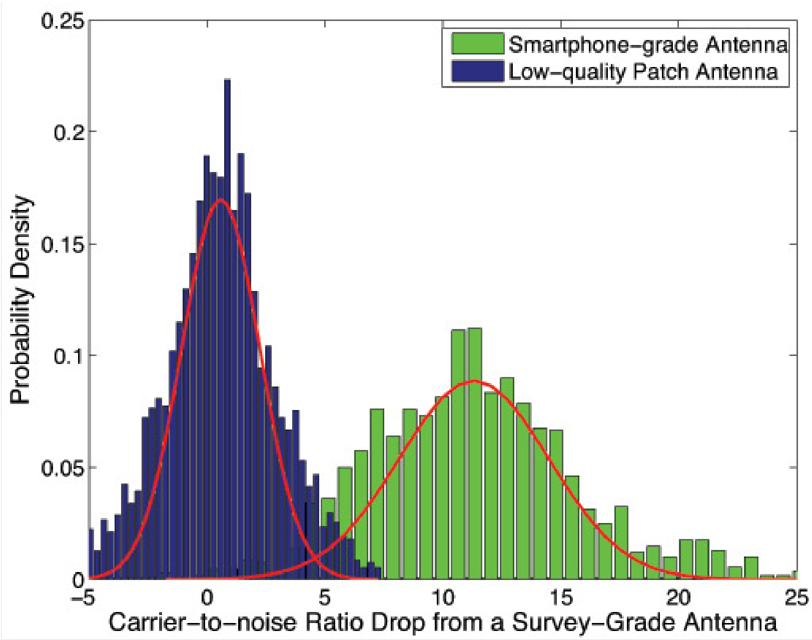

Figure 4. 5 *Comparison between smart phone-grade and low-quality patch antenna in the aspect of C/N_0 variation (Pesyna et al., 2014)*

The carrier to noise ratio (C/N_0) is regarded as an important parameter for the noise quantitative analysis. Figure 4.5 shows the variation of C/N_0 for low-quality patch and smartphone grade antenna against the geodetic antenna. The low-quality patch antenna has only an average of 0.6dB loss in gain compared to 11dB for smartphone grade, this leads to the latter antenna getting only 8% of the signal power of a geodetic antenna (Pesyna et al., 2014).

4.3.2 Phase residual between different grades of antennas

Apart from the architecture analysis of different grades of antennas, the different antennas are also compared based on their carrier phase residuals. Figure 4.6 shows the carrier phase residuals from the geodetic, low-quality patch and the smartphone grade antenna respectively. It was found that the STD of the phase residuals was the lowest for survey-grade antenna (around 3.4mm) followed by low-quality patch antenna (5.5mm) and smartphone grade antenna (11.4mm)(Pesyna et al., 2014). This is probably due to the low C/N_0 as a result of the large relative loss in low-quality antennas, which further leads to less resistance to the multipath and high noise in the signal. This will eventually lead to decreased performance with poor phase residuals and less precise results.

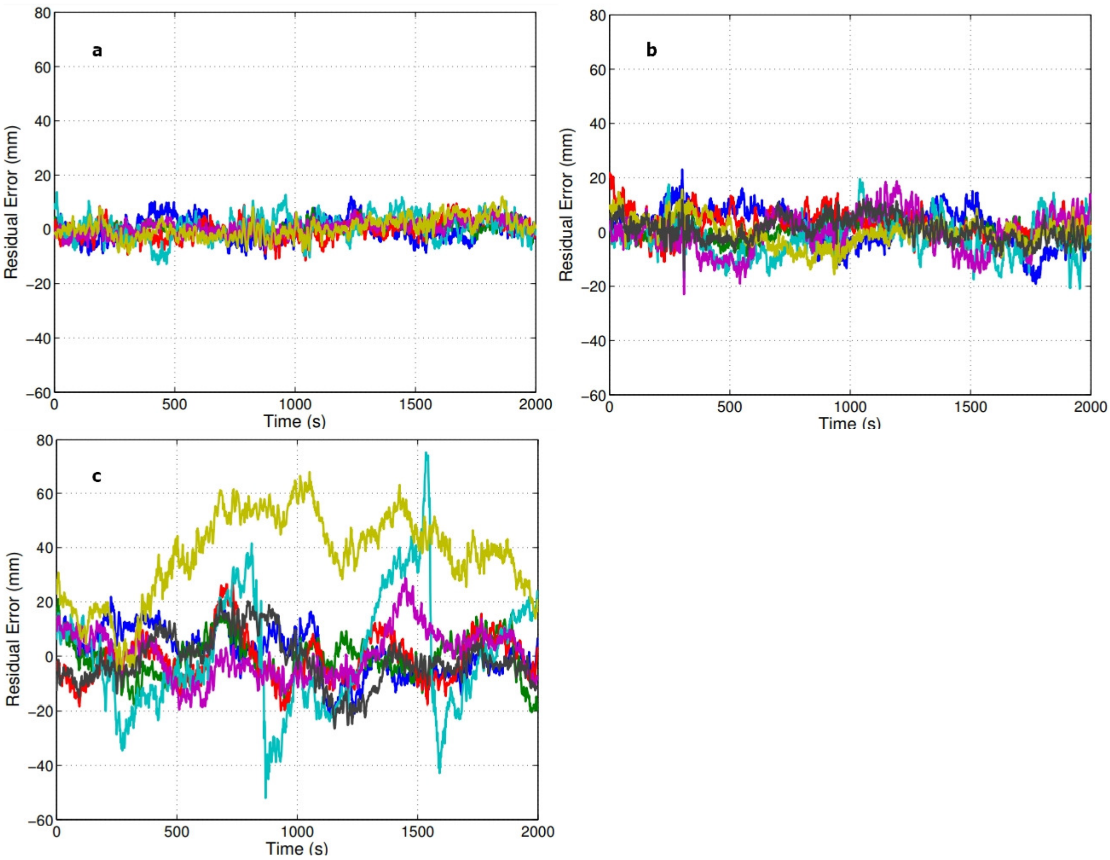

Figure 4. 6 *The double-differenced phase residual time histories with respect to the average of each APC for a. survey-grade, b. low-quality patch, and c. smartphone-grade antenna, respectively (Pesyna et al., 2014). The different colour represents different satellite pairs used in DD.*

Table 4. 4 *Comparison between costs of different grades of antenna*

	Mobile-phone grade	Patch antenna	Geodetic antenna
Cost	Several dollars	Around £100	£1000-3000

Table 4.4 lists the cost estimation of current in-market antennas. Based on the quality and performance of the antenna, the cost also differentiates, ranging from several dollars to thousands of dollars, with more expensive antenna, it is expected

the antenna will have a more sophisticated design, of larger size, low noise LNA, better multipath suppression and signal receiving capability, etc.

To summarise, the difference in the architecture design of different receivers would lead to different performances, the shortcoming of low-cost receivers would probably include single-frequency observation, higher noise level, etc. The hardware improvement of the low-cost receiver probably requires modification of the as-built structure of the receiver to be carried out with a certain extra cost, for example, a change to better quality LNA, more stable oscillator, better DSP, etc. However, the effect of enhancing the receiver hardware on its performance may not be obvious. It is examined that the carrier phase multipath level is almost the same between the consumer-grade and geodetic receivers, however for geodetic-grade and consumer-grade antennas, the difference is large (Takasu and Yasuda, 2008). Therefore, compared to receiver hardware improvement, a more cost-effective way is for antenna improvement to reduce multipath from surroundings by adding choke rings, etc.

4.4 Equipment used in this study

Two types of receivers used in this study are Leica GS10 and u-blox M8T and correspondingly, two grades of antennas (Leica AS10 and patch antenna) are adopted. According to the Leica Geosystems (2012), Leica GS10 models are high precision geodetic grade receivers to provide high performances even under severe and challenging conditions. The Leica GS10 uses a patented SmartTrack+ technology in its advanced measurement engine for GNSS measurements which makes Jamming resistant, high precision pseudorange, and low noise carrier phase measurement possible with minimum acquisition time. It has a maximum channel of 120 and can track a maximum of 60 satellites on two frequencies. The signals that could be tracked are GPS, GLONASS, Galileo, BeiDou, and SBAS. The GNSS measurements are both fully independent code and phase measurements of all frequencies. The accuracies of Leica GS10 are shown in Table 4.5 for different positioning techniques.

Table 4. 5 *Leica GS10 accuracies according to manual (Leica Geosystems, 2012)*

	Accuracy (RMS)
DGPS / RTCM	Typically 25 cm
Single Baseline (<30km) RTK	Horizontal: 8 mm + 1 ppm (rms) Vertical: 15 mm + 1 ppm)
Network RTK	Horizontal: 8 mm + 0.5 ppm (rms) Vertical: 15 mm + 0.5 ppm
Static (phase) with long observations	Horizontal: 3 mm + 0.1 ppm (rms) Vertical: 3.5 mm + 0.4 ppm
Static and rapid static (phase)	Horizontal: 3 mm + 0.5 ppm (rms) / Vertical: 5 mm + 0.5 ppm
Kinematic (phase)	Horizontal: 8 mm + 1 ppm (rms) / Vertical: 15 mm + 1 ppm

The geodetic antenna used is Leica AS10 type, the Leica AS10 SmartTrack+ antenna is a compact survey antenna with a built-in ground plane. The satellite signals that can be tracked are triple frequency GPS signal, GLONASS, Galileo, Compass, and SBAS signals. Leica AS10 can be used perfectly in combination with the Leica Viva GS10 receivers for a wide range of precision applications. The antenna has a gain of 29±3dB and is robustly built to withstand and protect against extreme conditions such as water, sand, vibrations, and an accidental drop from up to 2 metres.

On the contrary, the low-cost receiver used in this study are from u-blox receivers, an evaluation kit called EVK-M8T and short for (u-blox M8 Timing GNSS Evaluation Kit), the GNSS module used in the EVK-M8T are NEO/LEA-M8T, which can process multi-constellation measurements concurrently. The GNSS module boasted to acquire and tracks signal very sensitively with minimized power consumption and low duty-cycle operation with maximum reliability. The u-blox M8 engine has 72-channels and can receive GPS, GLONASS, Galileo, BeiDou, SBAS, and QZSS signals. Observations can be concurrently measured with 3 GNSS constellations. The oscillator module used for the clock is TCXO to provide precise timing aligned to GNSS time or UTC with 20ns accuracy. The raw measurements contain the pseudorange, carrier phase, Doppler, and message payloads. According to U-blox AG (2020), the position accuracy is 2.5 CEP (Circular Error Probable) in autonomous mode and 1 meter RMS in Differential mode. The u-blox NEO-M8T module used in the EVK-M8T incorporates an additional, off-chip LNA besides the integrated LNA in the antenna.

The antenna (ANN-MS) used in the evaluation kit is an active low-cost GPS / GLONASS / BeiDou patch antenna with a 3 m antenna cable. The patch antenna is flat, generally has a ceramic and metal body, and is mounted on a metal magnetic base plate with a PC housing. It has a built-in low noise amplifier with 29 dB gain and a 0.9 dB noise figure. The antenna is polarised with right-hand circular polarization (RHCP) and can withstand relative humidity with fair protection against dust and water.

In this chapter, different functionalities of different grades of receivers and antennas are examined. The GNSS receivers adopted in this study are also described with their GNSS tracking capabilities and accuracies. In the upcoming Chapter, the empirical studies adopting the low-cost GNSS receivers are discussed, several precision improvement approaches adopted by other researchers are also reviewed.

Chapter 5 Low-cost GNSS receivers' applications and possible precision improvement strategy

5.1 Recent applications of low-cost GNSS receivers

The development of low-cost GNSS sensors leads to various applications. In recent years, studies on different applications using low-cost GNSS sensors have been carried out, especially in its positioning and monitoring performances (Table 5.1). It is shown that certain applications conventionally implemented by survey-grade GNSS sensors could now be achieved with low-cost GNSS sensors such as landslide monitoring, PPP, RTK, etc. Among these applications, the employment of low-cost GNSS receiver in short baseline DD positioning and deformation monitoring is more relevant to this study, where corresponding empirical research is reviewed in detail in Section 5.2.

Table 5. 1 *List of Low-cost GNSS receiver applications in positioning and monitoring*

Author	Low-cost GNSS receiver application	Findings
Janssen et al. (2002)	Volcano deformation monitoring	~centimetre level accuracy
Knight et al.(2020)	Coastal sea-level measurement	~centimetre level accuracy
Stempfhuber et al.(2011) Henkel et al. (2014)	UAV position and altitude determination	1-3 cm accuracy
Notti et al. (2020)	Slope instability monitoring	millimetre accuracy
Wiśniewski et al.(2013)	Positioning accuracy evaluation	centimetre level precision
Heunecke et al.(2011) Cina and Piras (2015) Bellone et al. (2016) Biagi et al.(2016) Poluzzi et al.(2019)	Landslide monitoring Local monitoring Deformation monitoring	sub-centimetre level accuracy millimetre level accuracy
Odolinski and Teunissen (2016)	RTK performance	millimetre-level accuracy
Verhagen et al.(2010)	Multi-GNSS performance evaluation	centimetre level accuracy
Gill et al.(2017) Nie et al.(2020)	Precise point positioning (PPP) and Real-time PPP	few-decimetres
Wilkinson et al. (2017)	Earthquake fault slip detection	centimetre-level accuracy

5.2 Case studies: research on the accuracy of low-cost receivers in positioning and deformation

The accuracy of the low-cost GNSS receivers for various positioning modes has been assessed in previous studies. Alkan and Saka(2009) adopted a low-cost OEM GPS receiver and analysed its performance in kinematic applications. The low-cost OEM receiver could provide carrier phase measurement, with carrier smoothing algorithms to improve the pseudorange accuracy. The analysis of the GPS data led to kinematic positioning with centimetre level accuracy.

RTK with low-cost GNSS receivers has always been challenging due to its higher receiver noise, worse resistance to multipath, and poorer ambiguity resolution performance. Takasu and Yasuda (2008) evaluated the RTK GPS performance with several types of low-cost single-frequency receivers. The code and carrier phase multipath and antenna PCV were firstly evaluated using the field calibration method for different receiver and antenna models. Then the performance of RTK of various low-cost GNSS receivers and antennas combinations was evaluated in the aspect of positioning accuracy, fix rate, and TTFF for ambiguity resolution. Their results showed that the difference between geodetic-grade and consumer-grade antenna was large, especially for the APC stability and code multipath, consequently affecting the initialization of RTK. Therefore, to improve TTFF and gain better performance, a better grade of antenna should be used. However, for the geodetic grade and consumer-grade receivers, the carrier phase multipath level was similar, resulting in a similar accuracy for RTK results (Figure 5.1). It was also found that the low-cost single-frequency receivers still faced issues for ambiguity resolution which usually took a few minutes for time to first fix (TTFF), whereas, with dual-frequency receivers, ambiguity fix and resolution was much quicker. Quicker ambiguity resolution time was crucial for real-time applications. Therefore, it was still very challenging to use single-frequency receivers in a mobile environment prone to cycle slips. In summary, they concluded low-cost receivers might be suitable for continuous crustal deformation monitoring.

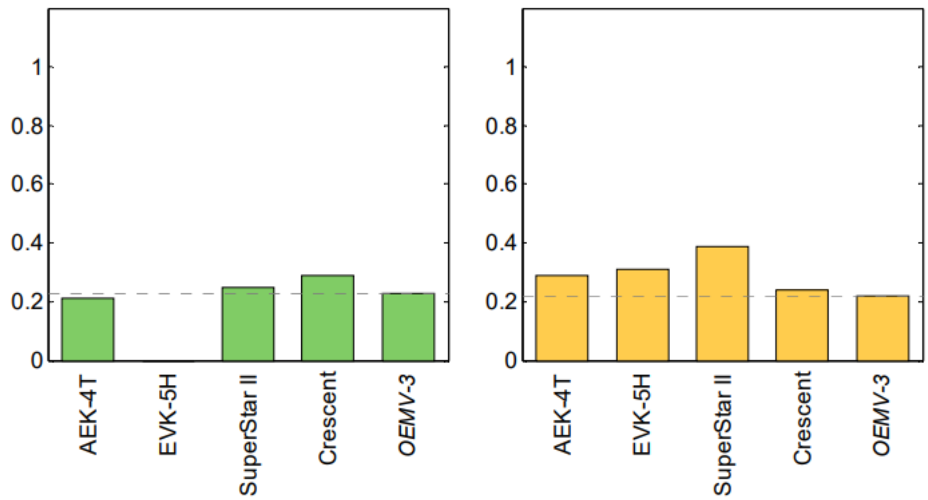

Figure 5. 1 *Comparison of receivers with the same antenna, (left) phase multipath (cm) and (right) code multipath (m) (Takasu and Yasuda, 2008)*

Manzino et al. (2018) assessed the static and kinematic positioning accuracy of low-cost receivers with GPS-GLONASS and GPS-BDS constellation in RTK and postprocessing. The low-cost receiver used was u-blox EVK-M8T. Their results showed that with an open sky view, millimetre level accuracy of fixed static solutions could be obtained for both multi-constellation with RTK and post-processing, indicating similar performance with geodetic receivers. Another experiment was also conducted for the RTK kinematic test where both low-cost receiver and geodetic receivers were used to monitor a car trajectory. The solutions using geodetic receiver were used as a reference to evaluate the accuracy of mass-market devices. The RMS of mass-market RTK solutions was summarised in Figure 5.2. It was shown that compared to geodetic solutions, the accuracy of the mass-market receiver was within 5mm RMS for GPS+BDS /GPS+GLONASS solutions. It could also be seen that the results of the RTK kinematic test showed comparable behaviour between solutions obtained from GPS-GLONASS and GPS-BDS constellation.

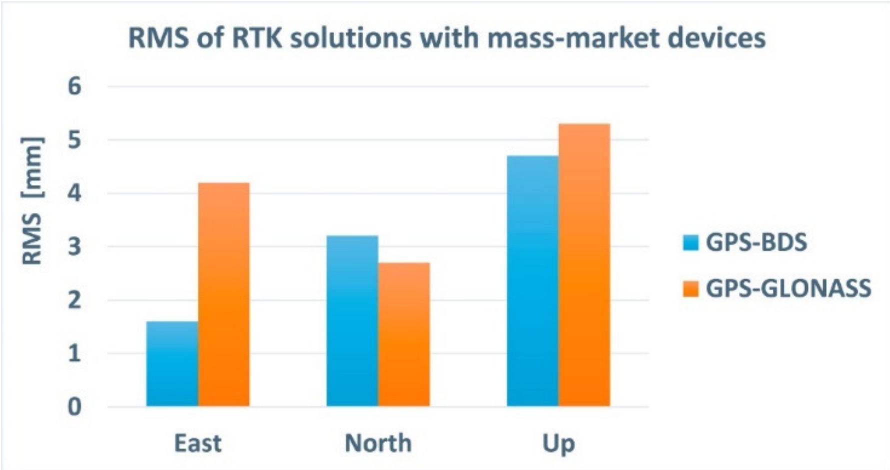

Figure 5. 2 *STDs of results obtained with mass-market devices for RTK kinematic test with respect to the reference solution using geodetic receiver configuration (Manzino et al., 2018)*

Takasu and Yasuda (2009) designed a low-cost single-frequency RTK-GPS receiver with RTKLIB adopting a u-blox LEA-4T module for raw measurements. Some field tests were carried out to evaluate its performance based on CPU/memory usage, the accuracy of solutions, and the fix ratio. Their results showed a 56.9% fix ratio, 3cm RMSE for E-W, 4.9cm RMSE for N-S, and 7.6cm RMSE for U-D for fixed solutions of a 7km baseline. By analysis of the results, they concluded that by excluding the false fix solution, the receiver could achieve standard RTK-GPS accuracy of 1cm+1ppm*baseline length in horizontal RMS. The fixing ratio was also reasonable at around 50%-60% based on a 7 km baseline. These results confirmed that the developed low-cost RTK_GPS receiver could be comparable to a single-frequency geodetic grade receiver.

Hamza et al. (2020) tested multi-frequency low-cost GNSS receivers for geodetic displacement monitoring purposes by using ZED-F9P with u-blox ANN-MB-00 antenna. The static survey and dynamic surveys were conducted with favourable surveying conditions and with short baselines in RTK mode, where they determined the position precision from a static survey and detected displacement from a dynamic survey. For both surveys, with low-cost GNSS rover, comparisons were made between different scenarios when different grades of base stations (low-cost and geodetic grade) were used. The results from the static survey showed that both baseline solutions with the low-cost and geodetic base were comparable and the precision was below 2mm for horizontal components. However, for height components, better performance was detected with the low-cost base probably owing to the unknown antenna calibration parameter. For the dynamic survey, the results showed that 3D displacements in a range of 10 mm could be detected by using a low-cost GNSS receiver with a high level of reliability, with higher accuracy detected from horizontal components than vertical components. The conclusion was drawn that the low-cost GNSS was applicable and could be used in the monitoring of natural hazards.

Biagi et al.(2016) investigated the accuracy and the reliability of low-cost u-blox GNSS for local monitoring. Two experiments were carried out. In the first experiment, u-blox LEA-4T was used as the rover and one geodetic receiver was used as reference forming a baseline of 65 m length and was continuously observed for one week, the results showed that STDs of the residuals were smaller than 5 mm both in the horizontal and vertical components (Figure 5.3). The second experiment used one u-blox NEO-7P receiver as the rover, with the base formed of two receivers, geodetic grade, and u-blox NEO-7P respectively. The baseline formed is around 130m. Designated displacement patterns were executed to the rover receiver. The displacement results from GNSS estimation were compared with the controlled value with known displacement. The baseline results formed by low-cost rover receiver and geodetic base showed an accuracy of sub-centimetre level in the horizontal and centimetre level in the vertical direction, with slightly worse baseline results formed from two low-cost receivers. The minimum horizontal displacement (i.e. 15mm) could be detected when a geodetic receiver is used as a base station. In summary, horizontal movements could be detected by local networks of low-cost GNSS receivers with sub-centimetre accuracy.

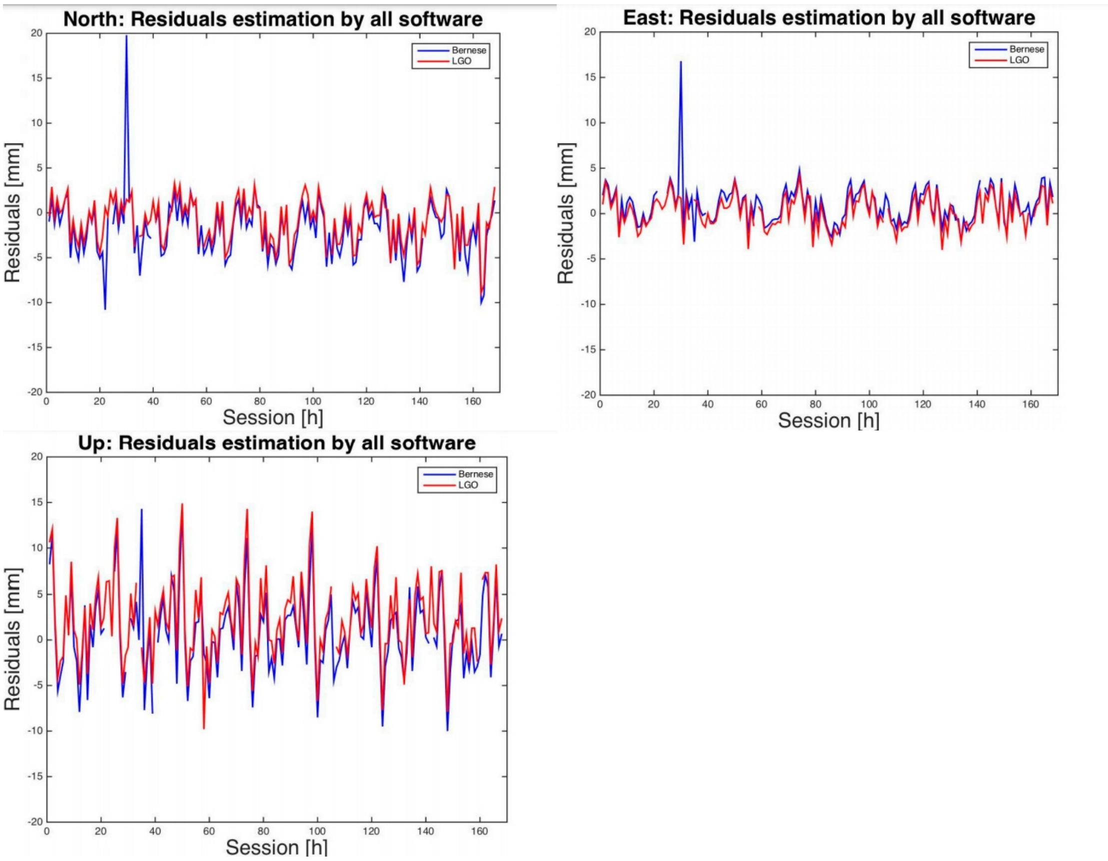

***Figure 5. 3** E/N/U hourly session of residuals from a static rover test for the first SBL experiment for accuracy assessment (Biagi et al., 2016)*

To assess the performance of different brands and models of low-cost receivers in geodetic monitoring, Caldera et al. (2015) conducted several experiments. In their study, the rover was established with an NVS AG GNSS patch antenna connecting to different models of low-cost receivers (a u-blox 4T, a u-blox 6T, and an NVS NV08C-CSM) through a signal splitter. The low-cost receivers used as the monitoring device in the experiment could all output single-frequency carrier phase measurement and the patch antennas were set up at a place with unobstructed views promising good visibility to the satellites. Four reference stations were set up; three continuous operating reference stations (CORS) with baseline length 7.5km, 9.5km, and 11km respectively to the rover and one virtual reference station (VRS) created with a baseline length of only 60m. The results were obtained with relative positioning forming various short baselines between each reference station and rover stations comprised of different low-cost receivers. The daily results were used for comparison purposes between low-cost receivers as well as between base stations. It is derived that the STDs of daily results of different baseline formations are all between 1mm-10mm within an observation period of 60 days depending on the baseline length and observation quality (Figure 5.4). Caldera et al. (2016) also evaluated and compared the performance of the low-cost receivers in the aspect of accuracy and fix ratio when the baseline length increases (Figure 5.5). Similarly, daily results are used with an observation period of 37 days. It is shown that, with the increase of baseline length, the accuracy and ambiguity fix rate tend to decrease.

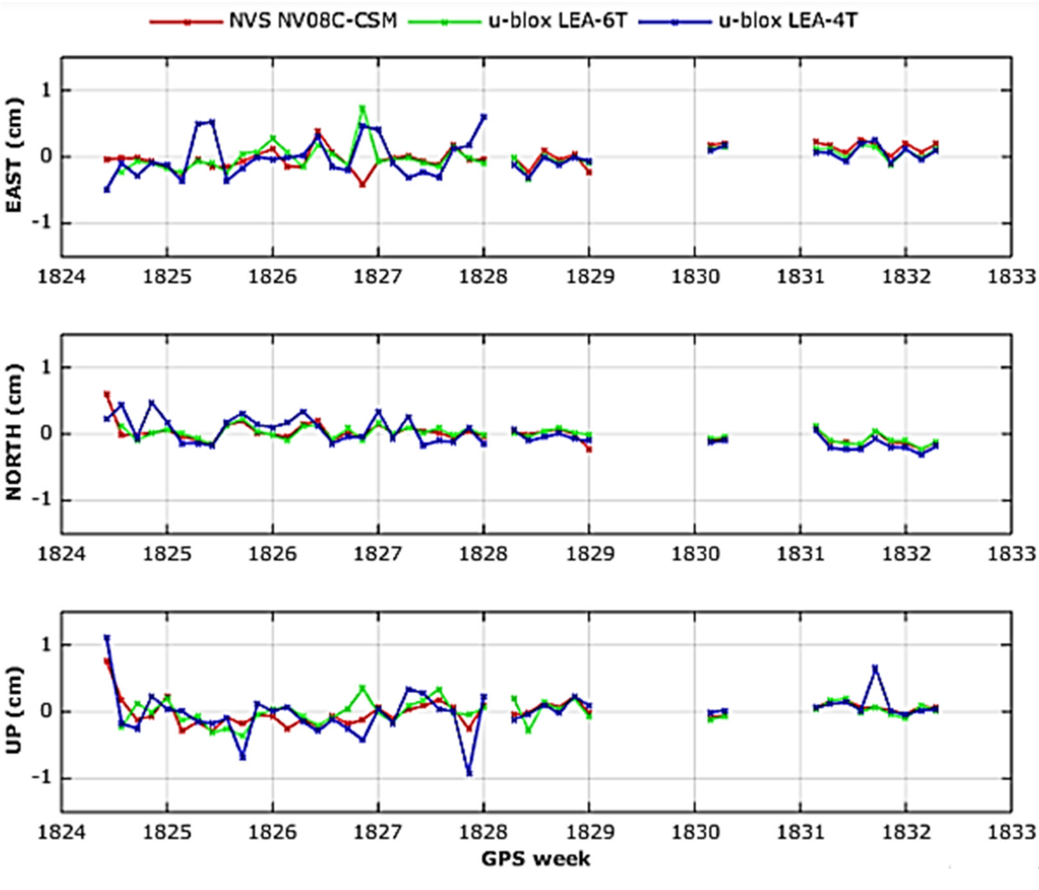

Figure 5. 4 *Daily solutions obtained by processing each low-cost receiver with respect to the VRS (Caldera et al., 2015)*

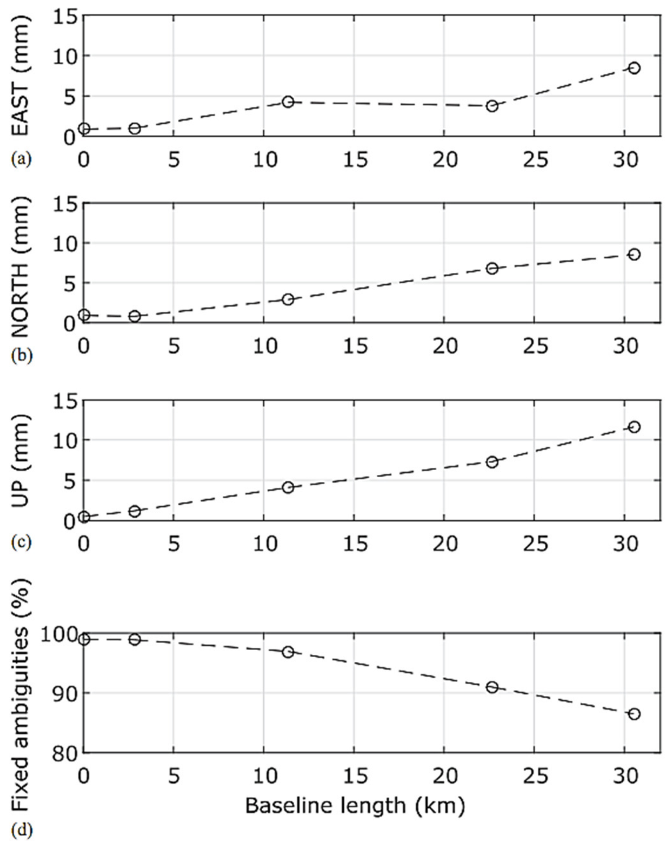

Figure 5. 5 *Error and ambiguity fix rate versus baseline length (Caldera et al., 2016)*

Cina and Piras (2015) tested the feasibility of mass-market GNSS receivers in landslide monitoring. In their experiment, both static rover and dynamic rover tests were conducted. In the static rover experiment, a low-cost receiver u-blox 5T was adopted together with a geodetic antenna as the rover station. The observations for VRSs were created based on the nearby GNSS network with NRTK at different baseline lengths of 0.1, 1, 5, 10, 20, 40 km. In the study, it was shown that for a single-frequency receiver, 5-minute was insufficient to achieve centimetre accuracy since it was not possible to fix the ambiguity resolution. Based on a session length of 10 min for a 10 km baseline, 80% of fixed solutions could be obtained with centimetre accuracy. For the dynamic test, a micrometric slide that could apply movement of sub-millimetre accuracy was used to impose displacement to the rover, the post-processed GNSS results were compared with the controlled known movement. The residuals between the GNSS estimates with the controlled displacement were shown in Figure 5.6. It could be seen that the effect of the geodetic antenna was crucial in improving the accuracy. The u-blox and geodetic antenna could even reach the same accuracy as the geodetic antenna and receiver. It was concluded that with 10 min initialisation for ambiguity fix, less than 1km baseline length, and by use of the external geodetic antenna, the performance was comparable between the mass-market receivers with high-end expensive receivers for monitoring static and low-frequency displacement.

Receivers	Residual East	Residual North	Residual h
(1) geodetic antenna and receiver	-2 ± 1	-5 ± 3	2 ± 5
(2) u-blox+ u-blox antenna	3 ± 3	-6 ± 3	-17 ± 9
(3) u-blox +geodetic antenna	-1 ± 1	-3 ± 3	-5 ± 4
(4) u-blox +geodetic antenna (Stop and go)	7 ± 2	-2 ± 4	2 ± 5

Figure 5. 6 *Residuals comparison between different combinations of antenna and receivers (Cina and Piras, 2015)*

To assess the best possible precision with the low-cost monitoring system and the performance of real-time solutions, Poluzzi et al. (2019) used a Trimble L1 antenna with a u-blox C94-M8P receiver and tested the system on a field test both using RTK solutions and postprocessing with a baseline of 50 m. Real-time accuracies obtained were 4mm and 8mm for horizontal and vertical solutions respectively. For postprocessing with 1 hour of data, 2mm accuracy could be derived in horizontal components and 5mm in vertical components (Figure 5.7). Both RTK and PPK results were generated after filtering. It could be seen that for both Figure 5.7a and Figure 5.7b, a decrease in RMS was shown with the increase of monitoring duration, indicating the improvement of accuracies with longer monitoring time.

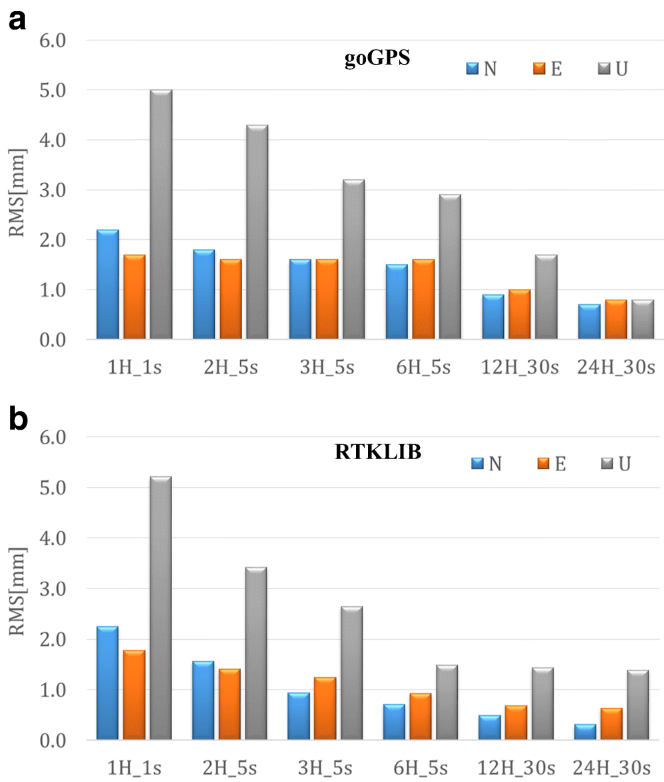

Figure 5. 7 *RMS of NEU components of each timeseries obtained with post-processing methods from respective goGPS (a) and RTKLIB (b) solutions (Poluzzi et al., 2019)*

Garrido-Carretero et al. (2019) evaluated the precision of GNSS field measuring systems in real-time kinematic (RTK) with a low-cost single-frequency u-blox NEO-

M8P using a single-base RTK solution with a baseline length of 350m. The accuracy obtained was 5.5 mm for the horizontal component and 11 mm for the vertical component. With comparison to respective accuracy ±2.5 mm for horizontal and ±4.5 mm for vertical coordinate from geodetic receivers, their results indicated that the low-cost receiver could reach a comparable positioning performance to survey-grade receivers in real-time positioning for short baselines by achieving centimetre-level precision in real-time, making it a low-cost choice for many surveying applications.

Based on the previously reviewed research, the common experimental practices to test the performance of the low-cost GNSS sensor, especially for monitoring purposes are

i) Most study sites are in open-sky environments with reduced multipath impact.
ii) Low-cost GNSS receivers are usually used as the rover, connected with geodetic antenna or patch antenna
iii) Base stations are usually geodetic grade receivers and antennas
iv) RTK or PPK are employed.
v) Short baseline/ very short baseline up to 10 km is formed,
vi) Displacement surveys are conducted with controlled and designated displacement for reference
vii) Free and open-source software is usually used for solution computation to reduce the budget such as RTKLIB or goGPS (Realini and Reguzzoni,2013).

By examining the results from various studies, it is concluded that centimetre to sub-centimetre level spatial accuracy could be achieved with relative positioning for baseline up to 10km by using single-frequency observations with low-cost receivers (Cina and Piras, 2015; Biagi et al., 2016; Realini et al., 2017). The short/ very short baseline is an important requirement for single-frequency low-cost receivers monitoring applications due to quick ambiguity fixing. For long baselines, the low fix ratio would present a concern with low-cost receivers (Cina and Piras, 2015; Takasu and Yasuda, 2009), in which case the geodetic dual-frequency receivers are still needed. Furthermore, many studies also underline that the unmodelled antenna parameter could include a bias in the precision estimation, especially in altimetric precision (Mader, 1999; Biagi et al., 2016; EL-Hattab, 2013; Hamza et al., 2020).

5.3 Case studies of precision improvement using a multi-antenna system

As examined in chapter 3, there are multiple approaches for precision improvement of the measurement by reducing the impact of multipath errors. In this study, we aim to incorporate multiple low-cost antennas and mitigate the multipath impact on solutions based on the spatial correlation of the closely-spaced patch antennas. To better understand established approaches, several case studies by using multi-antenna for solution precision improvement are studied and reviewed.

5.3.1 Code and carrier phase multipath mitigation with multi-antenna system

Ray and Cannon (2001) adopted a cluster of 5 GPS receivers and antennas to estimate and reduce code/carrier multipath errors by using the code pseudorange, carrier phase, and SNR information. The spatial correlation between measurement and geometry between the antennas was also used for the estimation of multipath for each satellite and each antenna couple. According to them, the multipath errors were spatially correlated between antennas placed close to each other.

Their algorithm firstly proposed several equations (details can be found in Ray and Cannon (2001)) with multipath parameters to represent i) the code and carrier phase multipath error, ii) the difference in code and carrier phase multipath error and SNR ratio between two closely-spaced antennas, iii) the relative geometry between the reflected signal relative phase at reference antenna and closely-located antenna. Then observation equations were formed for different sets of antenna pairs by combining equations from ii) and iii). An extended Kalman filter could be developed. The state vector was formed of unknown multipath parameters. The measurement to update the state vector was formed by SD (between antenna) code range and carrier phase observables after the correction based on the antenna spatial separation and SNR ratios. The design matrix was formed by the partial derivatives with respect to unknown parameters for the observation equation. The output of the filter was the unknown multipath parameters estimated for a single satellite which could be used to calculate the code and carrier phase composite multipath.

To verify the above algorithm, field tests were carried out with raw GPS L1 signal observations at a 1s rate. The setup of the experiment was shown in Figure 5.8, where five closely-spaced antenna-receiver were used as a reference station forming a special antenna array, in which the antenna positions in the multi-antenna system and relative geometry were carefully surveyed. The antenna model adopted was NovAtel Model 521 and the receivers used were NovAtel BeeLine receivers, all driven by the same oscillator. The location of the reference measurement site was near a concrete sidewall which may have a low-frequency multipath effect on the measurement. The user receiver adopted a NovAtel MillenniumTM receiver with a choke-ring antenna at around 500m baseline distance free from obstructing object in 100m range, also with L1 data measurement.

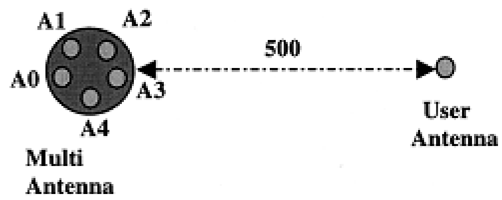

Figure 5. 8 *Layout of the reference station and rover station (Ray and Cannon, 2001)*

The collected data were firstly pre-processed. The SD code and carrier measurements between antennas for each satellite were computed together with SNR ratios. After state vectors were estimated through extended Kalman filtering, the estimated parameters were used to compute the code and carrier multipath errors for each satellite and all antennas. Then, the multipath impact on the observations could be reduced.

The efficiency of multi-antenna processing was assessed both in the measurement domain and position domain. In the measurement domain, to assess the impact in code multipath mitigation, the estimated result was compared with the code minus carrier technique. It was shown that the estimated values closely follow the measured values. For phase multipath mitigation in the measurement domain, the DD carrier phase residuals were examined before and after multipath correction. The results showed the effectiveness of the technique in a high multipath environment, decreasing the magnitude of the code residuals up to 65% and carrier residuals up to 50%.

In the position domain, the effectiveness of the code multipath mitigation technique was examined through DGPS. Position accuracies were computed for the smoothing versus no smoothing cases, as well as for the multipath correction versus no correction cases. It was shown an improvement was observed for the multipath corrected data for both carrier smoothed code data and data without smoothing. On the other hand, to assess the carrier phase multipath mitigation, a baseline test was devised by comparing results obtained with and without carrier multipath error correction in the measurement. It was verified that by this technique, Up to a 55% improvement in the 3D position accuracy was achieved for non-smoothed and carrier-smoothed code cases and up to 35% improvement in the ambiguity-fixed-carrier case.

In conclusion, the multi-antenna processing approach aimed to mitigate the low-frequency multipath which could not be suppressed by correlator-based techniques without the knowledge of relative geometry between the reflector and the antenna. This technique is achieved by forming an Extended Kalman Filter, in which the code and carrier multipath parameters (state vectors) are estimated and updated based on SD code and carrier observations or sometimes with SNR ratio between close-by antennas, while also incorporating the pre-surveyed precise relative geometry between them. Effective mitigation of multipath errors both in the measurement domain and position domain was shown by this method, especially with a high multipath environment. However, one drawback of such method was that the multipath effect is examined separately from each satellite and the multipath influence from the whole constellation was not covered and analysed.

5.3.2 Displacement monitoring using a dense array of low-cost GPS sensors

To assess the feasibility of displacement monitoring using low-cost GPS receivers, Jo et al. (2013) tested the performance of low-cost GPS chips commonly found in mobile phone or vehicle navigation systems in dynamic response detection. It was normally perceived that these types of receivers could only output C/A code measurement and had relatively low precision with a positioning resolution of several meters. Therefore, they were normally regarded as insufficient and not feasible for SHM applications. However, with dense arrays of such GPS sensors, a 20-30cm resolution was declared to be achieved in dynamic displacement monitoring and with more sensors used, higher precision could be expected.

In the experiment, the performance of low-cost single-frequency GPS chipsets with integrated antennas was evaluated for both static and dynamic conditions in the time and frequency domain. To assess the background noise characteristics over time and the concept of DGPS, the preliminary static calibration tests were conducted with four chipset GPS receivers placed at a fixed location on the roof free from obstruction. Four consecutive days' measurements with a 1Hz sampling rate were recorded. The results from static tests showed a strong correlation for measurements of one single receiver on different days due to the repeatability of the constellation, providing good weather. However, DGPS technique was not feasible due to weak correlation between static noise from the four GPS modules.

The dynamic displacement measurement by low-cost sensors was also tested for its feasibility in a dynamic condition. The test used a horizontal rotor blade, providing circular motions of various rotational speeds and amplitude. Four low-cost single-frequency GPS chipset sensors were placed on the rotor blade to track the motion for each test with different amplitude and different rotation frequencies. A sampling rate of 5 Hz was used during measurement under good weather conditions.

The results from the dynamic test showed that sinusoidal patterns due to dynamic motion could be detected from E/N components timeseries. The frequency of the sinusoidal circular motion could also be revealed from Power Spectral Density (PSD) analysis. Nevertheless, some significant low-frequency drift errors were present in the timeseries which might be caused by the 1/f-shaped noise detected in the spectrum. It was observed that these drift errors were uncorrelated between each sensor pair and by averaging the timeseries from four GPS sensors, the PSD of the resultant timeseries showed lower noise levels over the entire frequency range. To mitigate the low-frequency drift errors caused by 1/f-shaped noise, band-pass filters were used to clearly show the rotation amplitude derived from the GPS measurement. Figure 5.9 showed the PSD plot of GPS measurements for different rotation amplitude with the same frequency, one of the PSDs of four GPS data was compared with the PSD of the averaged data to show the noise reduction effect by the averaging process. It could be seen in Figure 5.9 that the rotational frequency could be derived, even for the 0.25 m amplitude case and after the averaging process, a lot of apparent peaks were detected, implying the decreased noise level.

In conclusion, it was implied that the low-cost chipset GPS measurements were contaminated by noise with 1/f-shape, making the detection of displacement of very low-frequency range (i.e., lower than 0.2 Hz) difficult. However, higher frequency ranges showed quite consistent behaviour in the frequency domain indicating that dynamic displacement of mid-scale cable-stayed bridges or structures with modal frequency larger than 0.2Hz could be feasible. It was also demonstrated the noise level could be potentially reduced with the average combination of measurements from multiple chipset sensors by mitigation of the uncorrelated noise between them. However, due to the resolution of the C/A code measurement, it was insufficient to obtain more precise results from the chipset sensor for deformation monitoring. Therefore, low-cost receivers that could make carrier phase observations should be further investigated.

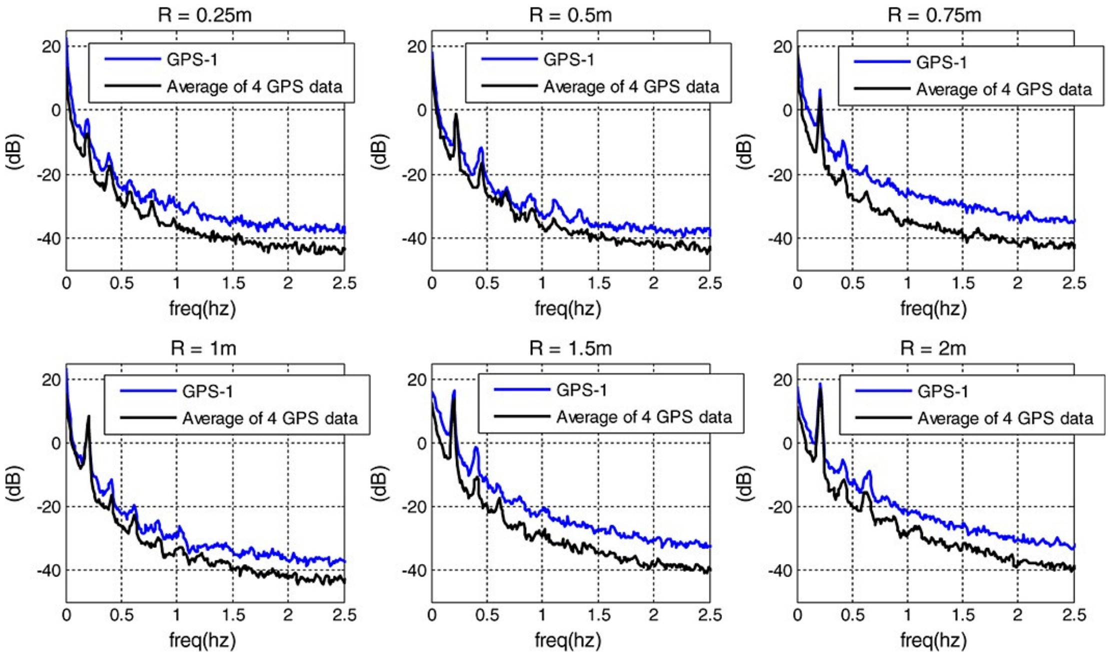

Figure 5. 9 *The averaging effect reflected on the spectral density for different amplitude oscillations (Jo et al., 2013)*

5.3.3 Improving the Low-Cost GPS Monitoring Quality by Using Spatial Correlations

To further improve the low-cost GPS receiver data from the multipath effects for short baselines, Zhang and Schwieger (2016) tested the approach by using the spatial correlation between several adjoined low-cost GPS stations set up with low-cost receivers and antennas.

In their experiment, the rover station formed of several low-cost GPS sensors (3*3 antenna array with a spacing of 0.5m) was established next to a metal wall on the roof with little obstruction to satellites. The measurements were recorded statically for 26 days with a 1Hz sampling rate. Each baseline result adopting different low-cost sensors was post-processed with a geodetic reference station forming ~500m baseline between rover and base. The daily static results were obtained for each baseline. The multipath-induced spatial correlation between each low-cost GPS sensor and reference low-cost sensor was analysed and employed for possible corrections to improve the measurement quality.

By cross-correlation between different baseline results, the correlation coefficient could be shown in Figure 5.10, both using station 4 and station 8 as reference. From Figure 5.10, it could be seen that the correlations of the errors were dependent on the distances between the antennas, the closer the two antennas, the higher correlation could be obtained. It was also seen the distance between the antenna and reflector would also influence the correlation, less correlation was detected between the reference antenna and the antennas closer to the reflector.

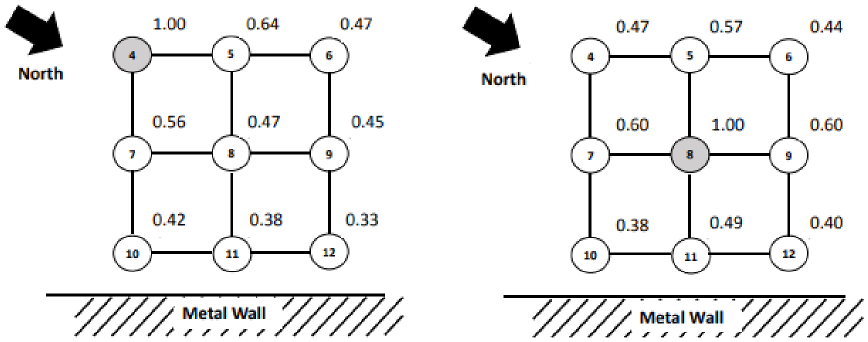

Figure 5. 10 *Maximum spatial correlation between baseline s-a4 (Left) and the other baselines respectively & between s-a8 (right) and the other baselines respectively (Zhang and Schwieger, 2016)*

By taking advantage of spatial correlation between the adjoined stations, the correlating errors in the coordinate residuals could be mitigated. To reduce the correlating errors, firstly a moving average filter was applied to reduce the non-correlating errors, then the cross-correlation was examined with the smoothed baseline solutions between different station couples. The spatial correlation obtained was then adopted to correct for the coordinate of one station along with the measurement from adjoining stations so that the accuracy and reliability could be improved. It was shown in Figure 5.11 on the left that similar patterns and high correlation could be detected for the baseline residuals of two adjoining stations on E and U components which resulted in significantly suppressed noise levels after correction using spatial correlation in corresponding E and U components (Figure 5.11 right). Nevertheless, for the N component, a poor correlation was identified in the residuals, resulting in little difference between the original and the corrected solution.

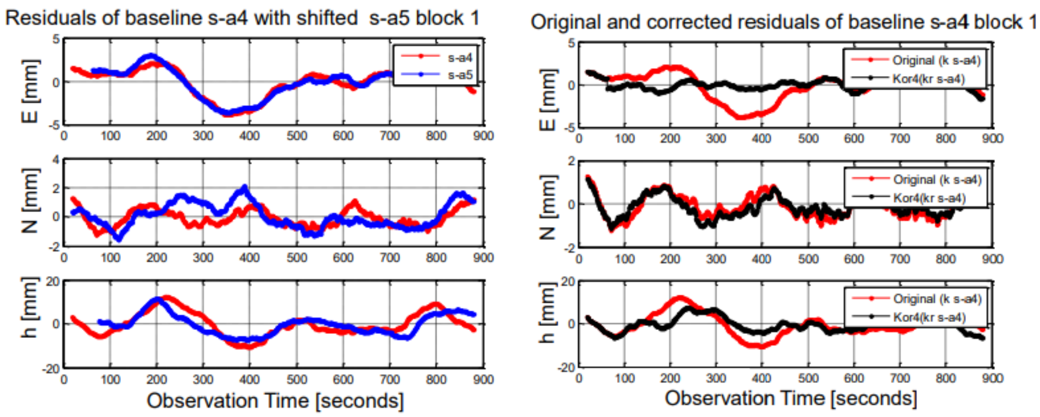

Figure 5. 11 *(Left)E/N/h (mm)original timeseries residuals of baseline s-a4 with shifted s-a5, (Right)The original timeseries residuals for baseline s-a4 and corresponding residuals of corrected timeseries using spatial correlation (Zhang and Schwieger, 2016)*

In conclusion, this study tested the possibility of using an array of low-cost GPS stations for SHM applications with a spatial correlation-based algorithm, particularly in a high multipath scenario. The algorithm based on spatial correlation of coordinates was used to reduce correlating errors between adjoining low-cost GPS stations. Generally, the algorithm worked better with higher spatial correlation. By using the algorithm, a significant improvement of the precision could be made with up to a 50% increase in precision compared to the original data. One possible improvement to the experiment was to reduce the spacing between adjoining stations to increase the spatial correlation between them.

5.3.4 Other multi-antenna approaches

Considering the above research, the first study estimates multipath based on an EKF using the relationship of multipath error and relative geometry between two closely aligned antennas. The second study tries to reduce the uncorrelated error by the averaging process. The third study analyses the spatial correlation and uses it as a parameter to reduce the correlating error within the coordinates.

Besides the aforementioned methods, other researchers also used multiple antennas for multipath mitigation. Vagle (2016) adopted antenna array processing by using signal spatial characteristics and beamforming techniques for multipath signal mitigation. The experiment showed that a six-antenna rectangular array was effective to mitigate short-range multipath signals. Improved performance with a pseudorange error reduction of up to 60% and position error reduction of up to 30% could be achieved by spatial smoothed results using beamformer. Kubo (2017) adopted a multi-antenna approach for multipath mitigation by connecting several patch antennas using an antenna switching device. The antenna switching device could switch the antenna according to the switching period, which was equivalent to the antenna in motion. The concept was to simulate a moving rover antenna by experimental design since with moving rover, the rapid variations of direct signal and reflected signal would largely mitigate the code and carrier multipath. Whereas strong multipath signals would impact the measurement when the rover antenna was static. By this method, the results obtained showed a clear better result than a single antenna.

In this chapter, empirical studies about the application of low-cost GNSS receivers are reviewed. Several methods for improving the precision of the measurement are also looked into. This chapter suggests the methodology to be used in this study. It also indicates the level of accuracy and precision to be expected by assessing low-cost GNSS receivers' performance from various research. In the following chapter, the experimental approach and analysis approach adopted in this study are summarised with reference to the literature review carried out in this Chapter.

Chapter 6 Overview of experimental and processing approach

Generally, the research could be classified into several stages sequentially as shown in Figure 6.1. such as experiment design, implementation, data acquisition, processing, and result analysis. In this Chapter, the experiment design, implementation, and GNSS engine processing are focused on. The detailed data analyses are introduced separately in each chapter later depending on different experiments.

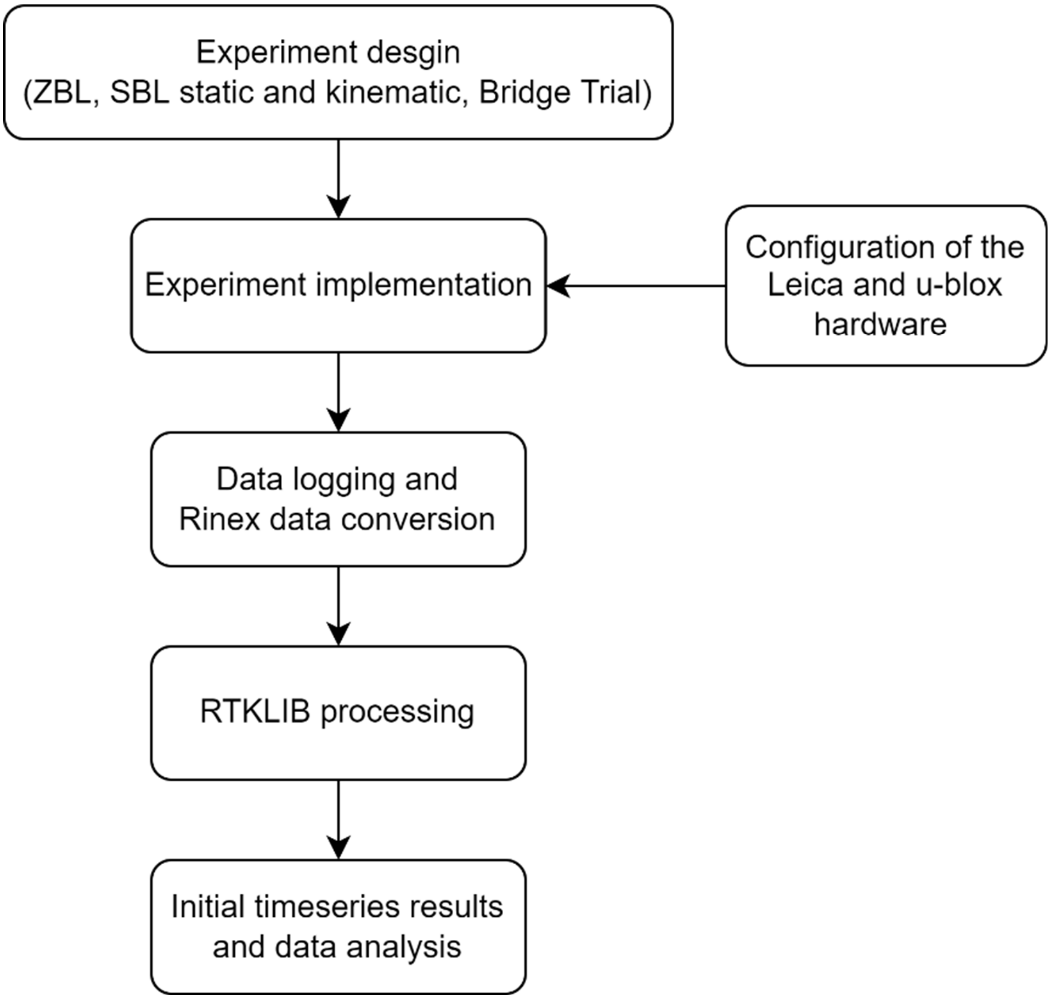

Figure 6. 1 *Flowchart for the overall specification design*

6.1 Progressive experimental and analytical approaches

To assess the performance of low-cost receivers, several experiments are planned progressively. The general workflow and layout of the experimental approaches used in the study are conceived as follows (Figure 6.2). Firstly, a zero-baseline (ZBL) test is conducted, then a short baseline (SBL) static test and kinematic test are carried out, and finally, the outcome obtained from ZBL and SBL test is applied in a real bridge monitoring trial.

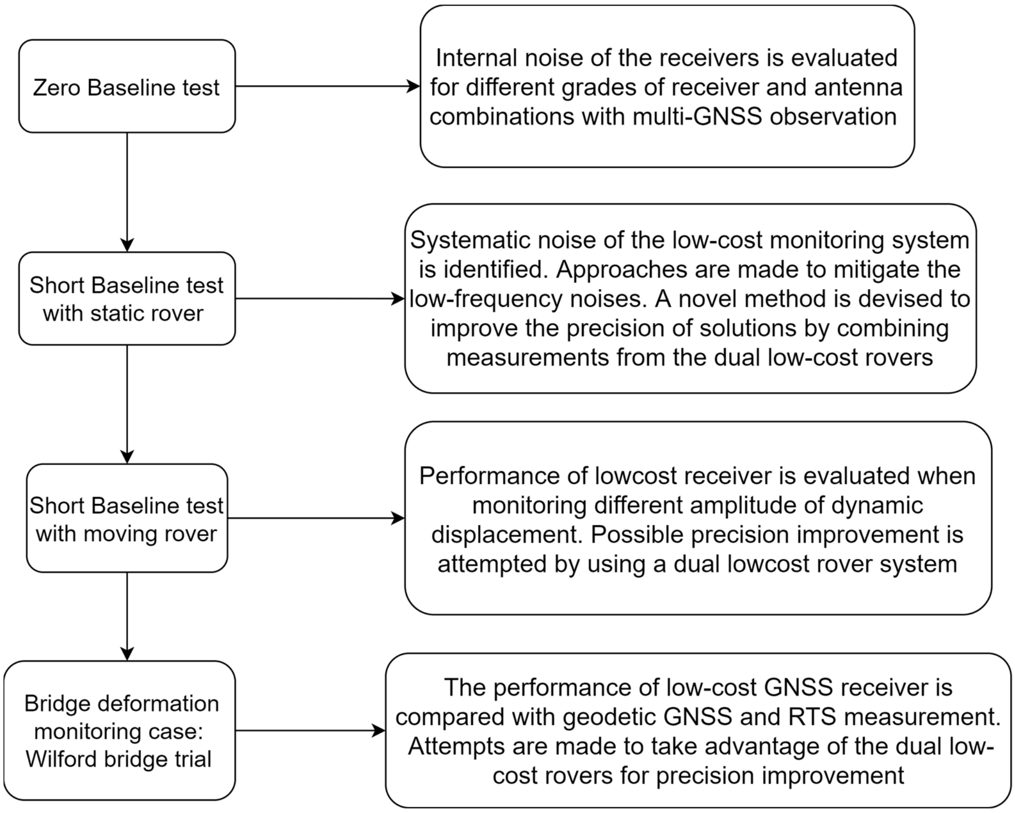

Figure 6. 2 *Workflow of different stages for testing the low-cost receivers' performance and potential outcome*

6.1.1 Zero-baseline test

In the first phase of the study, a ZBL test is implemented for the preliminary analysis of receivers. The general concept (Figure 6.3) is by connecting receiver pairs to the same antenna through a signal splitter, all external noise and errors would cancel due to differencing process. Therefore, the measurement residuals obtained from relative positioning between receiver pairs of the same model (rover and base) are solely related to the receiver's internal processing noise with the influence of satellite geometry (DOP). The measurement residuals are different for different grades of receiver pairs, due to the internal processing noise which is essentially an indicator of the receivers' quality and precision in code and carrier phase measurement. The ZBL test is conducted on a roof with an open sky view and low multipath. Multi-GNSS measurements are made by using different grades of antennas (patch/geodetic grade) in each case. For both cases, the antennas are connected to different grades of receiver pairs via a signal splitter and connection cables.

The analysis is done by assessing the impact of different parameters on the measurement residuals such as receiver grade (low-cost receivers both as the rover and the base, low-cost receiver as the rover and geodetic receiver as the base; geodetic receivers both as the rover and base), multi-GNSS constellations (GPS-only, GPS+Galileo, GPS+GLONASS, GPS+GLONASS+Galileo) and antenna grade (patch or geodetic). Baseline solutions are obtained and expressed as E/N/U timeseries. Spectral analysis is also carried out using Discrete Fourier Transform (DFT) to reveal the noise characteristics in each scenario. The residuals' precision is calculated and concluded for each case and precision variation of residuals is correlated to the variation of DOP value. However, ZBL is an idealistic test since only one antenna is used, which means most of the errors are cancelled through differencing process. Hence, it is not applicable for the evaluation of system noise in real deformation monitoring applications.

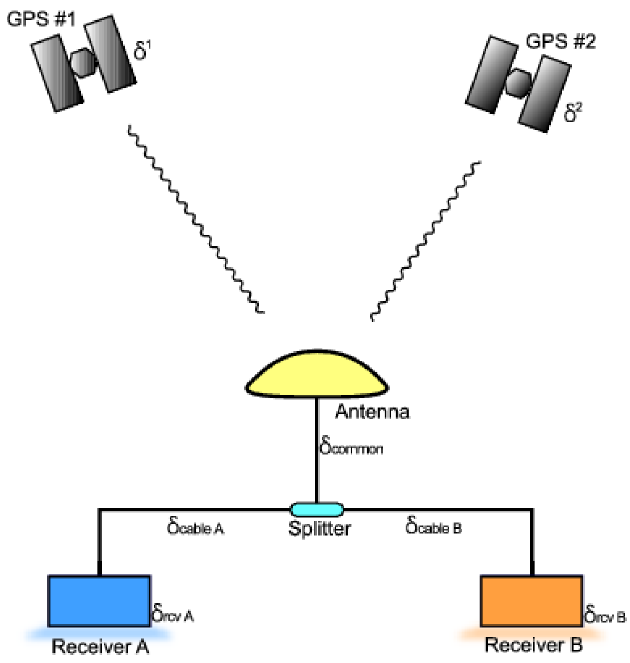

Figure 6. 3 *Concept of ZBL test, with antenna connecting to a receiver pair of A and B, from Kalibrasi GNSS by GSP admin in 2020 (http://www.jasasurveypemetaan.com/kalibrasi-receiver-gps-gnss/)*

6.1.2 Short baseline static test

In the second phase, a SBL test with a static rover is carried out (Figure 6.4). For conventional GNSS deformation monitoring applications, baselines are usually formed between the rover and reference stations. Therefore, to perform noise evaluation of a realistic deformation monitoring system, similar scenarios and conditions are simulated in the SBL static test. In the setup of the experiment, the rover stations are formed of two closely-spaced low-cost receivers/ patch antennas. There are two base stations established, one formed with a geodetic antenna and geodetic receiver, and the other consists of a patch antenna connecting to two different grades of receivers through a signal splitter. The experiment is conducted in the same measuring environment with ZBL test with good sky view and low multipath. Multi-GNSS measurements are made for both rover and base stations. Various SBLs (less than 20 meters) are formed between different rovers and bases.

In the SBL static test, baseline results are obtained by postprocessing for each closely-spaced low-cost rover station with respect to each different reference station. By analysing the results of the SBL test with the static rover, the measurement noise within the monitoring system could be evaluated which is mainly composed of errors such as multipath, PCV, receiver noise, antenna/cable noise, etc. Since two base stations are used, the base station's impact (base station receiver grade and base antenna grade) on the results is initially examined. The multi-GNSS (GPS+ Galileo) solutions are also compared to the GPS-only solutions to confirm the benefit of the inclusion of additional constellation observation. For precision improvement, approaches are also explored to take advantage of the two closely-spaced low-cost rovers. Two methods are adopted: (i) the weighted average combination (Figure 6.5), and (ii) the exclusion of the common errors of the rover-receivers, also known as Common Mode Error (CME) filtering (Figure 6.6). To assess the effectiveness of the CME method for low frequency noise mitigation, comparisons are made between the original, the CME filtered and the conventional adopted SDF results in forms of timeseries and spectra.

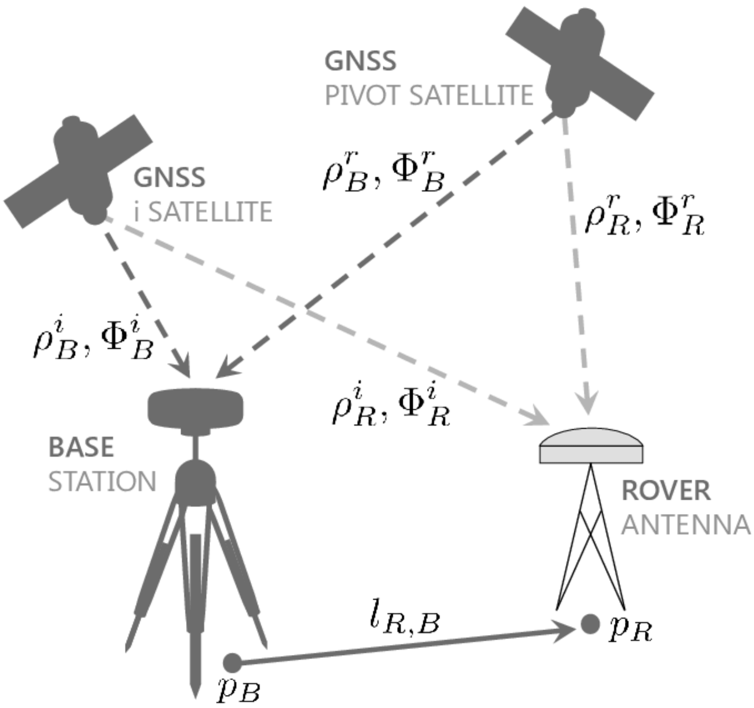

Figure 6. 4 *Concept of the SBL test (Medina et al., 2018). In the SBL static test, the rover is static, but in the SBL kinematic test, the rover is in motion. However, both processings are done in kinematic mode assuming the rover is not static*

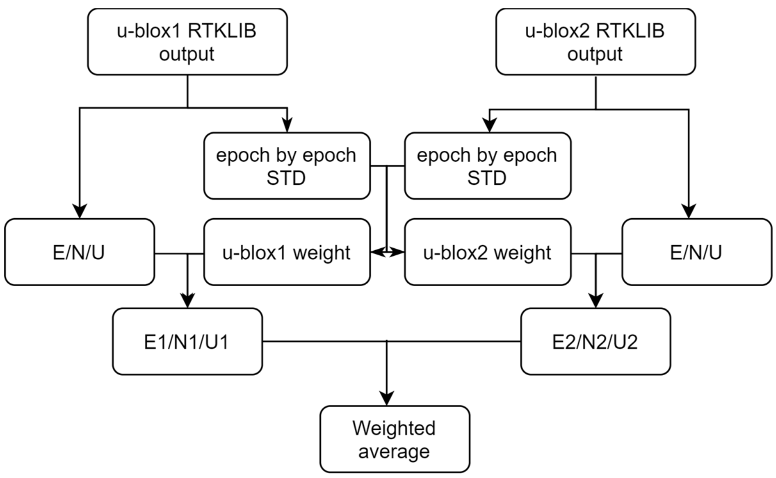

Figure 6. 5 *Flow-charts for weighted average computation (detailed calculation equations can be found in Equation 8.5)*

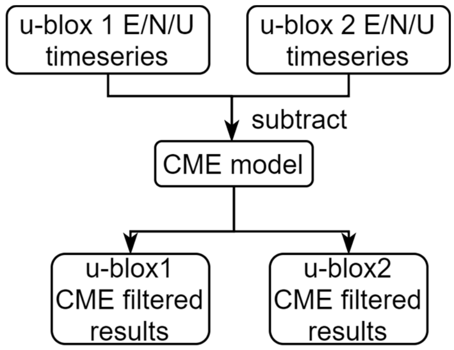

Figure 6. 6 *Flow-charts for CME filtered residuals computation (CME model can be constructed from Equation 8.2).*

6.1.3 Short baseline kinematic test

Following the SBL test with the static rover, in the third stage, SBL kinematic tests with moving rovers are conducted. The experiment aims to assess and improve the precision of low-cost receivers in measuring dynamic motions in comparison to geodetic results. The motion of the rover is imposed and driven by a rotation motor and follows a circular trajectory in the horizontal plane with a uniform angular velocity. Different radii for rotation are also designed. In the experiment, the measurement environment is similar to the previous two tests with no obstructions and little multipath. Three rover stations are formed, two closely-spaced low-cost rovers comprised of the low-cost receivers and patch antennas, and one geodetic rover consisted of a geodetic receiver and antenna. The three rover stations are placed in a way so that they are co-rotating simultaneously with the same radius. Two reference stations are used for two different scenarios, for the first case, the reference station uses a patch antenna connected to a low-cost and geodetic grade receiver through a signal splitter while in the second case, a geodetic antenna is used in the base. During the experiment, the rover and reference stations both record multi-GNSS measurements. Different SBLs (length shorter than 20m) are formed between rover and base stations and kinematic tests are carried out for several displacement amplitude.

The analysis is firstly performed to study the impact of base station receiver grade on the results. Then the precision of low-cost rovers and geodetic rover in monitoring circular motion of different rotation amplitude are evaluated. By assuming circular motion, two references for precision calculation are determined. One reference uses the best-fitted circle from planar E/N trajectory for planar precision calculation. The other reference uses the optimum sinusoidal model simulated from the E/N component from each GNSS measurement to evaluate the precision in E/N components. Both timeseries analysis and DFT spectral analysis are conducted with regard to the original timeseries as well as the residual timeseries. Several comparisons are made to assess the impact of different parameters on the rover solution precision such as different multi-GNSS used, rover station (receiver plus antenna) grade, and base antenna grade. On the other hand, approaches are made to improve the precision of solutions by taking advantage of the two closely-spaced low-cost receivers. In light of SBL static approaches, CME filtering and the averaging approach are attempted and analysed. The refined results are compared to the original and high-pass filtered results to evaluate the effectiveness of both methods.

6.1.4 Bridge Trials

One of the limitations of previous lab tests is the ideal location of the measurement site, i.e. on the roof with clear visibility to satellites and little multipath impact, which does not always account for practical monitoring scenarios. Therefore, in the final stage of the study, the low-cost monitoring system is applied in a real deformation monitoring project (Figure 6.7). A bridge trial is conducted to test the performance of the low-cost monitoring system. The bridge to be monitored is a short-span suspension bridge on a river with a relatively poor multipath condition. At the midspan of the bridge, four sensors are deployed, two closely-spaced low-cost GNSS rover stations formed of low-cost receivers and patch antennas, a geodetic GNSS rover station formed of a geodetic receiver and geodetic antenna, and a prismatic target for the RTS measurements. For both low-cost and geodetic monitoring stations, the same geodetic reference station consisted of a geodetic receiver and antenna is used forming a baseline length of around 50 meters from the rover station. Multi-GNSS (GPS+GLONASS) observations are made for all GNSS equipment. The RTS station aims at the prismatic target fixed on the midspan of the bridge and records measurements continuously and simultaneously with GNSS measurements. Both the reference GNSS station and RTS station are configured on the riverbank on stable ground free from excitations. To detect a clear displacement of the bridge, it is purposely imposed several patterns of loading by various human activities. The displacement and dynamics of the bridge are acquired by all measuring equipment during human-induced excitations.

The low-frequency measurement errors would contaminate the dynamic displacement measurement, especially for GNSS observations suffering from multipath errors. Therefore, data analysis is conducted firstly to mitigate the low frequency errors in the original timeseries. To mitigate the long period noise and reveal the dynamic response from the bridge, a Chebyshev high-pass filter is adopted. DFT spectral analysis is also applied to the timeseries to determine the bridge modal frequencies. Since the measurements recorded by each instrument are all regarding the bridge midspan, to evaluate the performance and accuracy of the low-cost GNSS rover, comparisons in both timeseries and DFT spectra are made between low-cost GNSS, geodetic GNSS, and RTS measurements for each excitation where the most accurate RTS results are used as reference. Attempts are also made by taking advantage of the two closely-spaced low-cost GNSS rovers for solution improvement, such as adopting the weighted average combination method for white noise mitigation or adopting and validating CME filtering for low frequency noise mitigation. Considering the measurement from different instruments and different techniques for precision improvement (weighted average, high-pass filter, CME filter), comparisons are made between i) separate low-cost GNSS solution, ii) weighted average combined solution, iii) geodetic GNSS solution, iv) RTS solution, and v) CME filtered solution. All solutions except CME filtered solution are subjected to high-pass filtering.

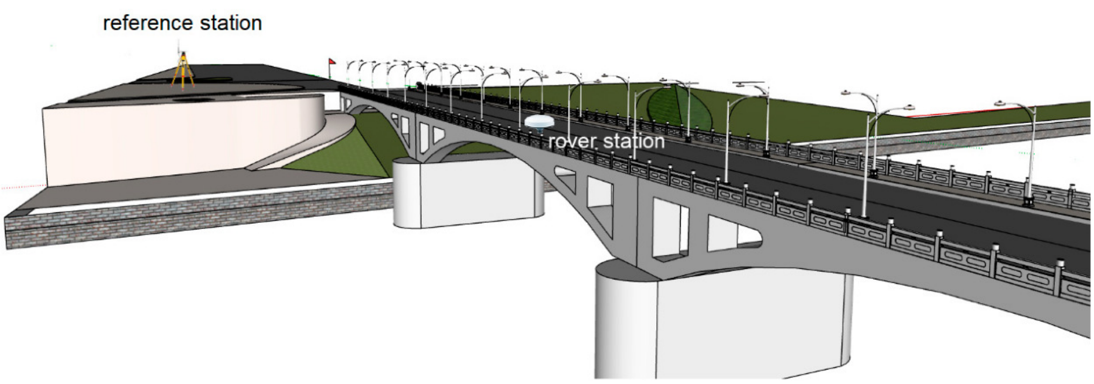

Figure 6. 7 *Concept of reference and rover station layout in a practical bridge GNSS monitoring project (Shen et al., 2019)*

6.2 Acquisition and Processing of the GNSS measurement

The logging of the data mostly happened in the software called ‘u-center 19.05’ where the u-blox receiver measurement could be configured. The ‘Baudrate’ was configured to 115200, which was a common practice adopted by many studies to accommodate message transmission payload. All messages not of our interest were disabled such as RTCM and NMEA messages, to maintain stable streaming of useful messages. Therefore, in the actual data acquisition, only u-blox raw observation message were recorded. All the other parameters in the u-blox settings for the data logging were remained unmodified by default, except for the ‘GNSS config’ and ‘RATE’ under ‘UBX-CFG’ message, where the GPS, Galileo, and GLONASS satellites were checked and enabled, the ‘Rates’ were also configured according to the GPS time, and the sampling frequency of the u-blox receiver was also adjusted accordingly (Figure 6.8).

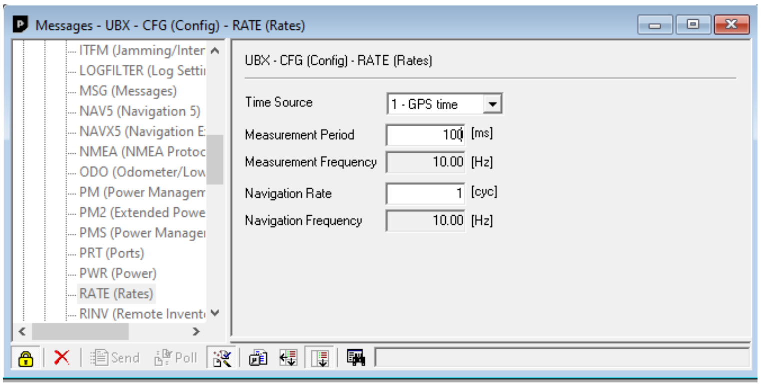

Figure 6. 8 *Configuration of the sampling rate of u-blox receiver in U-center 19.05*

The postprocessing of the baseline solutions was carried out using the free and open-source software RTKLIB developed by Takasu and Yasuda (2009) for GNSS measurement acquisition and processing. In this paper, only several modules of the software are used, such as ‘RTKCONV’ and ‘RTKPOST’. The ‘RTKCONV’ is utilised to convert the raw measurement with ‘.ubx’ format from u-blox receiver to RINEX format observation and navigation files. On the other hand, the ‘RTKPOST‘ is used for post-processing analysis of the RINEX measurements (observation and navigation message) to compute position solutions by various position modes (Figure 6.9), such as SPP, DGPS/DGNSS, Kinematic, Static, PPP, etc. To obtain the optimum position results, there are various options in 'RTKPOST' to manoeuvre, proper configuration of different options leads to the optimum positioning results. In this study, the SBL DD post-processing is focused on.

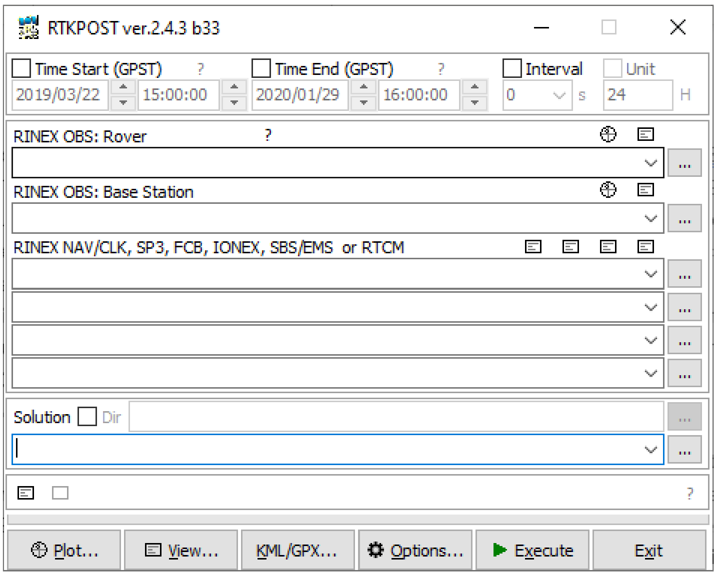

Figure 6. 9 *Main interface for configuration of observation files and navigation files to obtain the postprocessing results*

For SBL DD coordinate computation, in Setting 1 of the configuration options (Figure 6.10), the position mode is selected as kinematic, which denotes carrier-based kinematic positioning. The option for frequency type is chosen as L1. Since for low-cost u-blox receivers, only L1 single-frequency observation can be made. There are several options for Filter type; forward, backward, and combined, indicating the order and sequence of EKF. Normally, the forward filter is the default order. However, with combined forward and backward filters, the obtained results are sometimes smoother. The elevation mask and SNR mask could also be set with the minimum threshold to exclude satellites with low elevation angle and SNR. To exclude satellites below 15-degree elevation angle, a 15-degree elevation mask is used and the SNR mask is not defined and applied. The 'Rec dynamic' option offers a way of predicting the receivers' position with estimated receiver dynamics (velocity and acceleration). The 'Earth tides corrections' are turned off for SBL DD due to relative positioning between rover and base. Ionospheric and tropospheric correction are also unmodified by default with broadcast ionospheric correction and Saastamoinen model for tropospheric correction. Since the ionosphere and troposphere would affect the rover and base in a similar way which is largely mitigated through differencing over a SBL. The satellite ephemeris and clock are chosen as broadcast, the biases of which can also be cancelled through the DD process. The software also provides the option for the inclusion of satellite PCV and receiver PCV to define whether a PCV model is used for satellite and receiver antenna. Enabling RAIM (receiver autonomous integrity monitoring) FDE (fault detection and exclusion) would result in satellites with SSE (sum of squared errors) of residuals over a threshold to be excluded. Although the occurrence of broadcasting wrong ephemeris is relatively rare, this function could be extremely beneficial in filtering out malfunctioning satellites occasionally and preventing the interruption of positioning failure caused by the faulty satellites(Takasu, 2013). Another useful function is to manually exclude and include certain satellites for processing using the satellite inclusion and exclusion option. There are different navigation systems to be used; GPS, GLONASS, Galileo, QZSS, SBAS, BeiDou, and IRNSS. Different constellation combinations could be formed for positioning solutions.

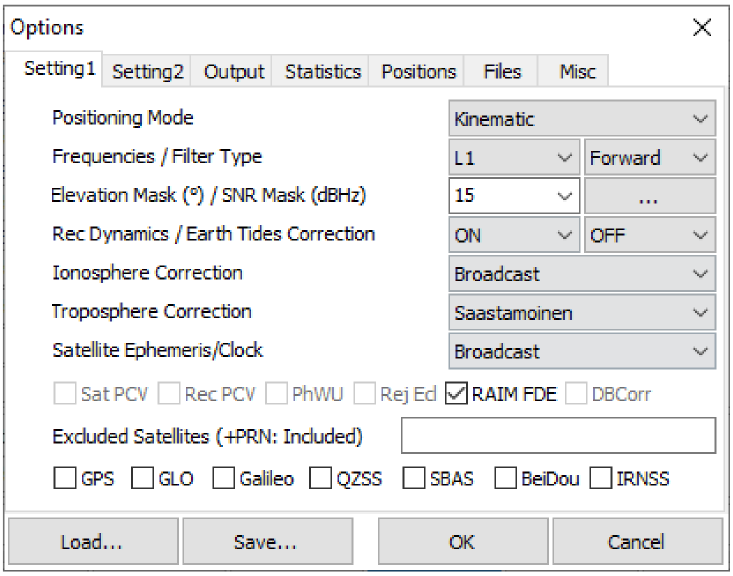

Figure 6. 10 *Setting1 options in RTKPOST*

In Setting 2 of the post-processing (Figure 6.11), the strategy for integer ambiguity resolution is chosen. There are several approaches for GPS; OFF, continuous, instantaneous, fix and hold, PPP-AR. OFF indicate there are no ambiguity resolution; continuous indicates continuously static integer ambiguities are estimated and resolved; instantaneous means the ambiguity is estimated and resolved epoch by epoch; fix and hold means if the validation of the continuous is ok, the ambiguities are tightly constraint to the resolved values (Takasu, 2013). For SBL DD, the continuous strategy is normally used and sometimes fix and hold could also be useful when there are no cycle slips. For the ambiguity resolution of the GLONASS and BeiDou, there are also options of fixing and not fixing the ambiguities. For GLONASS satellites, when the ambiguity resolution is turned on, only the same types of receiver pair for rover and base can be fixed. Different receiver pairs will result in IFB (inter-frequency bias) which cannot be cancelled through DD. Therefore, an option called ‘auto-calibration’, which estimates the receiver inter-channel bias term as a linear equation by frequencies can be used (Takasu, 2013). To validate the integer ambiguity resolution, the ratio of the sum of squared residuals from best integer ambiguity over the second-best integer ambiguity is used and set by a threshold value. The ambiguity resolution could be further limited by parameters such as the threshold for minimum lock count and elevation angle. If the lock count and elevation angle is below a certain threshold, the ambiguity is excluded. The outage count could also be set, indicating if the data outage is beyond a certain value, a reset of ambiguity estimation would initiate. The maximum age of differential which is the time difference between the observation data epochs of the rover receiver and the base station could be constrained by setting to a value. To pre-filter the bad measurement data, a threshold based on measurement GDOP and innovation (pre-fit residuals) were used. If the measurement GDOP and pre-fit residuals are beyond specified threshold, the observables are excluded as an outlier and removed from computation (Takasu, 2013). The number of iterations could also be set for the number of iterations used in the measurement update of the estimation filter.

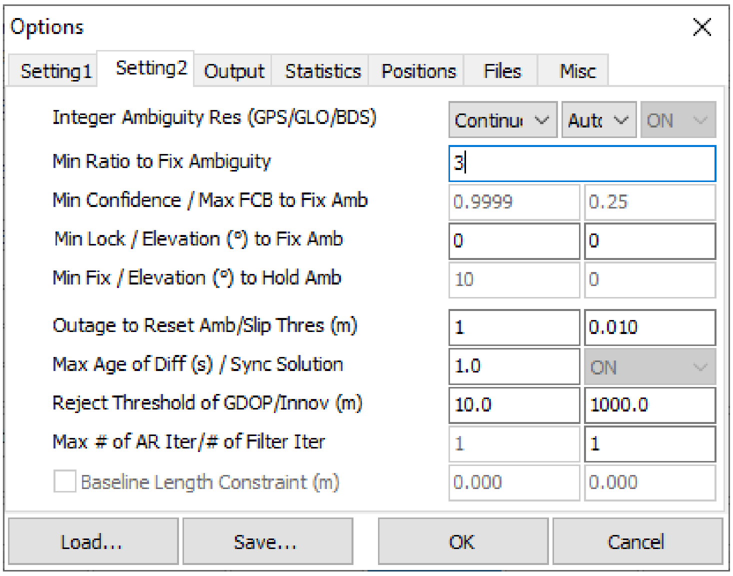

Figure 6. 11 *Setting2 options in RTKPOST*

In the Output tab (Figure 6.12), the solution format can be selected with options of XYZ-ECEF, Longitude/Latitude/Height, and E/N/U baseline. In this study for SBL DD kinematic processing, the local coordinate system 'E/N/U baseline' is adopted for the output, decomposing the baseline vector into E/N/U components. The E/N/U solutions are georeferenced with the GPST timestamps in hh:mm:ss format with 3 decimal places. The estimated states and carrier phase residuals could also be derived along with E/N/U baseline solutions by switching on the 'output solution status' option.

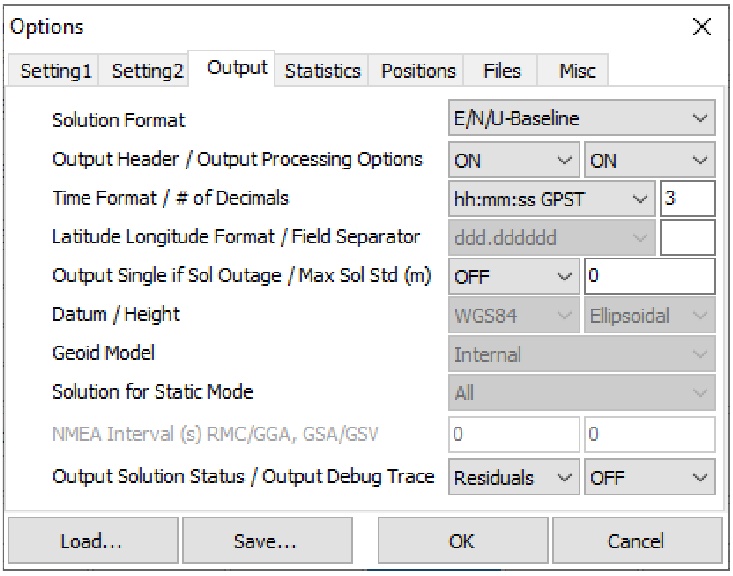

Figure 6. 12 *Output options in RTKPOST*

In the Statistics tab (Figure 6.13), the measurement errors(1-sigma) could be defined. Several parameters could be configured, such as code/carrier phase error ratio, carrier phase error a+b/sin(El), carrier phase error/Baseline, and the STD of Doppler frequency errors. The ratio of STDs of pseudorange errors to carrier-phase errors can be set by code/carrier phase error ratio. In the carrier phase error (a+b/sin(El), the 'a' (the base term) and 'b' (the elevation dependent term) can be configured. The errors from baseline length dependent term could be set by carrier phase error/Baseline.

For the processing noises, the STD of receiver acceleration process noise in the horizontal and vertical direction could be configured which is helpful when using the 'Receiver dynamics' for position estimations. Other process noises could be configured are the STD of carrier-phase bias (ambiguity), vertical ionospheric delay, zenith tropospheric delay, and the satellite clock stability.

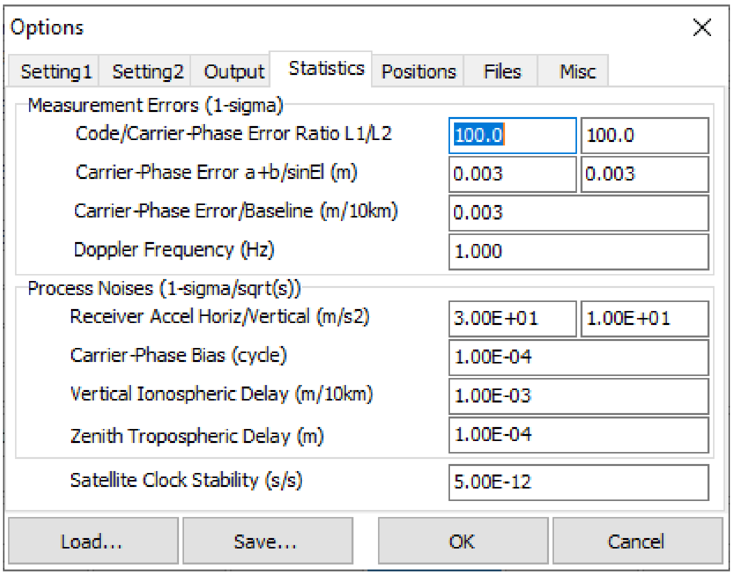

Figure 6. 13 *Statistics options in RTKPOST*

In the Position and File tab, there are fields to define and import the rover antenna PCV and base antenna PCV and base station positions. Some other information such as Geoid, DCB (differential carrier biases), EOP (Earth orientation parameter), OTL (Ocean tidal loading), and Ionosphere data file could also be imported, but since a SBL DD relative positioning is focused on in this paper, they are ignored. In the Misc configuration of the settings, an option called the time Interpolation of Base Station Observation Data can be turned on or off. If it is turned on, the base station data are linearly interpolated to the rover epoch and DD is made with them and if it is turned off, the nearest epoch of base station data is used for DD.

In this Chapter, the benchmark of the four experiments to be carried out is established. For each experiment, the experimental and analytical methods are proposed and clarified. The processing of the GNSS data in RTKLIB is also introduced. For each of the four experiments carried out in this study, a separate report is generated in each separate chapter from Chapter 7 to Chapter 10.

Chapter 7 Zero-baseline test

7.1 Introduction

A preliminary approach to evaluate the performance of low-cost receivers is through a zero-baseline (ZBL) test. The ZBL test is conducted to assess the internal noise level in low-cost receivers compared to geodetic receivers to indicate their different quality and performance. In ZBL experiment, a splitter, an antenna, and two or multiple receivers are usually required. In a proper ZBL set up, an open area with good satellite visibility is required to avoid any signal outage. A single antenna is adopted and connected to two/multi- receivers for observation via a signal splitter. The concept of ZBL is that satellite signals would firstly be received by an external GNSS antenna, transmitted via a signal splitter, and distributed to two/several separate GNSS receivers via signal splitter portals and connecting cables. Then the receivers would process and output the observations based on the signals tracked, different grade of receivers would have different quality of observations even though the same signals were received from the same antenna.

The ZBL tests commonly take the DD residuals between receiver couple as results. Receiver couple of the same model is used to represent the noise level of the same receiver used. In the ZBL experiment, the noise of the low-cost receiver and geodetic receiver model is represented by the DD residuals of the u-blox receiver couple of the same model and Leica receiver couple of the same model respectively. The comparison between the residuals would imply different noise levels or quality of two different receiver models.

The ZBL test quantifies the receivers' internal noise. With ZBL, most external biases and errors are ideally cancelled, such as satellite/receiver clock and orbit errors, ionospheric/tropospheric errors, antenna errors, and multipath errors, etc. All the aforementioned errors are eliminated through the differencing process. Therefore, the baseline results would only reflect the internal noise level of the receiver, making ZBL test ideal for the internal noise evaluation and comparison of different receivers. For example, if four receivers (2*model 1 and 2* model 2) are connected to the splitter, noise analysis could be conducted for each receiver couple by calculating the DD results between them as baseline residuals. The difference between the DD results of different receiver model couples would imply the different noise generated for different receiver models in the receiver signal processing.

For ZBL tests, the E/N/U baseline solution timeseries are derived. Baseline solutions refer to the vectorised distances between base and rover stations for each measurement epoch, which is decomposed into E, N, Up components according to the local E/N/U coordinate system. The ZBL test uses the same antenna for the rover and base stations. Therefore, if a baseline solution is computed, the DD baseline solutions should be zero theoretically if the receiver noise is not considered. The zero value is used as the reference with any deviation from zero value implying the noise level within the receiver.

Although the ZBL residuals reflect the receivers' internal noise, the ZBL GNSS measurements are still impacted by DOP especially for long periods of measurements when the constellation orbits create different relative satellite to receiver geometries leading to a variation in DOP. The reason that ZBL residuals are strongly correlated to the DOP is probably due to that most measurement errors are cancelled through differencing whereas the impact of DOP remains and becomes significant and amplified in influencing the residuals precision (Roberts et al., 2018). It is shown that ZBL results precision would improve for durations with low DOP when more satellites are tracked and good satellite to receiver relative geometry are formed, and vice versa.

7.2 Experiment procedure and setup

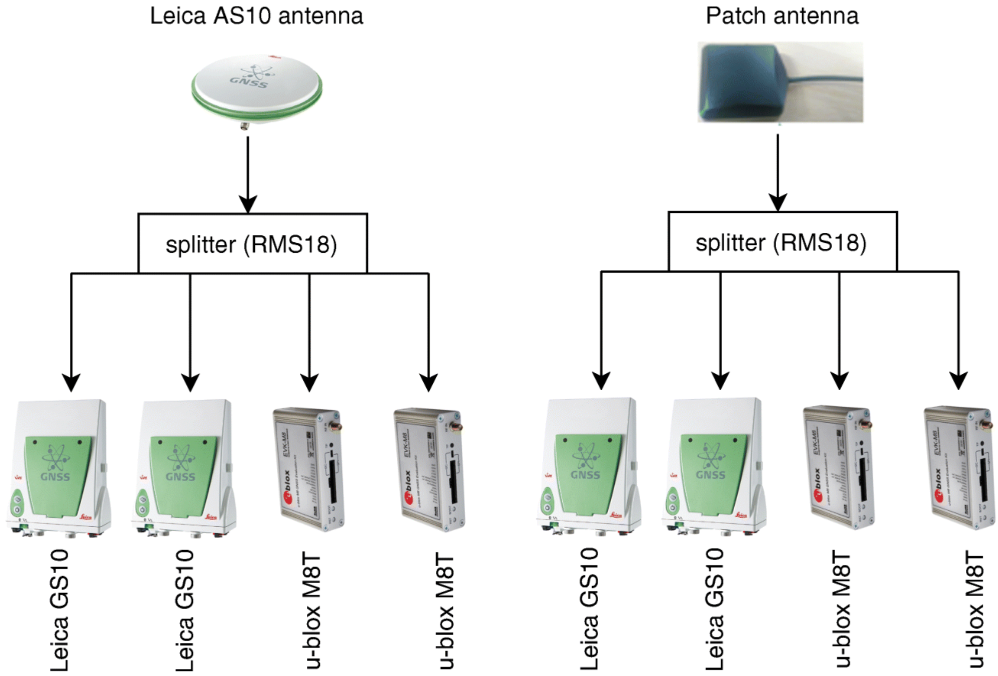

Figure 7. 1 *Deployment of the ZBL GNSS measurements (left) with Leica AS10 antenna (20/03/2018) and (right) with a patch antenna (22/03/2018)*

To evaluate and compare the internal noise level of a low-cost receiver against a geodetic receiver, the ZBL test was carried out. The possible impact from DOP, different multi-GNSS constellations and antenna grades was also identified. The ZBL experiment took place on the roof (Figure 7.2) of Nottingham Geospatial Building (NGB) from 20/03/2018 to 24/03/2018, at the University of Nottingham, UK. During the experiment, four GNSS receivers (2*low-cost and 2*Geodetic) were connected to a single antenna (geodetic or patch antenna) on different days. The two low-cost GNSS receivers were single-frequency (L1) u-blox (M8T module) receivers, with the capacity to record multi-constellation carrier phase measurements with nominal temporal accuracy of sub-microsecond (Wilkinson et al., 2017). The two geodetic receivers were dual-frequency Leica GS10 GNSS receivers, with nominal horizontal precision of 8mm±1ppm and vertical precision of 15mm±1ppm for post-processing in kinematic mode (Leica Geosystems, 2012). Two different types of antennas were also used for different sessions of measurement, both with the capacity to receive multi-constellation GNSS signals: (i) a low-cost patch antenna and (ii) a survey-grade geodetic antenna (Leica AS10). The low-cost patch antenna was acquired from the EVK-M8T kit and was mounted on a large ground plane for multipath suppression and the Leica AS10 geodetic antenna was commonly used in monitoring applications (Msaewe et al., 2021; Ioulia et al., 2018; Xue et al., 2021). The layout of ZBL experiments was shown in Figure 7.1 for both ZBL tests on 20/03/2018 with a Leica AS10 antenna and on 22/03/2018 with a patch antenna. For both tests, the antennas were connected to the GNSS receivers through a signal splitter (RMS18 Rack Mount Splitter) tracking GPS, GLONASS, and Galileo satellites. The RMS18 signal splitter was manufactured by GPS source, with a 12dB typical gain and capacity to pass GPS, GLONASS, and Galileo signals, The sampling rate of the measurements for both days was 1 Hz. A computer with 'u-center' software for logging u-blox receiver raw observations was used.

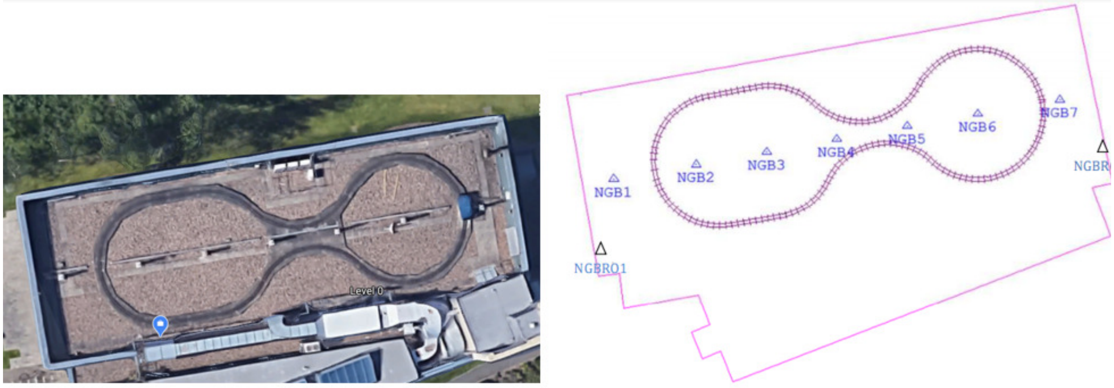

Figure 7. 2 *Sketch of the roof and the NGB (left satellite image; right plan view), the AS10 antenna, and patch antenna are mounted at control point NGB5 in separate days from 22/03/2018 to 24/03/2018 for data acquisition.*

7.3 GNSS data process and methodology of timeseries analysis

The raw GNSS records of u-blox and GS10 receivers were firstly converted to RINEX files using 'covbin'(a module in RTKLIB) and Teqc software, which were then processed in 'Rtkpost' in RTKLIB 2.4.3. The GNSS measurements of the four receivers were combined forming different base-rover couples and processed in DD kinematic mode. The same 'Rtkpost' configuration was applied for each base-rover combination: kinematic processing mode with continuous ambiguity resolution, Saastamoinen troposphere model, and broadcast ionosphere model (Table 7.1). The output of the processing was the timeseries of the baseline length in Northing, Easting, and Up component. For ZBL measurements, the baseline length between the base and rover receiver was zero. Therefore, the E/N/U baseline timeseries should range around zero and express the measurement noise.

For ZBL results, RTKPOST were firstly configured based on Table 7.1. After the original measurement format conversion to RINEX observations files, both rover and base station RINEX files were then imported to RTKPOST to form different base-rover DD combinations. The navigation messages used were downloaded from CDDIS NASA depositories in corresponding days with the GPS time and satellite's status, the ephemeris, and the almanac information. The output obtained from RTKLIB was a timeseries of E/N/U baseline solutions, parameters such as the standard error of solutions for each epoch, satellite number, SNR, DOP, and carrier phase residuals were also present in the solutions.

Table 7. 1 *Settings Configuration for RTKLIB 2.4.3 for ZBL test*

Settings	Options
Position mode	Kinematic
Frequency/Filter type	L1/Forward
Elevation Mask	15
Ionosphere Correction	Broadcast
Troposphere Correction	Saastamoinen
Satellite Ephemeris/Clock	Broadcast
RAIM FDE	Ticked
Constellation selection	GPS, GPS+Galileo, GPS+GLONASS, GPS+GLONASS+ Galileo
Integer Ambiguity Res	Continuous
Min Ratio to Fix Ambiguity	3
Output	E/N/U-Baseline
Time interpolation of Base station Data	ON
Datum	WGS84

During the data analysis, three combinations of base-rover formation were examined and analysed: (i) base and rover: u-blox receivers, (ii) base and rover: Leica receivers, and (iii) base: Leica receiver and rover: u-blox receiver. Furthermore, since GPS, Galileo, and GLONASS satellites signals were recorded, four different combinations of satellite constellation were examined: (i) GPS-only, (ii) GPS+GLONASS, (iii) GPS+GLONASS+Galileo, and (iv) GPS+Galileo, to evaluate the contribution of multi-GNSS constellations on the performance of the low-cost receiver. However, to achieve ambiguity resolution for the GLONASS measurements, the same model of receivers for base and rover were required due to Inter-Frequency Bias (IFB) (Wanninger, 2012). Hence for the combination Leica as base and u-blox as rover, only the GPS-only and GPS+Galileo solutions were produced.

The two-day experiments using two types of GNSS antennas resulted in six combinations of solutions (Table 7.2). The solution comparisons between different combinations showed the effect of different receivers and antennas' qualities (combinations A, B, D, and E). It was also evaluated the effect of using a low-cost receiver or geodetic receiver as base-reference (combinations A, C, D, and F). The timeseries analyses were carried out in MATLAB, by 1) E/N/U timeseries plotting and statistical calculation; 2) DOP timeseries plotting and calculation; 3) DFT spectral analysis of the timeseries.

Table 7. 2 *Different combinations of solutions for the ZBL GNSS measurements*

Combination	Base receiver	Rover receiver	Antenna
A	u-blox M8T	u-blox M8T	patch antenna
B	GS10	GS10	patch antenna
C	GS10	u-blox M8T	patch antenna
D	u-blox M8T	u-blox M8T	AS10
E	GS10	GS10	AS10
F	GS10	u-blox M8T	AS10

7.4 Zero-baseline results

7.4.1 Timeseries

The ZBL data analyses were applied to the E, N, and Up coordinate timeseries of all different combinations. In Figure 7.3 and 7.4, the E, N, Up coordinate timeseries of combination D and A for four different multi-constellations are presented. Additional timeseries could also be found for the other combinations in Appendix A (Figures S1-S4). A preliminary analysis of the timeseries reveals the variation of their range is due to the impact of the geometry of the current satellite constellation and the influence of the satellite systems. The GPS-only solution seems to have a similar precision with the GPS+Galileo solution (Figure 7.3 and 7.4, Table 7.3 and 7.4), apart from few durations (e.g. 22:00-23:00 or 10:00-11:00), when the GPS constellation geometry is weak. Regarding the GPS+GLONASS solution, it is seen a reduced precision with frequent occurrence of outliers, which will be further analysed. The GPS+GLONASS+Galileo solution seems to have similar performance as the GPS-only solution, apart from the periods of outliers that are produced due to the GLONASS constellation. Furthermore, the estimated STDs of the solution computed for each epoch by RTKLIB follows the same trend as the STD of the E/N/U timeseries, having the lowest STD for E component followed by N and U components. However, the estimated STDs of the solution for the epochs characterised as outliers (spikes) do not have a significant difference from that without outliers.

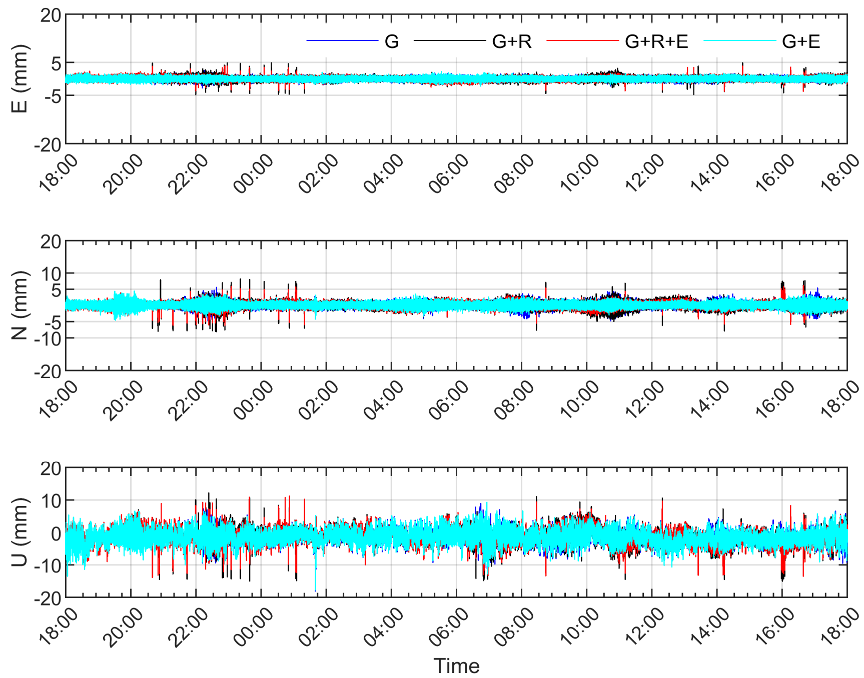

Figure 7. 3 *E/N/U coordinate timeseries of combination D. ZBL measurements for the four available solutions: G: GPS-only, G+R: GPS+GLONASS, G+R+E: GPS+GLONASS+Galileo, and G+E: GPS+Galileo. The G+E solution seems to be the most precise (i.e. the least variance), while the G+R solution seems to have the most outliers*

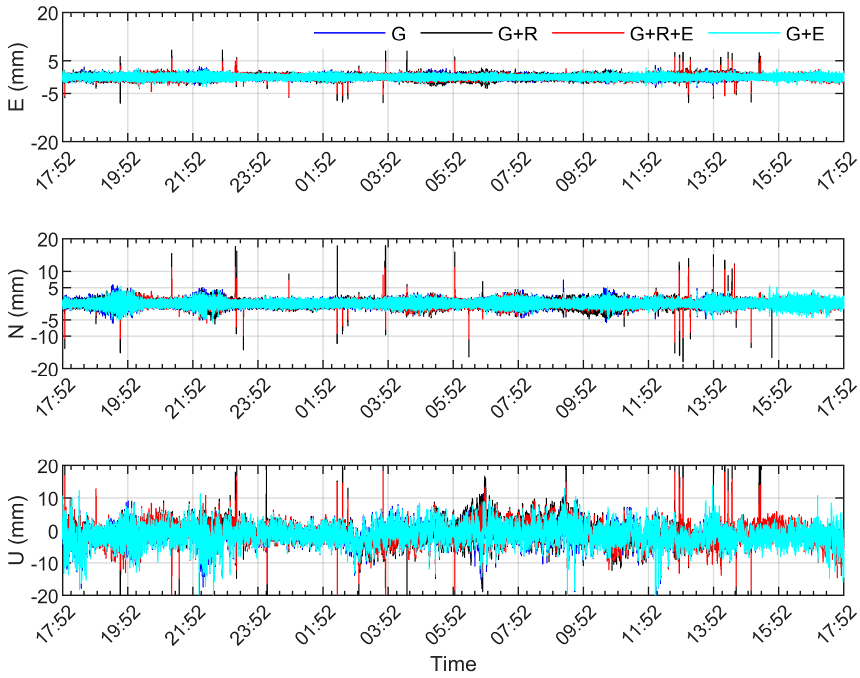

Figure 7. 4 *E/N/U coordinate timeseries of combination A. ZBL measurements for the four available solutions: G: GPS-only, G+R: GPS+GLONASS, G+R+E: GPS+GLONASS+Galileo, and G+E: GPS+Galileo. The performance of the different multi-GNSS solutions is similar to those of combination D.*

Table 7. 3 *Mean and STD of combination A. ZBL measurements for the four solutions (GPS: G; GPS+GLONASS: G+R; GPS+GLONASS+Galileo: G+R+E; GPS+Galileo: G+E), which are presented in Figure 7.3*

	E component		N component		U component	
Unit (mm)	mean	σ	mean	σ	mean	σ
G	0.01	0.47	0.00	0.77	-1.33	1.99
G+R	0.03	0.54	-0.02	0.85	-1.32	2.14
G+R+E	0.01	0.48	-0.00	0.72	-1.32	2.06
G+E	0.01	0.44	0.02	0.69	-1.36	2.01

Table 7. 4 *Mean and STD of combination D. ZBL measurements for the four solutions (GPS: G; GPS+GLONASS: G+R; GPS+GLONASS+Galileo: G+R+E; GPS+Galileo: G+E), which are presented in Figure 7.4*

	E component		N component		U component	
Unit (mm)	mean	σ	mean	σ	mean	σ
G	0.02	0.55	0.00	0.89	-1.40	2.79
G+R	0.03	0.62	-0.05	0.95	-1.04	2.86
G+R+E	0.02	0.55	-0.02	0.81	-1.08	2.73
G+E	0.02	0.52	0.01	0.82	-1.41	2.78

7.4.2 Spectral Analysis

Spectral analysis was also applied on the GNSS coordinate timeseries using Discrete Fourier Transform (DFT) to identify noise characteristics of the GNSS measurements. Figure 7.5 presents the spectra of combinations A, D, and E for GPS-only constellations, where it is observed that all three combinations have similar spectral characteristics for the horizontal components, with combination E resulting in the least noisy spectrum mainly for low frequencies (<0.01 Hz). Furthermore, the spectra of the u-blox timeseries exhibit similar characteristics regardless of the antenna used (patch or AS10). Regarding the Up component, there is a larger difference between the three spectra, with the combination E resulting again in the least noisy spectrum. It can also be noticed the impact of antenna quality is evident, as the spectrum of combination A is the noisiest especially for frequency larger than 0.01 Hz, indicating the level of the white noise band is amplified by the low-quality of the patch antenna. Spectra with similar results for GPS+GLONASS and GPS+GLONASS+Galileo are also shown in the Appendix A (Figures S5-S7).

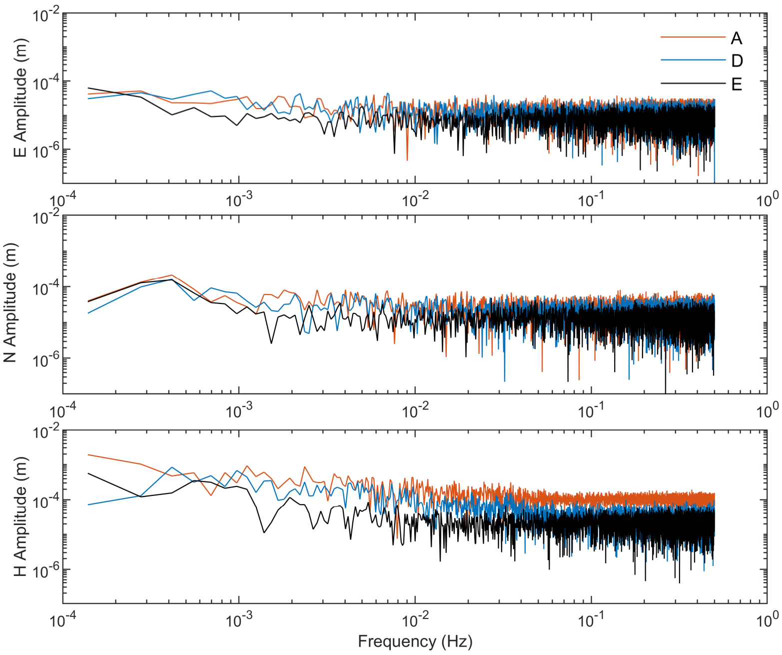

Figure 7. 5 *Spectra of E/N/U components for the solutions of the combinations A, D, and E using GPS-only constellation. It is evident that combination E (Leica receiver and antenna) has the least noisy spectrum. Also, the geodetic antenna reduces the u-blox receiver noise, with respect to the combination of the patch antenna, mainly in the Up component.*

7.5 Evaluation of the GNSS receiver performance

To investigate the impact of the satellite geometry on ZBL residuals, the ZBL timeseries were correlated with GDOP. GDOP is a parameter describing position uncertainty due to the satellite to receiver relative geometry. For ZBL test, the measurement noise is a result of position error due to the satellite geometry amplified by the receiver noise. Hence, to analyse the impact of the satellite constellation on the ZBL performance of the two different grades of GNSS receivers, the moving standard deviation (MSTD) of the coordinates timeseries is computed and correlated with the moving average of the GDOP timeseries using a time-window of 1800s (Figure 7.6). The ZBL timeseries analyses indicate that the lowest STD (noise) is achieved when the geodetic receivers are used both as the base and rover station (combinations B and E; Table 7.5), confirming the results of the spectral analysis (Figure 7.5). This is probably due to the low-cost receiver is characterised by more receiver internal noise compared to the geodetic receiver, leading to different GNSS timeseries noise levels especially for the ZBL measurement, where the receiver noise is the dominant error source. Furthermore, the noise levels of the combinations A, C, and D, F are at a similar level. It is also observed the combination A and D achieved a slightly lower noise level than combinations C and F respectively. The reason is probably due to the introduction of some extra errors when DD couples are formed between different types of receivers (u-blox and Leica) in ZBL where receiver noise is the dominant error of the result. A similar analysis was done for the GPS+Galileo solution for the different ZBL receiver grade combinations and provided in Figure S8. The GPS+GLONASS solution was not analysed due to the impact of the inter-frequency bias.

Generally, the pattern of the MSTD is similar for all the coordinate timeseries and in agreement with the GDOP timeseries, reflecting the impact of the GPS satellite constellation (Msaewe et al., 2017). For the horizontal components, there seems to be a constant difference in the noise level between the Leica (B, E) and u-blox receivers (A, D), as expressed by the ratio between their MSTD (Leica – to – u-blox), which fluctuates between 0.7-0.9 for N and E for geodetic antenna and 0.6-0.8 for N and E for patch antenna respectively, following the trend of the GDOP timeseries (Figure 7.7). In both E and N components, the ratio of the geodetic antenna is higher than that of the patch antenna indicating the improvement when switching from u-blox to Leica base is more obvious with patch antenna than that with a geodetic antenna. Regarding the Up component, the difference of the noise level between the Leica and u-blox receivers varies more randomly, ranging from 0.4-0.9, especially when the patch antenna is used. The correlation of the GDOP with the ratio of the Up component is not that clear, especially for the patch antenna, indicating the subjectivity of the noise level to the antenna.

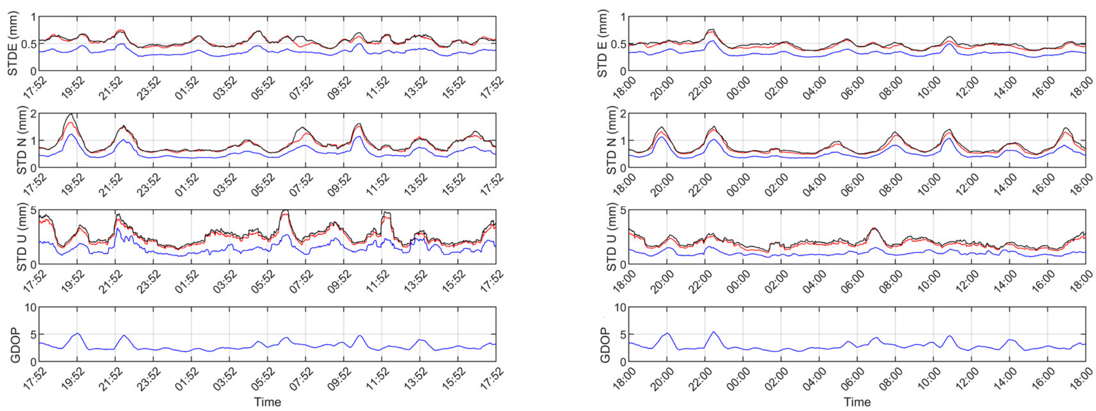

***Figure 7. 6** The MSTD of GPS-only timeseries for E/N/U and the corresponding GDOP moving average timeseries using (left) the patch antenna and (right) the geodetic antenna,*

having as base-rover; both Leica receivers (blue line), both u-blox receivers (red) and Leica (base) and u-blox (rover) receiver (black line). The precision of the GNSS timeseries reflects the GDOP variance. It is evident the impact of the antenna on the precision of the Up component.

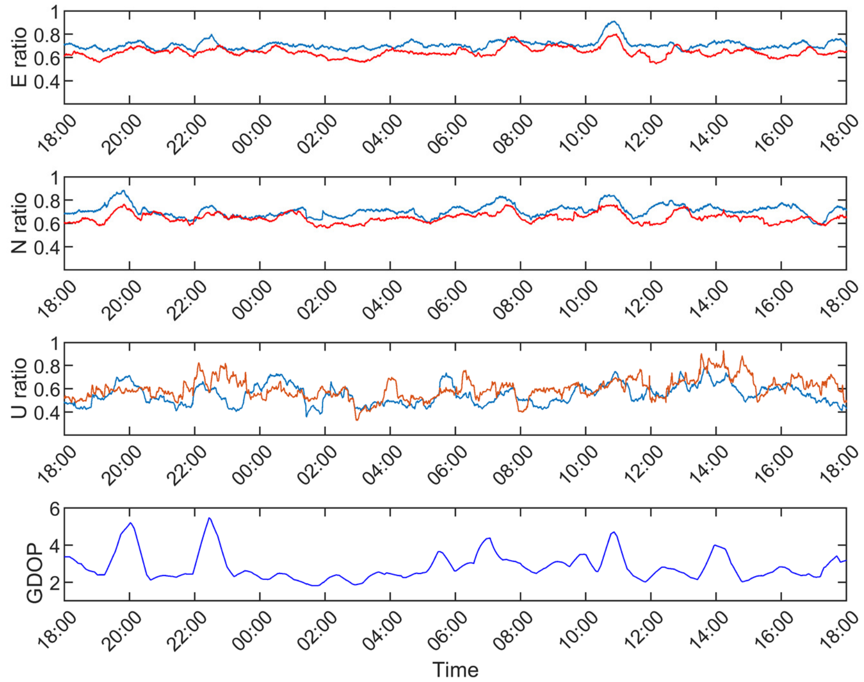

Figure 7. 7 *Ratio of STD between Leica and u-blox for each epoch for E/N/U, when using the geodetic antenna (blue line) and the patch antenna (red line) and the corresponding GDOP timeseries.*

From the spectra of Figure 7.8, it can be seen that for both geodetic antenna and patch antenna, the u-blox as rover and Leica as the base formation is generally having the largest noise level of the three, followed by u-blox receiver couple and least noise from Leica receiver couple, which is in correspondence to the timeseries result. However, it is also noted that for patch antenna, especially for N/U components, the noise reduction due to change of receiver grade is more towards higher frequencies (white noise) around 0.01-1 Hz. While for other circumstances, the reduction of noise due to receiver grade usually impacts the low-frequency components. This is probably due to the additional filtering of patch antenna noise from the geodetic receiver.

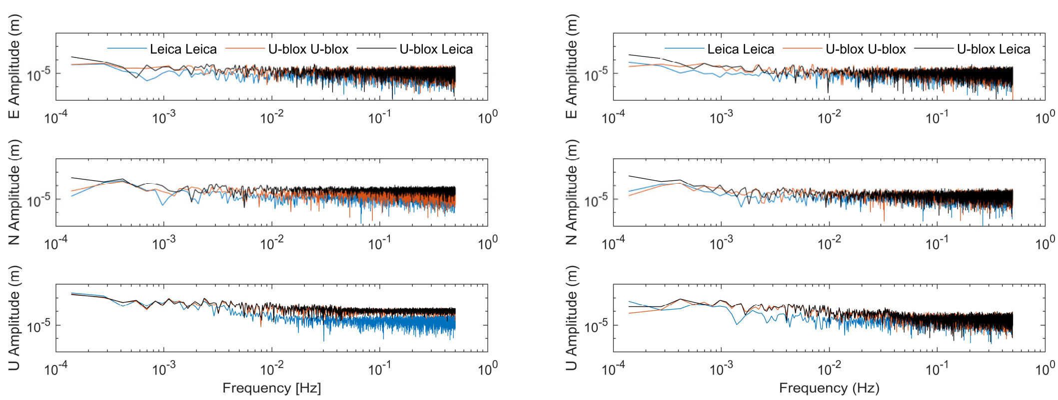

Figure 7. 8 *Spectra of GPS-only solutions for different rover-base formations. (Left) patch antenna, (Right) Leica AS10 antenna (Leica Leica stands for Leica receiver couple, U-blox*

U-blox stands for u-blox receiver couple and U-blox Leica stands for u-blox as rover and Leica as the base)

Table 7. 5 *The 24hr period STD (in mm) and data loss as a percentage with respect to the entire duration of the record, due to float solution and gross error removal for each GNSS solution. G: GPS-only, G+R: GPS+GLONASS, G+R+E: GPS+GLONASS+Galileo, G+E:GPS+Galileo. The percentage of data loss due to gross errors is specifically shown in the brackets.*

	E combination				B combination				D combination				A combination			
	E	N	U	Date Loss	E	N	U	Date Loss	E	N	U	Data Loss	E	N	U	Data Loss
G	0.3	0.6	1.2	0	0.4	0.6	1.9	0	0.5	0.8	2	0	0.5	0.9	2.8	0.11%
G+R	0.3	0.4	1.2	0	0.4	0.6	1.9	0	0.5	0.9	2.1	3.0% (0.24%)	0.6	1	2.9	1.7% (0.18%)
G+R+E	0.3	0.4	1.2	0	0.3	0.5	1.7	0	0.5	0.7	2.1	2.5% (0.23%)	0.6	0.8	2.7	1.5% (0.2%)
G+E	0.3	0.4	1.1	0	0.3	0.5	1.8	0	0.4	0.7	2	0	0.5	0.8	2.8	0.12%

7.6 Evaluation of the antenna's performance

The antenna's performance comparison is conducted through analysis of the MSTD of combinations A, C, and D, F (Figure 7.9). It is observed the highest precision is in the E component (sub-mm level) and then follows the N component (1-mm level); the small variations of MSTD are dominantly related to the GDOP variations. However, the patch antenna had an additional impact on the measurement noise, especially for the N component, which increase the difference between the solutions of combinations A and D up to 0.4 mm and 0.2 mm for N and E, respectively, and makes the correlation between STD and GDOP less strong, especially for relatively low GDOP values (GDOP <4). Regarding the Up component, the GDOP is related strongly to STD mainly for the combinations where the geodetic antenna is used (combination A and C), whereas for the combinations where patch antenna is used (combination D and F), a significant impact on the measurements noise could be seen, as it is observed the difference of the MSTD between the results of geodetic and patch antenna reaching even up to 2.5mm (combinations A and D). The impact of the patch antenna on the vertical component is also confirmed by the spectral analysis in Figure 7.5, where a larger difference is noted for Up spectra than E/N spectra. It is also seen that the high noise level is not always in agreement with the high GDOP values.

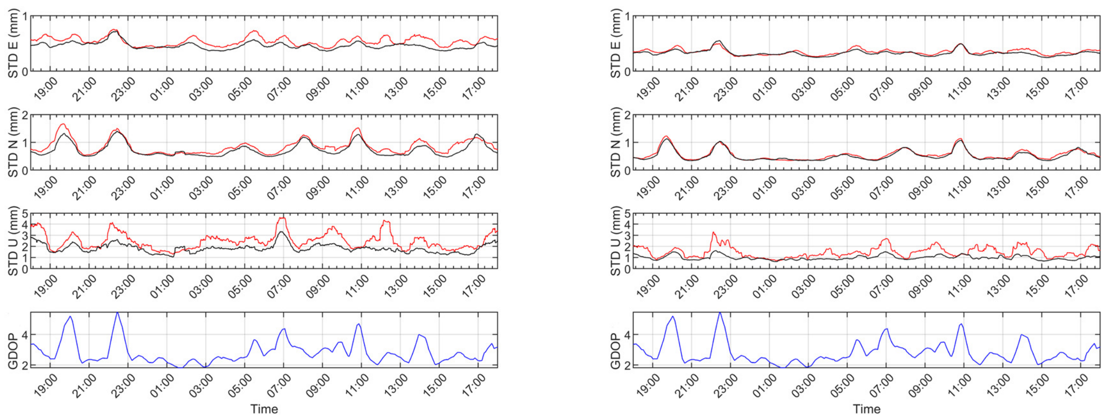

Figure 7. 9 *MSTD of GPS-only coordinates timeseries for the combinations with the patch (red line) and geodetic antenna (black line) for the ZBL measurements and having (left) u-*

blox receiver both as rover and base, and (right) Leica receiver both as rover and base. The E and N components generally follow the GDOP trend for both receivers. It is evident that the Up component is affected by the type of antenna

Also, the ratio of Leica-to-u-blox noise is generally higher for the geodetic antenna than the patch antenna (Figure 7.7), which also indicates the enhancement of the low-cost receivers' precision due to the geodetic antenna. Regarding the vertical component, the ratio is higher for the patch antenna, especially for periods of a poor constellation, which indicates the degradation of the Leica receiver precision due to the patch antenna.

From Figure 7.10, as can be seen for E/N components, comparing the noise with AS10 antenna and patch antenna, low noise can be detected with AS10 antenna especially at frequencies below 0.01 Hz, while for the white noise frequency, they are similar. A larger decrease in noise can be seen for Up components as compared to E/N when changing to the geodetic antenna which is also in congruence with timeseries results. For Up components, with Leica receiver couple, most noise is mitigated at low-frequency components (below 0.01 Hz) when antenna changed to geodetic grade, however with u-blox receiver couple, the change of antenna would also decrease the noise level in the white noise band. This indicates for Up components, the geodetic antenna AS10 could also filter out some white noise for the u-blox receiver couple.

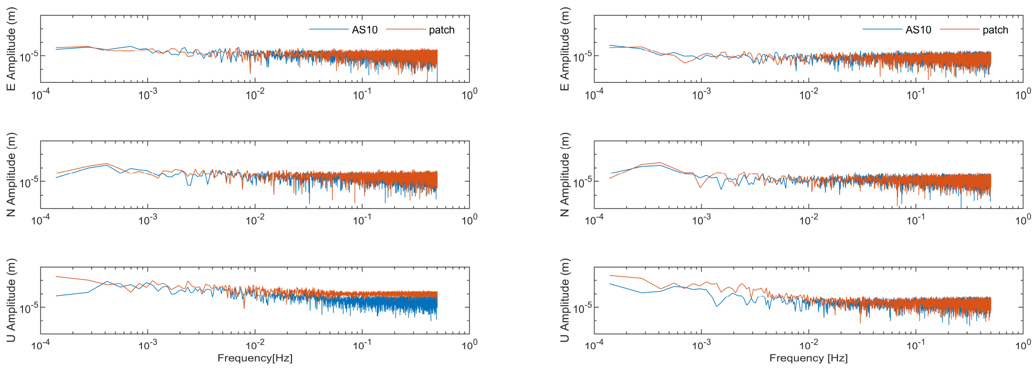

Figure 7. 10 *Spectra of GPS-only coordinates timeseries with patch and geodetic antenna (AS10) for the ZBL measurements having (left) u-blox receiver both as rover and base, and (right) Leica receiver both as rover and base.*

7.7 Evaluation of the multi-GNSS contribution

Table 7.5 presents the overall STD of the four GNSS solutions. For the performance of the Leica receivers, it is generally observed that the two multi-GNSS solutions, GPS+GLONASS+Galileo and GPS+Galileo, result in the best precision regardless of the antenna used. However, for periods of good GPS satellite constellation the achieved precision of GPS-only is practically the same with the multi-GNSS solution (Figure 7.11 and 7.12). Moreover, potential weak geometry of GLONASS satellite constellation or problematic function of GLONASS satellite could result to lower precision of multi-GNSS solution (for instance in Figure 7.11, N component for the period 07:30-08:00), which was also proved by Msaewe et al. (2017).

Focusing on the u-blox receivers, it is also observed that the highest precision is achieved by the GPS+Galileo, while the solutions including the GLONASS satellites

(GPS+GLONASS and GPS+GLONASS+Galileo) suffer from frequent outliers, as observed in Figure 7.3, 7.4, and Figure 7.12. Those outliers are the result of cycle slips occurring for the GLONASS satellites in the u-blox measurements. These outliers seem not to depend on (i) the type of the antenna as they occur regardless of which antenna was used, or (ii) the processing software, as the cycle slips occur also in the solution derived from Leica Infinity. To identify the reason for the cycle slips, the result is further looked into, the type/grade of the antenna is not a cause of the cycle slips however might affect the number of cycle slips, it is observed that with Leica receiver couple, cycle slip would not occur even changing from the geodetic antenna to patch antenna, however with u-blox receiver couple, cycle slips occur irrespective the antenna, but with geodetic antenna, fewer cycle slips are identified(Table 7.5). It is also observed that the majority of these cycle slips seem not to occur in the Leica measurements; result from Leica receiver couple would not have cycle slips with all combinations of constellations, but cycle slips (outliers) occur only with u-blox receivers when GLONASS observations were incorporated in the solution. This is because, with the same epoch, the satellites with low SNR causing cycle slips are automatically rejected by Leica receivers while they are accepted by u-blox receivers in processing. It is found that when both Leica and u-blox receivers are connecting to the same antenna, the u-blox receiver includes some low SNR GLONASS satellite observations, while the Leica receiver simply excludes them.

To further analyse the potential impact of the antenna type and the GLONASS satellite signal, the signal-to-noise ratio (SNR) of each satellite of the GPS and GLONASS satellites were examined for representative periods of gross errors. Based on Figure 7.3 and Figure 7.4, it was shown that most of the GLONASS satellites were experiencing cycle-slip conditions with u-blox receivers, the case where u-blox receiver couple with AS10 antenna was further investigated for the reason why outliers occur with the presence of GLONASS constellation for u-blox receivers. By comparing timeseries obtained by inclusion of particular GLONASS satellites and excluding them, it was observed that two particular GLONASS satellites (R06 & R08) have a significant impact on the timeseries by adopting them for computation compared to excluding them. More outliers could be detected when including them and by the exclusion of satellite R06 and R08, some of the gross errors (outliers) were mitigated from the timeseries at period (i.e. 14:30-15:00, 20:00-20:30)

Therefore, the SNRs of these two GLONASS satellites were studied. In Figure 7.13, the SNR measured by the u-blox receiver and Leica receiver regarding GLONASS R06 and R08 were plotted respectively. It was noted that regarding R06, the observation could be successfully recorded by the u-blox receiver, although a low SNR was detected. However comparatively for the geodetic receiver measurement, no observation for R06 was recorded during 22/03/2018. On the other hand, for the SNR plot of R08, it was shown that for some periods with low strength (SNR) GLONASS satellite signals, for instance, 14:30-15:00, 20:00-20:30, observations were recorded with u-blox receivers but not with Leica receiver even they had the same antenna configuration. This evidence suggested that the u-blox receiver could manage to record observations from the satellite, nevertheless, lack the ability to distinguish and filter out bad quality (low SNR) GLONASS signals as the Leica receiver. The cycle slips may be caused by the low strength GLONASS signals received by the u-blox receivers which are not filtered out and are still used for the solution calculation. On the contrary, the addition of the Galileo system in the GNSS solution seemed to enhance the precision of the GPS+Galileo solution and reduce the data gaps in the timeseries solution.

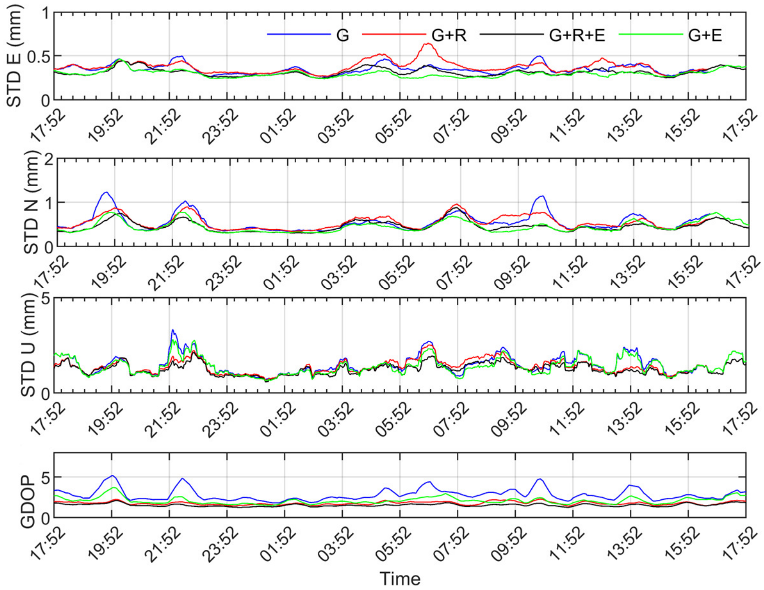

Figure 7. 11 *MSTD GNSS timeseries of Leica receiver both as rover and base using the patch antenna with GDOP timeseries for all four multi-GNSS solutions (G: GPS, G+R: GPS+GLONASS; G+E: GPS+Galileo; G+R+E: GPS+GLONASS+Galileo). It is observed that the GPS solution generally follows the trend of GDOP, whereas the G+R solution does not follow the corresponding GDOP trend, especially for the E component.*

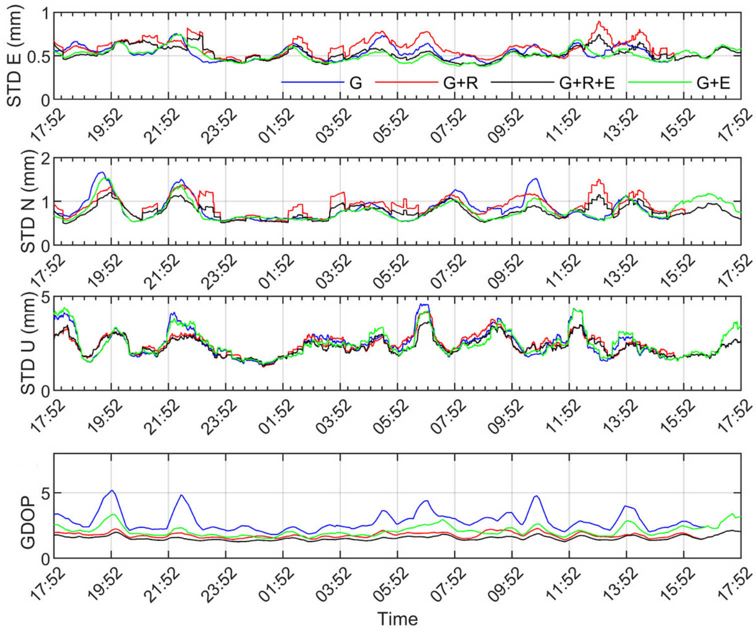

Figure 7. 12 *MSTD timeseries of u-blox receivers both as rover and base using the patch antenna with GDOP timeseries for all four multi-GNSS solutions. (G:GPS; G+R:GPS+GLONASS; G+E:GPS+Galileo; G+R+E:GPS+GLONASS+Galileo). Similar observations with Figure 7.11; the G solution generally follows the trend of GDOP, whereas the G+R solution does not follow the corresponding GDOP trend, especially for the E component.*

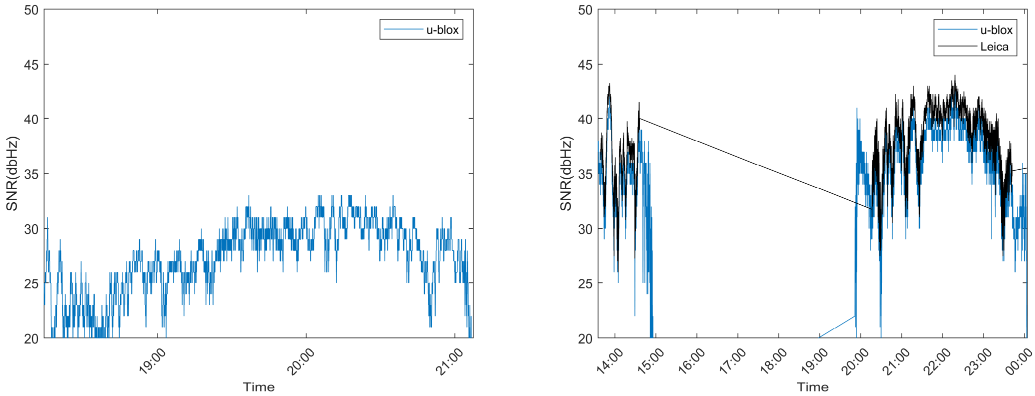

Figure 7. 13 *ZBL SNR timeseries comparison between u-blox receiver and Leica receiver when connecting to geodetic antenna Leica AS10 for (left) GLONASS R06, and (right) GLONASS R08 at 22/03/2018*

From the spectra in Figure 7.14, it is seen that for Leica receiver couple with AS10 antenna, multi-constellation could overall increase the precision and accuracy for E/N components, however, for other cases, it is not so obvious for the spectral analysis to detect the precision improvement form multi-constellation. The multi-GNSS solution normally would be more precise when GPS-only constellation is weak, while the timeseries shows most of the period, the multi-GNSS results seem to show similar results with GPS-only solutions indicating a little benefit of multi-GNSS when the GPS constellation is good, however, improvements are detected with short periods of time with multi-constellation (Figure 11& Figure 12).

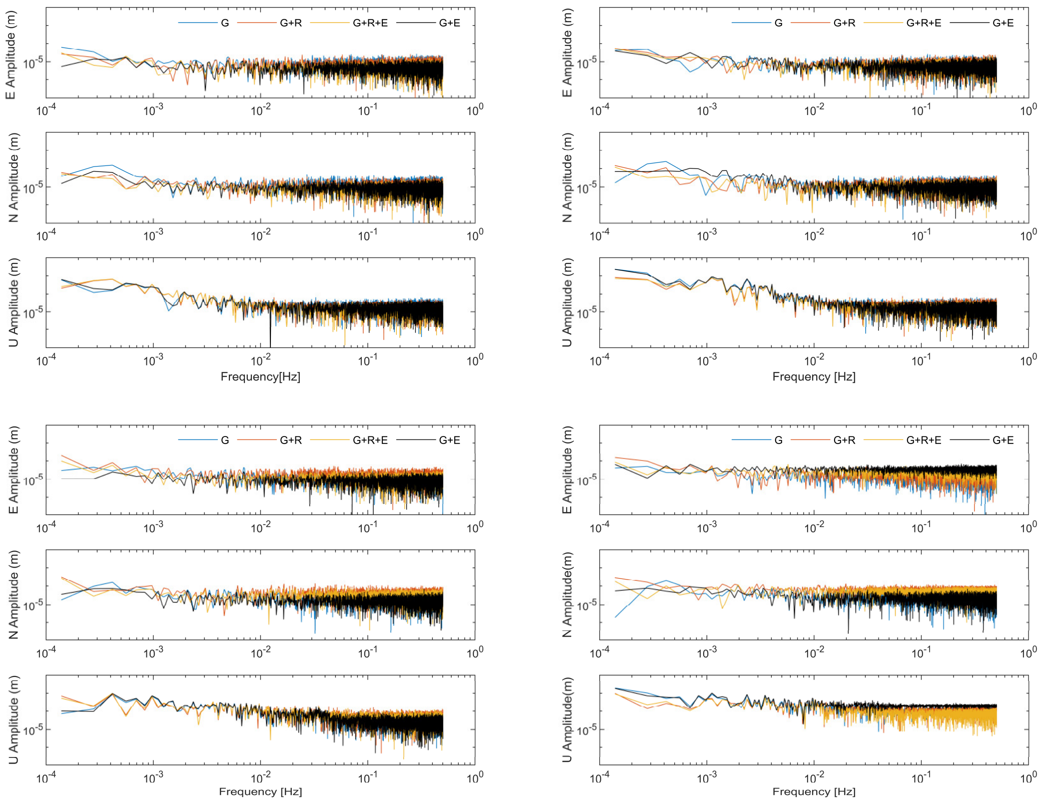

Figure 7. 14 *Spectra of E/N/U timeseries of different combinations A, B, D, E of different multi-GNSS constellations, (G; GPS-only, G+R: GPS+GLONASS, G+R+E: GPS+GLONASS+Galileo, G+E: GPS+ Galileo) i) Top left: Leica receiver couple with AS10*

antenna (E) Top right: Leica receiver couple with patch antenna (B) Bottom left: u-blox receiver couple with AS10 antenna (D), Bottom right: u-blox receiver couple with the patch antenna (A)

7.8 Evaluation of SNR

SNR is defined as the ratio of signal power to noise power usually expressed as the level of the desired signal to the level of background noise. It shows the signal quality and noise characteristics of GNSS measurement and serves as a measure of receiver tracking efficacy or for comparison of signal strengths between channels and satellites (Bilich et al., 2007). The SNR value is an observable recorded by GNSS receivers and depends on the receiver's front-end bandwidth, acquisition, and tracking parameters (Joseph and Petovello, 2010) and is sensitive to carrier phase multipath (Bilich et al., 2007). Furthermore, SNR is also a useful indicator for evaluating the GNSS receiver noise level from the observations after the signal processing of the receiver (Joseph and Petovello, 2010)

To study the impact of antenna grade and receiver grade on SNR measurement, SNR is examined and compared in two aspects; 1) comparisons of SNR measurement between different grades of receivers in processing the same signal coming from the same antenna; 2) comparison of SNR from different grades of antennas using the same receiver. The first comparison requires both u-blox receiver and Leica GS10 receiver connection to the same antenna, and by comparing the SNR value output from u-blox and Leica receiver measurement, the result would indicate the difference of noise generated within the u-blox receiver and Leica receiver. The second comparison requires measurements for different antennas on different days in the ZBL test, the SNR output from different antennas could be compared using the measurement from the same receiver, considering the repeatability of GPS constellations. The difference of SNR would indicate the impact of antenna grade on SNR measurement plus the atmospheric biases for different days.

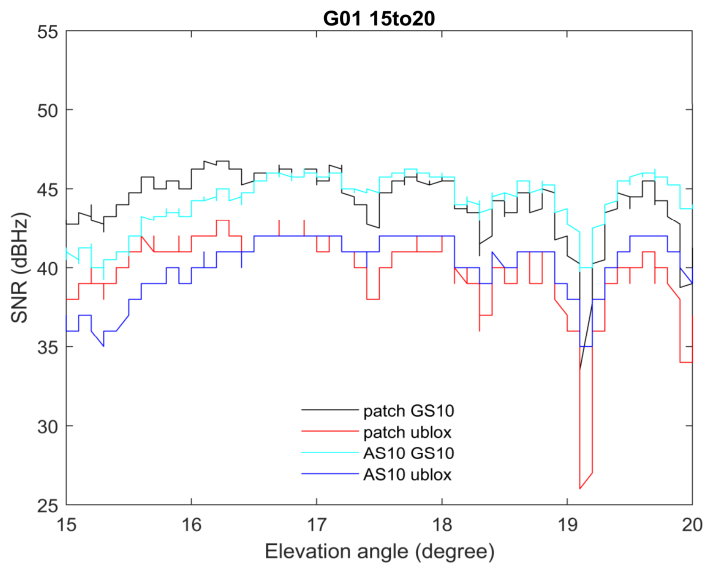

Figure 7. 15 *Comparison of SNR value of G01 satellite for different receiver-antenna formations (antenna-receiver : i)patch-GS10; ii)patch-u-blox;iii)AS10-GS10, iv) AS10-u-blox) within satellite elevation range 15-20*

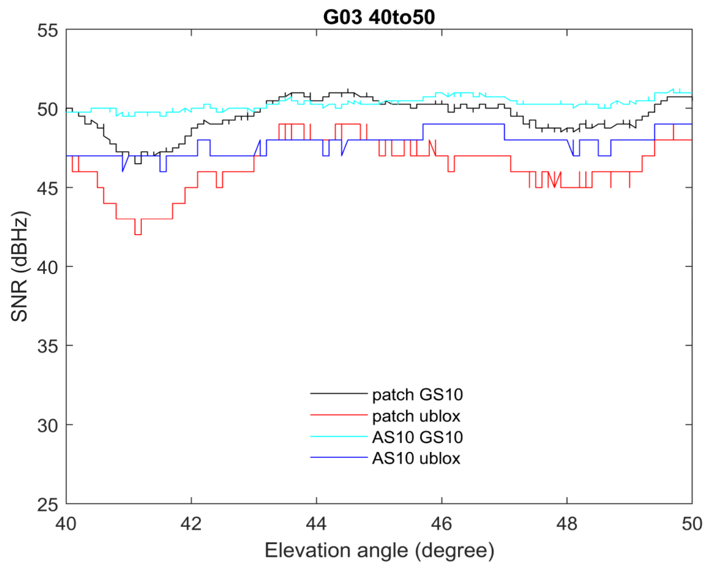

Figure 7. 16 *Comparison of SNR value of G03 satellite for different receiver-antenna formations (antenna-receiver: i) patch-GS10; ii) patch-u-blox; iii) AS10-GS10, iv) AS10-u-blox) within satellite elevation range 40-50*

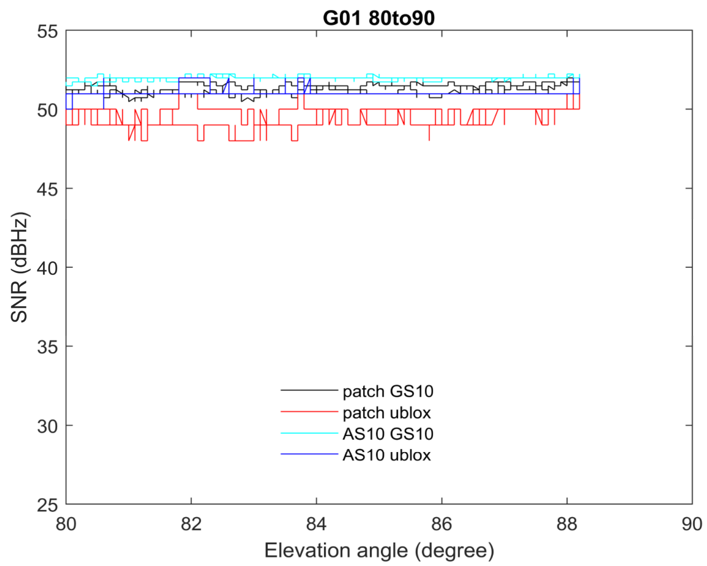

Figure 7. 17 *Comparison of SNR value of G01 satellite for different receiver-antenna formations (antenna-receiver: i)patch-GS10; ii)patch-u-blox; iii)AS10-GS10, iv) AS10-u-blox) within satellite elevation range 80 to 90*

It is shown three example SNR comparisons (Figure 7.15, Figure 7.16, Figure 7.17) between different receiver-antenna formations regarding satellites of different elevation angles. Satellites of three different elevation angle ranges are used (15-20, 40-50, and 80-90). It is clear that the SNR increases with an increase of elevation angle from Figure 7.15 to Figure 7.16, to Figure 7.17, the SNR range is around 35-45 dBHz for elevation angle 15-20, increase to 45-50 dBHz for elevation angle 40-50 and further increase to 50-55 dBHz for elevation angle 80-90.

Comparing the receiver grade, it is shown that the SNR value from Leica GS10 receiver and u-blox receivers is around 1-5 dB offset with each other depending on elevation angle, with larger elevation angle the SNR difference tend to decrease when at 15-20 elevation angle (Figure 7.15) the SNR of Leica GS10 receiver is around 4-5 dBHz larger, and at 40-50 elevation angle (Figure 7.16) the SNR of Leica GS10 is 2-3 dBHz larger, and at 80-90 elevation angle Figure 7.17), the SNR of Leica GS10 is 1-2 dBHz larger. It is also interesting to note the SNR measurements from Leica receivers are with a resolution of 0.25, however, the u-blox measurements of SNR values are with respect to integer values.

Comparing the antenna grade, generally, the SNR from AS10 should have larger values than the patch antenna. However, it is not clear from Figure 7.15 for the satellite of the elevation angle range of 15-20, as for lower elevation angle (15-16.5), the patch antenna SNR value is even larger than AS10 antenna, this phenomenon could be as a result of the ionospheric/ tropospheric biases, but for the elevation angle of 16.5-20, the SNR from AS10 output is slightly better (up to 1-2dBHz) than patch antenna. As of satellite of elevation angle 40-50 (Figure 7.16), there is more tendency to show that the SNR from AS10 is larger than that of patch antenna up to 5dBHz for both receiver couples, as is true for most of the elevation angle range within 40-50. Regarding satellite of elevation angle 80-90, the trend of AS10 having larger SNR value than patch antenna is clearer since for nearly all elevation angles, the AS10 is having SNR larger than patch antenna up to 2dBHz for both receiver couples. The increasing tendency of AS10 having larger SNR values than patch antenna with increasing of elevation angle could imply the atmospheric biases effect on SNR measurement, with low elevation angle, SNR is more prone to be impacted by ionosphere and troposphere biases. It is also observed that the difference of SNR between AS10 and patch antenna is slightly larger for u-blox receiver couple than Leica couple, especially for high elevation angle range (40-50, 80-90), this finding is in correspondence with Figure 7.9, where it is found the change of antenna grade has more impact on u-blox receivers than Leica receivers

7.9 Discussion and Summary

The ZBL study aims to investigate the noise characteristics of the low-cost u-blox receiver against Leica geodetic receivers subjected to different grades antenna and multi-GNSS constellation combinations. To fulfil the aim, the data analyses are carried out as listed in Table 7.6. Timeseries and spectra are generated. STDs for the timeseries of each case are calculated. Correlations are made between DOP values and MSTD timeseries. Comparisons are made between each timeseries and spectra to identify the impact of 1) receiver grade, 2) antenna grade, 3) multi-GNSS on the solutions. The SNR values measured from the different formations of receiver-antenna are also compared and studied.

Table 7. 6 *The timeseries and spectra generated for different scenarios for comparison and analysis;* indicate GLONASS timeseries are not taken into consideration when the u-blox receiver and Leica receiver are used as the rover and base respectively due to IFB problem.*

	Timeseries and Spectra Comparison		
Different Coupling and Combinations	u-blox receiver couple	Leica receiver couple	the u-blox receiver as the rover and Leica receiver as base
Patch antenna	GPS, GPS+Galileo, GPS+GLONASS*+Galileo, GPS+GLONASS*		
Leica AS10	GPS, GPS+Galileo, GPS+GLONASS*+Galileo, GPS+GLONASS*		

The approaches for data analysis and results comparison are summarised in following four categories.

- Receiver grade comparison: Timeseries and spectra of u-blox receiver couple and Leica receiver couple are compared for different multi-GNSS using different grades of antenna. The case where the u-blox receiver and Leica receiver is used as respective rover and base is also added for multi-constellation (GPS, GPS+Galileo). comparison.

From different receiver grades comparison, a lower internal noise level could be seen from the geodetic receiver (Leica GS10) than the low-cost u-blox receivers. The ZBL results of both also mostly correlate to the satellite to receiver relative geometry (DOP values), the case when u-blox is used as rover and Leica as the base station shows similar but a slight noisier pattern than the u-blox receiver couple. According to Table 7.5, the E / N STD is around 0.4-0.6mm and 0.7-1 mm for u-blox receivers in general. For Leica receivers, it's 0.3-0.4mm and 0.4-0.6 mm respectively and there is no significant difference using geodetic antenna or patch antenna. As for the Up component, similarly, a lower noise level is detected with geodetic receivers, having a STD of ~1.2mm with geodetic antenna and ~1.7mm with patch antenna. On the other hand, for u-blox receiver, the STD shows ~2.1mm with geodetic antenna and ~2.9mm with patch antenna respectively.

- Antenna grade comparison: Timeseries and spectra are compared when different grades of antenna (patch antenna or Leica AS10) are used for u-blox receiver couple and Leica receiver couple for GPS-only solution after synchronising the time lag due to different days' measurement. The case of using u-blox receiver as the rover and Leica receiver as the base is excluded due to having the largest noise level in its timeseries.

With regards to antenna comparison results, it is observed that for Leica receiver couple, no significant change is detected when changing patch antenna to geodetic antenna for E/N components. While for u-blox receiver couple, the effect of changing antenna grades is more noticeable. Regarding Up components, significant improvement in measurement precision can be shown when switching from patch antenna to geodetic antenna for both u-blox receiver couple and geodetic receiver couple, this indicates that the antenna grade has more impact on Up components than the E/N component. From Figure 7.9 It is noticed that for E/N/U components, a larger amount of precision improvement from the patch antenna to the geodetic antenna is observed for u-blox receiver couple than Leica receiver couple. For Leica receiver couple, the antenna grade seems to only influence the Up component whilst no significant impact on E/N components is detected.

- Constellation comparison: Timeseries and spectra of different receiver-antenna combinations for different multi-constellation (GPS, GPS+Galileo, GPS+GLONASS+Galileo, GPS+GLONASS) are compared.

Regarding multi-constellation comparison results, for epochs with strong GPS constellations, the multi-GNSS results are at similar precision with GPS-only results. Whereas for epochs with weak GPS constellation, the multi-GNSS could improve the

GPS-only results and gain better precision. (e.g. Figure 7.11 22:00-23:00, 10:00-11:00) However, a weaker GLONASS constellation could also potentially degrade the precision of the results (e.g. Figure 7.11 06:00-08:00, 12:00-13:00). Generally, the multi-constellation timeseries would be more precise and robust than GPS-only results although the precision improvement is not so significant for ZBL results (Table 7.5).

Another problem with u-blox solutions when GLONASS constellations are used for coordinate computation is the occurrence of multiple cycle slips (spikes) and data gaps in the timeseries. Further investigation suggests the u-blox receiver could not reject GLONASS observations with low SNR the same way as survey-grade receivers which would eventually result in gross errors in the timeseries. In contrast, no gross errors are observed for GPS+Galileo timeseries and a precision improvement for most epochs could be seen. But the disadvantage is that Galileo has a limited number of satellites to be tracked during some period of days compared to GLONASS system.

- SNR comparison: The SNR values are compared between different grades of receivers and different grades of antennas.

It is shown from the SNR results that the Leica receiver has a higher SNR value than u-blox receiver in tracking the same signal from both patch antenna and geodetic antenna. The offset is uniform at around 1-5dBHz depending on elevation angles. While for the SNR comparison between different grades of antennas, it is shown the SNR recordings from AS10 antenna are not necessarily larger than patch antenna especially for low-elevation angles (15-20), which might be a result of increasing atmospheric errors. However, as with the increasing elevation angle, a larger SNR value from AS10 antenna is noticed compared to the patch antenna.

Based on the ZBL results, it is verified that the carrier phase measurement errors between geodetic and low-cost receivers are comparable. The impact of multi-constellation, antenna, DOP is also examined based on the ZBL test. Although the ZBL study is a preliminary process for receiver noise evaluation, the results are over-optimistic due to large error mitigation by the differential process and employment of the same antenna (antenna LNA noise is also cancelled). Therefore, further study needs to be carried out for a more practical scenario. For most monitoring applications with the DD technique, a SBL (less than 10 km) is formed between the rover and base/reference station. It is essential to evaluate the property and characteristics of the noise level in the SBL GNSS measurement. Therefore, in the following Chapter, the GNSS system noise is evaluated based on a SBL test. Approaches are also made to reduce the long period noise in the SBL measurement scenario.

Chapter 8 Short baseline static test

8.1 Introduction

Following the ZBL test, the short baseline (SBL) test was conducted for system noise evaluation since ZBL test used over-simplified models which could not represent the measurement errors in real monitoring scenarios. In most GNSS deformation monitoring studies, a SBL formed of a rover and a reference station is commonly adopted, with reference station providing GNSS corrections for the rover, and the rover used for the displacement monitoring. The DD solutions could be obtained with the highest accuracy and precision (reaching cm-level for up to 10km SBL) compared to other GNSS techniques. This is due to the differencing process which cancels the satellite orbit and clock error, receiver clock error, and over SBLs, the ionospheric and tropospheric errors can also be largely mitigated.

However, one of the biases which could not be mitigated is the multipath, with a major impact on the measurement, producing a site-dependent bias from reflection or diffraction of local objects. More specifically, the satellite signals reaching the antenna would not only include direct signals from the satellite but also indirect signals, creating multipath errors. The carrier multipath can result in 0.001–0.03 m nominal error with a maximum 4.75 cm multipath for L1 carrier and 6.11 cm for L2 carrier (Bidikar et al.,2020). Based on previous studies, some approaches for the multipath mitigation have been suggested; 1) selection of monitoring site where multipath has the least influence on measurement, 2) through the customisation of the antenna, by adding a choke ring or ground plane for multipath signals absorption, 3) by analysis of the signal to noise ratio values of GPS signals (Axelrad et al., 1996), 4) by applying digital filters (wavelet filter, adaptive filter, etc) of different cut-off frequencies over the spectrum of the multipath (Satirapod and Rizos, 2005; Ge et al., 2000).

Apart from the multipath error, another source of error is related to the APC, namely, PCO and PCV. PCO is usually constant and used for determination of absolute positions, and therefore ignored. Due to the PCV, the actual APC shifts with varying elevation angle and azimuth to the satellite which leads to an error in pseudorange and carrier phase measurement. PCV is similar for the same model of antenna. With SBLs, the incoming signals from the same satellite will have almost the same azimuth and elevation between rover and base antenna, resulting in similar PCV errors. Therefore, if the same model of the antenna is used in the rover and base, PCV errors should be largely mitigated by differencing (Dawidowicz, 2011). To gain high precision positioning results, PCO and PCV should be modelled and pre-calibrated. PCOs and PCVs of certain antenna models are already calibrated and can be found online at NGS NASA (National Geodetic Survey). However, for the patch antenna, the antenna PCO and PCV corrections have not been defined yet.

The SBL static test is set up so that the GNSS rover station remains static, and a stable reference station is established at a close distance forming a SBL. Similar to the ZBL, the E/N/U baseline timeseries are obtained. In theory, the SBL solutions should remain uniformly constant if both rover and base stations are static. However, due to the adoption of the GNSS method, some GNSS measurement errors would be introduced. Therefore, any variations in the GNSS solutions would imply the biases from multipath, antenna (PCV, LNA), DOP, receiver noise, etc remaining in the SBL results. In this Chapter, approaches are made to evaluate and mitigate the errors in the SBL test.

8.2 Determination of the antenna spacing

During the experiment, a dual antenna-receiver system was established as the rover to test the potential for precision improvement. Since two antennas were adopted in the experiment, a preliminary study was conducted to examine the impact of antennas' spacing. The main concerns are that the close distance between two GNSS antennas could potentially result in interaction between them and lose tracking sensitivity due to signal shadowing and/or RF interference. This could also adversely affect the search pattern of the antennas, resulting in fewer satellites being tracked.

Although the spacing of multiple antennas depends on various factors, a general rule of thumb for spacing of two antennas is that the separation between them should not be less than a quarter of the wavelength (around 4.8cm for L1) and they should not be placed at distances of multiple wavelengths especially for the first 3-4 multiples. To test how the distance between patch antennas would affect the results, experiments were conducted on different days with varying distances (side by side (SBS), ~8cm, ~15cm, and ~30cm) between two antennas. Both antennas were placed with the same orientation and connected with u-blox receivers (u-blox M8T). A base station consisted of a geodetic antenna (AR25) and receiver (GR10) was also set up as the reference. The sampling frequency of the u-blox receivers was 10Hz and the base station sampling frequency was 1Hz. The measuring duration of different separation distances from each day was synchronised based on the GPS sidereal period to maintain the same GPS constellation.

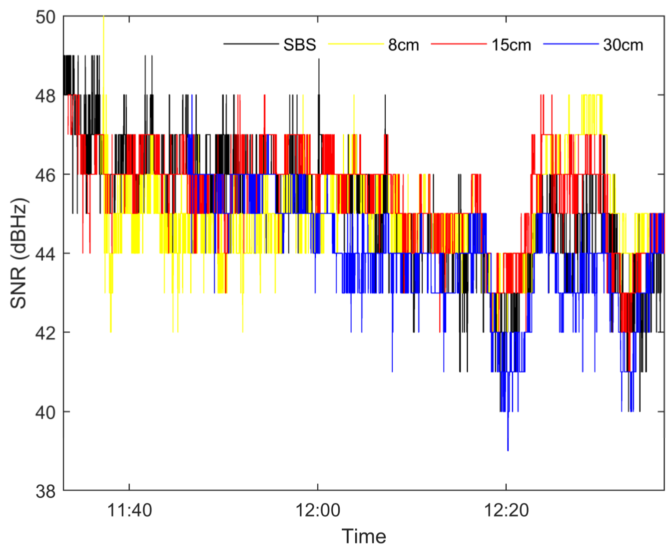

Figure 8. 1 *SNR for GPS satellite G10 with different antenna spacing distance (SBS: side by side; 8cm; 15cm;30cm)*

The effect of different separation distances of patch antennas was examined and compared by the SNR and the timeseries solutions. Shown in Figure 8.1 was the SNR comparison with different antenna separation distances for GPS satellite G10. It was shown that the impact of different separation distances on SNR was small with a difference of less than a few dBHz and the correlation of SNR with separation distance was not strong (Figure 8.1). It was also examined the resulted timeseries when using different separation distances. Since the sampling rate was different from the base station and rover station, time interpolation of base station data was configured where the base station observations are linearly interpolated according to time to match with the rover stations. And then DD kinematic processing was made.

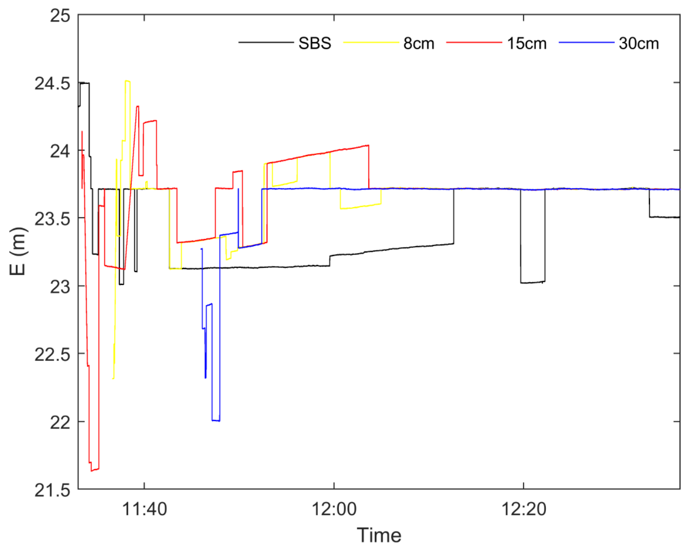

Figure 8. 2 *Eastings timeseries comparison with different antenna spacing distance (SBS: side by side; 8cm; 15cm;30cm)*

Figure 8.2 showed the effect of separation distance on the Easting timeseries, it could be seen that with patch antenna side by side (SBS), more false ambiguity fixes (cycle slips) were detected, with increasing distance between the antenna, the cycle slips was seen a decreasing trend. The minimum cycle slip was detected for ~30cm antenna separation. The settings for timeseries processing were the same for different distances, and the time for each day's measurement was synchronised to guarantee the same GPS constellation so that the different results obtained could only be due to the different distances between two patch antennas. The frequent occurrence of cycle slips implied a possible increase of interference and code/carrier phase errors with decreasing separation distance. Similar results could also be obtained from Northing and Up components.

8.3 Short baseline experiment procedure and setup

Based on the findings of ZBL test, SBL static test was deployed, where the main aims were, 1) to assess the impact of different GNSS base station formations (geodetic receiver and geodetic antenna, low-cost receiver and patch antenna, geodetic receiver and patch antenna) on the SBL DD solutions with low-cost receiver and patch antenna as the rover, and 2) to investigate the potential performance enhancement from a single low-cost GNSS rover by adopting a dual low-cost GNSS system (i.e. deployment of two closely-spaced low-cost GNSS rover stations) and by applying the sidereal filtering (SDF) and common mode error (CME) filtering for error mitigation.

The experimental layout of SBL test was presented in Figure 8.3 and the experiment was carried out on the roof of Nottingham Geospatial Building (NGB). The dual GNSS rover-system station consisted of two closely-spaced low-cost GNSS stations, which were formed by two u-blox receivers and two patch antennas. The two patch antennas were mounted on a large metal plate for multipath reduction, orientated to the same azimuth, and placed 30cm distance apart roughly in E-W direction to retain similar multipath conditions and avoid any signal interference. In addition, two base stations were set up on the roof within 30m distance from the rover station: (i) one base station with a patch antenna mounted on a metal plinth connected to a Leica GS10 and a u-blox M8T receiver via a signal splitter (RMS18) and (ii) the other base station formed by Leica GR10 receiver connected to a Leica AR25 antenna. Multi-constellation (GPS, GLONASS, Galileo) signals were observed and multi-GNSS measurements were recorded by all receivers with a 1 Hz sampling rate during three separate days (from 16:04 06/08/2018 to 19:09 08/08/2018). Same models of GNSS receivers and antennas were used as in the ZBL measurements to have consistency in the GNSS results, except the high-grade GNSS base station consisted of a choke-ring antenna (Leica AR25) to evaluate the potential impact of the antenna grade on the performance of the low-cost receivers.

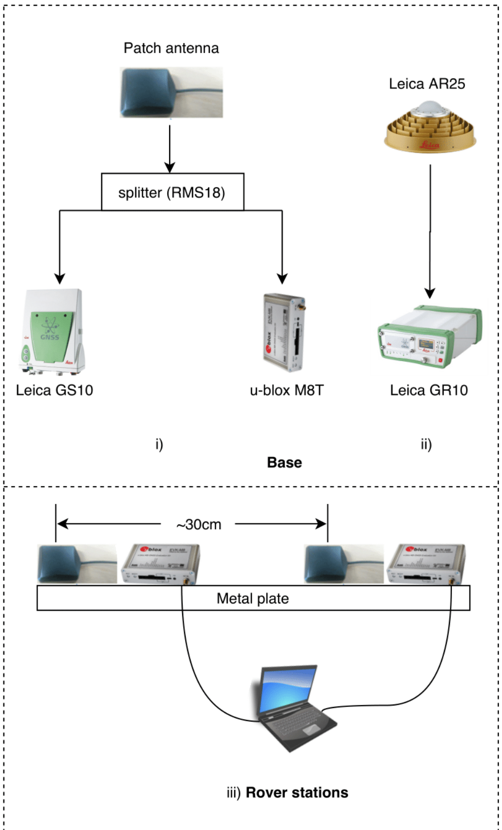

Figure 8. 3 *The layout of the SBL measurements. Two different setups for base station:(i) patch antenna connecting to a geodetic and a low-cost receiver through a signal splitter and (ii) choke-ring antenna connecting to geodetic grade receiver. The dual GNSS rover-system station consists of two closely-spaced rover stations (30cm apart), with each using a patch antenna connecting to the u-blox receiver.*

8.4 GNSS processing and methodology for timeseries analysis

The u-blox GNSS data was acquired by 'u-center' software installed on a laptop and logged in '.ubx' format. The Leica GNSS observations were stored in '.m00' format in the internal SD card. Using a similar RINEX conversion process as described in ZBL, the raw data were converted in standard RINEX observation format. After downloading the navigation message from CDDIS NASA, the RINEX observation files and navigation messages were then imported and processed in RTKPOST module in RTKLIB 2.4.3. The settings used for the RTKLIB 2.4.3 for SBL coordinate computation were shown in Table 8.1. The solutions obtained were computed epoch by epoch with corresponding GPS timestamps, including parameters such as E/N/U baseline solutions, STDs of the position estimation, number of satellites, age of differential between base and rover, the solution type, etc. The DOP, SNR, pseudorange and carrier phase residuals could also be extracted and obtained from the solutions.

Table 8. 1 *RTKLIB configuration for SBL test (other settings are by default)*

Settings	***Options***
Position mode	Kinematic
Frequency/Filter type	L1/Forward
Elevation Mask	15
Ionosphere Correction	Broadcast
Troposphere Correction	Saastamoinen
Satellite Ephemeris/Clock	Broadcast
RAIM FDE	ticked
Constellation selection	GPS, GPS+Galileo, GPS+GLONASS, GPS+GLONASS+ Galileo
Integer Ambiguity Res	Continuous
Min Ratio to Fix Ambiguity	3
Output	E/N/U-Baseline
Time interpolation of Base station Data	ON
Datum	WGS84
Base station position	Average of a single position

Table 8. 2 *Different scenarios for the processing SBL results*

Combination	Base receiver	Base antenna	Rover receiver	Rover antenna
G	U-blox M8T	patch antenna	u-blox M8T	patch antenna
H	GS10	patch antenna	u-blox M8T	patch antenna
I	GR10	Choke-ring antenna (AR25)	u-blox M8T	patch antenna

Table 8.2 listed the SBL formations which were processed; each one resulted in two GNSS timeseries for the two low-cost GNSS rover stations. Similar to the ZBL measurements, the GPS-only and GPS+Galileo solutions were processed for all the three SBL formations, while the GPS+GLONASS+Galileo solution was processed only for the formation with u-blox receivers as base and rover due to the IFB. The

combinations H and I were compared against combination G to evaluate the impact of the base receiver and antenna respectively.

To enhance the precision of the low-cost GNSS results, the SDF and CME methods were applied in the analysis of the GNSS SBL timeseries. The SDF is a technique to remove the orbit related errors, such as multipath or PCV (Schmid et al., 2007), which depends strongly on the period of the full satellite orbit for the satellite system (Ragheb et al., 2007). The periodic orbit of the GPS satellites in their trajectories results in each satellite appearing at the same position about 4min earlier from the previous sidereal day, defining the main principle of SDF that the relative geometry between the satellites and the antenna repeats between successive sidereal days with a time lag. SDF could be used both in the observation domain as well as coordinate domain (Ragheb et al., 2016). In this study the SDF is applied only in the coordinate domain, and only to the GPS-only solutions. The SDF technique can be also applied to Galileo and GLONASS constellation solutions, however, the difference in orbit period presents a problem as the constellation for Galileo and GLONASS repeats every 10 and 8 sidereal days, respectively (Eissfeller et al., 2007). To be more specific, GLONASS has a constellation repetition period of 8 sidereal days for a complete 17-revolution and Galileo has a constellation repetition period of 10 sidereal days for a complete 17-revolution. Therefore, to apply SDF to a multi-GNSS system, for example, GPS+Galileo, a 10-sidereal day should probably be taken into account for GPS+Galileo constellation to appear at the same location. For SDF of other multi-constellation, data measurement for longer periods (even up to months) may be needed to maintain the same multi-GNSS constellation. The calculation of the SDF model for each component (E, N, U) is given by the Equation 8.1.

$$SDF\_E_i = \frac{\sum_{j=0}^{n-1} E_{(i-j*T)}}{n} \qquad SDF\_N_i = \frac{\sum_{j=0}^{n-1} N_{(i-j*T)}}{n} \qquad SDF\_U_i = \frac{\sum_{j=0}^{n-1} U_{(i-j*T)}}{n}$$

Equation 8. 1 *The SDF model computation*

Where

- *i* stands for current epoch
- j stands for the number of days from the current day
- T stands for optimal lag
- n is the total number of days stacked

After aligning the timeseries of consecutive days according to the constellation repetition period, Equation 8.1 constructs the SDF model which consists of periodic errors related to the satellite orbit by stacking the timeseries and calculating the average based on multiple days' measurements to improve the precision and robustness of the filter (Ragheb et al., 2007). The GPS constellation has a ground repeat period of one sidereal day during which GPS satellites make two full orbits, so that the GPS satellite would appear at the same location and the relative geometry between the GPS constellation and the receiver remains nearly unchanged after every sidereal day. Orbit related biases will also remain nearly unchanged providing the same antenna and reflector environment. Although the repeat periods of different satellites may vary, and the orbital periods of the same satellite also change with time. For SDF in the coordinate domain, an optimum sidereal lag is used to take account the orbiting periods for each satellite. It was reported by Ragheb et al. (2007) based on the autocorrelation of coordinates and Choi et al. (2004) based on satellite orbit analysis by calculating the mean orbit repeat period, the optimal sidereal lag is around 23h 55m 55s, around 9 seconds earlier than the nominal sidereal period.

It could be feasible to calculate each satellite orbital period based on Keplar's 3rd law and broadcast ephemeris (navigation message) and derive the optimal orbit repeat period by calculating the mean of the orbit repeat period of individual satellite (Choi et al., 2004) or to calculate the optimal sidereal lag by autocorrelation of the coordinate timeseries (Ragheb et al., 2007). By satellite orbit analysis using the obtained navigation message, the optimal orbit repeat period of GPS constellation would be the same universally and is calculated to be in agreement of the 23h 55m 55s sidereal repeat period. Therefore, 23h 55m 55s is adopted in this research as the modified sidereal lag to align the timeseries for each sidereal day. On the other hand, since SDF is only applied in the coordinate domain, the period variation of a single GPS satellite would not have much impact on the results.

The CME technique is based on the assumption that the GNSS records of closely-spaced stations are spatially correlated and include partly common errors. The CME error computation is based on the weighted average of the residual timeseries, also known as weighted stacking expressed by the equation 8.2 (Nikolaidis, 2002):

$$CME_t^i = \frac{\sum_{j=1}^{n} \frac{R_t^i}{\sigma_i^2}}{\sum_{j=1}^{n} \frac{1}{\sigma_i^2}}$$

Equation 8. 2 *CME model computation*

Where

- CME_t^i is the common-mode error at station i at time t
- R_t^i is the coordinate timeseries for the station i at time t
- σ_i^2 is the inverse of the square of the RMS of the station coordinate
- n is the number of stations.

In our SBL experiments, the two closely-spaced u-blox receivers were ~30cm apart, receiving the satellite signals under similar observation conditions, with the main difference of slightly shifted multipath phase between the two GNSS stations. The latter makes the CME method less effective than the SDF for the mitigation of multipath induced errors. However, the main advantage of CME against the SDF is that it does not require multiple days of recording to apply the CME method and it assumes errors are spatially correlated between closely-spaced receivers and impact similarly on the coordinate, making it applicable for multi-GNSS data. The CME method has been applied successfully for geodetic grade receivers in GNSS networks (Habboub et al., 2020). As it is unlikely to have closely-spaced (in m-range) geodetic-grade receivers due to their high cost, the application of CME in closely-spaced GNSS receivers, as examined in this study, is practically feasible only for low-cost GNSS receivers.

The application of SDF, CME filtering, and their combination followed the steps presented in Figure 8.4. For the application of the SDF, the GPS timeseries of the three days were aligned and stacked using Equation 8.1, where the common period (from 16:20 to 19:20) was used to model the multipath induced error for each of the two low-cost GNSS rover stations. For the CME method, the GNSS timeseries of the two low-cost GNSS receivers of each day were used to define the common error between the two stations using Equation 8.2. For both SDF and CME, the modelled error was subtracted from the GPS/GNSS timeseries to refine the GPS/GNSS timeseries precision. The combination of CME and SDF methods is done by applying the SDF method to the residual timeseries derived from the CME filtering which is expected to obtain an extra precise result.

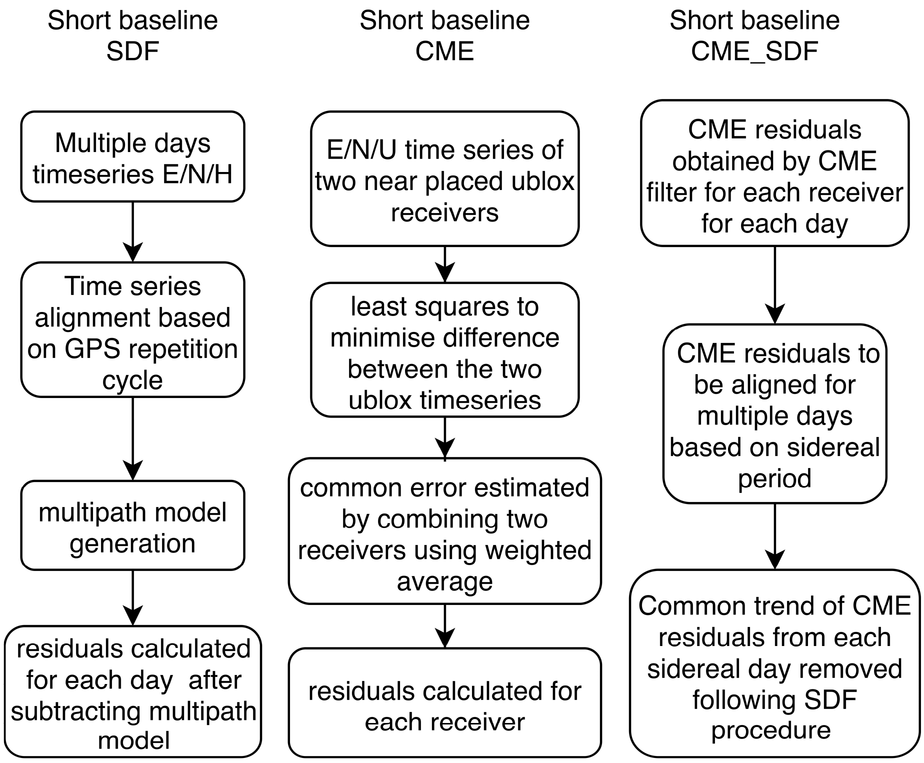

Figure 8. 4 *Flow diagram of methodology/procedures for the application of sidereal filtering (SDF), common mode error (CME), and their combination.*

8.5 Short baseline results

After the coordinate computation in RTKLIB, due to the adoption of two u-blox rovers and different formations of base stations, as well as multi-constellation, as a result, multiple E/N/U coordinate timeseries could be generated. To improve the precision of measurement and take advantage of the spatial correlation between two closely-spaced low-cost stations, several approaches (Figure 8.5) are proposed after baseline solutions are obtained from different rover-base couples. To test the efficiency of different approaches, the two baselines formed between each of two u-blox rovers and base station consisted of the u-blox receiver and patch antenna were processed. The residuals obtained from different error mitigation approaches were also compared.

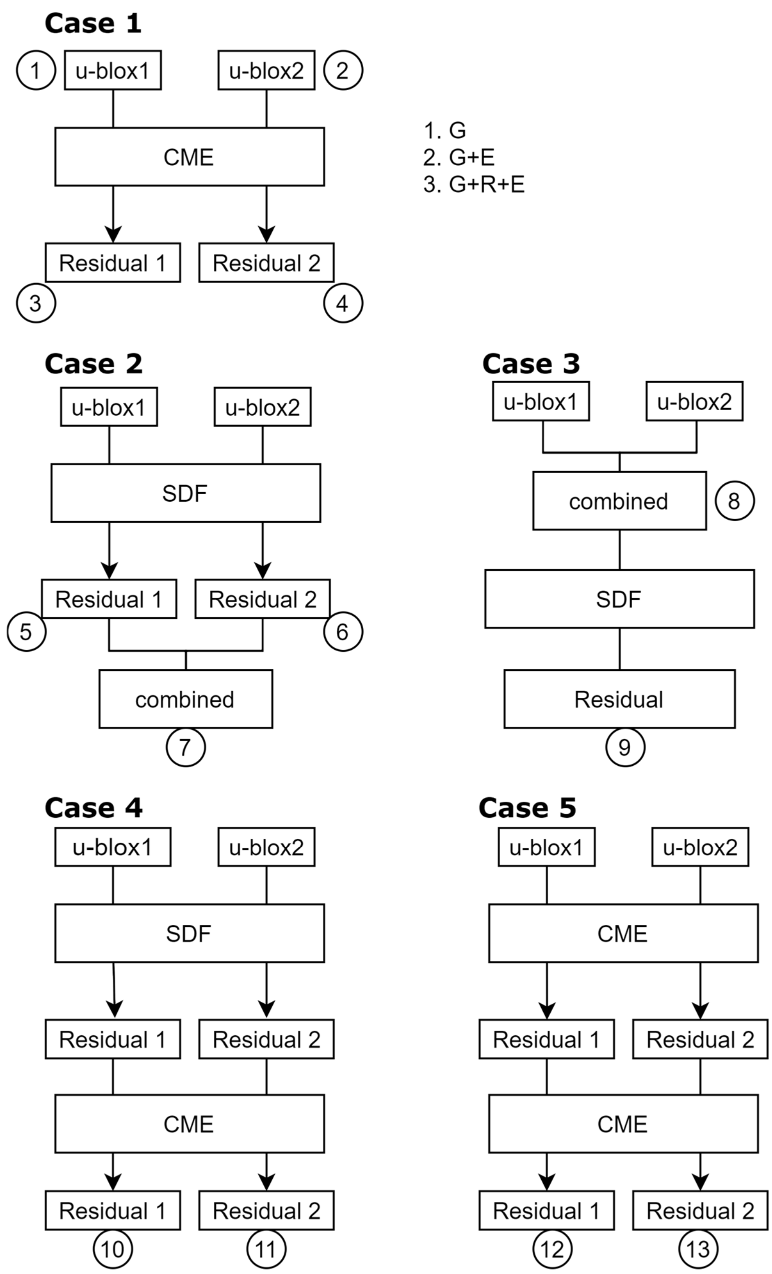

Figure 8. 5 *Different cases and approaches for processing dual low-cost GNSS system for better precision, each annotation from 1 to 13 illustrates corresponding solution for each process. Solution 1&2 represent the u-blox1 and u-blox2 original timeseries respectively. Solution 3&4 represent the residuals after CME filter for u-blox1 and u-blox2 correspondingly. Different multi-GNSS solutions (G, G+E, G+R+E) could also be obtained for solution 1-4. Solution 5&6 represent the u-blox1 and u-blox2 SDF residual timeseries respectively and solution 7 represents the average/weighted average combined solution. Solution 8 represents the average/weighted average combined u-blox1 and u-blox2 original timeseries and solution 9 is the SDF residual of solution 8. Solutions 10-13 illustrate residuals for the combined filter by using CME and SDF but with different filtering order. For solution 5 to 13, since SDF regarding GPS constellation is used, only GPS-only solution is derived.*

Figure 8.6 illustrates the initial timeseries of u-blox2 before applying SDF and the residual timeseries after SDF. It is noticed that the correspondence of the initial timeseries between each day is due to the repeatability of the GPS constellation. A multipath model is also constructed by stacking multiple days' timeseries according to Equation 8.1 and then subtracted from the initial timeseries to obtain the SDF residuals. Figure 8.7 shows the initial timeseries of two u-blox receivers, the constructed CME model using Equation 8.2, and the CME residuals timeseries after subtracting the CME model. Table 8.3 and 8.4 presents the mean and the STD of the timeseries derived before and after the application of SDF and CME methods respectively in correspondence with Figure 8.6 and Figure 8.7. It can be observed that the precisions of timeseries are both significantly improved after the application of SDF and CME, as the Eastings STD has been reduced to 0.8 and 1.7 mm for SDF and CME residuals, respectively. The same precision improvement is also observed with N/Up components.

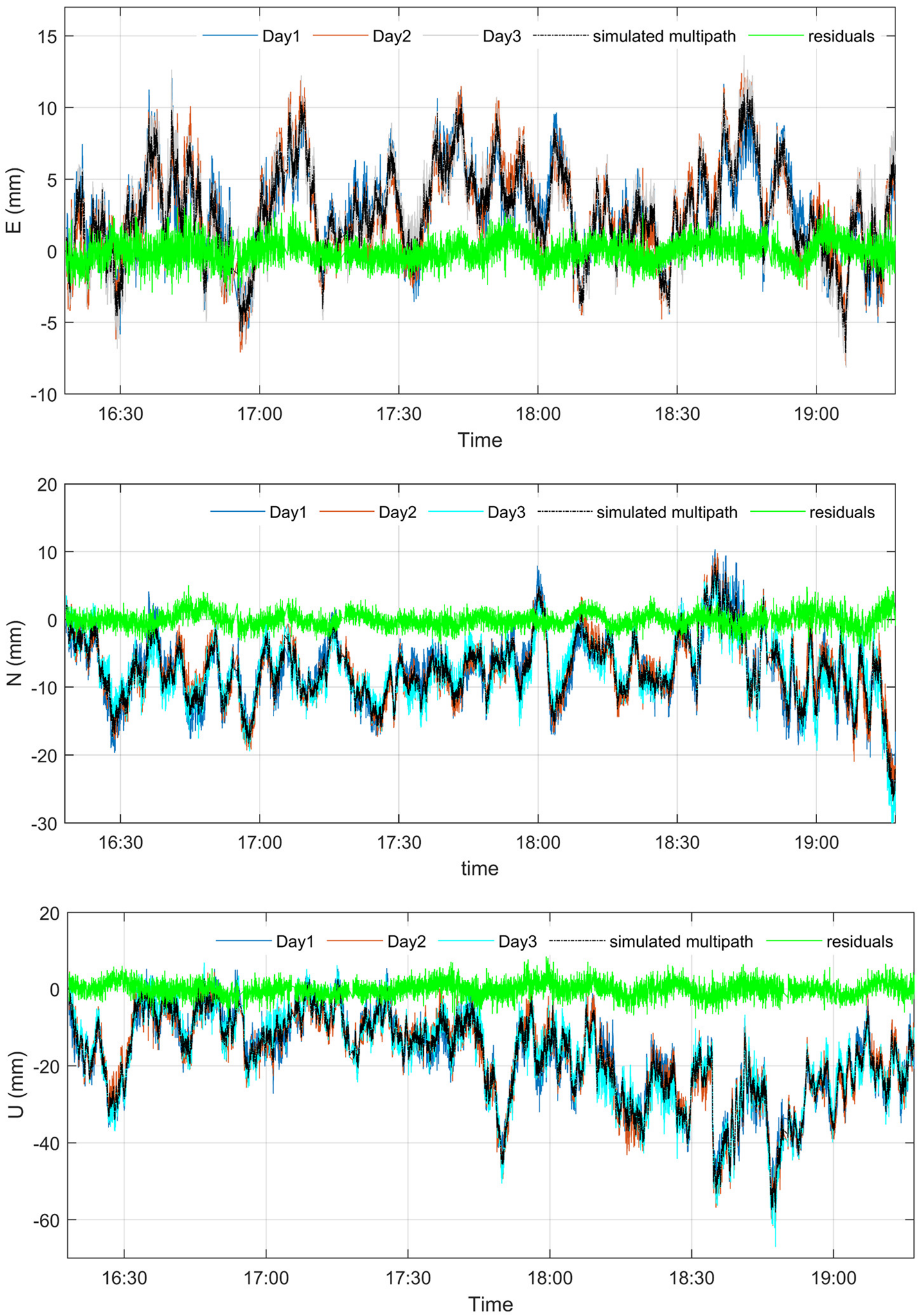

Figure 8. 6 *The timeseries of (i) u-blox2 GPS-only E/N/U solution for three successive days of measurements, (ii) the multipath model based on the SDF, and (iii) the resultant residuals timeseries after subtracting the multipath error from the initial timeseries. The precision of the residuals timeseries reduces to 1-2 mm level.*

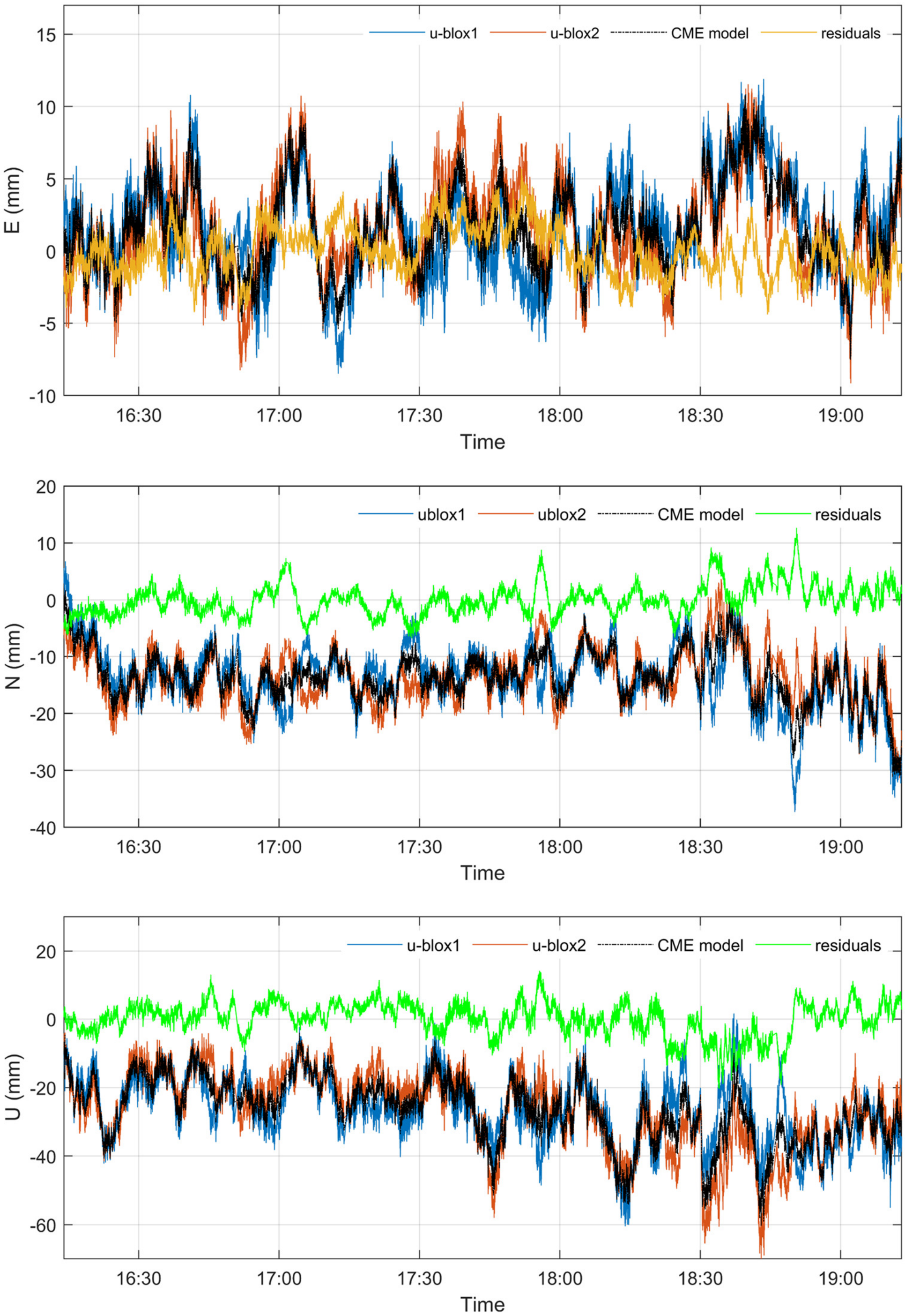

Figure 8. 7 *The timeseries of (i) u-blox1 and u-blox2 GPS-only E/N/U solution for Day 2, (ii) the CME model based on the timeseries of two u-blox receivers, and (iii) the resultant residual timeseries after subtracting the CME model from the initial timeseries. The residuals timeseries follow the low-frequency signal trend and its range is at sub cm-level.*

Table 8. 3 *Mean and STD of u-blox2 E/N/U component GPS timeseries for the three days measurements and residuals (Day2) after the application of the SDF method*

	Unit (mm)	Day1	Day2	Day3	SDF Residuals
E	Mean	2.7	2.7	2.7	0
	STD	3.1	3.3	3.3	0.8
N	Mean	-7.5	-7.4	-7.4	0
	STD	5.2	4.8	4.8	1.2
U	Mean	-18.1	-18.0	-18.0	0
	STD	11.1	11.4	11.7	2.0

Table 8. 4 *Mean and STD of E/N/U component GPS timeseries for the u-blox stations of Day 2 and residuals after the application of the CME method*

	Unit(mm)	u-blox1	u-blox2	CME Residuals
E	Mean	1.5	1.5	0
	STD	3.3	3.3	1.7
N	Mean	13.6	13.6	0
	STD	5.5	4.8	2.7
U	Mean	-26.6	-26.6	0
	STD	9.6	11.4	4.9

8.6 Evaluation of the impact of the GNSS base station on low-cost GNSS rover performance

Figure 8.8 presents the MSTD with 15-min moving window of the E component timeseries for u-blox2 rover, with three different available base stations (low-cost GNSS station, Leica receiver with patch antenna, Leica receiver with AR25). The GPS-only and GPS+Galileo solutions are produced since the IFB problem for GLONASS constellation between the u-blox rover and Leica base receiver is not accounted for. It is observed that for the case when the patch antenna is employed in the base, there is no significant influence on both GPS-only and GPS+Galileo solutions from different grades of base receivers. However, for the base station formed of Leica receiver and geodetic antenna, there is an apparent precision improvement compared to other formations of base stations, especially for the GPS-only solution which reaches even 3mm for the E component. This implies that a change in base station antenna grade could improve on the precision, nevertheless, change of base station receiver grade has little impact on precision improvement.

Furthermore, by applying SDF and CME method there is a significant improvement in the low-cost receiver precision, which is reduced below 2mm for Eastings for both methods (Figure 8.9). For the SDF method, the same accuracy is achieved regardless of the receiver type (geodetic or low-cost) when connected to a patch antenna. However, there is an improvement in the precision, reaching up to 0.4mm, when using a geodetic antenna (AR25) at the base station. Regarding the application of the CME method, the same precision is achieved regardless of the type of the GNSS antenna or receiver used in the base station, probably due to the potential errors introduced by the receiver and/or antenna of the base station, are limited through the CME method of the two closely-spaced low-cost stations. Finally, it is also observed that the SDF method can achieve a higher precision than that of the CME method with the GPS-only results. By conducting similar analysis to N and U timeseries, the same observations could be made. (Figure 8.10, Figure 8.11, Figure 8.12, Figure 8.13)

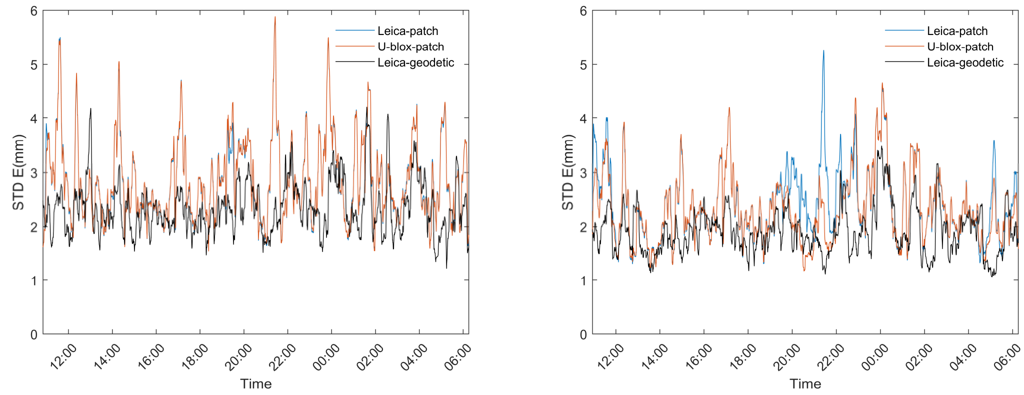

Figure 8. 8 *The timeseries of MSTD of the u-blox2 E components for Day2 by using (i) u-blox with patch antenna, (ii) Leica receiver with patch antenna, and (iii) Leica receiver with geodetic antenna as base stations, derived from (left) GPS-only solutions and (right) GPS+Galileo solutions. The solutions having Leica receiver and geodetic antenna as the base have the lowest STD, whereas the solutions with patch antenna used in the base station have the same STD regardless of the receivers used.*

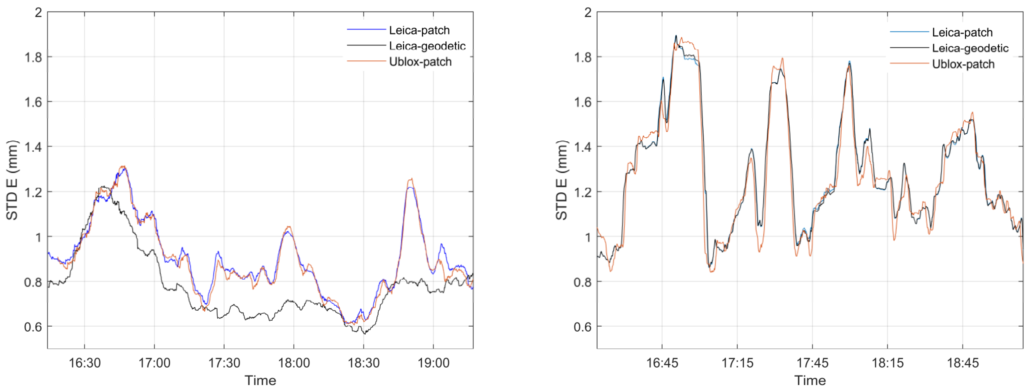

Figure 8. 9 *The GPS-only MSTD timeseries of the u-blox2 E component for Day2 after using (left) SDF and (right) CME analysis when(i) u-blox with patch antenna, (ii) Leica receiver with patch antenna, and (iii) Leica receiver with geodetic antenna are used in base stations. The SDF leads to a lower STD for the solution using Leica receiver with geodetic antenna as the base, whereas for the CME all three solutions have the same level of STD*

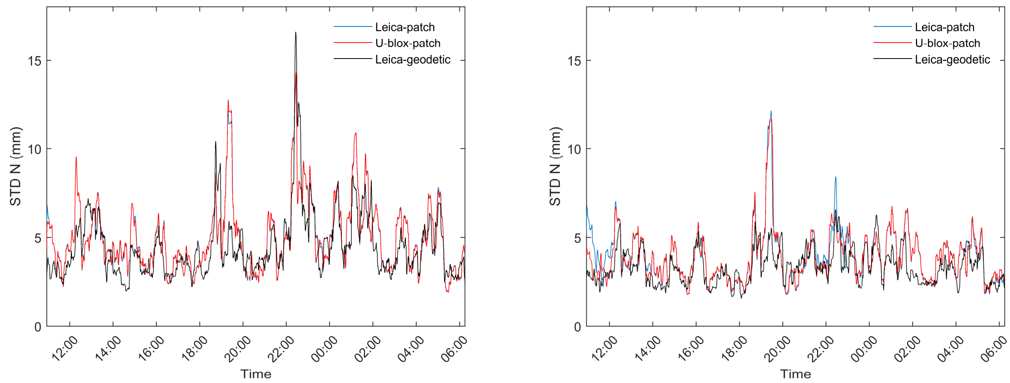

Figure 8. 10 *The timeseries of MSTD of the u-blox2 N components for Day2 by using (i) u-blox with patch antenna, (ii) Leica receiver with patch antenna, and (iii) Leica receiver with geodetic antenna as base stations, derived from (left) GPS-only solutions and (right) GPS+Galileo solutions. The solutions having Leica receiver and geodetic antenna as the base have the lowest STD, whereas the solutions with patch antenna in the base station have the same STD regardless of the receiver used.*

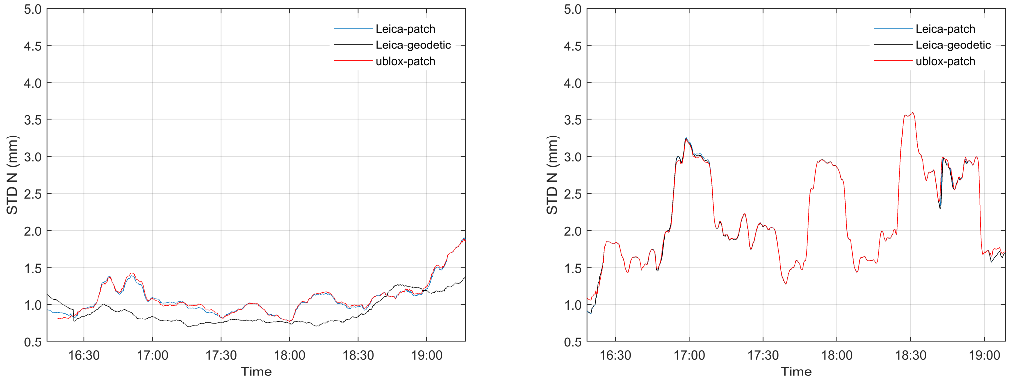

Figure 8. 11 *The GPS-only MSTD timeseries of the u-blox2 N component for Day2 after using (left) SDF and (right) CME analysis when (i) u-blox with patch antenna, (ii) Leica receiver with patch antenna and (iii) Leica receiver with geodetic antenna are used as base stations. The SDF leads to a lower STD for the solution using Leica receiver with geodetic antenna as the base, whereas for the CME all three solutions have the same level of STD.*

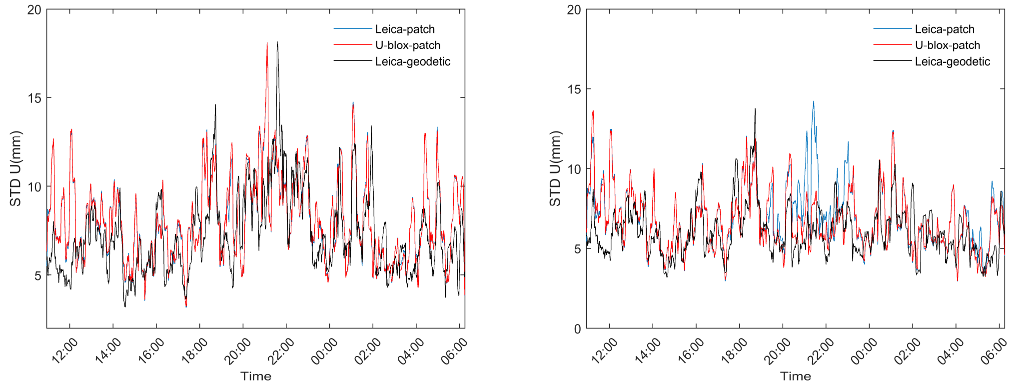

Figure 8. 12 *The timeseries of MSTD of the u-blox2 U components for Day2 by using (i) u-blox with patch antenna, (ii) Leica receiver with patch antenna, and (iii) Leica receiver with geodetic antenna as base stations, derived from (left) GPS-only solutions and (right) GPS+Galileo solutions. The solutions having Leica receiver and geodetic antenna as the base have the lowest STD, whereas the solutions with patch antenna in the base station*

have the same STD regardless of the receiver used.

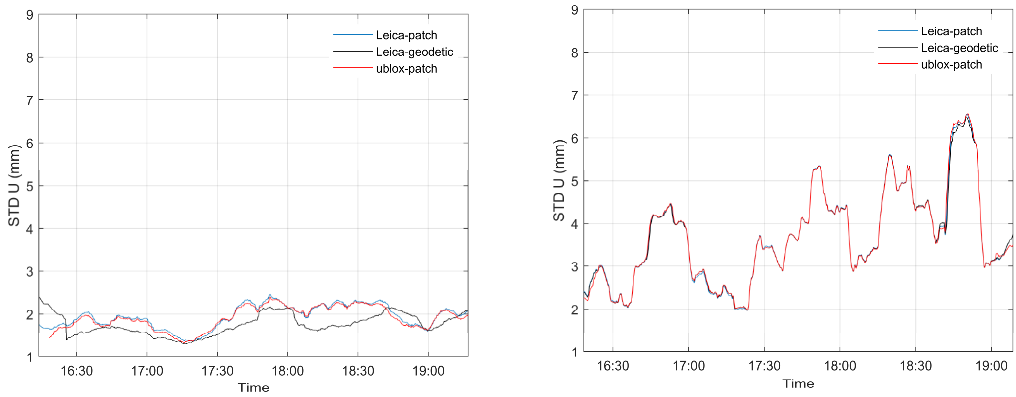

Figure 8. 13 *The GPS-only MSTD timeseries of the u-blox2 U component for Day2 after using (left) SDF and (right) CME analysis when (i) u-blox with patch antenna, (ii) Leica receiver with patch antenna and (iii) Leica receiver with geodetic antenna are used as base stations. The SDF leads to a lower STD for the solution using Leica receiver with geodetic antenna as the base, whereas for the CME all three solutions have the same level of STD.*

8.7 Evaluation of the performance of low-cost receivers in SBL static test

8.7.1 Evaluation of the performance of the single low-cost multi-GNSS station

The GNSS timeseries of the two low-cost GNSS receivers are analysed, and the MSTD is computed for three days. In Figure 8.14, it is presented the MSTD timeseries of the Day2 u-blox2 coordinate timeseries between 16:20 and 19:20 of the GPS-only, GPS+Galileo, and GPS+GLONASS+Galileo solutions for combination G (Table 8.2). Since only a 3-hour slot is studied, a moving window of 200s is used to show the detailed comparison between each MSTD timeseries. It is obvious that for most of the period, the multi-GNSS solution leads to higher precisions than the GPS-only solution. By comparing the MSTD of the multi-GNSS solution against the GPS-only solution for u-blox2, the periods when the multi-GNSS solutions are of higher precision is computed as a percentage of the examined period (Table 8.5). It is found that the GPS+Galileo solutions lead to higher precision than the GPS-only solution for more than 70% of the examined periods, especially for the Northing and Up components. The precision is even higher when the GLONASS constellation is included, as the multi-GNSS solution gives better precision than the GPS-only solution for more than 75% of the period. Similar results are obtained based on the analysis of the u-blox1 receiver data (Table 8.6).

However, the multi-GNSS solution results in more data gaps, which could correspond to float or even no solution (Table 8.7). For example, for u-blox2 timeseries in Day3, the GPS-only solution has the highest availability for all the days reaching up to 99%, while the GPS+Galileo solution leads to slightly lower availability with 97% of the GNSS recording period. The GLONASS constellation reduces the availability of the multi-GNSS solution further, dropping to 86% of the recording period. As is examined in ZBL test, this is probably a result of the cycle slips produced by GLONASS satellites in u-blox receivers, which is limited in the records of other GNSS receivers (e.g. Leica

GS10), as the poor quality of the signals of problematic GLONASS satellites are rejected.

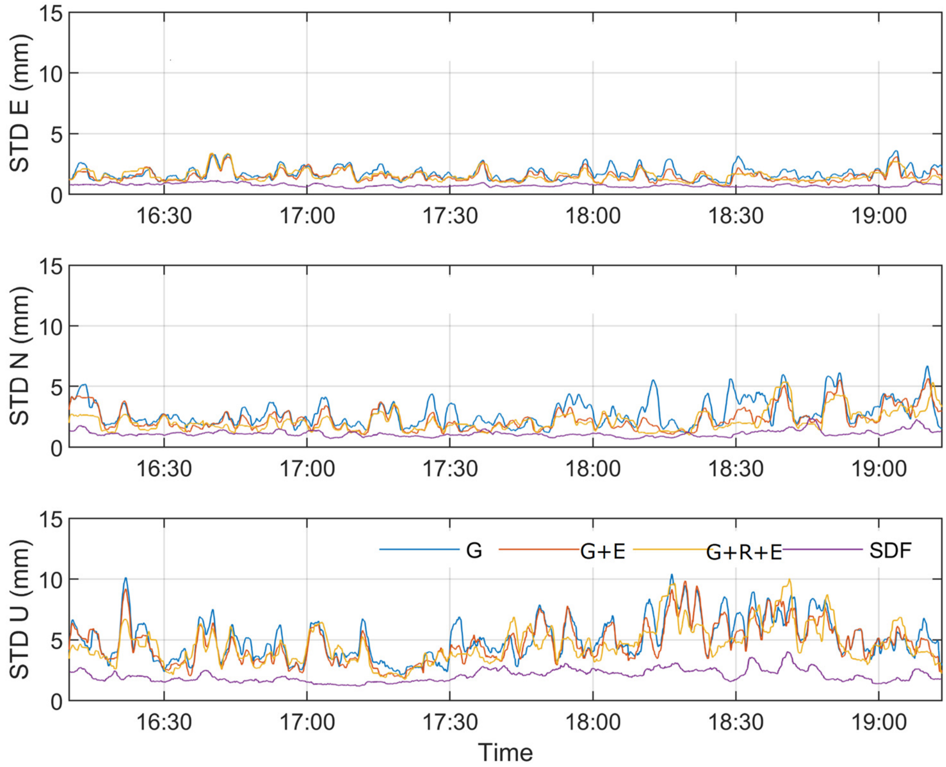

Figure 8. 14 *The MSTD of the u-blox2 coordinate timeseries of Day2 for GPS-only (G), GPS+Galileo (G+E), and GPS+GLONASS+Galileo (G+R+E) solutions, and the SDF residuals with GPS-only constellation. The SDF timeseries has generally the lowest STD for all E/N/U components from any other GNSS solutions.*

Table 8. 5 *Comparison between the MSTD of u-blox2 coordinate timeseries for the three GNSS solutions (GPS-only (G), GPS+GLONASS+Galileo (G+R+E), GPS+Galileo (G+E)). The comparison is expressed as a percentage with respect to the examined period.*

MSTD (%)	*G+E* smaller than *G*			*G+R+E* is smaller than *G*		
	E	N	U	E	N	U
Day1	68.9%	80.7%	68.8%	78.5%	85.2%	87.9%
Day2	78.7%	79.5%	81.7%	78.2%	87.6%	86.8%
Day3	69.3%	75.0%	83.9%	77.7%	93.0%	91.7%

Table 8. 6 *Comparison between the MSTD of u-blox1 coordinate timeseries for the three GNSS solutions (GPS-only (G), GPS+GLONASS+Galileo (G+R+E), GPS+Galileo (G+E)). The comparison is expressed as a percentage with respect to the examined period.*

MSTD (%)	*G+E* smaller than *G*			*G+R+E* is smaller than *G*		
	E	N	U	E	N	U
Day1	66.5%	85.9%	77.2%	74.4%	95.0%	83.3%
Day2	83.0%	81.9%	81.5%	85.8%	88.2%	80.8%
Day3	69.3%	87.2%	83.6%	77.9%	89.7%	90.2%

Table 8. 7 *Percentage of fixed solution within the examined period by including Galileo and GLONASS (Data gaps are created due to multi-GNSS)*

Percent	Day1		Day2		Day3	
	u-blox1	u-blox2	u-blox1	u-blox2	u-blox1	u-blox2
G	93%	99%	99%	99%	99%	99%
G+E	98%	98%	99%	98%	98%	97%
G+R	93%	85%	94%	82%	92%	89%
G+R+E	92%	81%	91%	78%	89%	86%

Table 8. 8 *Comparison of the MSTD of the u-blox2 coordinates timeseries derived after the application of SDF against all the multi-GNSS u-blox2 coordinate timeseries. The comparison indicates whether the MSTD of the SDF timeseries is smaller than that of the multi-GNSS solutions and it is expressed as a percentage with respect to the examined period.*

	MSTD of SDF residuals smaller than MSTD of multi-GNSS (%)		
	E	N	U
Day1	96.0%	87.8%	97.5%
Day2	100.0%	92.2%	96.3%
Day3	97.5%	84.5%	95.8%

Furthermore, the application of SDF in the GPS-only solution leads to a significant reduction of the noise level, which is significantly lower than any of the multi-GNSS solutions, with u-blox2 SDF residuals' MSTDs for the horizontal and vertical components lower than 2mm and 4mm respectively (Figure 8.14). By comparing the GPS SDF residuals' MSTD timeseries with that of multi-GNSS solution, it is evident that the GPS SDF residuals are more precise than any multi-GNSS solutions at least 85% of the recording period (Table 8.8).

8.7.2 Evaluation of the performance of the dual low-cost GNSS rover-system

8.7.2.1 Filtering techniques based on different days (SDF) or different receivers (CME)

Figure 8.15 presents the MSTD of the E/N/U component of the low-cost GNSS u-blox2 receiver for the different multi-GNSS solutions after the application of the CME filtering (Case 1 Solution 4, Figure 8.5). It is compared against the corresponding MSTD of the GPS-only solution after application of the SDF (Case 2 Solution 6, Figure 8.5). It is observed that the CME GPS+GLONASS+Galileo solution is the most precise among other CME multi-GNSS solutions, apart from periods (e.g. 16:50-17:10, ~17:30) where the poor quality of GLONASS satellite(s) signal reduce the precision of the multi-GNSS solutions. The comparison is also presented in Table 8.9 between the MSTD of three multi-GNSS solutions (GPS, GPS+Galileo, GPS+GLONASS+Galileo) after the application of CME and expressed as a percentage with respect to the examined period. It is confirmed that the CME GPS+GLONASS+Galileo timeseries is the most precise for ~70% of the recording period for any of the three days. The smallest improvement of the precision is observed in the Easting component with multi-GNSS solutions, as a high precision (i.e. <2mm) is already achieved by all CME multi-GNSS solutions (Figure 8.15). This is probably due to the satellite constellation and the deployment of the two low-cost GNSS rover stations, which had E-W direction baselines.

Furthermore, by comparing the MSTD of the SDF GPS-only u-blox2 timeseries with the CME GNSS timeseries (Figure 8.15), it is obvious that the SDF GPS-only solution does not vary significantly, whereas the CME GNSS solutions vary especially for the time intervals around 18:00 or 19:00. However, by comparing the achieved precision for the entire period, it is observed that a lower MSTD (higher precision) is obtained for the SDF GPS-only solution than the CME GPS-only solution for ~60-80% of the timeseries (Table 8.10). On the contrary, similar or higher precision is achieved from the other two CME GNSS solutions (GPS+Galileo and GPS+GLONASS+Galileo) compared to the SDF GPS-only solution, with the CME GPS+GLONASS+Galileo timeseries achieving better precision than SDF GPS-only solution for even up to ~60-70% of the timeseries (Table 8.10, Table 8.11). Although CME residuals could improve the overall result and even achieve similar or better performance than SDF residuals in the aspect of time-domain (percentage of CME residuals having better precision than SDF is around or more than 50%). However, compared to SDF residuals, the performance of CME filter is worse at certain periods, especially for the duration (e.g. ~ 17:00 and ~18:00). This is probably due to increased differences of multipath error between two u-blox receivers, which could not be accurately modelled by CME. The larger deviation of errors between two u-blox receivers makes the use of the CME filter less effective. Whereas the SDF residuals are mostly stable meaning multipath mitigation is more effective with SDF. Therefore, further analysis of the residuals after CME filtering is conducted to show if the multipath effect is still existent.

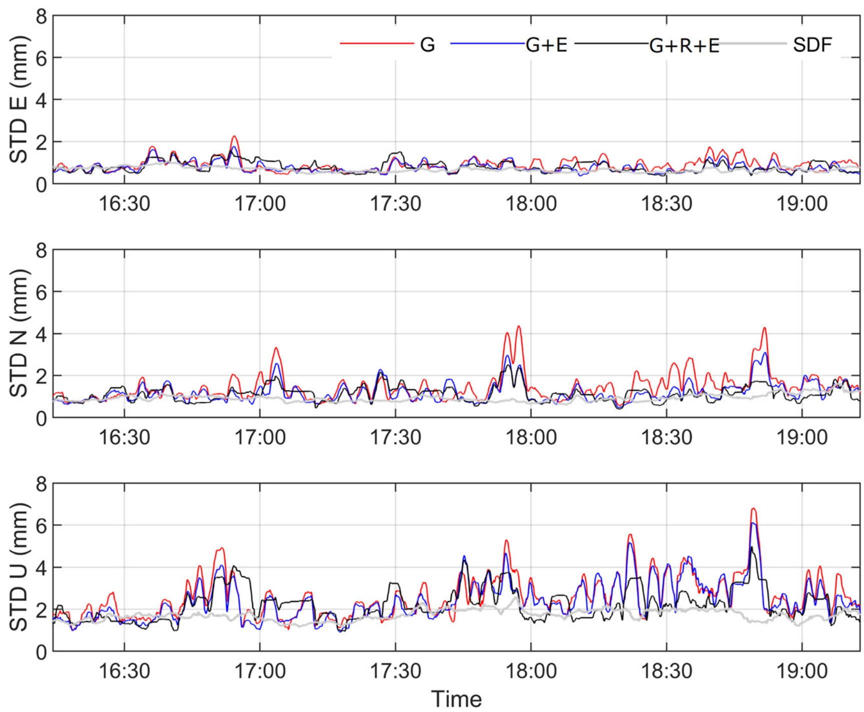

Figure 8. 15 *Comparison of the MSTD between the u-blox2 coordinate timeseries of Day 2 after application of the SDF for GPS-only solution and all the available multi-GNSS solutions after applying CME method (G: GPS-only, G+E: GPS+Galileo, G+R+E: GPS+GLONASS+Galileo).*

Table 8. 9 *Comparison between the MSTD of the u-blox2 coordinate timeseries after the application of CME for the three multi-GNSS solutions (G: GPS-only, G+E: GPS+Galileo G+R+E: GPS+GLONASS+Galileo). The comparison is expressed in percentage of the examined period*

STD (%)	Day1			Day2			Day3		
	E	N	U	E	N	U	E	N	U
G+R+E < G	62%	74%	76%	74%	74%	74%	67%	79%	82%
G+E < G	70%	73%	77%	73%	80%	72%	69%	83%	75%
G+R+E < G+E	55%	71%	66%	57%	65%	65%	63%	71%	71%

Table 8. 10 *Comparison of the MSTD of the u-blox2 GPS-only SDF coordinates timeseries and the three u-blox2 GNSS coordinate CME timeseries (G: GPS-only, G+E: GPS+Galileo, G+R+E: GPS+GLONASS+Galileo). The comparison is expressed in the percentage of the examined period.*

STD (%)	SDF < G CME			SDF < G+E CME			SDF < G+R+E CME		
	E	N	U	E	N	U	E	N	U
Day 1	58%	63%	69%	41%	48%	48%	38%	38%	44%
Day 2	74%	85%	86%	62%	67%	80%	56%	58%	68%
Day3	60%	64%	66%	51%	41%	48%	49%	35%	33%

Table 8. 11 *Comparison of the MSTD of the u-blox1 GPS-only SDF coordinates timeseries and the three u-blox1 GNSS coordinate CME timeseries (G: GPS-only, G+E: GPS+Galileo G+R+E: GPS+GLONASS+Galileo). The comparison is expressed in percentage of the examined period.*

STD (%)	SDF < G CME			SDF < G+E CME			SDF<G+R+E CME		
	E	N	U	E	N	U	E	N	U
Day 1	47%	56%	62%	36%	37%	42%	33%	27%	33%
Day 2	60%	63%	70%	47%	46%	60%	42%	33%	45%
Day3	52%	47%	53%	42%	27%	38%	41%	21%	26%

The analysis of the CME GPS-only solutions for the common period of the three days shows that there is some repeatability in the pattern of their MSTD, with a time lag of ~4 min, indicating a potential presence of multipath induced error in the solution (Figure 8.16). Thus, to enhance even further the CME GPS-only solution, the SDF was applied in the CME GPS-only timeseries. Figure 8.17 presents the MSTD of the SDF-CME GPS-only solution against the CME GPS-only solution, where it is observed that the precision is further improved in the horizontal components and dropping below 1mm, while for the Up component it is reduced below 2mm. Likewise, by applying the SDF to the GPS-only solutions of the two low-cost GNSS rover stations first and then the CME method to remove any potential common error between the two GPS timeseries, similar precision could be derived indicating that the sequence of the application of SDF and CME in the GPS solutions of the two GNSS rover stations does not affect the achieved precision. (Figure 8.18; Table 8.12)

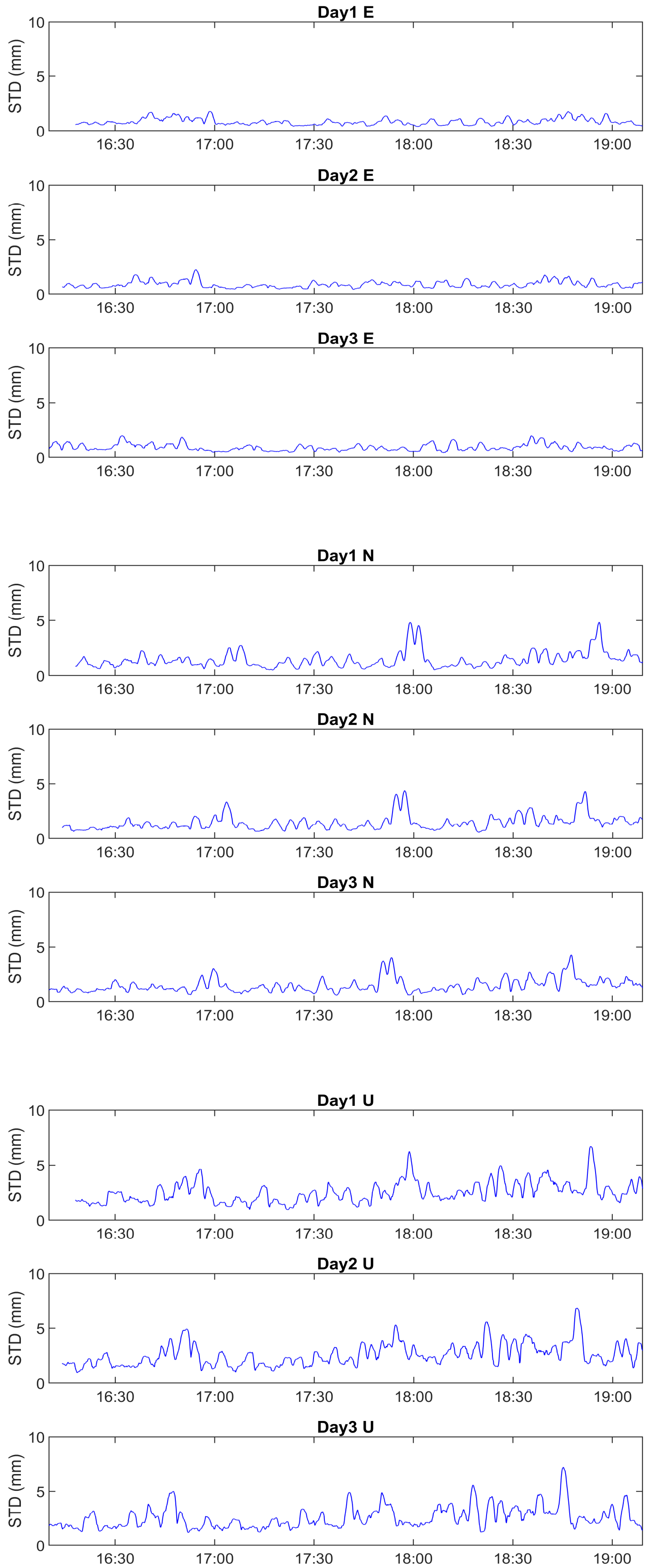

***Figure 8. 16** The u-blox2 E/N/U GPS-only coordinates timeseries after CME filtering for the three consecutive days. It is evident the repetition of some error anomalies (for instance ~18:00 in Day 1), appearing with a time lag of ~4 min, indicating potential multipath induced errors.*

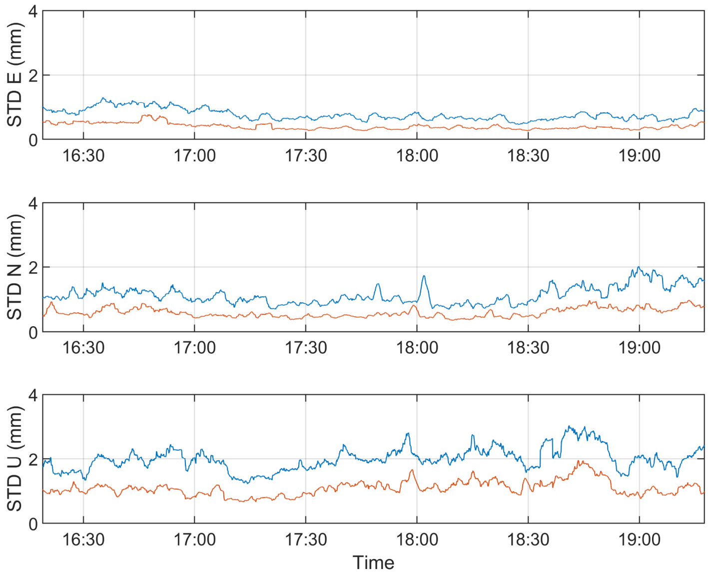

***Figure 8. 17** The MSTD of u-blox2 GPS-only coordinate timeseries after the application of SDF (blue) and CME-SDF (red) for Day1. It is evident that the application of CME and SDF methods achieve higher precision than SDF only method, reaching up to 1mm and 2mm for horizontal and vertical components, respectively.*

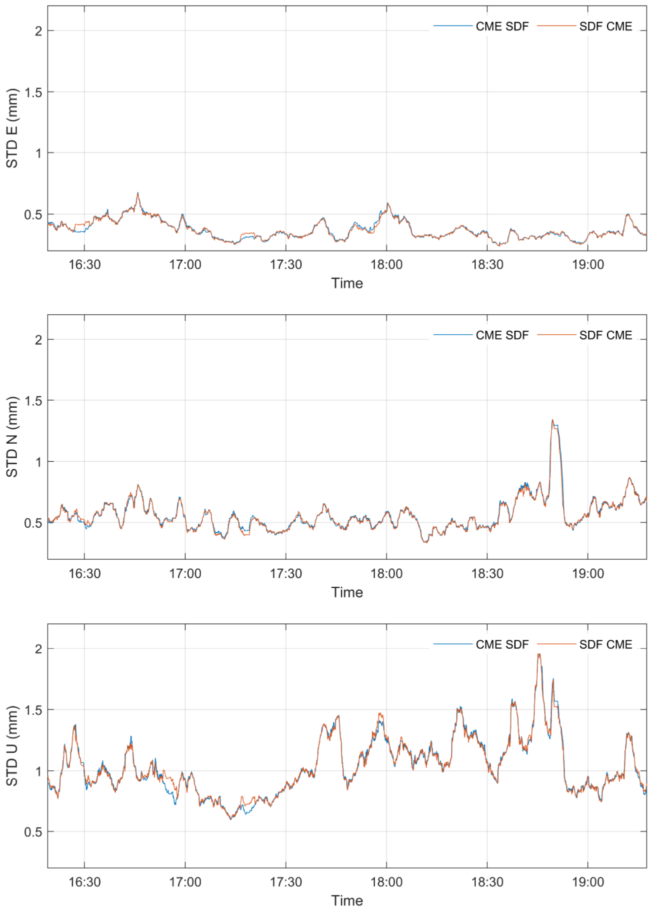

Figure 8. 18 *E/N/U residuals from the combination of CME filter and SDF with different filtering sequences (CME SDF or SDF CME) for u-blox2 Day2 (CME SDF: apply CME filter first followed by SDF, SDF CME apply SDF first followed by CME filter)*

Table 8. 12 *U-blox1/u-blox2 residuals STD after the combined filter of CME and SDF with different filtering sequences (CME SDF or SDF CME) of the examined period (16:20-19:20) in different days (CME SDF: SDF followed by CME filter; SDF CME: SDF followed by CME filter)*

STD (mm)	U-blox1						U-blox2					
	SDF CME			CME SDF			SDF CME			CME SDF		
	Day1	Day2	Day3	Day1	Day2	Day3	Day1	Day2	Day3	Day1	Day2	Day3
E	0.55	0.48	0.58	0.68	0.52	0.61	0.55	0.48	0.58	0.55	0.48	0.57
N	0.79	0.86	0.89	0.90	0.89	0.92	0.79	0.86	0.89	0.83	0.88	0.89
U	1.56	1.43	1.60	1.84	1.49	1.67	1.56	1.43	1.60	1.78	1.52	1.62

8.7.2.2 Combination of the two receivers by average/weighted average

The approaches of using the average or weighted average of the two low-cost rover receivers are also applied to improve the precision of the solution. The weighted average of initial data and incorporation of the averaging process to SDF is examined. The averaging process was also implemented for CME residuals of two receivers, however, since the CME model was created based on the weighted average of two u-blox receiver timeseries, combining of CME residuals with weighted average is only a process of reverse operation which leads to nearly zero value of average/weighted average of CME residuals. For the process of combining two u-blox receiver data in SDF, the average and weighted average results are also compared between each other.

Equation 8.3 shows the average process between u-blox1 and u-blox2 each epoch which is calculated by simply averaging between u-blox1 and u-blox2 measurements for E/N/U components. Equation 8.4 and Equation 8.5 shows the weighted average process for each epoch where the STD of the position estimates from RTKLIB output are used as weight. Equation 8.4 calculates the weighted coefficients for each u-blox measurement. The weighted coefficient of two u-blox receivers is then multiplied by respective longitudinal/lateral/vertical solutions at the corresponding epoch and combined to obtain the weighted average results shown in Equation 8.5.

$$E_{ave} = \frac{E_{u-blox1} + E_{u-blox2}}{2}$$

$$N_{ave} = \frac{N_{u-blox1} + N_{u-blox2}}{2}$$

$$U_{ave} = \frac{U_{u-blox1} + U_{u-blox2}}{2}$$

Equation 8. 3 *Average calculation between two u-blox solutions*

$$\mathrm{W1} = \frac{\frac{1}{\sigma^2_{u-blox1}}}{\frac{1}{\sigma^2_{u-blox1}} + \frac{1}{\sigma^2_{u-blox2}}} \qquad \mathrm{W2} = \frac{\frac{1}{\sigma^2_{u-blox2}}}{\frac{1}{\sigma^2_{u-blox1}} + \frac{1}{\sigma^2_{u-blox2}}}$$

Equation 8. 4 *Weighted average coefficients for two u-blox solutions*

$$E_{weighted-ave} = E_{u-blox1} * W1 + \; E_{u-blox2} * W2$$

$$N_{weighted-ave} = N_{u-blox1} * W1 + \; N_{u-blox2} * W2$$

$$U_{weighted-ave} = U_{u-blox1} * W1 + \; U_{u-blox2} * W2$$

Equation 8. 5 *Weighted average calculation between two u-blox solutions*

Where

- $W1$ and $W2$ stand for the weighted coefficient for u-blox1 and u-blox2 results respectively
- $\sigma_{u-blox1}$ and $\sigma_{u-blox2}$ are the STDs of u-blox1 and u-blox2 position estimates for each epoch
- $E/N/U_{ave}, E/N/U_{weighted-ave}, E/N/U_{u-blox1}, E/N/U_{u-blox2}$ stand for Eastings/Northings/Up solutions for average combination, weighted average combination, u-blox1, and u-blox2 respectively.

Firstly, the weighted average was applied on two u-blox receivers' initial timeseries between the common period (16:20-19:20). It is shown that, with the weighted average of two u-blox data, the E/N/U components are generally obtaining slightly more precise results compared to separate u-blox solutions both for GPS-only constellation and multi-constellation (Table 8.13). This is probably due to partially mitigation of white noise by the averaging process.

Table 8. 13 *STDs of initial timeseries for u-blox1, u-blox2, and weighted average combination of them under multi-constellations (G: GPS-only, G+E: GPS and Galileo, G+R: GPS+GLONASS, G+R+E: GPS+GLONASS+Galileo) within the examined period for three days. The weighted average results are generally better than each u-blox result separately.*

	STD (mm)	u-blox1			u-blox2			Weighted Average		
		E	N	U	E	N	U	E	N	U
Day1	G	3.1	6.3	9.1	3.1	5.1	11.0	2.6	5.1	9.0
	G+E	3.2	4.0	8.0	2.7	5.1	9.6	2.6	3.8	7.8
	G+R	3	4.1	8.7	2.7	4.9	8.3	2.5	4.0	7.4
	G+R+E	2.7	3.6	7.1	2.6	3.6	7.3	2.4	3.1	6.4
Day2	G	3.3	5.5	9.6	3.3	4.8	11.4	2.9	4.4	9.3
	G+E	2.7	4.9	9.2	2.8	4.0	10.2	2.4	4.0	8.6
	G+R	3.3	4.3	7.5	2.9	4.1	8.1	2.6	3.7	6.8
	G+R+E	2.9	3.9	7.4	2.4	3.9	7.5	2.3	3.5	6.5
Day3	G	3.9	6.1	9.7	3.3	4.8	11.7	3.2	4.8	9.6
	G+E	3.3	5.5	9.8	2.8	4.2	7.7	2.7	4.5	8.0
	G+R	2.9	3.9	8	3.2	5.1	7.9	2.7	4	7.1
	G+R+E	2.6	3.9	6.3	2.8	4.6	8.5	2.4	3.9	6.5

The averaging process is then applied and incorporated with SDF. There are two approaches to achieve SDF with combination between two u-blox receivers; 1) combine the two timeseries first and then apply the SDF, corresponding to Case 3 in Figure 8.5 and 2) apply the SDF first separately for each receiver and combine the

SDF residuals, corresponding to Case 2 in Figure 8.5. It is studied how the sequence of weighted average combination and SDF would affect the results. By comparing Table 8.14 and Table 8.15, generally, the sequence of SDF and weighted average combination has minimal impact. This is also confirmed in Figure 8.19 that slight deviations could only be seen from the Easting component, as for the N/U components, the MSTD timeseries nearly overlay.

Table 8. 14 *STDs of residuals when the initial timeseries was combined first with weighted average and then subjected to SDF*

STD (mm)	Day 1	Day 2	Day 3
E	0.98	0.79	0.99
N	1.60	1.14	1.66
H	2.32	2.01	2.23

Table 8. 15 *STDs of residuals when residuals of each u-blox receiver were obtained using SDF first and then combined with the weighted average*

STD (mm)	Day 1	Day 2	Day 3
E	0.97	0.79	0.99
N	1.61	1.14	1.66
H	2.32	2.01	2.23

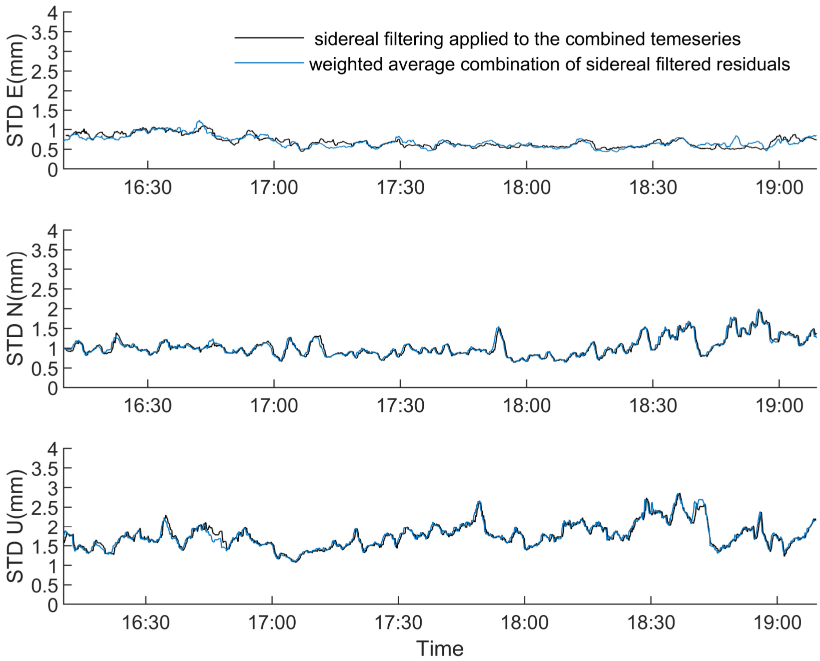

Figure 8. 19 *Day1 MSTD (moving window 200s) of E/N/U residuals obtained from 1) SDF applied on the weighted average combined initial timeseries and 2) weighted average of SDF residuals from two u-blox solutions*

The average/ weighted average of the SDF residuals from two u-blox receivers is compared against the SDF residuals of each receiver separately to study the precision improvement by a combination of the two u-blox receivers. Based on Table 8.16, it is observed a negligible difference between the average and weighted average combination, as can also be shown from Figure 8.20, Figure 8.21, Figure 8.22, where the weighted average overlay with the average timeseries. This probably results from a similar measuring environment for the two receivers where the weights between these two receivers are similar. The weights of the two u-blox receivers were plotted in Figure 8.23-8.25, it is shown the weight for both receivers mostly oscillate around 0.5, more specifically ranging between 0.4-0.6 for E/N and between 0.49-0.51 for Up (Figure 8.23, Figure 8.24, Figure 8.25), resulting in similar weighted average solutions with the average solutions.

It can also be shown in Table 8.16 that regardless of the base station, the average and weighted average would normally have better (lower STD) if not similar precision with the more precise u-blox receiver solution of the two. This is further verified in Figure 8.20, Figure 8.21, Figure 8.22, and Table 8.13. In Figure 8.20-22, the epochs when the weighted averaged results are worse than any of two u-blox solutions are highlighted yellow. Other non-highlighted epochs represent the cases when the weighted average combination has the lowest STD which are quantified in Table 8.17 and expressed as the percentages over the examined duration for E/N/U components. It is derived that the weighted average combination of the residuals after SDF is better than any separate SDF residual of the two receivers ~70% of the examined time. The periods highlighted in yellow at the top right of Figure 8.20-8.22 are also highlighted in the bottom right correspondingly and correlated with the MSTD difference between u-blox1 and u-blox2 solutions. It is implied that if the MSTD difference between u-blox1 and u-blox2 is larger than a threshold, the weighted average combination would be ineffective in precision improvement from a single u-blox receiver. This threshold is component dependent and is roughly around ±0.2-0.3mm for E/N components, and ±0.5mm for Up component.

The comparison between Table 8.18, Table 8.10, and Table 8.11 shows an indirect way of comparing the combined SDF residuals with separate SDF residuals from each u-blox receiver by using the CME residuals as the reference. It indicates that the combined results are normally better than individual SDF residuals as a larger percentage is shown that combined SDF residuals are better than CME residuals.

Table 8. 16 *E/N/U STDs of SDF residuals for each u-blox receiver separately and combined (average/weighted average) for different base stations (low-cost base, geodetic base) on three separate days*

Base (Receiver & Antenna)	STD Residual (mm)	u-blox1			u-blox2			Weighted/average		
		Day1	Day2	Day3	Day1	Day2	Day3	Day1	Day2	Day3
U-blox Patch	E	1.3	1.0	1.4	1.0	0.8	0.9	1.0	0.8	1.0
	N	2.0	1.7	2.2	1.6	1.2	1.6	1.6	1.2	1.7
	U	3.1	2.9	3.0	2.5	2.0	2.5	2.3	2.0	2.2
Leica GR10 Leica AR25	E	1.2	0.9	1.1	0.8	0.7	0.8	0.8	0.6	0.8
	N	1.7	1.7	1.9	1.2	0.9	1.2	1.1	1.0	1.3
	U	3.2	2.8	3.0	2.1	1.8	2.2	2.1	1.8	2.0

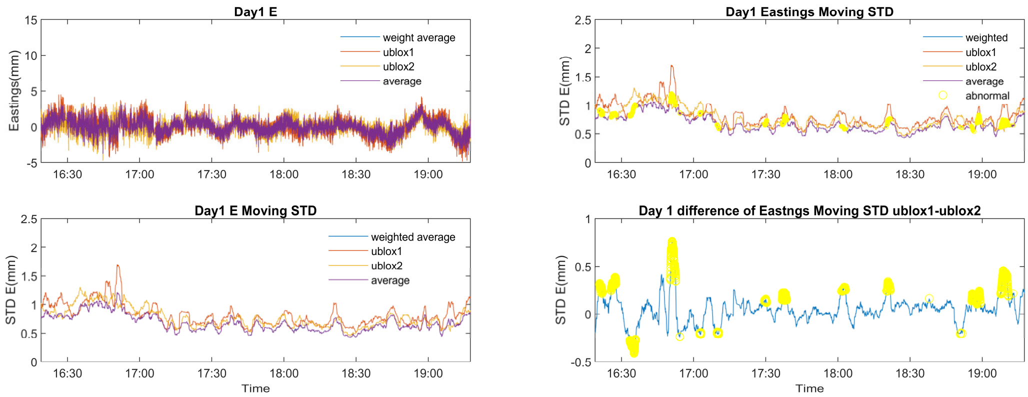

Figure 8. 20 *(Top left) Day1 Eastings SDF residuals timeseries for u-blox1, u-blox2, average, and weighted average of u-blox1, u-blox2 results, (Bottom left) MSTD of the top left timeseries with moving window of 200s, (Top right) same figure with the bottom left with the inclusion of yellow dots highlighting periods when the weighted average results are worse than either u-blox1 or u-blox2 solutions, (Bottom right) Timeseries of MSTD difference between u-blox1 and u-blox2 for each epoch, the yellow highlighted part corresponds to that of top right*

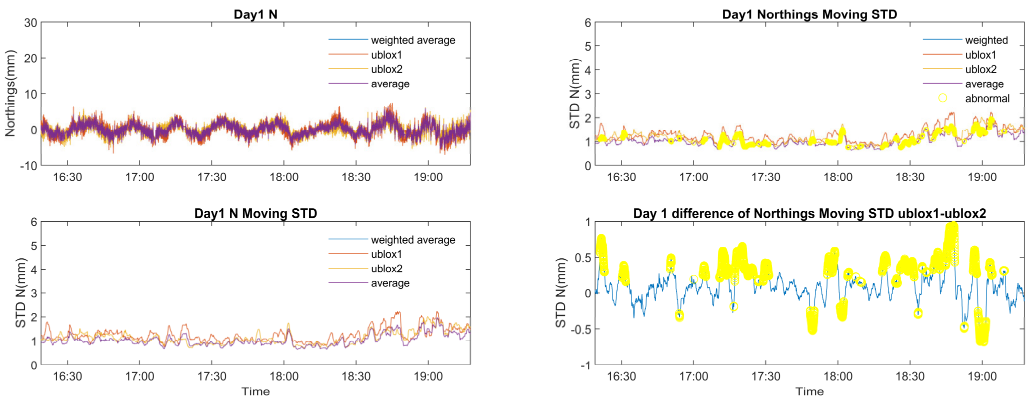

Figure 8. 21 *(Top left) Day1 Northings SDF residuals timeseries for u-blox1, u-blox2, average, and weighted average of u-blox1, u-blox2 results, (Bottom left) MSTD of the top left timeseries with moving window of 200s, (Top right) same figure with the bottom left with the inclusion of yellow dots highlighting periods when the weighted average results are worse than either u-blox1 or u-blox2 solutions, (Bottom right) Timeseries of MSTD difference between u-blox1 and u-blox2 for each epoch, the yellow highlighted part corresponds to that of top right*

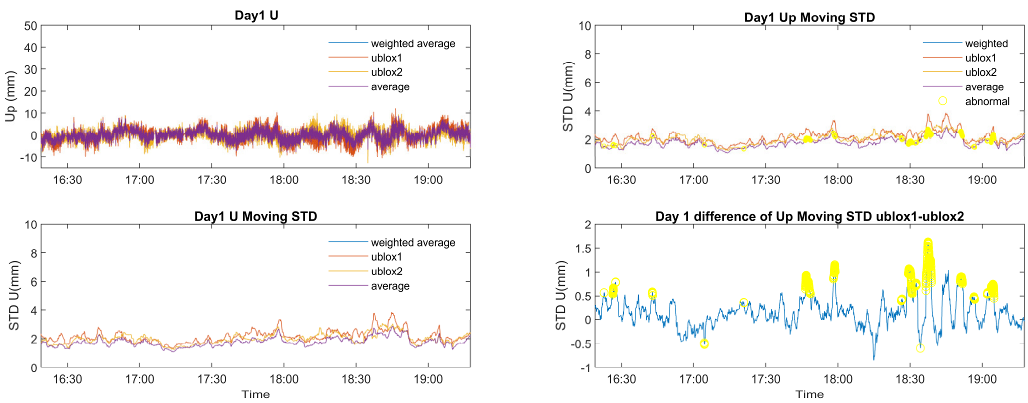

Figure 8. 22 *(Top left) Day1 Up SDF residuals timeseries for u-blox1, u-blox2, average, and weighted average of u-blox1, u-blox2 results, (Bottom left) MSTD of the top left*

timeseries with moving window of 200s, (Top right) same figure with the bottom left with the inclusion of yellow dots highlighting periods when the weighted average results are worse than either u-blox1 or u-blox2 solutions, (Bottom right) Timeseries of MSTD difference between u-blox1 and u-blox2 for each epoch, the yellow highlighted part corresponds to that of top right

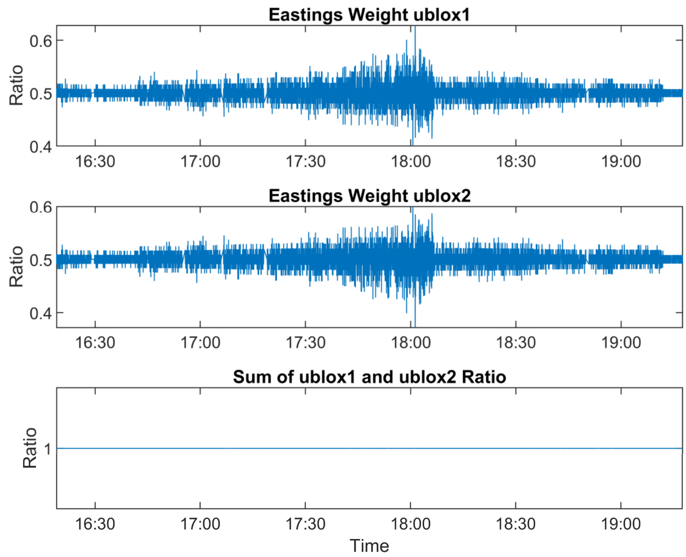

Figure 8. 23 *Timeseries of weights used in the weighted average for u-blox1 and u-blox2 Eastings combination, and the sum of the u-blox1 and u-blox2 weight, the range of the weight is between 0.4-0.6. The u-blox1 and u-blox2 ratio sum up to 1*

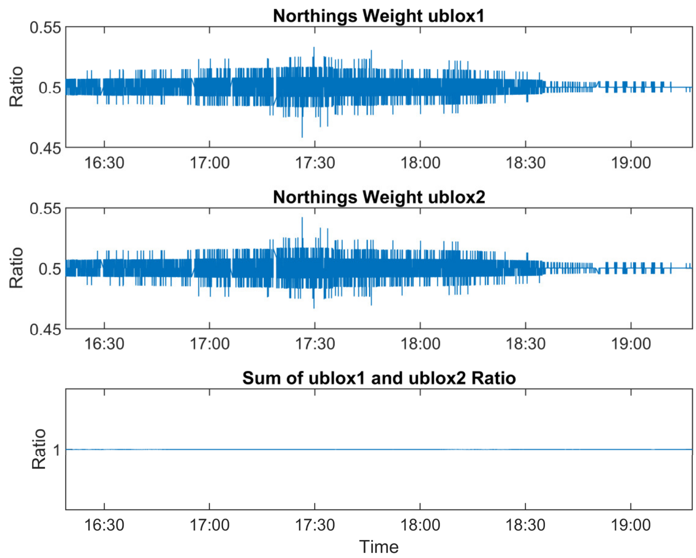

Figure 8. 24 *Timeseries of weights used in the weighted average for u-blox1 and u-blox2 Northings combination, and the sum of the u-blox1 and u-blox2 weight, the range of the weight is between 0.4-0.6. The u-blox1 and u-blox2 ratio sum up to 1*

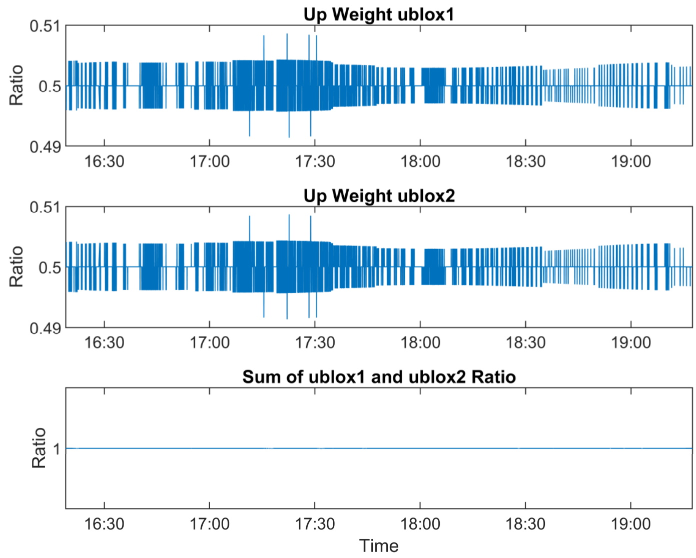

Figure 8. 25 *Timeseries of weight used in the weighted average for u-blox1 and u-blox2 Up combination, and the sum of the u-blox1 and u-blox2 weight, the range of the weight is between 0.4-0.6. The u-blox1 and u-blox2 ratio sum up to 1*

Table 8. 17 *The percentage of the period when combined SDF residuals are the most precise compared to separate u-blox1, u-blox2 SDF residuals over the examined period for E/N/U components for three days*

	E	N	U
Day1	89.8%	70.4%	91.6%
Day2	90.1%	77.3%	80.9%
Day3	84.3%	67.6%	90.7%

Table 8. 18 *Comparison of the MSTD of the combined u-blox receiver SDF residual coordinates timeseries and u-blox1& u-blox2 multi-GNSS coordinate CME timeseries*

STD (%)	% of combined SDF residuals having the smallest STD compared to both u-blox								
	G CME			G+E CME			G+R+E CME		
	E	N	U	E	N	U	E	N	U
Day 1	65%	73%	81%	52%	55%	65%	49%	43%	59%
Day 2	84%	90%	95%	74%	75%	85%	64%	61%	73%
Day3	69%	76%	81%	63%	46%	64%	63%	38%	50%

8.8 Timeseries filtering with high-pass filtering

GPS position estimates of 1-Hz sampling are subjected to low frequency (0.001 – 0.04 Hz) errors which can be mitigated by SDF (Choi et al., 2004). Alternatively, with digital filtering, multipath and other GPS low frequency related errors of low frequency could also be mitigated, however, the determination of cut-off frequency presents a problem.

To determine the cut-off frequency of the high-pass filter, firstly, spectral analysis adopting DFT is applied on the initial timeseries and the SDF residual timeseries. It is compared the initial timeseries spectrum with the spectrum of residuals after SDF (Figure 8.26). It is noticed that the amplitude of both the coloured noise region (< ~0.01Hz), as well as the white noise (>~0.01Hz), are reduced with the application of the SDF. This shows not only could the applied SDF reduce the long period noise effectively (i.e. multipath, or orbit-related errors), but also decrease the level of random white noise.

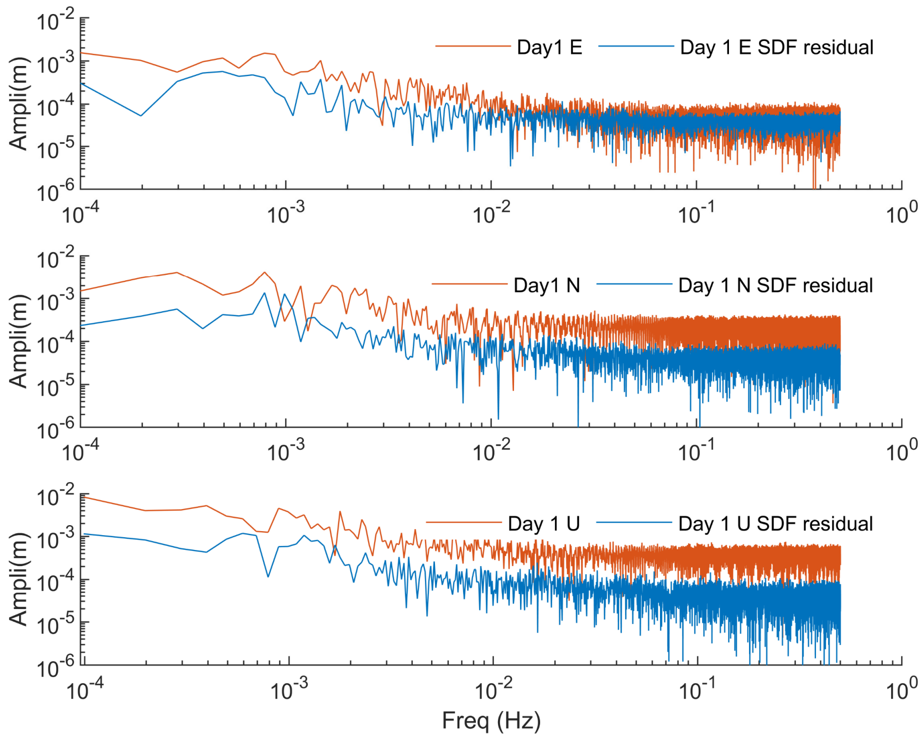

Figure 8. 26 *Day1 u-blox1 Eastings/Nothings/Up DFT spectra for the initial timeseries and residuals timeseries after SDF within the examined period*

Several cut-off frequencies around 0.01Hz are selected and applied in the high-pass filter to obtain the residuals of the same STD as that of SDF residuals. In the data analysis, a Butterworth high-pass filter with an order of 5 and sampling frequency of 1Hz is used. Several cut-off frequencies from 0.001Hz-0.035Hz are applied on the timeseries. The STDs of resultant residuals are calculated. The STDs of obtained residuals from different cut-off frequencies are compared and matched against the STD of residuals from SDF, from which the optimum cut-off frequency could be determined. With trials and errors, the optimum high-pass cut-off frequency can be obtained (Table 8.19). It is shown that the optimum cut-off frequencies range between 0.004-0.035Hz, corresponding to the 0.001-0.04 Hz low-frequency noise mitigated from SDF (Choi et al., 2004) and spectra (Figure 8.26).

Table 8. 19 *E/N/U optimum cut-off frequency for Butterworth high-pass filter to achieve same STD with residuals from SDF for each u-blox receiver in three days*

Optimum frequency (Hz)	u-blox1			u-blox2		
	E	N	U	E	N	U
Day1	0.004	0.004	0.007	0.009	0.007	0.015
Day2	0.015	0.007	0.009	0.035	0.02	0.035
Day3	0.004	0.004	0.008	0.02	0.007	0.015

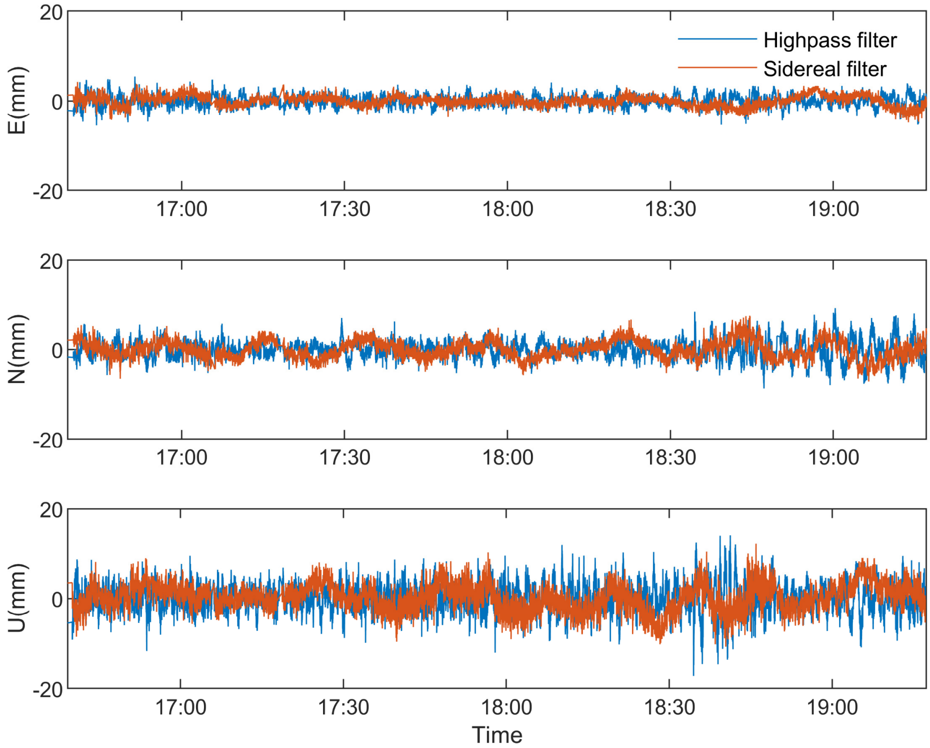

Figure 8. 27 *Day1 u-blox1 E/N/U timeseries comparisons between high-pass filtered residuals and SDF residuals within the examined period*

Further comparison is conducted between residuals timeseries subjecting to SDF and Butterworth high-pass filter for E/N/U components for Day 1 u-blox1 data. (Figure 8.27). The cut-off frequency of the high-pass filter is configured to ensure both residuals timeseries to have the same STD within the examined period. Comparing the two timeseries, it is shown that due to eliminating the low-frequency noise, the high-pass filtered residual timeseries are mostly expressed by white noise, in contrast, low-frequency components still can be seen from SDF residuals timeseries, which is also verified by the presence of coloured noise in the spectral analysis of SDF residuals (Figure 8.26).

8.9 Discussion and Summary

The SBL static experiment aims to assess the noise of the low-cost monitoring system for SBLs and explore potential approaches for low-cost solution improvement. To achieve this aim, a novel approach of adopting a closely-spaced dual low-cost rover is used for the experiment deployment, several different methods are attempted and proved useful in precision enhancement, such as 1) adopt a geodetic grade base station antenna, 2) SDF, 3) CME filtering, 4) multi-GNSS observation, 5) data combination by weighted average, 6) use of a high-pass filter. Each approach is tested with comparisons and conclusions summarised.

Based on the comparison of the solutions with different formations of base stations above, it is observed that the low-cost GNSS rover station performs similarly regardless of the base station receiver grade (geodetic or low-cost) when the base station adopts patch antenna. On the other hand, the performance of the low-cost GNSS rover station is improved by using a base station consisted of a geodetic receiver and geodetic antenna, reducing the noise level of the E component even to 2mm. The application of multi-GNSS solutions can also enhance the performance of the low-cost GNSS rover station. However, the multi-GNSS seems to have less availability, due to data gaps and float solutions, which is amplified by using observations of GLONASS satellites. Another precision improvement approach is by applying SDF to GPS-only timeseries. It is found that the application of SDF decreases the noise level of the SBL solution significantly, especially when the patch antenna is employed in the base station. The improvement in GPS timeseries by applying the SDF method is well-known for geodetic-grade receivers. However, for low-cost GNSS receivers, the SDF method probably has a larger improvement in the precision due to the higher noise level and less ability to reject the multipath effect of the low-cost GNSS receivers.

Apart from multi-GNSS solutions and SDF for each receiver, the formation of a dual low-cost GNSS rover system is also assessed for its potential precision improvement from a single low-cost rover. Due to the spatial correlation between the two closely-spaced of low-cost rovers of the same model, the CME filtering method is implemented with different multi-GNSS solutions to remove partially common errors from both rovers. By comparing different multi-GNSS CME results, it is again shown that the CME multi-GNSS solution has better precision than CME GPS-only solution with the trade-off of reduced availability (occurrence of floated solutions and data gaps) especially by including GLONASS satellites. Hence, compared to other multi-GNSS solutions, CME GPS+Galileo solution is generally more precise and reliable with less data loss. A better precision is observed for CME GPS+Galileo residuals than that of SDF GPS-only around or more than 50% of the time within the examined period (Table 8.10, Table 8.11). However, the SDF GPS-only residuals seem to have smaller fluctuation in the amplitude during the examined period, especially for the vertical component (Figure 8.15). By applying the CME filter and subsequent SDF to the GPS-only timeseries, the highest precision could be achieved, which reaches 1mm for the horizontal components and 2mm for the vertical component.

By utilising the two closely-spaced low-cost rovers, the solution precision enhancement could also be accomplished by the combination of two receiver coordinate timeseries with the weighted average. A precision improvement is firstly confirmed from the weighted average combination of the original timeseries compared to individual low-cost timeseries solutions. Then, the weighted averaging process is also incorporated with SDF, where the SDF residuals timeseries from both u-blox rover solutions are weighted average combined epoch by epoch. Similarly, it is shown that the combined SDF residuals are generally more precise than the SDF residuals from separate measurement. The low-frequency errors of the timeseries could also be largely mitigated with a high-pass filter. The same STD could be achieved between SDF results and high-pass filtered residuals. However, compared to SDF residuals timeseries, the low frequency components are mostly removed in the high-pass filtered residuals.

Figure 8.28 presents the original timeseries of SBL GPS solution formed of low-cost GNSS rover (u-blox2 receiver & patch antenna) and low-cost GNSS base station (u-blox receiver & patch antenna), and timeseries of improved precision from various approaches; (i) use high-end base station consisted of a dual-frequency receiver and geodetic antenna, (ii) use dual low-cost GNSS rover-system with application of CME, SDF or both. It is evident the GPS solution precision enhancement by the dual low-cost GNSS rover system and by applying the CME and SDF methods (Figure 8.28). The precision with the application of the SDF and/or CME filtering is increased significantly even reaching sub-mm level for the horizontal components and 1-2 mm level for the vertical component (Table 8.20), which is even better than the precision achieved when the geodetic receiver and antenna are used in the base station. Furthermore, it is demonstrated that the precision enhancement of GPS solution by different filtering methods is across the entire frequency band of the recording; the level of the coloured and white noise is significantly reduced (Figure 8.29).

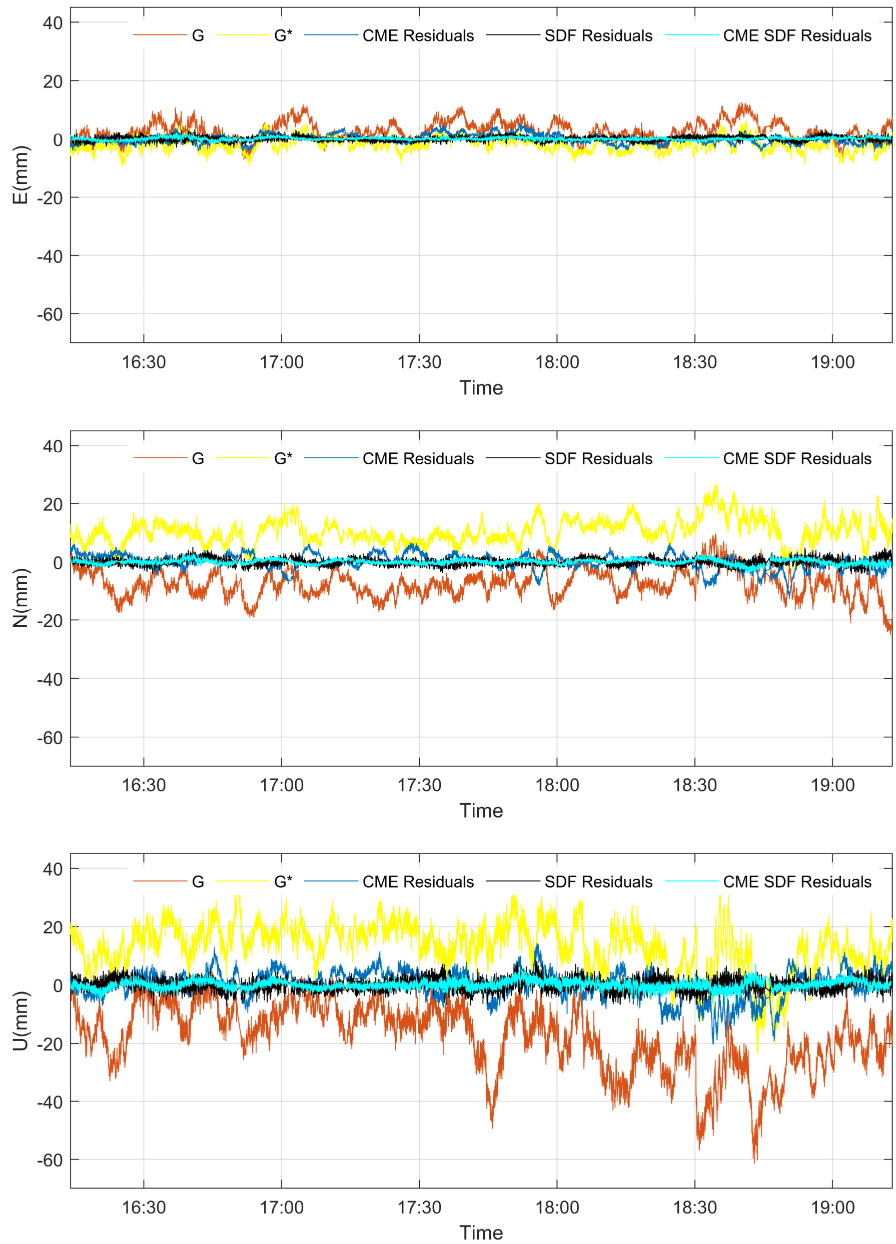

Figure 8. 28 *The u-blox2 GPS-only E/N/U coordinate timeseries for different analysis approaches: (red) initial GPS-only timeseries with low-cost GNSS base station, (yellow) GPS-only timeseries with geodetic receiver and antenna for base station, (blue) CME GPS-*

only timeseries, (black) SDF GPS-only timeseries and (cyan) CME and SDF GPS-only timeseries. It is evident that the application of the combination of CME and SDF leads to the highest precision of 1-2 mm-level.

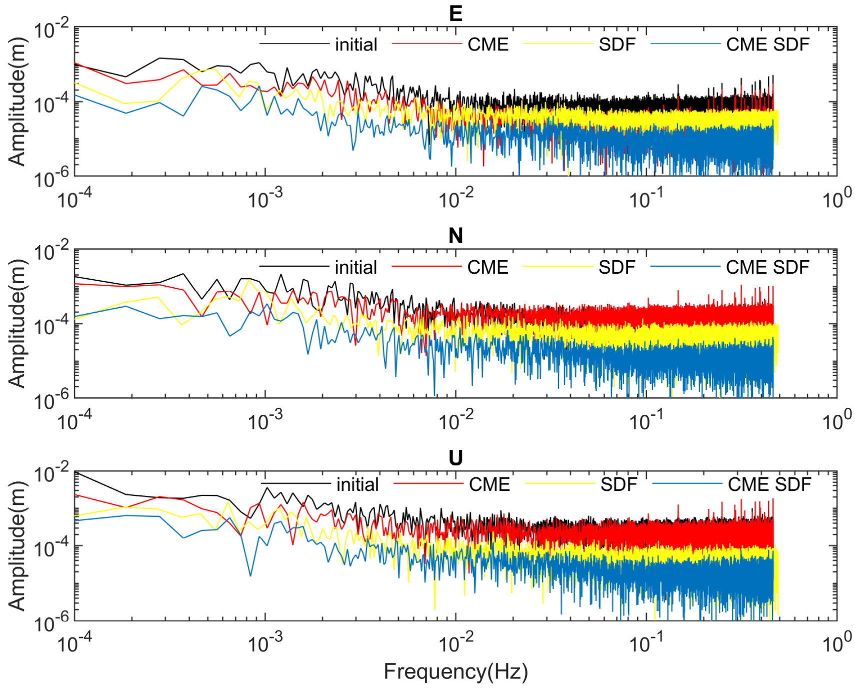

Figure 8. 29 *Spectra of the E/N/U timeseries of u-blox2 receiver, for different solutions: (i) GPS-only, (ii) CME GPS-only solution, (iii) SDF GPS-only solution, and (iv) CME and SDF GPS-only solution. The application of CME and SDF leads to the spectrum with the lowest coloured and white noise level.*

Table 8. 20 *STD of E/N/U coordinate timeseries of u-blox1, u-blox2, and weighted average combined solution for Day2 by adopting different approaches: (i) GPS-only solution having low-cost grade base station, (ii) GPS-only solution having geodetic grade base station,(iii) GPS+Galileo and GPS+GLONASS+Galileo solution having low-cost grade base station, (iv) CME multi-GNSS solutions of different satellite constellations (GPS-only, GPS+Galileo, and GPS+GLONASS+Galileo), (v) SDF GPS solution and (vi) CME-SDF GPS solution. Similar results are also obtained for Day1 & Day3.*

STD (mm)	u-blox1			u-blox2			Combined (Weighted average)		
	E	N	U	E	N	U	E	N	U
G (u-blox + patch base)	3.3	5.7	9.7	3.3	4.8	11.4	2.9	4.4	9.3
G (Leica GR10 + AR25 base)	2.7	5.0	8.6	2.6	4.6	8.6			
G+E (u-blox + patch base)	2.7	4.9	9.2	2.8	4.0	10.2	2.4	4.0	8.6
G+R+E (u-blox + patch base)	2.9	3.9	7.4	2.4	3.9	7.5	2.3	3.5	6.5
CME G	1.7	2.7	4.9	1.7	2.7	4.9			
CME G+E	1.4	2.0	4.6	1.4	2.0	4.6			
CME G+R+E	1.2	1.7	3.9	1.2	1.5	3.5			
SDF	1.0	1.7	2.9	0.8	1.2	2.0	0.8	1.2	2.0
CME-SDF	0.5	0.9	1.5	0.5	0.9	1.5			

In Table 8.20, the approaches for low-cost timeseries precision improvement are summarised in an order of increasing effectiveness. Firstly, the precision of the initial timeseries could be enhanced by using a higher-grade base antenna. On the other hand, compared to GPS-only solution, the multi-GNSS results are also shown to be more precise. By weighted average combination, a further precision improvement is noticed from each u-blox initial timeseries. The next level of improvement is from the CME filtering, the CME filtered residuals show a trend of increasing precision with inclusion of multi-constellation (i.e. from GPS-only CME to multi-GNSS CME) with a compromise in data loss due to the incorporation of different GNSS. Compared to GPS SDF results, similar or better precision could be identified from multi-GNSS CME residuals up to 80% of the examined period (Table 8.11). However, GPS SDF residuals still maintain a high precision overall with low fluctuations, whereas the multi-GNSS CME residuals oscillate with a wide range of precisions over different periods which results in an overall better performance from SDF. By the weighted average combination, the precision of separate u-blox SDF results could be further enhanced. Finally, the most precise solution is obtained from the combined filter of CME and SDF.

The current study has proven that effective precision improvement is feasible by previous examined approaches (use of survey-grade base antenna, multi-GNSS, SDF, CME, high-pass filter, weighted average, etc). However, further investigation is required to assess if the low-cost solution could be optimised by including more low-cost monitoring stations. Also, the SDF was only applied for the GPS satellite constellation restricting the application. The potential use of SDF for multi-GNSS observations (Galileo, GLONASS, etc.) may enhance even further the precision by using multi-GNSS solutions and not only GPS-only solutions. Finally, a more advanced modified version of CME, potential application of spatial analysis techniques (Habboub et al., 2020), and the geometric constrain of the SBL between the two closely-spaced low-cost receivers may lead to more efficient modelling of the common-mode error (Zhang et al., 2019). In the next chapter, a SBL kinematic test is conducted. The precision of the low-cost receivers is assessed against a geodetic receiver in a dynamic setting.

Chapter 9 Short baseline kinematic test

9.1 Introduction

Following the SBL static test, a kinematic test is proposed to study the properties of measurement error and precision when the rover is in motion. It is assumed that SBL GNSS measurement error for dynamic motion might behave differently compared to static test in a way such that measurement noise could be amplified by the receiver dynamics and correlates to the amplitude of the motion. Therefore, to evaluate the SBL GNSS kinematic measurement noise, a SBL test with rover executing kinematic motion is designed. A SBL is also adopted for the kinematic test so that through the DD process, the satellite clock/orbit and receiver clock errors could be cancelled, and the atmospheric errors could be largely mitigated. The SBL configuration leaves the multipath, PCV, antenna/receiver/cable noise the major sources of error within the monitoring system with the impact from DOP. However, regarding a dynamic environment scenario, the multipath conditions vary drastically which limits its impact in solution degradation since the false solutions from multipath signals quickly fail to converge and only the direct signals result in stable solutions when the GNSS antenna is moving.

The aim of the SBL kinematic experiment is to analyse the low-cost GNSS measurement noise in monitoring the dynamic motion of different amplitude by comparing against geodetic GNSS measurement. The objectives are, 1) to evaluate the precision and determine the model frequency from both the low-cost and geodetic GNSS measurements for motions of different displacement amplitude, and 2) to assess the performance of different approaches for solution precision enhancement with the dual low-cost rover system. In the SBL test, three rovers are deployed (2*low-cost grade & 1* survey-grade) for kinematic motion tracking. The motion of the antennas is executed by a rotation device in a pre-designed pattern and the GNSS measurement noise is calculated with reference to the statistically simulated model from the pre-configured circular motion imposed by the rotation device.

9.2 Short baseline kinematic experiment

The SBL kinematic experiment was carried out from 01/2020 to 03/2020 on the roof of Nottingham Geospatial Building (NGB) to guarantee an open sky view for satellite tracking (Figure 9.1). The aim was to study the noise characteristics of the low-cost GNSS receiver when monitoring the dynamic motions of different amplitude, with reference to the dual-frequency GNSS receiver. The setup of the experiment was similar to SBL static test, with the only difference being that the experimental device executed dynamic motion where the GNSS receivers were mounted. The experiment was carried out on separated days with different base station antennas. On 28/01/2020, the geodetic AS10 antenna was used in the base and on 12/03/2020, the patch antenna was adopted. When the patch antenna was used in the base, a metal ground plane of around ~15cm diameter was used to reduce multipath. In the experiment, both base station antennas were located at NGB5 on the roof and connected to a signal splitter (GPS source RMS18), diverting the signals to two receivers (u-blox M8T and Leica GS10) via two ports (Figure 9.3).

The rover stations were mounted on the experimental device placed on NGB3 plinth on the roof creating a SBL of less than 15 metres from the base station. The experimental device was formed by two symmetrical flat metal blades, which were fixed on a rotation motor. The motor was designed to drive the blade to rotate in a circular motion at a constant frequency. On each blade, there were six screw threads with distances from the rotation centre at 5cm, 10cm, 20cm, 30cm, 40cm, and 50cm (Figure 9.2), providing different circular displacement amplitude. Two low-cost u-blox rovers were mounted on one blade: two closely-spaced patch antennas were attached on a large ground plate to guarantee multipath mitigation and fixed on the thread via a pillar. Each patch antenna was placed to guarantee the rotation radius was the same as designated with the same orientation to azimuth. The patch antennas were connected to separate u-blox receivers. Two raspberry pi3 models were also employed for the logging of respective u-blox measurements due to limited space and obstacles of cable for laptop deployment. The geodetic rover was mounted on the blade opposite to the low-cost rover regarding the rotation centre. The geodetic antenna (Leica AS10) was fixed to the thread on the blade through a pillar and connected to a Leica GS10 receiver. The patch antennas and the geodetic antenna were placed on different rotation blades with the same rotation radius symmetrically to each other during each test. Six different tests were carried out, one for each rotation radius from the rotation centre. Each test lasted about 10-15 min, and the GNSS measurements were recorded with a 10 Hz sampling frequency.

For different experiment sessions with different base antenna configuration (AS10 antenna or patch antenna), the patch antennas and geodetic antenna were both placed at the same rotation radius (50cm, 40cm, 30cm, 20cm, 10cm, 5cm) simultaneously on each side of the blade. However, due to space limitation for Leica rover in the 5cm test, only the two u-blox rovers were deployed. Therefore, for tests with rotation radii of 50cm, 40cm, 30cm, 20cm, and 10cm, observations were acquired from both u-blox receivers and Leica receiver, whereas for the 5cm rotation test, only u-blox receiver data were acquired.

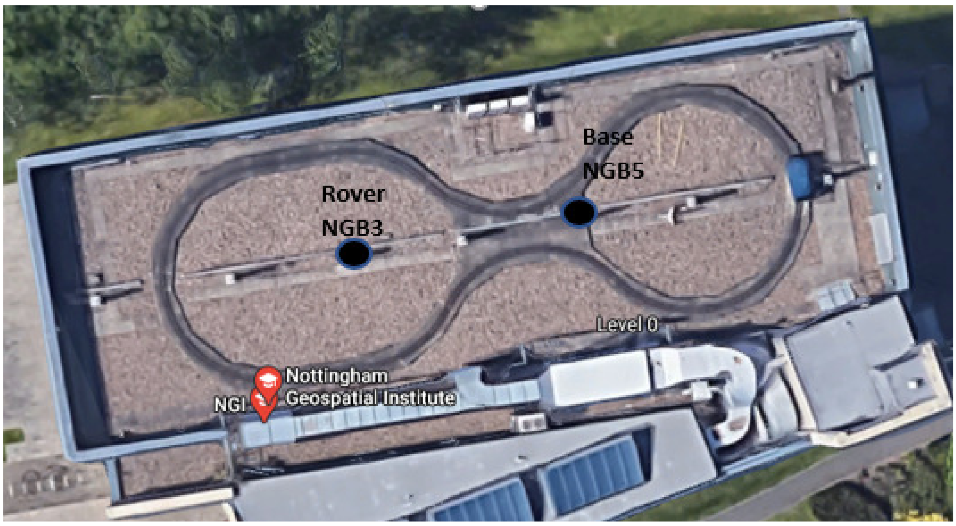

Figure 9. 1 *Plan view of the roof and the locations of Rover on NGB3 and Base on NGB5*

Figure 9. 2 *(Left) The experimental device, which consists of the two symmetrical blades with five screw threads with distances of 5cm, 10cm, 20cm, 30cm, 40cm, and 50cm on each side of the rotation centre and the motor at the base of the blades. (Right) The deployment of the rover equipment on NGB3 with 10 cm rotation radius regarding the rotation centre, on one side the two patch antennas are each connected to the u-blox M8T receiver each recording observations using Raspberry pie with a power bank for power supply.*

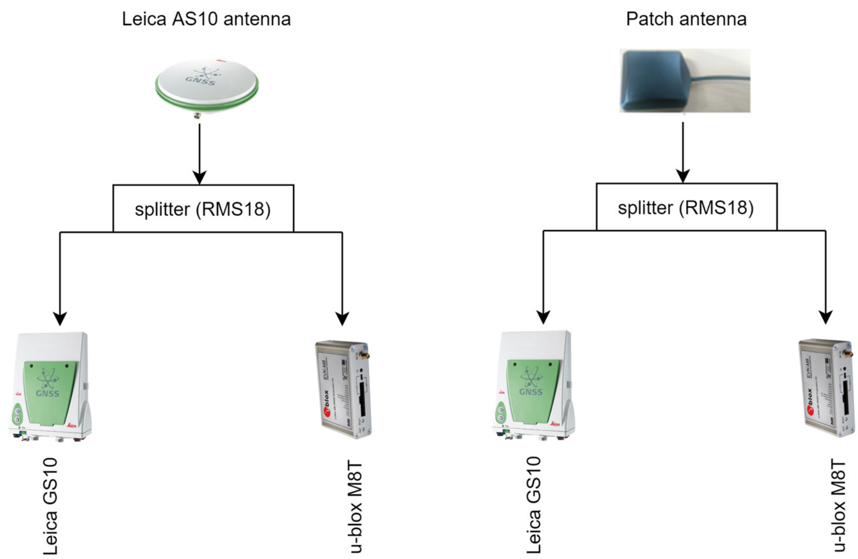

Figure 9. 3 *The layout of the base station set-up at NGB 5, with use of different base antenna on different days (with AS10 antenna as the base on 28/01/2020 and patch antenna as the base on 12/03/2020)*

9.3 GNSS data processing and methodology of timeseries analysis

The data processing was conducted in a modified version of RTKLIB 2.4.3 (demo5 b33c) customised by Everett (2020) for SBLs formed between different combinations of rover stations (2*u-blox rovers and 1*Leica rover) and base stations (Table 9.1). For each case, there were three rover stations, two low-cost rovers comprised of the same u-blox model and patch antenna, and one geodetic rover comprised of Leica GS10 and AS10. There were four different formations of the base station, 1) patch antenna & u-blox receiver, 2) patch antenna & Leica receiver, 3) geodetic antenna & u-blox receiver, 4) geodetic antenna & Leica receiver. Each rover-base formation (Case A, Case B, Case C, Case D in Table 9.1) was processed for tests with different rotation amplitude for GPS-only and GPS+Galileo solutions. For all the three rovers (2 *u-blox rovers and 1*Leica rover), the GNSS data for 50cm, 40cm,30cm, 20cm, 10cm rotation tests were processed. On the other hand, for the 5cm rotation radius, only u-blox rover data were measured and processed.

Table 9. 1 *Different cases of SBL formations with rovers (2*low-cost rover and 1*geodetic rover) and different bases*

Case	Rover		Base	
	antenna	Receiver	antenna	Receiver
A	patch patch AS10	U-blox M8T U-blox M8T Leica	AS10	u-blox
B	patch patch AS10	U-blox M8T U-blox M8T Leica	AS10	Leica
C	patch patch AS10	U-blox M8T U-blox M8T Leica	patch	u-blox
D	patch patch AS10	U-blox M8T U-blox M8T Leica	patch	Leica

Table 9. 2 *Settings configuration for RTKLIB 2.4.3 demo5 b33c for SBL dynamic test (a more detailed version could be found in Appendix C)*

Settings	***Options***
Position mode	Kinematic
Frequency/Filter type	L1/**Combined**
Elevation Mask	15
Rec Dynamics/Earth Tide Correction	**ON**/OFF
Ionosphere Correction	Broadcast
Troposphere Correction	Saastamoinen
Satellite Ephemeris/Clock	Broadcast
Constellation selection	GPS, GPS+Galileo, GPS+GLONASS, GPS+GLONASS+ Galileo
Integer Ambiguity Res	Continuous
Min Lock/Elevation to fix ambiguity	0,15
Outage to reset ambiguity/slip threshold	20,0.05
Max age of differential	1
Reject threshold of GDOP/Innov	30,1000
AR filter	ON
Min Ratio to Fix Ambiguity	3
Output	E/N/U-Baseline
Time interpolation of Base station Data	ON
Datum/Height	WGS84/Ellipsoidal
Base station position	Average of a single position
Code/Carrier phase Error Ratio L1/L2	300,300
Carrier phase error a+b/sin El (m)	0.003,0.003
Receiver Accel Horizontal/Vertical	3, 1

The GNSS observation data were processed in a modified version of RTKLIB, as the processing from original RTKLIB resulted in multiple false fixes with incorrect ambiguity resolution. For the SBL kinematic processing, settings were firstly configured based on the SBL static test. However, this resulted to several false fixes (cycle slips) in the timeseries. Therefore, several parameters were adjusted to mitigate false fixes, such as changing the 'Filter type' from 'Forward' to 'Combined' and tweaking the 'Code/Carrier phase Error Ratio L1/L2' from 100 to 300, etc. The detailed postprocessing configuration used for the SBL kinematic test was shown in Table 9.2, which are determined based on Everett (2018a).

The outputs for each SBL were obtained in E/N/U baseline solutions. Since the rovers were monitoring a circular rotation reflected by the change of baseline length periodically, the timeseries would also reflect the periodic sinusoidal pattern. The reference for this experiment was hence based on optimum circular and sinusoidal wave models constructed with the GNSS measurements which assume an idealistic circular motion from the motor. Any deviations from the circular model were considered as the measurement noise.

The procedure for timeseries analysis was shown in Figure 9.4. For E/N timeseries, the planar trajectory of the moving rover was first plotted as scatter points with N as y-axis and E as x-axis. Then the scatter points were modelled based on an optimum circular model fitted using the Pratt method with least squares (Pratt, 1987). The precision of the planar measurement was indicated by R residuals, which calculates the measurement residuals by subtracting the radius of the modelled circle from the distance of each measurement (scatter point) to the simulated rotation centre. Then, E/N/U residuals were calculated to assess the measurement precision in respective E/N/U component. For E/N residuals, an optimized sinusoidal model was simulated as the reference, the sinusoidal models were constructed based on the Easting/Northing timeseries with a moving window of 100s. For each section of the 100s period, the residuals were calculated epoch by epoch by subtracting the E/N sinusoidal models from corresponding E/N timeseries. For each experiment of different rotation amplitude (5cm, 10cm, 20cm, 30cm, 40cm, 50cm), 10 minutes (600s) timeseries was examined. The timeseries was split into six equal parts of 100s duration and a separate sinusoidal model was simulated for each time window of 100s. The sinusoidal fit model designed by Seibold (2021) was employed specifically for sine curve fitting for noisy timeseries. The parameters for modelling the sinusoidal equations were estimated by Fast Fourier transform (FFT) and nonlinear fitting where the frequency, amplitude, and phase of the largest FFT peak were used as initial values for the regression analysis. The Up component used the average of the Up timeseries as the reference since there should be no movement in the Up direction during the test. Therefore, the Up residuals only expressed measurement noise in Up direction.

Besides the precision analyses, the DFT spectral analyses were also conducted on each SBL original (R/E/N/Up) timeseries as well as the residuals (R, E/N/Up) timeseries. The impact of the base station on the precision of the GNSS timeseries was also examined in terms of base antenna grade (AS10 and patch antenna) and base receiver grade (Leica and u-blox) since different base stations were used.

Approaches for precision enhancement were also explored by taking advantage of a closely-space dual low-cost GNSS rover system. Based on SBL static test, both CME filtering and weighted average combination were proved effective in precision improvement for two closely-spaced rovers. Therefore, these two approaches were further tested in the SBL kinematic experiment. The initial timeseries of u-blox1 and u-blox3 were firstly subjected to a low-pass filter to extract the low frequency errors followed by a cross-correlation analysis. In the case of a strong correlation, the low-frequency error model was produced by averaging u-blox1 and u-blox3 low-frequency components which was then subtracted from original u-blox1, u-blox3 and the average combined timeseries of u-blox1 and u-blox3 (Figure 9.5). Another method was by applying a direct high-pass filter to the u-blox1, u-blox3, and average combined solution of u-blox1 and u-blox3 timeseries (Figure 9.6).

.

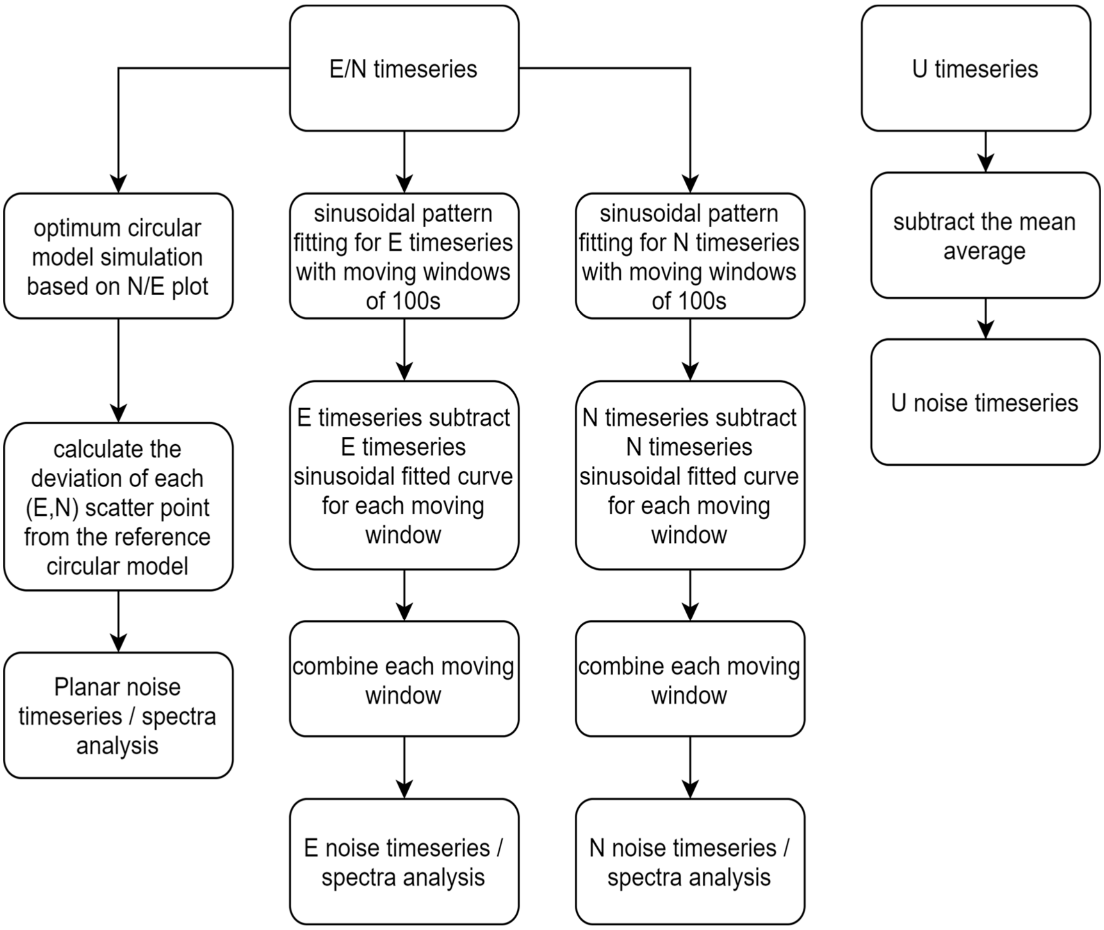

Figure 9. 4 *Flow diagram for the noise evaluation of the kinematic monitoring system*

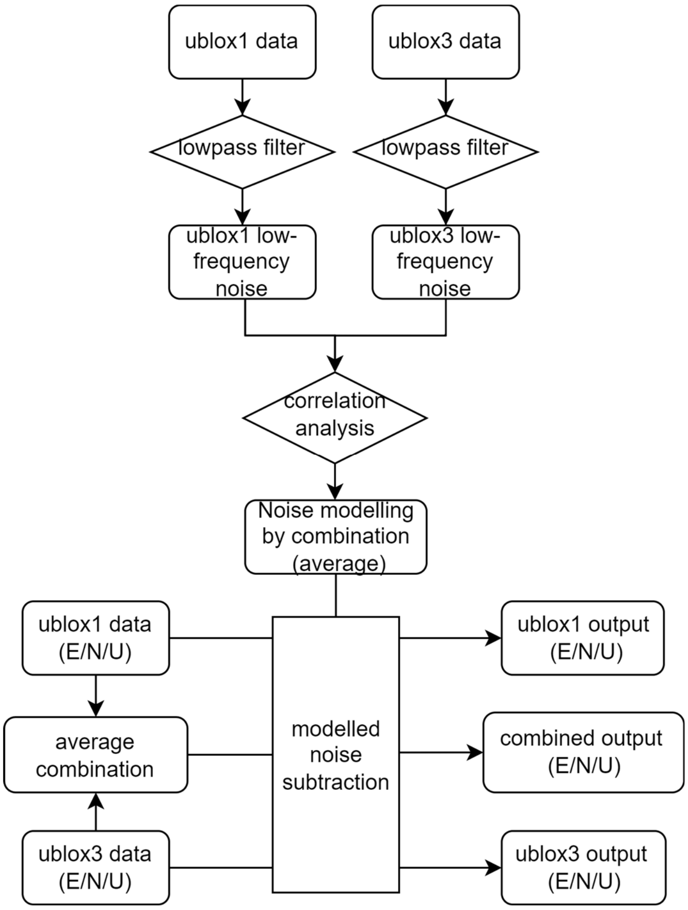

Figure 9. 5 *Flow diagram of proposed approach of precision improvement by CME filtering*

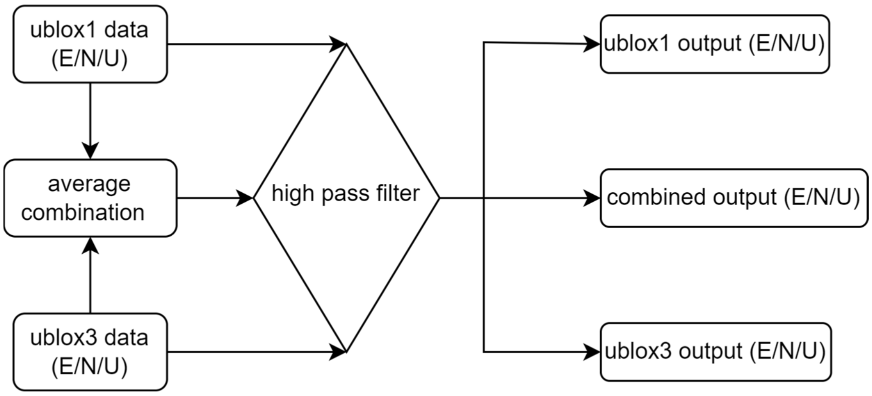

Figure 9. 6 *Flow diagram of proposed approach of precision improvement by High-pass filtering*

9.4 Short baseline kinematic results

The analyses were carried out based on Figure 9.4, the result for one case is demonstrated below as an example. The solutions used for the example analysis is GPS+Galileo solution from ~20cm rotation test when u-blox1& patch antenna is used for the rover and Leica receiver &AS10 antenna is adopted for the base. In Figure 9.7, the scatter points are firstly plotted for N/E GNSS baseline results. Then the N/E planar trajectory is simulated by fitting a circle based on the scatter points using the Pratt method (Pratt, 1987; Chernov, 2021), determining the optimum circle radius and centre coordinates (Figure 9.7). The E/N/U timeseries and DFT spectra are plotted in Figure 9.8. The y-axis of the E/N original timeseries are shifted to oscillate around zero by setting the centre of the fitted circle as the origin. For U timeseries, the average of the data is subtracted from the timeseries to examine the noise in Up direction.

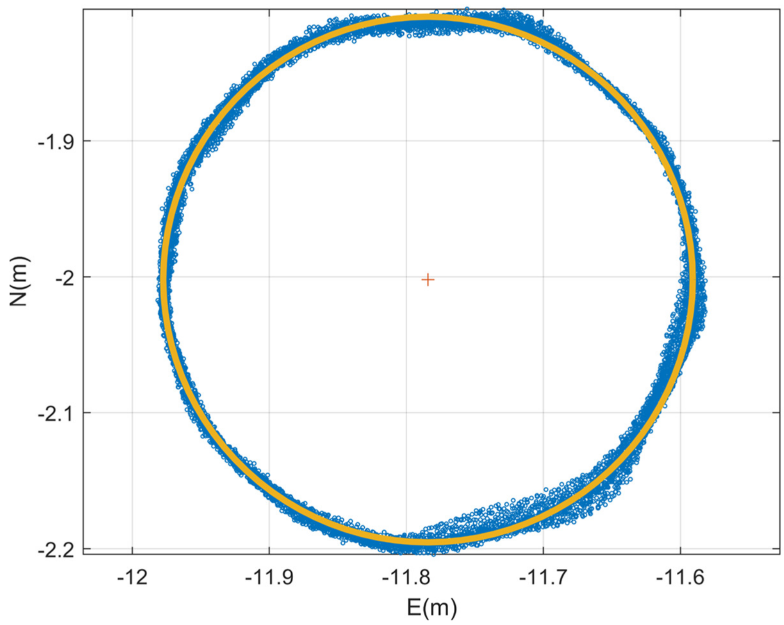

***Figure 9. 7** The scatter plot of Northings versus Eastings for G+E solutions with u-blox1 receiver & patch antenna as the rover and Leica receiver& AS10 antenna as the base with ~20cm rotation radius and the fitted circle based on Pratt method (orange) with the corresponding centre.*

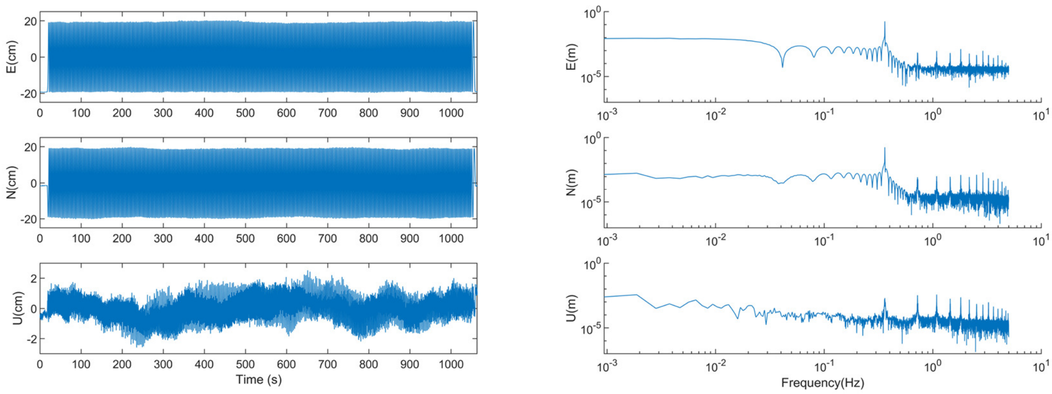

***Figure 9. 8** (Left)E/N/U timeseries after shifting near-zero value; showing oscillation motion in E/N direction, and noise in Up direction (E/N shift based on the centre of the circle, U shifts based on the average of U coordinate); (Right) Corresponding spectra based on DFT analysis*

It is shown in Figure 9.8, the E/N timeseries express periodic patterns of sinusoidal oscillations with amplitude around 20cm with measurement noise in Up timeseries. In E/N/U spectra, the first peaks for all the components appear at ~0.362 Hz, indicating the rotation frequency. However, spikes could also be identified at integer multiples of 0.362Hz, which might be due to periodical round-off error in circular movement caused by GNSS measurement quantization error (Jo et al., 2013), or a result of motor harmonics (Hannon et al., 2016). In Figure 9.8 E/N/U DFT spectra, several lower frequency aliases are also found due to higher frequency harmonics beyond Nyquist frequency mirrored at Nyquist point (Figure 9.9). The harmonic behaviour in the GNSS measurement could be caused by the rotation device as the rotation machine is usually considered a source to generate harmonics since windings embedded in slots cannot be perfect sinusoidally distributed resulting in distorted magnetomotive forces (Wakileh, 2003).

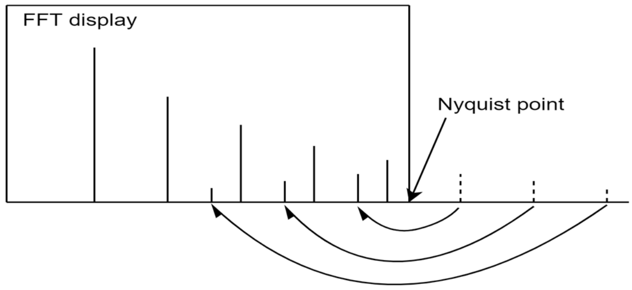

Figure 9. 9 *The behaviour of high frequency harmonics beyond Nyquist point creating aliasing problem, from 'Unfolding of Aliased Components by Increasing the Sample Rate' by LSPO (n.d.) https://storm.uni-mb.si/CoLoS/applets/aliasing/index.html). As can be seen that the higher frequency harmonics beyond Nyquist point are folded back into the FFT display causing aliasing problem, since the aliases in the FFT display are actually higher frequency components displayed at lower frequencies*

Studies have been conducted to apply a band-stop filter to attenuate any frequencies between the band specified, in this case, a band-stop filter with a lower limit of 0.20Hz and an upper limit of 0.55Hz is used. This effectively suppresses the signals with a frequency band between 0.20Hz and 0.55Hz, where it is believed to be the dominant frequency range of the circular motion, therefore after the band-stop filter, the resultant timeseries contains the noise after the dominant circular motion is largely mitigated. However, like most of the filters, for example, low-pass filters, high-pass filters, band-pass filters, etc, the band-stop filter could potentially create step response, overshoot, and ringing problems in the timeseries which would happen mostly at the beginning or end of the timeseries. In the analysis, the distorted timeseries are ignored. And a period of stable oscillation (500s-900s) is used for the spectral analysis later. Figure S9 in Appendix A shows that after removing the obvious circular motion from the Easting timeseries by a Chebyshev band-stop filter with a band-stop frequency between 0.2Hz-0.55Hz, frequencies at 0.362Hz and integer multiples of frequency could still be detected from the residuals' spectra. This indicates that occurrence of multiple higher frequency maybe not directly relates to the signal processing of the circular motion of the antenna, such as aliasing, but could be a result of the measurement noise in the horizontal component caused by rotor harmonics.

In the precision analysis of GNSS measurement, the GNSS planar precision is represented by the STD of radius residuals calculated by Equation 9.1. The timeseries and spectra of radius residuals are examined in Figure 9.10.

$$Radius\ residual = D - R$$

Equation 9. 1 *Calculation of radius residuals*

Where

- *D* represents the distance of each (E, N) coordinate to the estimated centre of the fitted model for every epoch
- *R* represents the radius of the best-fit circle.

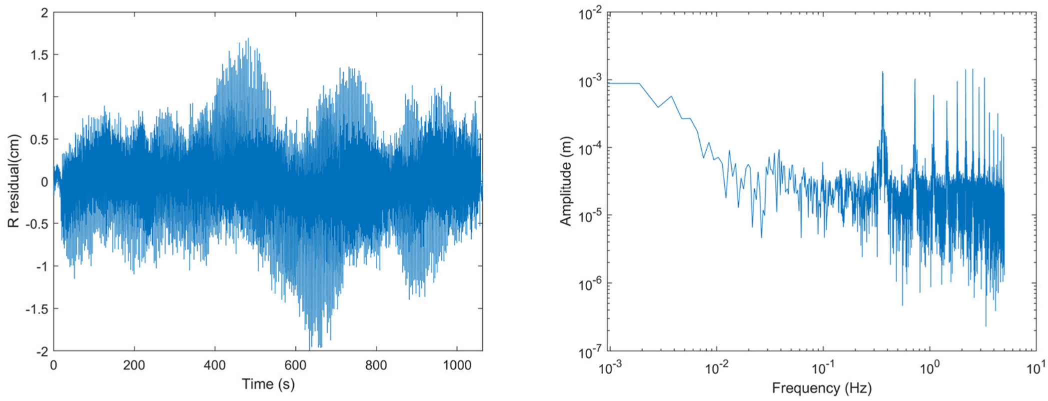

Figure 9. 10 *(Left) R residual timeseries for GPS+Galileo solution of ~20cm rotation radius test when u-blox1& patch antenna are adopted as the rover, Leica receiver & AS10 antenna as the base, (Right) corresponding DFT spectral analysis*

The measurement precisions in E/N/U components are also examined separately. Sinusoidal models are constructed for respective E/N component with a moving window of 100s and subtracted from corresponding E or N initial timeseries. For each E/N/U precision analysis, a 10-minute (600s) testing period within the oscillation is used. Therefore, the residuals from 6 sections of the 100s period are combined to obtain the E/N residuals timeseries of the examined period (Figure 9.11). The Up residuals timeseries after subtracting the mean value from the initial Up timeseries is also presented accordingly. From the E/N/U residuals' DFT spectra, it is shown that a periodic pattern with frequency ~0.350-0.360 Hz could still be identified from the residuals timeseries. Similar analyses are also carried out for tests with different amplitude of rotations, different base stations for both GPS-only and GPS+Galileo solution following the same procedure.

In summary, from the frequency analysis of the E/N initial timeseries, the motor rotation frequency can be determined considering uniform rotation frequency applied by the rotation motor in tests with different rotation radii and when different rovers are adopted (u-blox1, u-blox3, Leica). For all scenarios, dominant frequencies of around 0.361-0.362 Hz can be detected in both E/N DFT spectra which are also verified by the FFT process used in the sinusoidal curve fitting. The Up spectrum also shows a dominant frequency occurring at around 0.362Hz indicative of the rotation frequency although no displacement is expected. This could be due to practically imperfect and unfixed rotation in the horizontal plane provided by the motor, creating periodic noise by wobble and vibration in the vertical direction. From residuals' spectra, a frequency of around 0.360 Hz is shown for R residuals and a frequency range around 0.33-0.38 Hz is detected for E/N residuals. This indicates the frequency of the horizontal noise is consistent with the rotation frequency, and the horizontal noise could be rotation related.

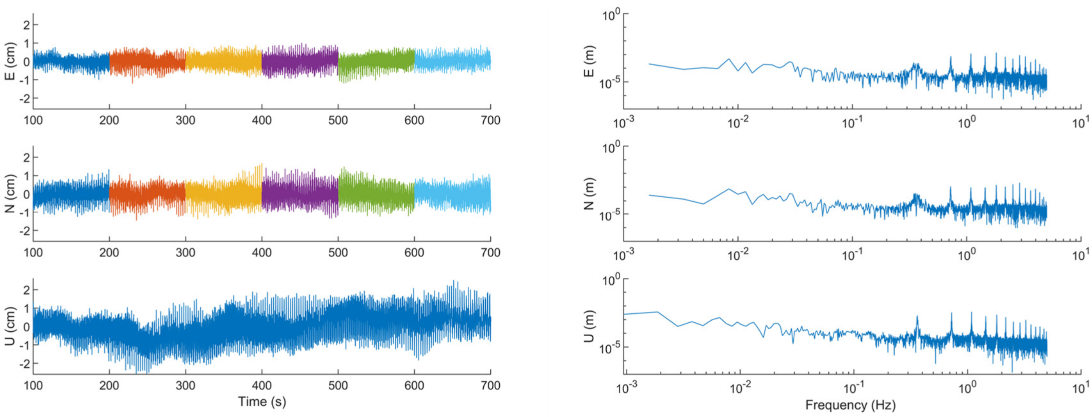

Figure 9. 11 *(Left) E/N/U residual timeseries for G+E solutions with u-blox1 receiver & patch antenna as the rover and Leica receiver& AS10 antenna as the base with ~20cm rotation radius, (Right) Corresponding DFT spectral analysis of E/N/U residuals*

9.5 Evaluation of the impact of the GNSS base station receiver grade on low-cost GNSS rover performance

From the baseline static test, it was found that the base station receiver grade has little impact on the precision of the rover stations if the antenna is the same. The impact of the GNSS base station receiver grade is also examined in the SBL kinematic test. It is compared in Figure 9.12 and Figure 9.13 the impact of base station receiver grade on Leica rover and u-blox rover results respectively when the base station uses AS10 antenna. Figure 9.14 and Figure 9.15 compares again the impact of base station receiver grade on Leica rover and u-blox rover results when base station uses patch antenna. It is shown the impact of different grades of base station receiver is limited on both u-blox and Leica rovers regardless of base station antenna, with a difference ~0.4-0.5mm for E STD, ~0.8 mm for N STD, and up to 1.2 mm for U STD. Similar conclusions are derived from tests with other amplitude of rotation for multi-GNSS solutions, illustrating the negligible impact of base station receiver grade.

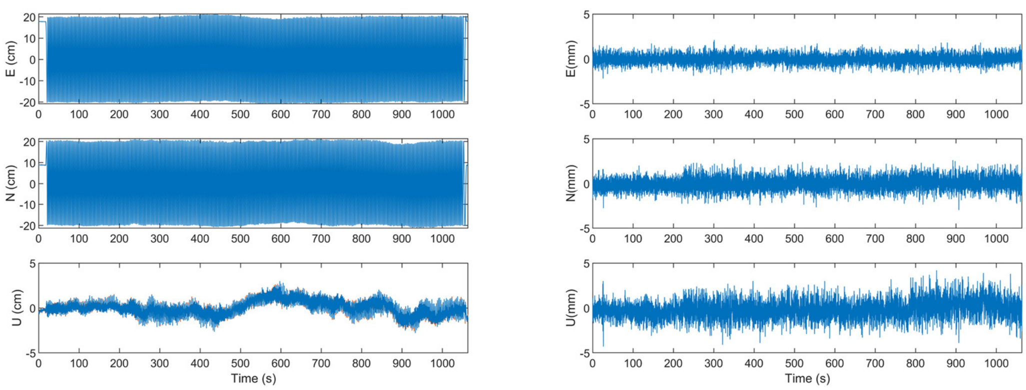

Figure 9. 12 *(Left) E/N/U timeseries of GPS-only solution for case B as the base and Leica receiver&AS10 antenna as the rover (red line) and E/N/U timeseries for case A as the base and Leica receiver&AS10 antenna as the rover (blue line). (Right) The difference between the E/N/U timeseries by adopting different base station receivers (case A vs case B)*

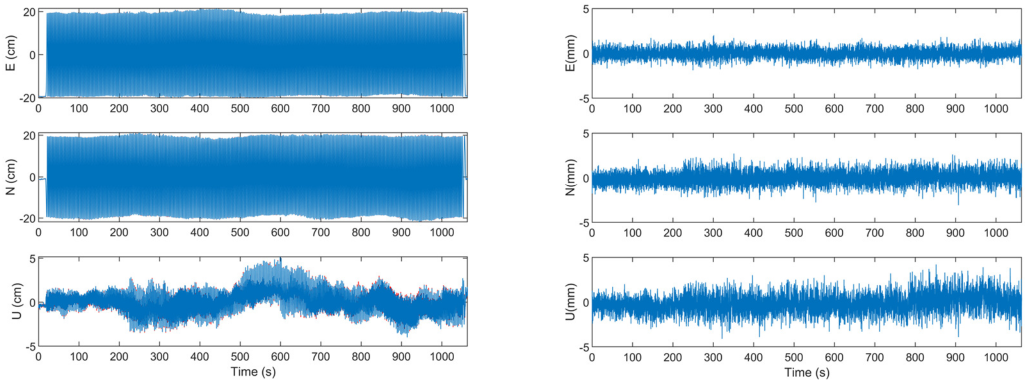

Figure 9. 13 (Left) E/N/U timeseries of GPS-only solution for case B as the base and u-blox1 receiver & patch antenna as the rover (red line) and E/N/U timeseries for case A as the base and u-blox1 receiver & patch antenna as the rover (blue line). (Right) The difference between the E/N/U timeseries by adopting different base station receivers (case A vs case B)

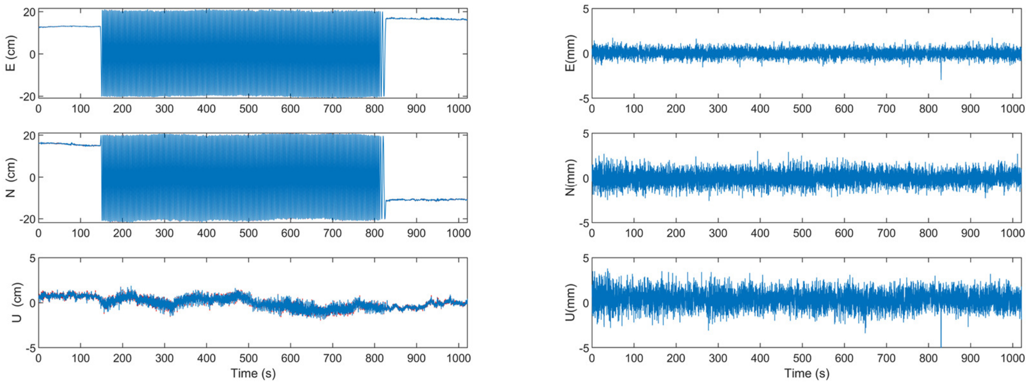

Figure 9. 14 *(Left) E/N/U timeseries of GPS-only solution for case D as the base and Leica receiver- AS10 antenna as the rover (red line) and E/N/U timeseries for case C as the base and Leica receiver- AS10 antenna as the rover (blue line). (Right) The difference between the E/N/U timeseries by adopting different base station receivers (case C vs case D)*

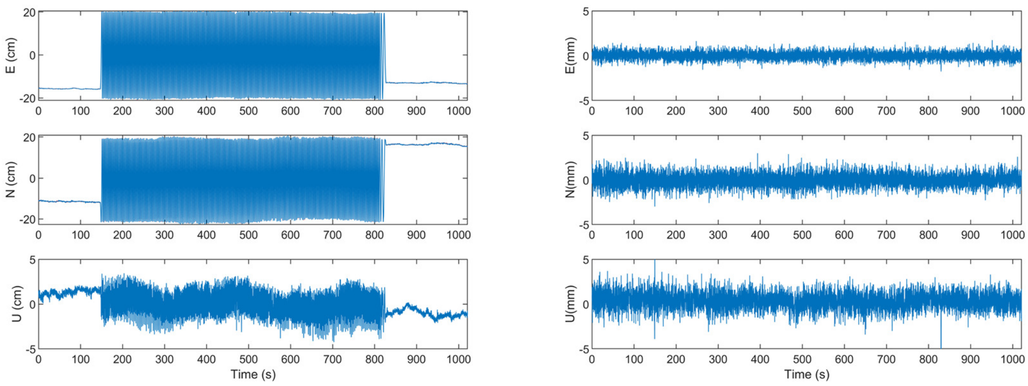

Figure 9. 15 *(Left) E/N/U timeseries of GPS-only solution for case D as the base and u-blox1 receiver & patch antenna as the rover (red line) and E/N/U timeseries for case C as the base and u-blox1 receiver & patch antenna as rover (blue line). (Right) The difference between the E/N/U timeseries by adopting different base station receivers (case C vs case D)*

9.6 Evaluation of the impact of the GNSS constellation on low-cost GNSS rover performance

In 9.4, sample results are illustrated for GPS+Galileo solution of 20cm rotation radius by adopting u-blox rover and Leica base. Similar analyses are also applied to other cases with different rotation amplitude, different constellations, and different base station formations. The Radius/E/N/U residuals' precisions and the corresponding dominant frequencies from initial and residuals' timeseries are derived. Table 9.3, Table 9.4, and Table 9.5 present the radius of the fitted circle and the STD of the radius residual for Leica and two u-blox rovers when Leica AS10 is used in the base. Similarly, Table 9.6, Table 9.7 and Table 9.8 show the Leica and the two u-blox results respectively when the patch antenna is used in the base. In Table 9.3-9.8, both GPS and GPS+Galileo solutions are presented with different rotation amplitude.

Table 9. 3 *Radius of the modelled circle and STD of radius residuals for various rotation amplitude based on GPS and GPS+Galileo solution with Leica as rover receiver and for different base station receiver grade (Base antenna: AS10). The table is generated based on a period of 10 min within the rotation experiment*

Unit (mm)	Leica rover_u-blox base				Leica rover_Leica base			
	GPS		GPS+Galileo		GPS		GPS+Galileo	
Rotation Radius	R	STD Residual	R	STD Residual	R	STD Residual	R	STD Residual
100	104.7	2.9	103.8	2.5	104.7	2.9	103.9	2.5
200	200.3	5.2	200.0	3.0	200.3	5.2	199.9	2.8
300	301.0	2.6	300.6	2.1	301.1	2.6	300.6	2.1
400	401.2	2.7	401.1	2.1	401.2	2.7	401.1	2.0
500	504.7	3.8	504.5	2.5	504.7	3.7	504.5	2.5

Table 9. 4 *Radius of the modelled circle and STD of radius residuals for various rotation amplitude based on GPS and GPS+Galileo solution with u-blox1 as rover receiver and for different base station receiver grade (Base antenna: AS10). The table is generated based on a period of 10 min within the rotation experiment*

Unit (mm)	U-blox1 rover_u-blox base				U-blox1 rover_Leica base			
	GPS		GPS+Galileo		GPS		GPS+Galileo	
Rotation Radius	R	STD Residual	R	STD Residual	R	STD Residual	R	STD Residual
50	47.6	4.8	47.6	4.4	47.6	4.8	47.6	4.4
100	103.3	7.5	101.2	5.8	103.3	7.5	101.2	5.8
200	193.7	8.1	193.2	4.4	193.7	8.0	193.2	4.4
300	307.2	4.3	307.0	3.3	307.2	4.3	307.0	3.3
400	401.7	3.8	401.6	3.2	401.6	3.8	401.6	3.1
500	501.6	6.7	501.4	4.3	501.6	6.7	501.4	4.3

Table 9. 5 *Radius of the modelled circle and STD of radius residuals for various rotation amplitude based on GPS and GPS+Galileo solution with u-blox3 as rover receiver and for different base station receiver grade (Base antenna: AS10). The table is generated based on a period of 10 min within the rotation experiment*

Unit (mm)	U-blox3 rover_u-blox base				U-blox3 rover_Leica base			
	GPS		GPS+Galileo		GPS		GPS+Galileo	
Rotation Radius	R	STD Residual	R	STD Residual	R	STD Residual	R	STD Residual
50	47.7	6.3	46.7	5.4	47.7	6.3	46.6	5.4
100	102.0	10.9	97.0	7.1	102.0	10.8	97.0	7.1
200	190.1	7.5	191.2	4.8	190.1	7.5	191.2	4.8
300	294.1	4.8	294.2	4.3	294.1	4.8	294.2	4.3
400	397.0	4.0	397.3	3.8	397.0	4.0	397.3	3.8
500	500.0	7.5	499.4	4.3	500.0	7.5	499.4	4.3

Firstly, it is observed from all the cases that the base station receiver grade (i.e., Leica or u-blox receiver) has a minimal impact on the precision of the GNSS rover receiver. A precision improvement (even up to 3.8 mm) could be seen by incorporating Galileo to the GPS (Table 9.5 with 100mm rotation radius case). Comparing the radius precision for different rotation radius for both GPS and GPS+Galileo solution, a larger STD variation in GPS solution is observed than GPS+Galileo solution, indicating the robustness of GPS+Galileo solution for different rotation amplitude. It is observed in Table 9.3, the radius precision of Leica GPS solution for 20cm rotation radius is significantly larger than the rest of the rotation radii. Nevertheless, the precision is improved with GPS+Galileo solution leading to a less significant difference compared to other rotation amplitude. A similar improvement for u-blox results is also observed by adding Galileo constellation when the rotation radius is ~ 20cm and ~50cm. This indicates a possible weaker GPS geometry for ~20 cm and ~50cm rotation test, which is however resolved by the contribution of Galileo constellation leading to a precision similar to other rotation amplitude. Furthermore, from Table 9.3, 9.4, and 9.5, it is derived that higher precisions are normally achieved with Leica than u-blox rovers, regardless of the rotation amplitude or different constellations used (GPS or GPS+Galileo). More specifically, the radius precision of Leica and u-blox GPS+Galileo solution is ~2-3mm and ~3-5.5mm respectively, when AS10 antenna is used in the base.

Table 9. 6 *Radius of the modelled circle and STD of radius residuals for various rotation amplitude based on GPS and GPS+Galileo solution with Leica as rover receiver and for different base station receiver grade (Base antenna: patch). The table is generated based on a period of 10 min within the rotation experiment*

Unit (mm)	Leica rover_u-blox base				Leica rover_Leica base			
	GPS		GPS+Galileo		GPS		GPS+Galileo	
Rotation Radius	R	STD Residual	R	STD Residual	R	STD Residual	R	STD Residual
100	105.5	4.9	104.8	2.8	105.5	4.9	104.8	2.8
200	202.8	4.0	202.8	3.3	202.8	4.0	202.8	3.2
300	305.5	4.0	305.5	3.2	305.4	4.0	305.4	2.9
400	405.1	3.6	404.5	2.9	405.1	3.6	404.5	2.9
500	509.3	4.0	509.3	3.2	509.3	4.0	509.3	3.1

Table 9. 7 *Radius of the modelled circle and STD of radius residuals for various rotation amplitude based on GPS and GPS+Galileo solution with u-blox1 as rover receiver and for different base station receiver grade (Base antenna: patch). The table is generated based on a period of 10 min within the rotation experiment*

Unit (mm)	U-blox1 rover_u-blox base				U-blox1 rover_Leica base			
	GPS		GPS+Galileo		GPS		GPS+Galileo	
Rotation Radius	R	STD Residual	R	STD Residual	R	STD Residual	R	STD Residual
50	51.9	5.1	51.3	5.1	51.9	5.1	51.2	5.1
100	103.7	12.5	102.6	7.6	103.6	12.5	102.6	7.6
200	202.2	7.6	202.2	6.9	202.2	7.6	202.2	6.9
300	304.8	6.8	302.4	4.5	304.9	6.8	302.4	4.5
400	405.6	4.8	404.6	4.3	405.6	4.9	404.6	4.2
500	502.3	4.7	501.8	4.3	502.3	4.6	501.8	4.3

Table 9. 8 *Radius of the modelled circle and STD of radius residuals for various rotation amplitude based on GPS and GPS+Galileo solution with u-blox3 as rover receiver and for different base station receiver grade (Base antenna: patch). The table is generated based on a period of 10 min within the rotation experiment*

Unit (mm)	U-blox3 rover_u-blox base				U-blox3 rover_Leica base			
	GPS		GPS+Galileo		GPS		GPS+Galileo	
Rotation Radius	R	STD Residual	R	STD Residual	R	STD Residual	R	STD Residual
50	57.1	5.1	58.5	4.6	57.2	5.1	58.5	4.6
100	106.8	10.6	101.9	6.2	106.7	10.7	101.8	6.2
200	202.8	10.4	199.4	7.4	202.7	10.4	199.3	7.4
300	299.7	6.9	300.4	5.5	299.8	6.9	300.1	4.9
400	400.1	5.6	400.6	4.9	400.2	5.6	400.6	4.9
500	497.5	4.9	498.1	3.9	497.5	4.9	498.1	3.9

Compared to the conclusions when the geodetic antenna is used in the base, similar observations can be made for both GPS and GPS+Galileo solutions when the patch antenna is used in the base, regarding 1) the impact of base station receiver grade, 2) comparison between GPS and GPS+Galileo solution, 3) precision comparison between Leica and u-blox rover (Table 9.6-9.8). It is also noticed that for cases when both u-blox rovers (u-blox1 and u-blox3) are adopted with either Leica AS10 or patch antenna in the base, the STD is comparatively larger for the tests of ~10cm rotation radius than any other radii for both GPS-only and GPS+Galileo solutions (Table 9.4, Table 9.5, Table 9.7, Table 9.8). This is probably due to the interference caused by the AS10 antenna that is mounted at a higher elevation and placed relatively close to the patch antennas, which consequently causes a shadowing effect on the signal transmitted to the patch antennas. The radius precisions of Leica and u-blox GPS+Galileo solutions are ~3mm and ~4-7.5mm respectively when the patch antenna is used in the base (Table 9.6, Table 9.7, Table 9.8). By comparing with the results when AS10 antenna is used in the base, it is shown that in general, higher precision solutions could be derived with the geodetic base antenna (Leica AS10).

Table 9. 9 *E/N/U residuals STD of various rotation amplitude based on GPS and GPS+Galileo solution with Leica, u-blox1, u-blox3 rover, and different base station receiver grade (Base antenna: AS10). The table is generated based on a period of 10 min within the rotation experiment*

R (mm)	Leica						U-blox1						U-blox3					
	G			G+E			G			G+E			G			G+E		
	E	N	U	E	N	U	E	N	U	E	N	U	E	N	U	E	N	U
50							**2.4**	**4.4**	**6.0**	**2.1**	**4.0**	**5.7**	**4.9**	**6.8**	**7.8**	**3.4**	**5.8**	**8.1**
100	**1.8**	**3.4**	**3.4**	**1.3**	**2.5**	**2.5**	**4.6**	**9.4**	**12.2**	**3.7**	**7.0**	**11.0**	**4.9**	**13.0**	**14.4**	**3.7**	**9.1**	**9.0**
200	**3.1**	**4.4**	**4.3**	**1.7**	**2.7**	**2.4**	**5.4**	**7.3**	**9.3**	**3.2**	**4.4**	**6.5**	**4.6**	**7.5**	**10.2**	**3.1**	**4.8**	**6.6**
300	**2.2**	**2.8**	**4.0**	**1.8**	**2.2**	**3.4**	**3.1**	**4.8**	**6.4**	**2.4**	**4.0**	**4.7**	**3.2**	**4.6**	**4.9**	**2.8**	**4.6**	**4.7**
400	**2.2**	**3.1**	**3.8**	**1.8**	**2.5**	**3.1**	**2.8**	**4.2**	**6.9**	**2.5**	**3.3**	**5.5**	**2.7**	**4.7**	**6.8**	**2.4**	**4.4**	**4.7**
500	**2.8**	**4.3**	**5.3**	**2.5**	**2.9**	**3.0**	**4.3**	**9.3**	**19.1**	**3.3**	**4.6**	**7.9**	**3.6**	**9.3**	**12.3**	**2.9**	**4.6**	**6.3**

Table 9. 10 *E/N/U residuals STD of various rotation amplitude based on GPS and GPS+Galileo solution with Leica, u-blox1, u-blox3 rover, and different base station receiver grade (Base antenna: patch). The table is generated based on a period of 10 min within the rotation experiment*

R (mm)	Leica						U-blox1						U-blox3					
	G			G+E			G			G+E			G			G+E		
	E	N	U	E	N	U	E	N	U	E	N	U	E	N	U	E	N	U
50							**2.6**	**5.8**	**12.7**	**2.9**	**5.5**	**9.7**	**2.6**	**4.9**	**10.2**	**2.6**	**4.9**	**8.9**
100	**2.2**	**4.6**	**3.7**	**1.9**	**2.3**	**2.3**	**6.3**	**13.5**	**12.7**	**4.7**	**7.9**	**9.9**	**3.7**	**11.1**	**10.7**	**3.0**	**7.4**	**9.6**
200	**2.6**	**4.1**	**3.2**	**2.4**	**3.5**	**2.3**	**4.1**	**7.6**	**11.2**	**3.6**	**7.1**	**9.0**	**5.5**	**10.1**	**16.2**	**4.1**	**8.2**	**12**
300	**2.6**	**3.9**	**3.4**	**2.2**	**2.9**	**2.1**	**4.0**	**6.4**	**9.7**	**2.8**	**4.8**	**6.1**	**3.8**	**6.9**	**8.2**	**3.2**	**4.8**	**5.3**
400	**2.6**	**3.0**	**2.8**	**2.4**	**2.4**	**2.3**	**3.7**	**4.8**	**5.9**	**3.3**	**4.9**	**4.8**	**3.6**	**5.7**	**6.4**	**3.1**	**5.7**	**5.9**
500	**3.2**	**3.7**	**3.1**	**3.0**	**3.2**	**2.5**	**4.3**	**6.4**	**6.3**	**3.8**	**6.3**	**5.9**	**3.7**	**5.3**	**6.8**	**3.2**	**5.0**	**4.4**

Table 9.9 and 9.10 present the STDs of GPS-only and GPS+Galileo residuals for each E/N/U component for different rotation amplitude. Figure 9.16 and Figure 9.17 are plotted respectively to compare the E/N residuals STD between the u-blox and Leica rover based on different rotation amplitude GPS and GPS+Galileo solutions. It is shown again a better precision could be achieved with the Leica rover as compared to u-blox rovers for both GPS and GPS+Galileo solutions. It is also noted that a better precision could be obtained with GPS+Galileo than GPS-only.

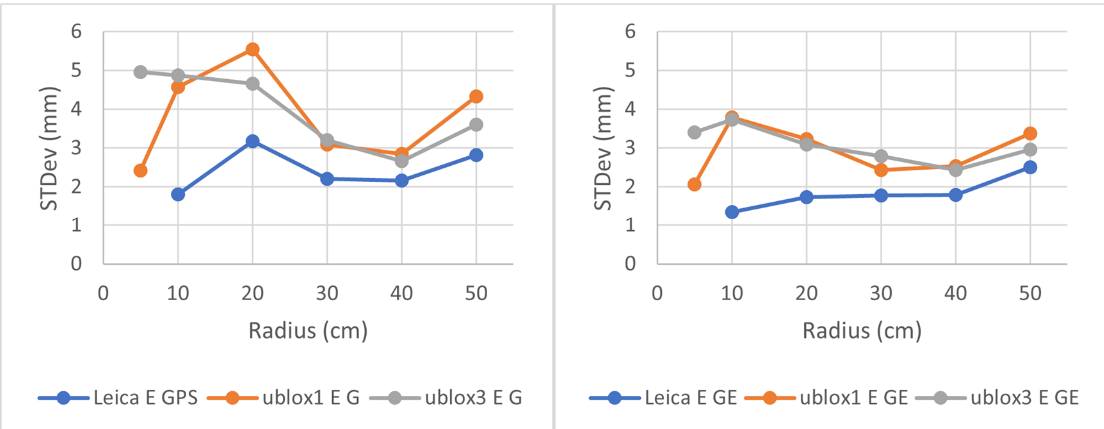

Figure 9. 16 *E residual STD for different rover stations (Leica, u-blox1, and u-blox3) when the base station adopts Leica receiver with AS10 antenna for different rotation amplitude; (Left) GPS-only solution and (Right) GPS+Galileo solution (STD calculated based on 10 min oscillation period)*

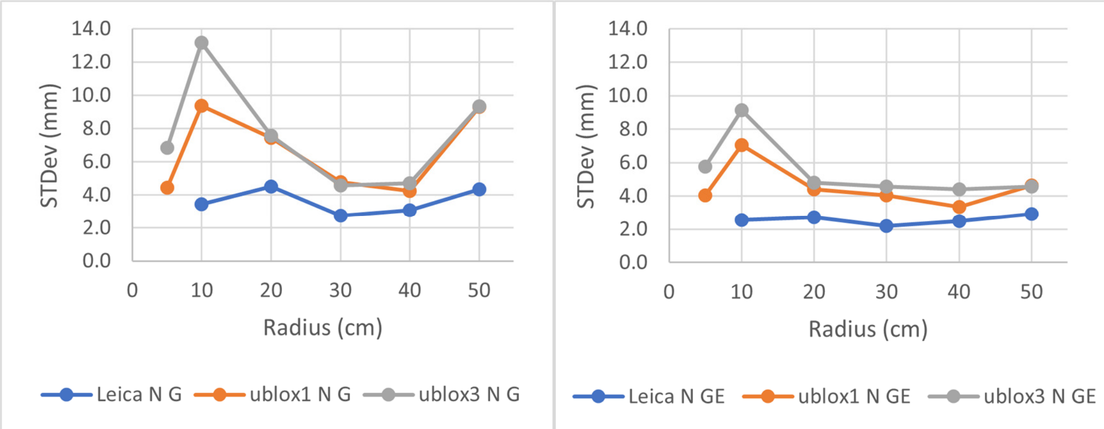

Figure 9. 17 *N residual STDs for different rover stations (Leica, u-blox1, and u-blox3) when the base stations adopt Leica receiver with AS10 antenna for different rotation amplitude; (Left) GPS-only solution and (Right) GPS+Galileo solution (STD calculated based on 10 min oscillation period)*

9.7 Evaluation of the impact of the base station antenna grade on low-cost GNSS rover performance

Figure 9.18, Figure 9.19, Figure 9.20 are plotted based on Table 9.9 and Table 9.10 to illustrate the impact of different grades of base station antenna on E/N precisions, with rover stations consisted of Leica, u-blox1, and u-blox3 respectively. It can be derived that the Northings residual is worse than Eastings residual precision, and regardless of rover stations used, the results adopting AS10 base antenna are generally better than that with patch base antenna.

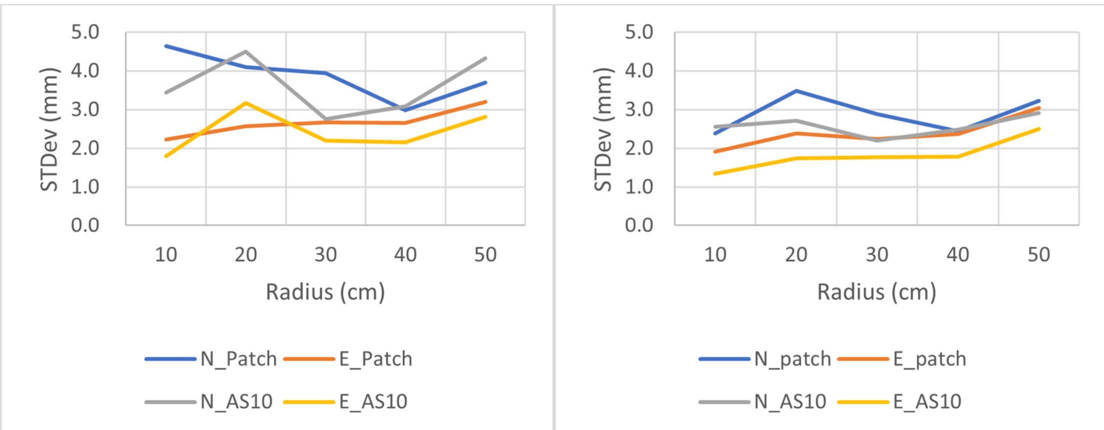

Figure 9. 18 *E/N residuals STD when the rover station adopts Leica receiver& Leica AS10 antenna and base station adopts Leica receiver & patch antenna or Leica receiver & AS10 antenna, (Left) GPS-only solution, (Right) GPS+Galileo solution, E_Patch, N_patch stand for the Easting, Northing residual with patch antenna as base antenna respectively, E_AS10, N_AS10 stand for the Easting, Northing residual with Leica AS10 antenna as base antenna respectively. The STDs are all calculated based on a 10 min-oscillation period.*

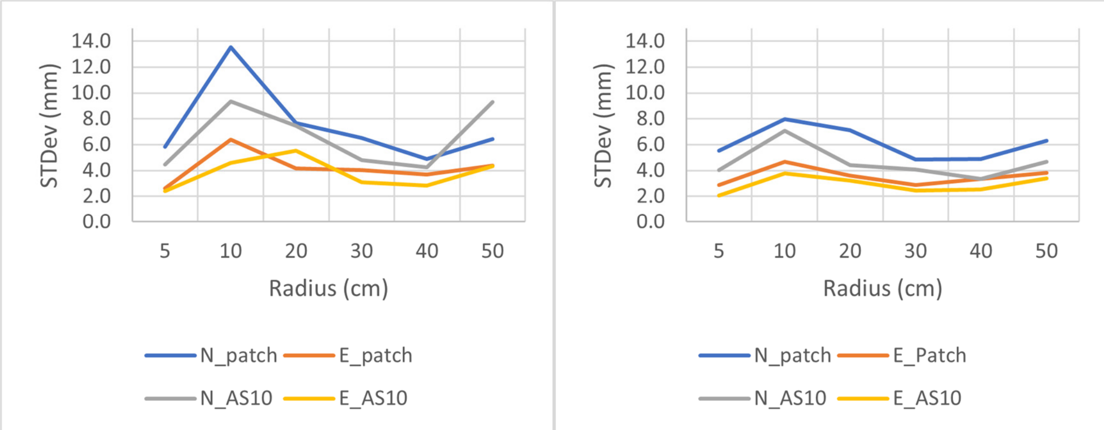

Figure 9. 19 *E/N residuals STD when the rover station adopts u-blox1 receiver& patch antenna and base station adopts Leica receiver & patch antenna or Leica receiver & AS10 antenna, (Left) GPS-only solution (Right) GPS+Galileo solution, E_Patch, N_patch stand for the Easting, Northing residual with patch antenna as base antenna respectively, E_AS10, N_AS10 stand for the Easting, Northing residual with Leica AS10 antenna as base antenna respectively. The STDs are all calculated based on a 10 min-oscillation period*

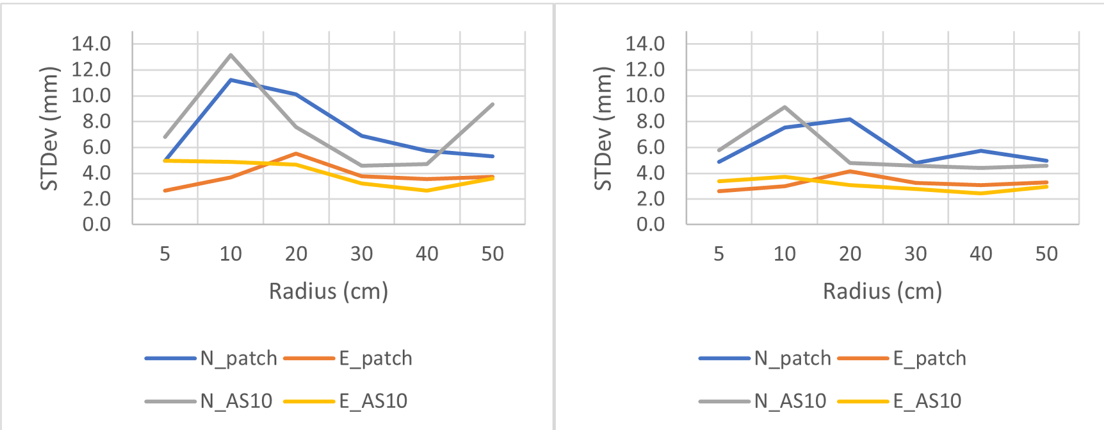

Figure 9. 20 *E/N residuals STD when the rover station adopts u-blox3 receiver& patch antenna and base station adopts Leica receiver & patch antenna or Leica receiver & AS10 antenna, (Left) GPS-only solution (Right) GPS+Galileo solution, E_Patch, N_patch stand for the Easting, Northing residual with patch antenna as base antenna respectively, E_AS10, N_AS10 stand for the Easting, Northing residual with Leica AS10 antenna as base antenna respectively, The STDs are all calculated based on a 10 min-oscillation period.*

Similarly, the impact of different base antenna grades is also examined based on the STD of R residuals (Figure 9.21). It could be seen that for both GPS-only and GPS+Galileo constellations, the precision derived from results using AS10 base antenna is normally better than when patch base antenna is adopted. On the other hand, a significant precision improvement could also be detected by including Galileo to the GPS, especially when the patch antenna base is adopted. In summary, the findings indicate the importance of using a high-grade base antenna in Easting, Northing, and horizontal precision improvement.

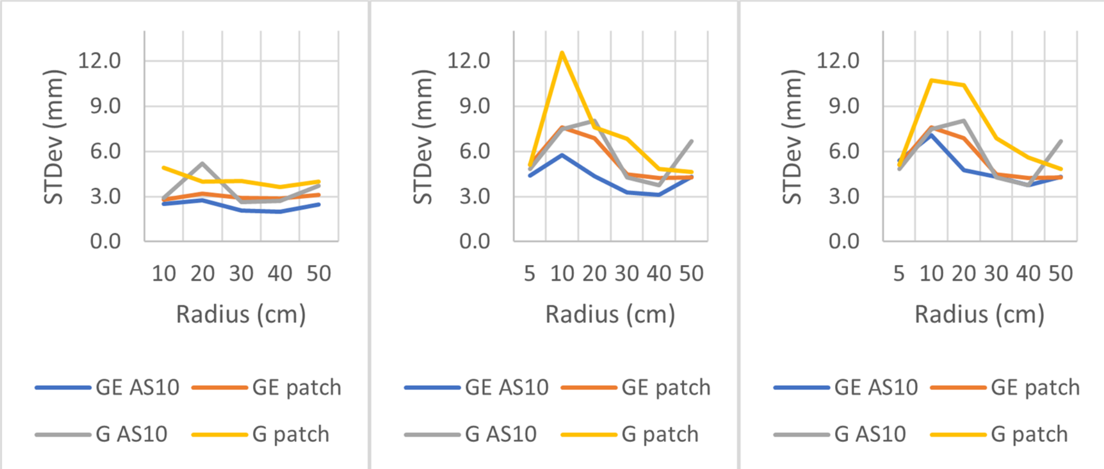

***Figure 9. 21** Radius residual comparison between different base station antenna (AS10 or patch) and between different constellation (G: GPS-only and GE: GPS+Galileo) for different rover stations; (Left) Leica rover, (Middle) u-blox1, and (Right)u-blox3*

9.8 Precision improvement by combined analysis of the two low-cost receivers' measurement

For the precision improvement of low-cost monitoring solutions, three different methodologies were proposed and tested: 1) average combination of the original timeseries, 2) CME filter, and 3) High-pass filter. By adopting each method or a combination between them, the precisions obtained from several different approaches were evaluated and compared. In the analysis, the precisions were derived for the following results: 1) original separate and average combined low-cost timeseries, 2) CME filtered separate and average combined low-cost timeseries, 3) High-pass filtered separate and average combined low-cost timeseries, 4) Original geodetic timeseries, 5) High-pass filtered geodetic timeseries.

9.8.1 Average combination of the original timeseries

The precision improvement is firstly assessed by average combination of u-blox1 and u-blox3 original timeseries. The results from Leica AS10 base antenna and patch base antenna are presented in Table 9.11, Table 9.12 correspondingly. In both tables, the E/N/U precisions are produced for two separate u-blox, Leica, and average-combined results for different rotation amplitude considering GPS and GPS+Galileo solutions. It can be observed that the precisions derived from both u-blox receivers are comparable indicating the general consistency and validity of the two low-cost results, especially for GPS+Galileo solution. By average combination, a general precision improvement is identified compared to separate u-blox solution. However, in cases where a larger precision deviation is detected between the u-blox solutions, the average combined approach is less effective.

***Table 9. 11** E/N/U residuals STD (mm) derived from i) separate u-blox1 and u-blox3 original timeseries ii) the average-combined solution between u-blox1 and u-blox3 original results iii) Leica original results, for different rotation radius, different constellation (GPS-only & GPS+Galileo) having Leica AS10 as the base antenna.*

	R	GPS-only				GPS+Galileo			
	(cm)	U-blox1	U-blox3	combined	Leica	U-blox1	U-blox3	combined	Leica
E	5	2.4	4.7	2.9		2.1	3.4	2.2	
	10	4.9	4.8	3.4	1.9	4.3	3.7	2.4	1.6
	20	5.5	4.7	4.0	3.2	3.2	3.2	2.5	1.9
	30	3.1	3.3	2.4	2.3	2.4	2.8	2.1	1.8
	40	2.9	2.9	2.3	2.4	2.7	2.7	2.1	2.0
	50	4.1	3.5	3.0	2.8	3.2	2.9	2.5	2.5
N	5	4.5	6.7	4.4		4.1	5.8	3.8	
	10	6.1	11.5	5.8	3.5	6.4	7.7	4.7	2.8
	20	7.8	7.8	5.7	4.8	4.8	4.6	3.6	2.8
	30	5.0	4.7	3.5	2.9	4.3	4.5	3.0	2.4
	40	4.3	4.9	3.7	3.2	3.7	4.7	3.4	2.7
	50	8.1	8.0	6.6	4.0	4.3	4.3	3.3	2.8
U	5	6.4	8.3	4.8		6.5	8.6	4.5	
	10	11.1	17.1	10.4	3.7	10.4	10.0	7.3	2.7
	20	12.7	14.0	10.2	8.4	8.1	7.7	5.4	3.1
	30	6.8	5.5	5.0	4.9	5.0	5.6	4.1	4.1
	40	8.1	8.7	6.6	5.4	6.8	6.2	5.5	4.3
	50	18.6	13.0	13.8	7.1	9.0	7.0	6.5	4.7

***Table 9. 12** E/N/U residuals STD (mm) derived from i) separate u-blox1 and u-blox3 original timeseries ii) the average-combined solution between u-blox1 and u-blox3 original results iii) Leica original results, for different rotation radius, different constellation (GPS-only & GPS+Galileo) having patch as the base antenna.*

	Radius	GPS-only				GPS+Galileo			
	(cm)	U-blox1	U-blox3	combined	Leica	U-blox1	U-blox3	combined	Leica
E	5	2.7	2.8	2.1		2.8	2.7	2.3	
	10	6.3	3.4	3.7	2.2	4.5	2.9	2.8	1.8
	20	4.0	4.2	2.7	2.2	3.5	3.3	2.7	2.6
	30	4.3	4.1	3.1	2.1	2.9	3.3	2.5	1.8
	40	3.7	3.6	2.9	2.7	3.4	3.2	2.9	2.4
	50	4.6	3.8	3.4	3.2	3.9	3.3	3.1	3.0
N	5	5.8	4.8	4.5		5.3	5.0	4.7	
	10	13.7	10.8	9.6	4.7	7.8	6.7	5.5	2.4
	20	8.7	9.5	7.0	3.5	7.8	8.7	6.2	3.1
	30	6.2	6.4	5.4	3.4	5.0	4.8	3.6	2.4
	40	5.0	5.6	4.4	3.0	5.0	5.6	4.7	2.5
	50	6.4	5.3	5.2	3.7	6.2	5.0	5.2	3.2
U	5	14.2	14.5	10.9		11.3	11.5	8.7	
	10	14.0	12.5	9.7	6.0	11.1	10.5	7.6	4.0
	20	12.8	19.8	14.0	4.1	9.2	13.2	9.3	3.1
	30	12.4	10.9	9.2	6.1	7.8	6.5	5.4	3.8
	40	7.3	7.4	5.6	5.7	5.7	6.8	4.4	4.7
	50	7.2	7.1	6.0	4.6	7.2	6.1	5.5	5.2

9.8.2 CME filter

Further precision improvement of the low-cost GNSS timeseries is evaluated by CME filtering. Firstly, the E/N/Up original timeseries of two u-blox receivers are filtered by applying an 8th order Chebyshev low-pass filter, with passband frequency of 0.1Hz and passband ripple of 1dB. The output of the low-pass filter is plotted for both u-blox1 and u-blox3 representing the low-frequency noise component of the E/N/U GNSS timeseries (Figure 9.22). It is shown that the low-pass filtered long period noise is suppressed in both Eastings and Northings compared to Up components, suggesting reduced multipath's impact in horizontal plane than in vertical axis due to rovers' planar rotation. Both outputs from u-blox1 and u-blox3 are subjected to correlation analysis to determine the correlation coefficient. It is shown in Table 9.13 the correlation coefficients between u-blox1 and u-blox3 low-pass filtered timeseries for both GPS and GPS+Galileo solutions when different base antennas are used.

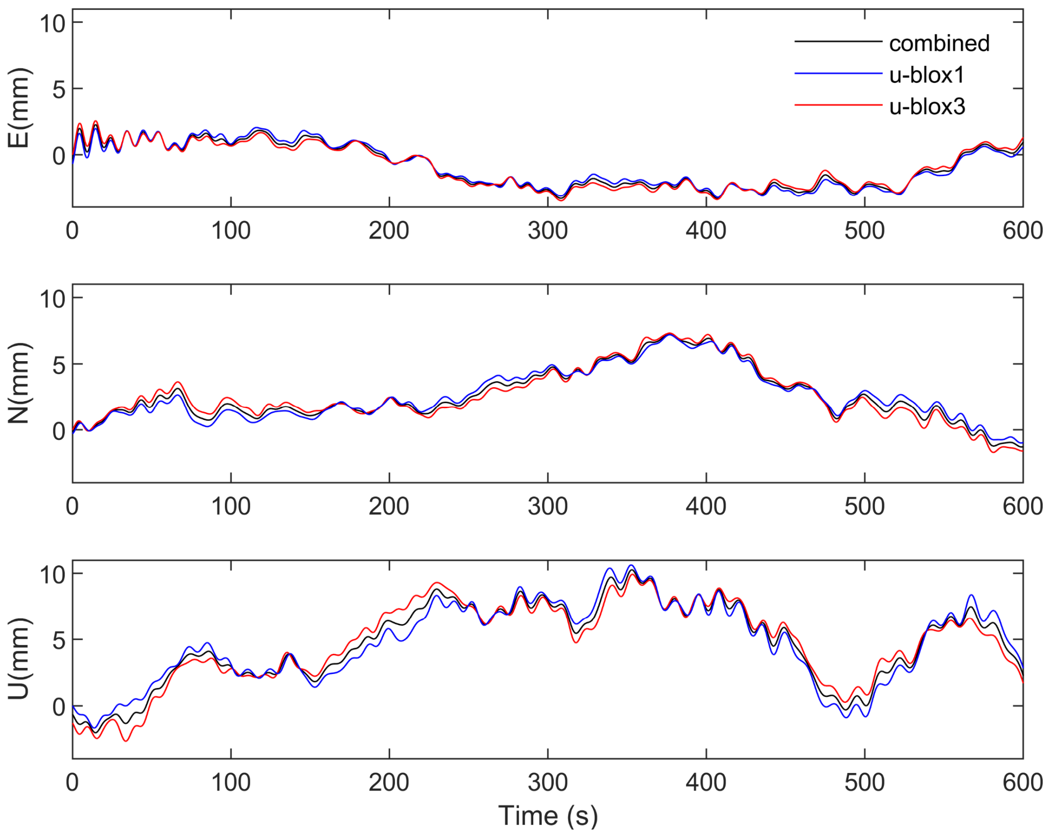

Figure 9. 22 *The low-pass filtered solutions of the initial E/N/U timeseries for u-blox1, u-blox3, and the combined case. The initial E/N/U timeseries is based on GPS+Galileo solutions of 20cm rotation test with Leica receiver&AS10 as the base station.*

It can be seen in Table 9.13 that the computed correlation coefficient is generally larger than 0.8, indicating a high correlation between the low-frequency component of two u-blox timeseries, as a result of the potential common errors in the low-frequency band. The CME model is constructed by the low frequency components of u-blox1 and u-blox3. By subtracting the CME model from the initial timeseries, low-frequency noise could be mitigated, leading to a potential precision enhancement of the GNSS timeseries. In the analysis, the established low frequency noise model is subtracted from the initial timeseries of u-blox1, u-blox3, and their average-combined timeseries respectively. Figure 9.22 presents the low-pass filtered timeseries for both u-blox1 and u-blox3, and the low-frequency CME model simulated by averaging them.

Table 9. 13 *Correlation coefficient derived from the analysis between the low-frequency components of the u-blox1 and u-blox3 timeseries, after applying the low-pass filter. The correlation coefficient was estimated for both GPS-only and GPS+Galileo timeseries, for all rotation radii, and with different base station antennas.*

R (cm)	Base antenna											
	Leica AS10						Patch					
	GPS-only			GPS+Galileo			GPS-only			GPS+Galileo		
	E	N	U	E	N	U	E	N	U	E	N	U
5	0.94	0.97	0.78	0.95	0.98	0.82	0.94	0.88	0.85	0.96	0.94	0.93
10	0.89	0.77	0.29	0.97	0.97	0.65	0.92	0.85	0.82	0.91	0.88	0.78
20	0.95	0.87	0.95	0.97	0.96	0.93						
30	0.91	0.91	0.91	0.81	0.95	0.90	0.94	0.90	0.61	0.58	0.93	0.66
40	0.94	0.91	0.94	0.93	0.82	0.95	0.79	0.97	0.91	0.96	0.95	0.88
50	0.97	0.94	0.93	0.96	0.98	0.97	0.88	0.91	0.83	0.98	0.88	0.96

Table 9. 14 *E/N/U residuals STD (mm) after removing the low frequency noise from the original timeseries by CME filtering for u-blox1, u-blox3, and average-combined solution. The results are presented for different rotation radii and different constellations (GPS-only, GPS+Galileo) when the base antenna adopts AS10.*

	Radius	GPS-only			GPS+Galileo		
	(cm)	U-blox1	U-blox3	combined	U-blox1	U-blox3	combined
E	5	2.4	4.6	2.8	2.1	3.4	2.2
	10	4.7	4.7	3.1	4.1	3.6	2.1
	20	5.4	4.6	3.9	3.1	3.2	2.4
	30	3.1	3.3	2.4	2.4	2.8	2.1
	40	2.9	2.9	2.4	2.7	2.7	2.2
	50	4.1	3.5	3.0	3.2	2.9	2.4
N	5	4.1	6.5	4.0	3.8	5.7	3.5
	10	6.0	11.6	5.9	6.1	7.4	4.3
	20	7.8	7.7	5.7	4.4	4.7	3.5
	30	4.9	4.6	3.4	4.2	4.3	2.9
	40	4.2	4.9	3.7	3.6	4.7	3.3
	50	8.0	8.0	6.6	4.3	4.3	3.2
U	5	6.3	8.2	4.5	6.4	8.5	4.3
	10	11.1	17.1	10.4	10.4	10.0	7.3
	20	10.9	12.3	7.9	7.5	7.1	4.5
	30	6.6	5.1	4.6	4.9	5.4	3.9
	40	7.5	8.0	5.7	6.5	5.7	5.0
	50	18.2	11.6	12.9	8.1	6.0	5.3

Table 9. 15 *E/N/U residuals STD (mm) after removing the low frequency noise from the original timeseries by CME filtering for u-blox1, u-blox3, and average-combined solution. The results are presented for different rotation radii and different constellations (GPS-only, GPS+Galileo) when the base antenna adopts the patch antenna.*

	Radius (cm)	GPS-only U-blox1	GPS-only U-blox3	GPS-only combined	GPS+Galileo U-blox1	GPS+Galileo U-blox3	GPS+Galileo combined
E	5	2.7	2.7	2.1	2.7	2.5	2.2
	10	6.3	3.4	3.7	4.5	2.9	2.8
	20						
	30	4.3	4.1	3.6	2.9	3.3	2.5
	40	3.7	3.6	2.9	3.4	3.2	2.9
	50	4.5	3.8	3.4	3.8	3.3	3.0
N	5	5.6	4.7	4.4	5.2	4.9	4.6
	10	13.4	10.5	9.3	7.7	6.5	5.2
	20						
	30	5.9	6.1	5.0	4.7	4.5	3.3
	40	5.0	5.6	4.3	5.0	5.6	4.7
	50	6.4	5.2	5.2	6.2	5.0	5.2
U	5	13.1	11.8	8.3	9.1	9.5	5.8
	10	13.3	11.5	8.4	10.2	9.8	6.6
	20						
	30	12.0	9.5	8.0	7.1	5.8	4.5
	40	6.3	6.9	4.5	5.3	6.4	3.8
	50	7.0	7.1	5.9	6.5	5.2	4.5

The E/N/U precisions are analysed for CME filtered GPS and GPS+Galileo timeseries and are presented in Table 9.14 and Table 9.15 for respective AS10 base antenna and patch base antenna for different rotation radius. It can be seen from Table 9.14 and Table 9.15, after CME filtering of the original timeseries, with GPS+Galileo solution, the precision is generally improved compared to GPS-only result. Precision improvement could also be seen by the average combination from the separate low-cost result.

9.8.3 High-pass filtering

Another approach for possible precision improvement is through high-pass filtering. The function of high-pass filter is to effectively mitigate the low-frequency component below the cut-off frequency, leaving the high-frequency component of interest. In the analysis, a Chebyshev high-pass filter with 8th order, passband frequency of 0.1Hz, and passband ripple of 1dB is adopted. Following the flow diagram in Figure 9.6, the high-pass filter is firstly applied to Leica, u-blox1, u-blox3, the u-blox1&u-blox3 average-combined original timeseries to mitigate the low frequency noise. Then the precision analysis was assessed with the high-pass filtered E/N/U components for different constellations and different base antenna (AS10 or patch antenna) and is presented in Table 9.16, Table 9.17 respectively. It can be seen from both Table 9.16 and Table 9.17 that similar conclusions can be made for the high-pass filtered results with the original and CME filtered results. The precision could be improved by multi-constellation measurement as well as the average combination between the two rovers' solutions.

Table 9. 16 *E/N/U residuals STD (mm) after applying Chebyshev high-pass filter to the original timeseries for u-blox1, u-blox3, and average-combined solution. The results are presented for different rotation radii and different constellations (GPS-only, GPS+Galileo) when the base antenna adopts AS10 antenna.*

	Radius (cm)	GPS-only				GPS+Galileo			
		U-blox1	U-blox3	combined	Leica	U-blox1	U-blox3	combined	Leica
E	5	2.1	4.3	2.5		1.9	3.0	2.0	
	10	4.3	4.3	2.8	1.3	3.7	3.3	1.9	0.9
	20	5.0	4.1	3.5	2.5	2.8	2.8	2.2	1.5
	30	2.7	2.9	2.1	1.9	2.1	2.6	1.9	1.6
	40	2.9	2.9	2.4	2.0	2.4	2.4	1.9	1.8
	50	3.8	3.2	3.1	2.5	2.9	2.7	2.7	2.2
N	5	3.7	5.9	3.6		3.4	5.1	3.1	
	10	5.4	10.6	5.2	3.1	5.5	6.7	3.7	1.7
	20	7.0	7.0	5.0	3.9	4.2	4.0	3.1	2.2
	30	4.5	4.1	3.1	2.4	3.9	4.0	2.6	1.9
	40	4.2	4.9	3.7	2.6	3.2	4.4	3.1	2.2
	50	7.6	7.8	6.4	3.4	4.0	4.0	3.1	2.5
U	5	5.8	7.5	4.0		6.0	8.0	3.9	
	10	10.5	16.1	9.8	3.2	9.9	9.2	6.9	2.2
	20	9.9	11.4	7.0	4.7	6.9	6.6	4.0	2.5
	30	5.9	4.3	3.9	4.0	4.3	4.8	3.4	3.4
	40	6.4	7.0	4.6	3.5	5.8	5.0	4.4	3.0
	50	17.3	10.8	12.2	4.8	7.6	5.6	5.0	2.8

Table 9. 17 *E/N/U residuals STD (mm) after applying Chebyshev high-pass filter to the original timeseries for u-blox1, u-blox3, and average-combined solution. The results are presented for different rotation radii and different constellations (GPS-only, GPS+Galileo) when the base antenna adopts the patch antenna.*

	Radius (cm)	GPS-only				GPS+Galileo			
		U-blox1	U-blox3	combined	Leica	U-blox1	U-blox3	combined	Leica
E	5	2.2	2.2	1.6		2.4	2.2	1.9	
	10	5.8	3.0	3.4	1.7	4.1	2.6	2.6	1.4
	20	4.0	4.2	2.7	2.2	3.2	3.1	2.8	2.2
	30	4.7	3.9	4.1	1.8	3.9	3.0	3.7	1.5
	40	3.3	3.2	2.5	2.3	3.1	2.9	2.6	2.1
	50	4.1	3.4	2.9	2.8	3.8	3.3	3.0	2.6
N	5	5.3	4.3	4.1		5.0	4.7	4.4	
	10	12.3	9.6	8.4	3.5	7.1	6.0	4.8	1.9
	20	8.7	9.5	7.0	3.5	7.1	8.0	5.7	2.7
	30	6.8	5.5	5.3	2.6	4.3	4.0	3.0	1.8
	40	5.2	4.4	4.0	2.5	4.6	5.3	4.5	2.1
	50	6.0	4.7	4.8	3.2	6.2	5.0	5.2	2.8
U	5	12.1	9.8	6.9		8.4	8.5	4.9	
	10	12.3	10.5	7.6	3.5	9.5	9.1	6.0	2.4
	20	12.8	19.8	12.8	4.1	8.7	11.8	8.6	2.6
	30	10.7	8.3	7.2	3.5	6.2	5.2	3.9	2.1
	40	5.5	6.2	3.8	2.7	4.7	5.8	3.2	2.4
	50	6.2	6.4	5.2	3.1	5.9	4.6	3.9	2.6

9.8.4 Comparison analysis between different precision improvement techniques

The performance of precision improvement is also compared between different approaches. Based on Tables 9.12-9.17, Figure 9.23-9.25 are plotted to demonstrate the effect of average-combination, CME filtering, high-pass filtering approach on precision improvement. The precision obtained from the original geodetic timeseries is used as a reference against which precision improvement by different methods is analysed. Apart from the direct precision comparison, it is also expressed as a ratio of precision improvement from the reference value (precision from original Leica timeseries), with negative values representing an improvement of precision and positive values as degradation (Figure 9.26-9.28). The ratio when the rotation radius is 5cm is not included in Figure 9.26-9.28 due to the lack of Leica reference for 5cm rotation radius measurement. The ratio is calculated by Equation 9.2:

$$Ratio = \frac{Precision^{*} - Precision\ of\ Leica}{Precision\ of\ Leica}$$

Equation 9. 2 *Improvement of precision for different cases from Leica original results as a percentage*

Where

- 'Precision of the Leica' represents the STD of E/N/U residual from original timeseries for Leica rover
- 'Precision*' represents the STD of E/N/U residual from original, CME filtered or high-pass filtered timeseries for Leica rover, u-blox rover, and u-blox average-combined case.

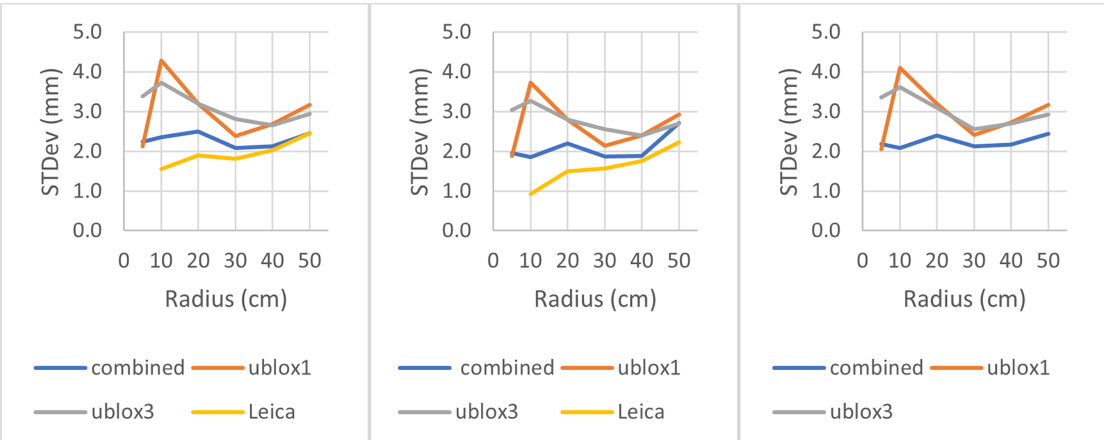

Figure 9. 23 *(Left) Easting residuals STD (mm)derived from the original timeseries of u-blox1, u-blox3, average-combined, and Leica GPS+Galileo solutions for different rotation radius; (Middle) Easting residuals STD (mm)derived from the high-pass filtered timeseries of u-blox1, u-blox3, average-combined, and Leica GPS+Galileo solutions for different rotation radius; (Right) Easting residuals STD (mm)derived from the CME filtered timeseries of u-blox1, u-blox3, average-combined GPS+Galileo solutions for different rotation radius. The results presented in the figures are all with respect to the geodetic base station with Leica receiver and AS10 antenna*

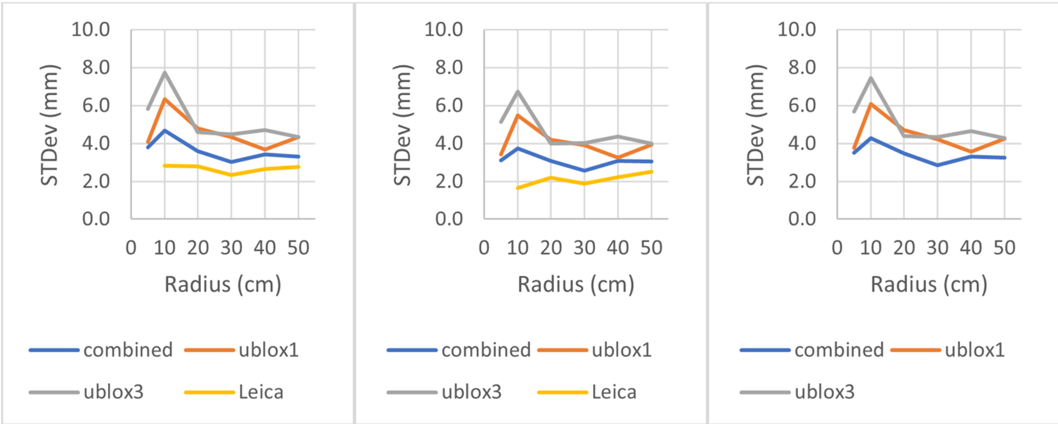

Figure 9. 24 *(Left) Northing residuals STD (mm)derived from the original timeseries of u-blox1, u-blox3, average-combined, and Leica GPS+Galileo solutions for different rotation radius; (Middle) Northing residuals STD (mm)derived from the high-pass filtered timeseries of u-blox1, u-blox3, average-combined, and Leica GPS+Galileo solutions for different rotation radius; (Right) Northing residuals STD (mm)derived from the CME filtered timeseries of u-blox1, u-blox3, average-combined GPS+Galileo solutions for different rotation radius. The results presented in the figures are all with respect to the geodetic base station with Leica receiver and AS10 antenna*

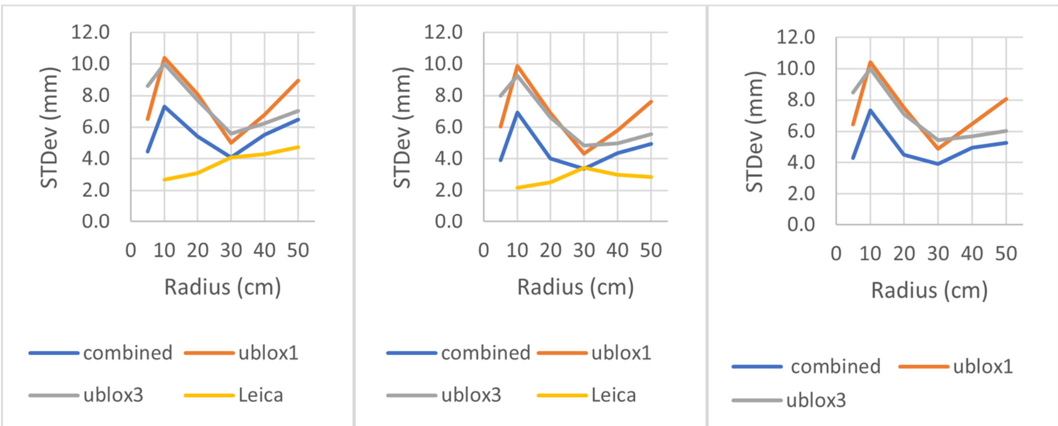

Figure 9. 25 *(Left) Up residuals STD (mm)derived from the original timeseries of u-blox1, u-blox3, average-combined, and Leica GPS+Galileo solutions for different rotation radius; (Middle) Up residuals STD (mm)derived from the high-pass filtered timeseries of u-blox1, u-blox3, average-combined, and Leica GPS+Galileo solutions for different rotation radius; (Right) Up residuals STD (mm)derived from the CME filtered timeseries of u-blox1, u-blox3, average-combined GPS+Galileo solutions for different rotation radius. The results presented in the figures are all with respect to the geodetic base station with Leica receiver and AS10 antenna*

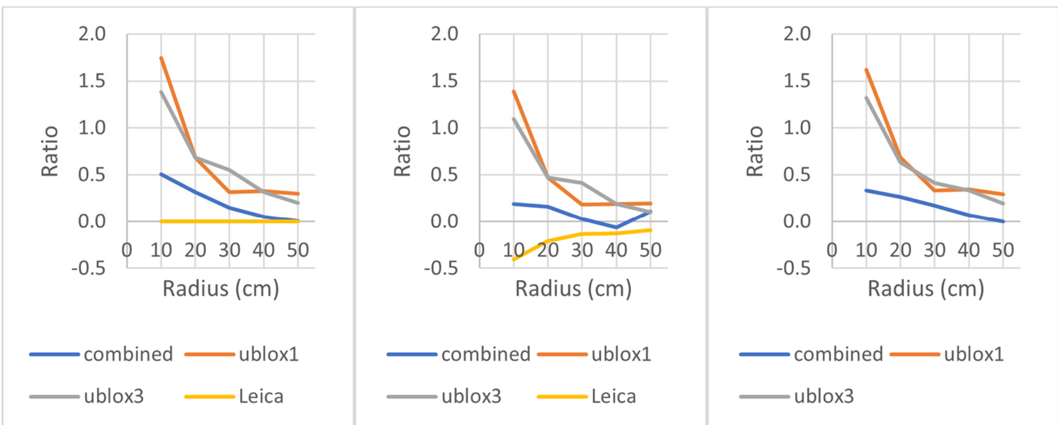

Figure 9. 26 *Precision improvement with reference to original Leica result expressed as ratios for Easting components (positive value for precision degradation and negative for precision improvement) (Left) original timeseries of u-blox1, u-blox3, average-combined, and Leica GPS+Galileo solutions for different rotation radius; (Middle) high-pass filtered timeseries of u-blox1, u-blox3, average-combined, and Leica GPS+Galileo solutions for different rotation radius; (Right) CME filtered timeseries of u-blox1, u-blox3, average-combined GPS+Galileo solutions for different rotation radius. The results presented in the figures are all with respect to the geodetic base station with Leica receiver and AS10 antenna.*

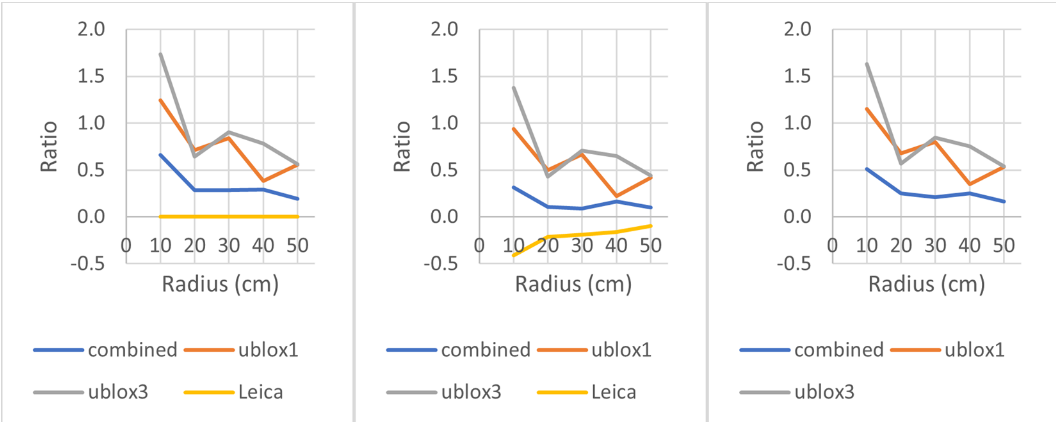

Figure 9. 27 *Precision improvement with reference to original Leica result expressed as ratios for Northing components (positive value for precision degradation and negative for precision improvement) (Left) original timeseries of u-blox1, u-blox3, average-combined, and Leica GPS+Galileo solutions for different rotation radius; (Middle) high-pass filtered timeseries of u-blox1, u-blox3, average-combined, and Leica GPS+Galileo solutions for different rotation radius; (Right) CME filtered timeseries of u-blox1, u-blox3, average-combined GPS+Galileo solutions for different rotation radius. The results presented in the figures are all with respect to the geodetic base station with Leica receiver and AS10 antenna.*

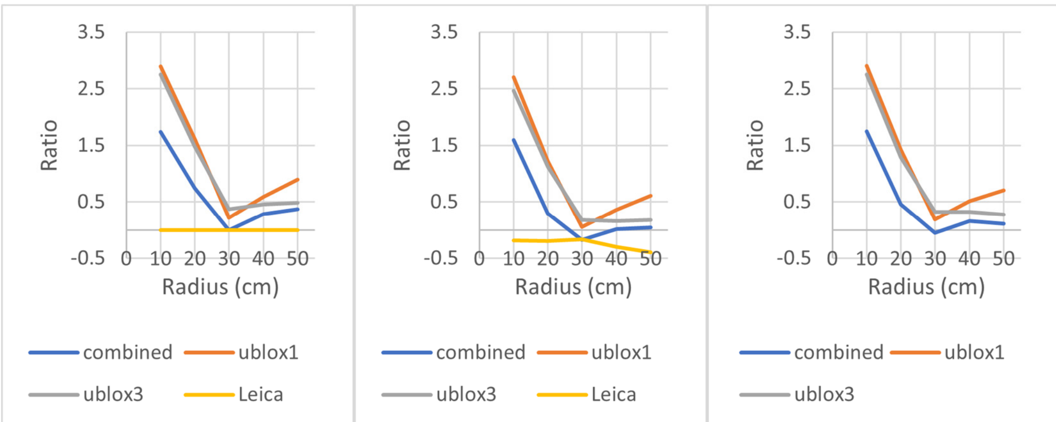

Figure 9. 28 *Precision improvement with reference to original Leica result expressed as the ratio for Up components (positive value for precision degradation and negative for precision improvement) (Left) original timeseries of u-blox1, u-blox3, average-combined, and Leica GPS+Galileo solutions for different rotation radius; (Middle) high-pass filtered timeseries of u-blox1, u-blox3, average-combined, and Leica GPS+Galileo solutions for different rotation radius; (Right) CME filtered timeseries of u-blox1, u-blox3, average-combined GPS+Galileo solutions for different rotation radius. The results presented in the figures are all with respect to the geodetic base station with Leica receiver and AS10 antenna.*

The average combination is achieved by averaging u-blox1 and u-blox3 results and it is applied in three cases, i) to the original timeseries, ii) to the original timeseries then subjected to CME filtering, and iii) to the original timeseries then subjected to high-pass filtering. It is derived from Table 9.12-17 and Figure 9.23-9.28 that in all the scenarios, generally, the average combination between the two u-blox data would improve the solution precision. The precision improvement by the average combined approach is calculated as a percentage compared to the higher precision attained by separate u-blox1 and u-blox3 receivers using Equation 9.3.

$$Precision\ improvement = \frac{Precision|_{ublox1/ublox3} - Precision|_{average-combined}}{Precision|_{ublox1/ublox3}}$$

Equation 9. 3 *Percentage of precision improvement by average combined solutions*

Where

- $Precision|_{ublox1/ublox3}$ stands for the better precision obtained from separate u-blox1 and u-blox3 solution
- $Precision|_{average-combined}$ stands for the the precision attained from average-combined solutions.

For the original timeseries, the precision is seen to be improved by up to 30% by averaging approach. For the CME filtered timeseries, it is shown that the average combined results could improve the precision by 40%. For the high-pass filtered timeseries, the maximum precision improvement could even reach 42%.

The precision improvement could also be achieved with GPS+Galileo multi-GNSS solution. Compared to precision obtained by GPS-only solution, the GPS+Galileo results would lead to improved precision both for u-blox1 u-blox3 separate solutions, Leica solution, and the average combined u-blox1 and u-blox3 solution. The precision improvement is more efficient especially when the GPS solution is weak, leading to even up to ~10mm precision improvement from GPS-only to GPS+Galileo solution (Table 9.14 Up components with 50cm rotation radius). Precision improvement by multi-constellation measurement is observed for all rotation radii for different grades of base antenna configurations. The precision improvement is probably due to improved satellite geometry and reduced DOP by the inclusion of Galileo satellites observations. It is shown that depending on GPS and Galileo constellations, the maximum precision improvement by addition of Galileo could even reach 63% compared to GPS-only solution.

In each figure from Figure 9.23-9.28, an abnormal behaviour is detected for precisions from both u-blox receivers in monitoring circular motions of ~10cm rotation radius. This phenomenon can be observed from both GPS-only and GPS+Galileo solutions irrespective of base station grade. The occurrence of this issue is probably due to the interference from the closely mounted AS10 antenna during the experiment as examined earlier. The higher elevation of the AS10 antenna could shadow the signal transmitted to the patch antenna and create multipath problems, which consequently degrades the measurement precision.

Precision improvement is also evaluated and compared between different filtering approaches, such as CME filter and high-pass filter. The results show improved precision can be achieved by filtering the low frequency noise first from the original timeseries prior to the precision analysis. Compared to precision obtained from original timeseries, slightly more precise results could be achieved with CME filtering with precision improvement normally less than 0.5mm for E/N components, for the Up component, the precision improvement could even reach a maximum of 3mm. A further improvement of precision could be achieved by prior high-pass filtering of the initial timeseries.

9.9 Discussion

The analysis firstly confirms that the base station receiver grade would not have a significant impact on the results if the same base antenna is used, with up to 1mm difference for Eastings/ Northings and up to ~1.5mm for Up component. Then from the DFT spectra of E/N/U original GPS and GPS+Galileo timeseries, dominant frequencies of 0.361-0.362Hz could be detected for all rotation timeseries regardless of different rotation radii, different rover-base formation. The same dominant frequency is expected from E/N spectral analyses and should be in correspondence with the motor rotation frequency since the GNSS measurements are made to detect the periodic pattern due to uniform planar circular rotation. Nevertheless, similar frequencies are also shown in Up solutions indicating rotation-related periodic noise due to imperfect horizontal motion.

The GNSS measurement biases for scenarios regarding different constellations, different rover and base formations, and different rotation amplitude are also studied and represented by parameters such as R residuals, E/N/U residuals. The STDs of R residuals, E residuals, N residuals represent the precision of GNSS measurement in the horizontal plane. On the other hand, the measurement precision in the vertical axis is represented by Up residuals STD. Comparing the precisions obtained from different rotation amplitude for each case, no significant variations are found with the increase of rotation radii. Therefore, the precisions obtained using different rotation radii are assumed normally distributed. Table 9.18 summarises R precision from different rotation amplitude. with a 95% confidence interval.

Table 9. 18 *Margin of error with 95% confidence level for R precision considering all rotation radii for GPS-only and GPS+Galileo solutions, μ is calculated by the average of the precision obtained from different rotation radius, and σ is the standard error*

Base antenna	Rover station	margin of Error (mm) (μ±1.96σ)	
		GPS-only	GPS+Galileo
AS10	Leica	3.4 ±0.9	2.4 ±0.3
	U-blox1	5.9±1.3	4.2±0.7
	U-blox3	6.8±1.8	5.0 ±0.9
Patch	Leica	4.1±0.4	3.1 ±0.2
	U-blox1	6.9±2.2	5.5 ±1.1
	U-blox3	7.3 ±1.9	5.4±0.9

By comparing μ between GPS-only and GPS+Galileo solution, it could be inferred that multi-constellation configuration would normally lead to a better precision. It is also noticed that smaller σ (confidence interval) is detected for GPS+Galileo solutions, indicating more stable and robust results can be achieved with GPS+Galileo multi-constellation. The precision comparison is also conducted between different grades of rovers. It is implied that better precision (μ) and robustness (σ) would be obtained by geodetic rovers than low-cost u-blox receivers. Table 9.18 also shows the influence of base antenna on results, with generally worse precision (μ) exhibited from patch base antenna solutions than solutions with AS10 base antenna.

Table 9. 19 *Margin of error with 95% confidence level for E/N/U residuals precision considering all rotation radius for GPS-only and GPS+Galileo solutions, μ is calculated by the average of the precision obtained from different rotation radii, and σ is the standard error*

Base antenna	Rover	Margin of Error (mm) (μ±1.96σ)					
		E		N		U	
		G	G+E	G	G+E	G	G+E
AS10	Leica	2.4 ±0.4	1.8 ±0.3	3.6 ±0.6	2.6 ±0.2	4.2 ±0.6	2.9±0.3
	U-blox1	3.8±0.9	2.9±0.5	6.6 ±1.8	4.6 ±0.9	10.0±3.7	6.9±1.7
	U-blox3	4.0±0.7	3.0 ±0.3	7.7 ±2.3	5.6±1.3	9.4 ±2.6	6.6±1.3
Patch	Leica	2.6 ±0.3	2.4 ±0.3	3.9 ±0.5	2.9 ±0.4	3.2±0.3	2.3 ±0.1
	U-blox1	4.2±0.9	3.5±0.5	7.4±2.3	6.1±0.9	9.8 ±2.2	7.6±1.6
	U-blox3	3.8±0.7	3.2 ±0.4	7.3±1.9	6.0 ±1.1	9.8 ±2.6	7.7±2.2

Similar conclusions could be drawn by E/N/U measurement precision (Table 9.19): i) the improved precision and robustness with multi-constellation, ii) improved precision using geodetic rover compared to low-cost rovers. However, by evaluating the impact of base antenna grade, it is shown that the precision of E/N components would be improved in general with geodetic base antenna, but performance for U component is sometimes worsened with geodetic base antenna as compared to patch base antenna. This phenomenon is also identified by Hamza (2021) and justified by uncalibrated antenna parameters, since the uncalibrated PCV errors tend to exert more impact on the vertical estimates (Biagi et al., 2016).

Table 9. 20 *Precision improvement for E/N/U component by different approaches shown as an example when the rotation with the radius of 30cm is measured*

Cases	Precision (mm)		
	E	N	U
U-blox1 GPS-only solution with patch base antenna	4.3	6.2	12.4
U-blox1 GPS+Galileo solution with patch base antenna	2.9	5.0	7.8
U-blox1 GPS+Galileo solution with AS10 base antenna	2.4	4.3	5
Combined GPS+Galileo solutions by averaging of u-blox1 and u-blox3 original timeseries with AS10 base antenna	2.1	3	4.1
Combined GPS+Galileo solutions by averaging of u-blox1 and u-blox3 original timeseries with AS10 base antenna then applying the CME filter	2.1	2.9	3.9
Combined GPS+Galileo solutions by averaging of u-blox1 and u-blox3 original timeseries with AS10 base antenna then applying a high-pass filter	1.9	2.6	3.4

Different approaches to improve the precision of low-cost rover measurement are also investigated (Table 9.20). It is firstly shown that precision could be enhanced by including multi-constellation observations. The adoption of a better grade geodetic antenna at the base station is also proved beneficial in obtaining more precise results in E/N components. Then precision improvement attempts are made by processing of the timeseries, such as average combination, CME filtering and high pass filtering. Firstly, it is shown by simply averaging the two original low-cost timeseries, precision could be enhanced. To further mitigate the low frequency errors in the original results and take advantage of the closely-spaced GNSS sensors, a low-pass filter is applied to the two low-cost rovers' original timeseries to obtain the CME. It is proved that with CME removal, the precision of E/N/U residuals could be improved both for separate and average combined low-cost solutions. The low-frequency noise mitigation by application of a high-pass filter to the original timeseries (separate and average-combined low-cost solution) is also tested resulting in a further improvement of precision from CME filtering.

9.10 Summary

In this chapter, the precision of low-cost GNSS rovers in measuring the dynamic motion of different amplitude is examined under favourable measurement conditions. The performance of low-cost rover is evaluated with reference to geodetic rover solution under different configurations, such as adopting different grades of receiver/ antenna for base station and using different constellations for GNSS solution computation. Frequency analyses are conducted to derive the dominant rotation frequency using low-cost rover measurements in comparison to geodetic solutions. It is also investigated potential precision improvement by incorporating a dual closely-spaced low-cost rover system and by adopting different filtering techniques.

From the analyses, it is concluded that:

- The precision and certainty could be largely improved from GPS-only solution by including Galileo constellation.
- No significant impact on the results' precision is detected by adopting different grades of base station receivers. However, better base antenna would generally lead to a precision improvement for E/N components.
- The low-cost GNSS measurement precisions in monitoring kinematic movements are around 3-4mm for Easting, 5-6mm for Northing, and 7-8mm for Up for GPS+Galileo solution.
- By reducing the low frequency biases in the measurement, CME and high-pass filtering could enhance the precision.
- The precision could be improved by average processing between the two low-cost original results, with further improvement by applying the CME filter and high-pass filter to the average-combined solution
- From the spectra, consistent dominant rotation frequency of ~0.362Hz can be derived from both low-cost and geodetic receiver measurement with a high accuracy.

The results from both SBL static and kinematic tests suggest that solution with enhanced precision could be obtained by the average-combination approach regarding a closely-spaced dual low-cost rover system in comparison to the solution from a single low-cost rover. This implies the potential precision improvement by a cluster of closely-spaced low-cost rovers. A strong positive cross-correlation is also detected between the low-frequency components of the two closely-spaced rovers both in SBL static and SBL kinematic test which is a prerequisite for CME filtering. However, the high cross-correlation is obtained based on favourable measurement conditions with good satellite visibility and relatively low multipath. Although progresses in precision evaluation and enhancement for low-cost GNSS receivers are made based on SBL kinematic test, low-cost GNSS applications and the CME approach still need to be investigated and verified in a multipath challenging environment. In the next Chapter, the low-cost GNSS receivers are tested in a practical bridge monitoring project under a multipath challenging environment. The approaches of combined processing by CME filter and average-combination between two low-cost stations are also implemented to assess their applicability.

Chapter 10 Wilford bridge experiment

10.1 Introduction

In the ZBL and SBL tests, the measurement conditions are relatively ideal with an open sky satellite visibility on the roof and comparatively low multipath due to few obstructions from surrounding structures. However, in a real monitoring scenario, idealistic measurement condition is not always guaranteed, factors such as multipath, satellites visibility and weather conditions, etc may also impose an impact on the measurement. Hence, the Wilford Suspension Bridge trial is conceived to test the feasibility of low-cost GNSS equipment in displacement monitoring and in revealing the structures' modal frequencies in a practical monitoring environment。

The Wilford suspension bridge is located on river Trent, in Nottingham. It is a short-medium span pedestrian suspension bridge frequently used for SHM purposes in empirical studies (Meng et al., 2007; Meo et al., 2006; Psimoulis et al., 2016). The experiment is designed so that the deformation of the bridge could be measured by different types of instruments: low-cost GNSS sensor, geodetic GNSS sensor, and robotic total station (RTS). The RTS is an automated instrument determining 3D coordinates of the target points in a pre-defined coordinate system by combining horizontal angle, vertical angle, and distance measurement. In the experiment, the measurement differences and results between different devices are quantified. The results from low-cost GNSS are verified between each other and compared against geodetic GNSS and RTS results to evaluate the performance of the low-cost receiver in the bridge deformation monitoring. The RTS solution is chosen as the reference due to its highest accuracy and precision.

For GNSS measurements, the environment of the testing site is multipath challenging due to multipath reflection from the river Trent, overhang suspension cables, pedestrians, handrails, etc. This is more problematic for patch antennas since they have less capability of rejecting multipath compared to geodetic antennas. To mitigate the multipath impact on GNSS measurement, the conventional method is to apply a high-pass filter (Ioulia et al., 2018; Psimoulis et al., 2016; Yu et al., 2014), which leaves the filtered data only containing the high-frequency displacement response. Besides the conventionally adopted high-pass filtering technique, the study also explores the possibility of CME filtering in removing low-frequency errors since two closely-spaced low-cost stations are deployed as rovers. However, due to the complex multipath conditions, the phase and amplitude of multipath error between closely-spaced rover stations could deviate significantly which may potentially lead to invalidation of CME filtering. Therefore, cross-correlation of low-frequency components from the two low-cost rovers is firstly analysed to determine if they are subjected to similar long-period noise. The solution derived from the average combination between the two low-cost GNSS timeseries is also examined for potential precision and accuracy improvement with comparison to each separate low-cost GNSS, geodetic GNSS, and RTS solutions.

To study the accuracy of displacement measured with different equipment, different loads are imposed intentionally to the bridge, forcing the bridge to deform so that a clear deformation of the bridge could be captured and recorded. During the experiment, the bridge is excited with various patterns of load by different human

activities such as walking, jumping, swinging, and marching. The corresponding measurements from different sensors (2*u-blox receivers, 1* Leica receiver, RTS) are recorded and further analysed to evaluate their performance.
The Wilford bridge experiment aims to evaluate the performance of low-cost GNSS receivers in monitoring cm-level dynamic displacement and their abilities to analyse the modal frequency from the timeseries, by comparing against survey-grade GNSS and RTS results, with objectives to explore the possibility of precision/accuracy improvement with the dual low-cost receiver system.

10.2 Experiment procedure and setup

The experiment was conducted on a 69-meter span suspension bridge with twin dual steel suspension cables mainly for pedestrian use (Figure 10.1). In the experiment, several sensors were deployed along the bridge to monitor response from the bridge (Figure 10.2). It was established four Leica rovers (Leica GS10 and AS10), two at the quarterspan of the bridge on the south side (location A, D) and two at midspan: one on the north side (location B) and one on the south side (location C). The GNSS antennas at the midspan (location B, C) of the bridge were also integrated with 360-degree reflective prisms used as targets for RTS measurement (Figure 10.3). At location C, two closely-spaced patch antennas each connected to u-blox M8T receivers (Figure 10.4) were also deployed. Both two patch antennas were attached to a ground plane and clamped firmly to the handrails. A laptop with u-center installed was used for the data acquisition for the u-blox receivers. The Leica RTS TS30 was set up on a tripod at the riverbank aiming at prism located at location B. On the other hand, the Leica RTS MS60 was deployed on the other side of the bridge aiming at the prism located at location C. Both RTS equipment (TS30 and MS60) was configured to record and generate coordinates automatically at a maximum sampling rate regarding the centre of the target (prisms) in a pre-defined coordinate system. However, due to the unstable sampling rate of RTS, the actual acquisition frequency is in the range of 5-7Hz (Psimoulis et al., 2007). The coordinate system used for the RTS was pre-configured to the bridge axis, with x-axis parallel with longitudinal of the bridge and y-axis parallel with lateral of the bridge (Figure 10.5). As for GNSS measurements, both Leica and u-blox GNSS rover receivers were configured to record GPS, Galileo, GLONASS satellites observations at a 10Hz sampling rate. The GNSS reference station (Leica GS10 & AS10) and two RTS stations were all established on the riverbank in a stable condition free from excitations. The reference GNSS station was also configured to take GPS, GLONASS, and Galileo measurements. However, due to technical problems, only GPS and GLONASS measurements were made for the reference station. Several excitations were generated by a group of 8 people with different loading patterns and activities, such as walking, jumping, swinging, and marching. It is summarised the duration and type of each activity (Table 10.1).

Figure 10. 1 *Wilford suspension bridge on River Trent*

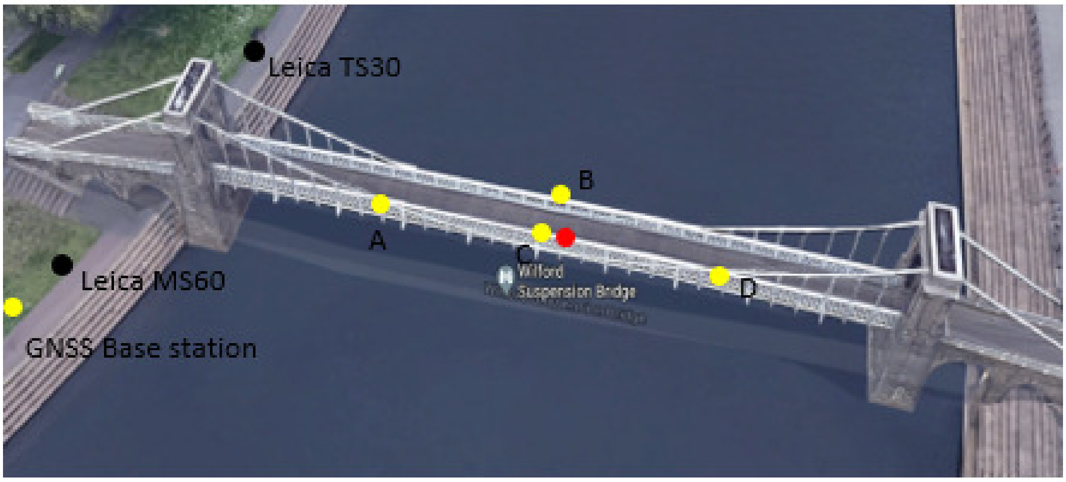

Figure 10. 2 *Location of the equipment and sensors along the riverbank and the bridge*

Figure 10. 3 *Leica AS10 antenna at midspan (Left) location B& (Right) location C of the bridge with reflective prisms mounted underneath the GNSS antenna as the target for RTS measurement.*

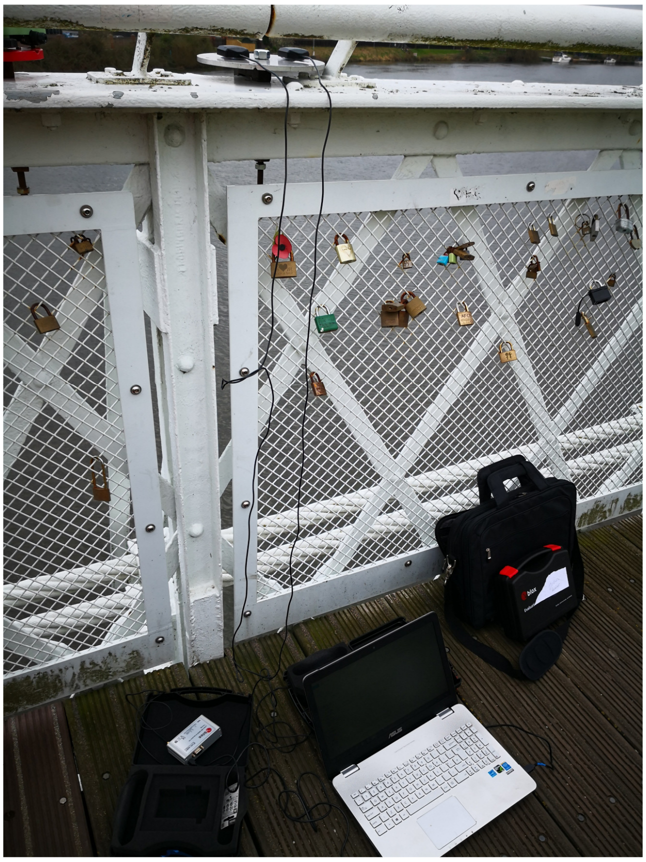

Figure 10. 4 *Low-cost monitoring stations at midspan of the bridge (location C)*

Table 10. 1 *Excitation activities and durations recorded by stopwatch, the stopwatch time is later transferred to UTC and GPS time to pinpoint the occurrence of excitations in the timeseries (00:00:00 stopwatch time correspond to 15:17:51 UTC)*

Event number	Start	End	Activity
01	0:05:57	0:07:00	Whole group walk along the bridge from west to east end
02	0:07:55	0:08:44	Half group walk back from east to west end
03	0:10:06	0:10:31	Two half groups on both ends walk to bridge midspan
04	0:12:00	0:12:45	Whole group jump in the middle of the bridge in midspan in different patterns
05	0:13:51	0:14:41	Whole group jump on the north side of the bridge in midspan at the same time
06	0:17:35	0:18:15	Whole group jump on the south side of the bridge in midspan at the same time
07	0:20:36	0:21:24	Whole group spread along the bridge in the middle and jump at the same time
08	0:23:35	0:24:15	Whole group jump on the north side of the bridge in midspan at the same time
09	0:26:55	0:27:51	Whole group swing the bridge
10	0:29:10	0:30:00	Whole group jump on north side of bridge
11	0:31:07	0:31:58	Whole group march on the bridge
12	0:34:30	0:39:38	Whole group stand in the midspan of the bridge

10.3 RTS and GNSS data processing and analysis

10.3.1 Data processing

For RTS, coordinate computation could be output directly from the instrument in a user-defined coordinate system. For GNSS data processing, the GNSS observations were processed in RTKLIB 2.4.3 demo5 b33c modified by Everett (2020) based on RTKLIB 2.4.3 (Takasu and Yasuda, 2009). The E/N/U baseline GPS and GPS+GLONASS solutions were computed for baselines formed of Leica and u-blox rovers and Leica base. Table 10.2 lists the settings used (detailed configurations could be found in Appendix F).

Table 10. 2 *Settings configuration for RTKLIB 2.4.3 demo5 b33c for Wilford Bridge test GNSS processing (a more detailed version could be found in Appendix F)*

Settings	***Options***
Position mode	Kinematic
Frequency/Filter type	L1/**Forward**
Elevation Mask	15
Rec Dynamics/Earth Tide Correction	**ON**/OFF
Ionosphere Correction	Broadcast
Troposphere Correction	Saastamoinen
Satellite Ephemeris/Clock	Broadcast
RAIM FDE	Ticked
Constellation selection	GPS GPS+GLONASS
GPS Integer Ambiguity Res	Continuous
GLONASS Ambiguity Res	Auto Calibration
GLONASS Hardware Bias	-0.055
Min Lock/Elevation to fix ambiguity	0,15
Outage to reset ambiguity/slip threshold	20,0.05
Max age of differential	1
Reject threshold of GDOP/Innov	30,1000
AR filter	ON
Min Ratio to Fix Ambiguity	**1**
Output	E/N/U-Baseline
Time interpolation of Base station Data	ON
Datum/Height	WGS84/Ellipsoidal
Base station position	Average of a single position
Code/Carrier phase Error Ratio L1/L2	300,300
Carrier phase error a+b/sin El (m)	0.003,0.003
Doppler Frequency	1Hz
Receiver Accel Horiz/Vertical	3, 1

Comparing the configurations with the SBL kinematic test, the major differences were firstly a **forward** filter was used instead of the **combined** filter and secondly the 'Min Ratio to Fix Ambiguity' was reduced from **3** to **1**. By changing the filter type, the backward filter, which served as the ambiguity resolution verification and augmentation of the forward filter was avoided to reduce the computing load and to make real-time applications potential with forward-only filter. The reason to change the minimum ambiguity resolution ratio from 3 to 1, was due to the overall poor multipath in the bridge monitoring environment. As a result, the ambiguity resolution validation threshold should be adjusted accordingly for an easier derivation of fixed solutions, although the drawback was the less confidence in the ambiguity resolution which could lead to possible false fixes/cycle slips when a wrong integer ambiguity was computed.

The third major difference is from the method used for GLONASS ambiguity resolution. The GLONASS ambiguity resolution is processed by auto-calibration taking into account of the receiver inter-channel bias terms and estimates it as a linear equation by the frequencies. For the GPS+GLONASS baseline solution formed by u-blox M8T rover and Leica GS10 base, the a-prior correction of HW bias for GLONASS is -0.055m between u-blox M8T and Leica (Everett, 2018b), which is then input into the settings of the software to resolve GLONASS ambiguity.

10.3.2 Cycle slips in GNSS solutions

In the bridge deformation analysis, the GPS+GLONASS solution was used. On one hand, this is due to the overall precision improvement by the inclusion of multi-constellation. On the other hand, it is also examined that by the inclusion of GLONASS constellation, false fixes/cycle slips frequently occurring in the GPS-only solution also tend to be mitigated leading to a more consistent timeseries with increased reliability. The false ambiguity fixes/cycle slips refer to issues in GNSS solutions whose ambiguity is resolved to a wrong integer number. The occurrence of cycle slips is probably due to a change in observation environment where the measurement conditions get more challenging or have simply changed by passing-by pedestrians.

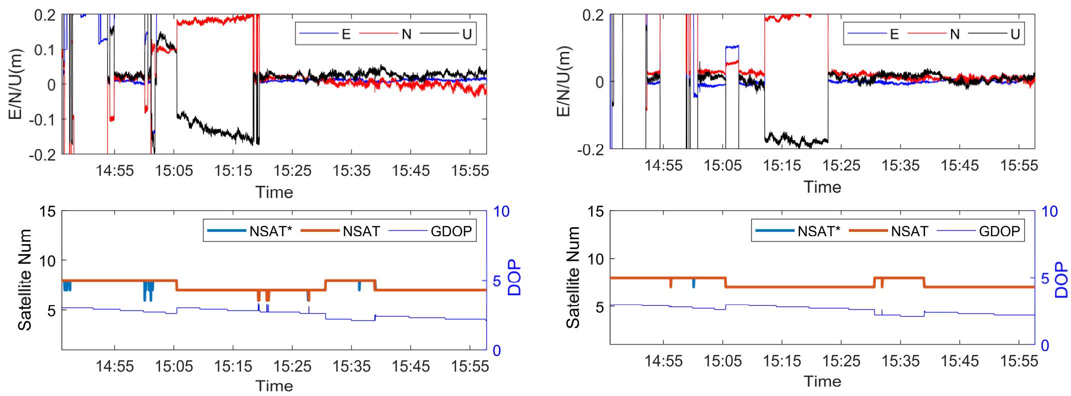

***Figure 10. 5** E/N/U timeseries with y value shifted to around zero and the corresponding number of satellites (NSAT) and GDOP timeseries for the whole measurement period for GPS-only solutions; (Left) u-blox1 and (Right) u-blox2. The occurrence of cycle slips can be identified. The NSAT* denotes the number of valid satellites used for solution computation, NSAT and GDOP denote the number of satellites tracked above 15-degree elevation angle and corresponding GDOP.*

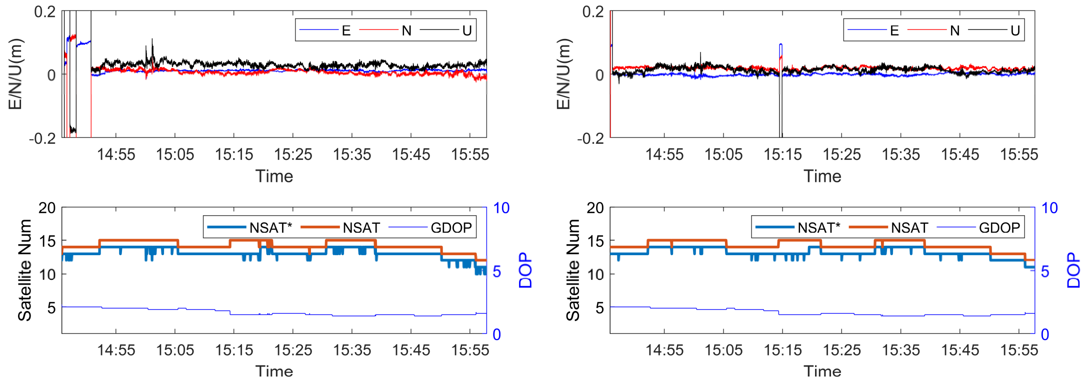

Figure 10. 6 *E/N/U timeseries with y value shifted to around zero and the corresponding number of satellite (NSAT) and GDOP timeseries for the whole measurement period for GPS+ GLONASS solutions; (Left) u-blox1 and (Right) u-blox2. The occurrence of cycle slips can be identified. The NSAT* denotes the number of valid satellites used for solution computation, NSAT and GDOP denote the number of satellites tracked above 15-degree elevation angle and corresponding GDOP.*

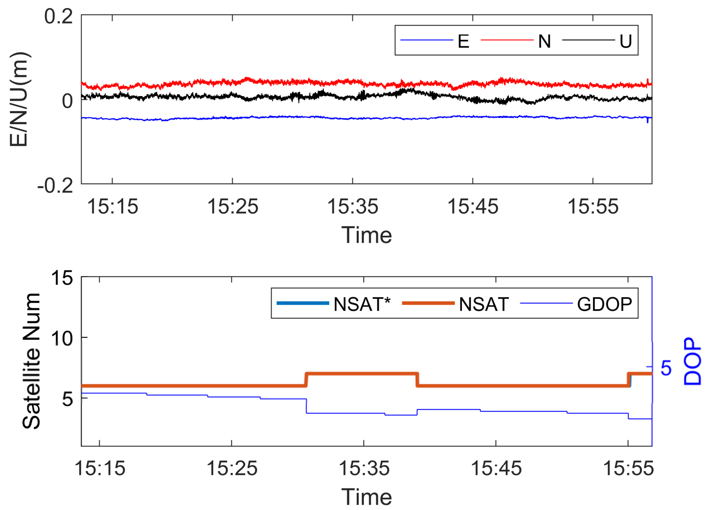

Figure 10. 7 *E/N/U timeseries with y value shifted to around zero and the corresponding number of satellite (NSAT) and GDOP timeseries for the whole measurement period for Leica GPS-only solutions; No occurrence of cycle slips can be shown. The NSAT* denotes the number of valid satellites used for solution computation, NSAT and GDOP denote the number of satellites tracked above 15-degree elevation angle and corresponding GDOP.*

The reason for the occurrence of cycle slips is further explored by correlation with NSAT and DOP (GDOP). If no correlation is identified, the SNR values when cycle slips occur are also investigated. It is shown in Figure 10.5 the occurrence of cycle slips in correlation to a sudden drop in NSAT* and a corresponding increase in GDOP, for the period ~14:45, ~15:00, and ~15:05. The ambiguity resolution at the beginning of the timeseries is also shown to be problematic leading to cycle clips even after the convergence, with correct ambiguity fixing time reaching even up to 15 minutes after the occurrence of the cycle slip (from 15:05 to 15:20).

In Figure 10.6, cycle slips for both u-blox1 and u-blox2 GPS+GLONASS solutions are detected at ~14:47 and ~ 15:00 due to a reduction in NSAT*. It is also noticed that in both u-blox1 and u-blox2 GPS+GLONASS NSAT* timeseries, variations of NSAT* (usually at a magnitude of 1) often occur over multiple short periods, which could cause increased uncertainty in GPS+GLONASS solutions. This is because instantaneous vibrations of NSAT could lead to vibrations of DOP, which would consequently affect the measurement precision. Compared to NSAT* vibrations in GPS-only timeseries (Figure 10.5), much more frequent NSAT* vibrations could be detected in GPS+GLONASS timeseries, which could be due to the incompatibility between GLONASS and the u-blox receivers as examined in the ZBL test. Most NSAT* vibrations occur locally, however, if it occurs during excitations, the potential precision degradation could lead to a less accurate displacement amplitude determination. It is shown that cycle slips tend to occur when NSAT* reduces, alternatively, cycle slips could be mitigated by including additional satellites (Figure 10.6 left, around 14:50). Despite some cycle slips being directly related to the satellite number instability and increase of DOP, cycle slips could also be a result of a change in SNR.

When there is no strong correlation between NSAT/DOP and cycle slip occurrence (Figure 10.5, 15:12-15:22), the SNR values of different satellites are examined (Figure 10.8), during which a pattern of abnormal oscillation with significant SNR variations is detected for G32 and G14. There are also other SNR- induced cycle slips which are normally resulted from a SNR reduction during the corresponding period. For example, the occurrence of the cycle slip in Figure 10.5 ~15:00 for u-blox2 GPS timeseries, is a result of SNR drop for G06 and G02, etc. The reason for the cycle slip occurring ~15:15 for u-blox2 GPS+GLONASS timeseries in Figure 10.6 is also investigated by examining SNR. To identify the satellite (s) causing the cycle slip, it is checked if the cycle slip is fixed by excluding certain satellites. By trials and errors, it is found that by excluding G32, the cycle slips could be effectively fixed. Therefore, the SNR timeseries for G32 is plotted, and the period of 15:14:29-15:14:55 is pinpointed corresponding to the occurrence of cycle slip (Figure 10.9). It is shown that the cycle slips occur due to an SNR decrease in the enclosed region.

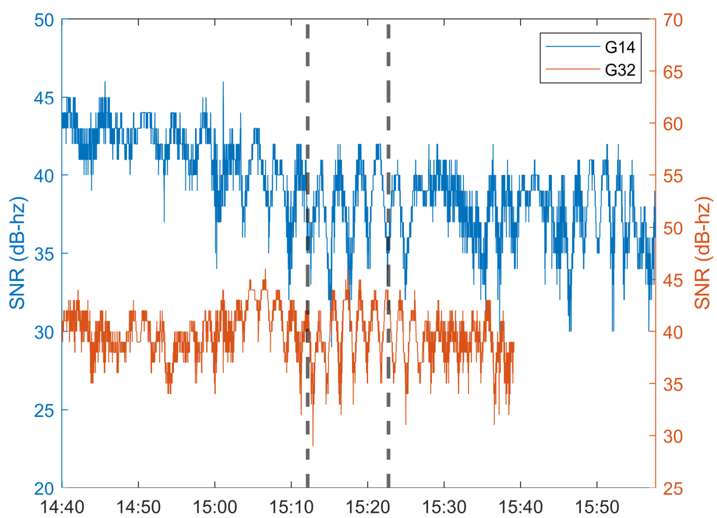

Figure 10. 8 *Detection of an abnormal pattern of SNR values for G14 and G32 as enclosed by the dashed line*

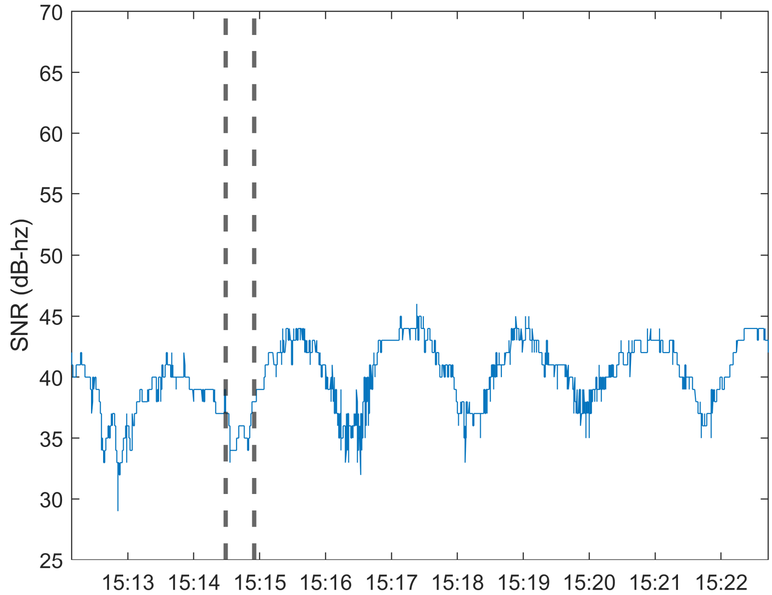

Figure 10. 9 *SNR of G32 for cycle slip period as enclosed by the dashed line*

To summarise, the cycle slips could occur with a change in NSAT/DOP, or by unstable SNR variations. The occurrence of cycle slips is also shown dependent on the receiver/ antenna used. For geodetic receiver and antenna pairs, no false fixes/cycle slips are detected even with GPS-only solution (Figure 10.7). While on the other hand, frequent false fixes could be found for low-cost receivers and patch antennas under same measuring condition. This indicates better quality of antenna and receiver would tend to reduce the occurrence of the false fixes/cycle slips probably due to comparatively high SNR and precise GNSS observations. Comparing GPS with GPS+GLONASS timeseries, the benefit of multi-GNSS (GPS+GLONASS) in false fixes/cycle slips mitigation could be clearly shown. The impact of multi-GNSS on the accuracy of low-cost monitoring results is also researched later since both GPS and GPS+GLONASS timeseries are not affected by cycle slips during the period of excitation.

10.3.3 BCS transformation

When analysing the displacement of the same target, the results from separate equipment were produced in different coordinate systems creating a problem for further analysis. Therefore, they were firstly converted and transformed to a uniform coordinate system usually referred to the coordinate system of the structure, where measurement could be interpreted meaningfully. For bridge monitoring applications, the bridge coordinate system (BCS) was conventionally constructed with x, y, z axes, where the x-axis was defined parallel to the longitudinal axis of the bridge, z-axis in the vertical direction, and y-axis determined using the right-handed rule. In the bridge trial, the RTS coordinate system was configured to coincide with the BCS. Therefore, RTS recordings would reflect measurement in BCS directly. On the other hand, by processing GNSS observations, E/N/U baseline solutions were obtained in the local ENU coordinate system for both Leica and u-blox rovers. To convert it to BCS, the local ENU coordinate system was rotated clockwise by 12 degrees (Figure 10.10) using the coordinate transformation matrix (Equation 10.1). The transformation matrix rotates points in xy-plane clockwise by an angle θ, and translates the points to a new coordinate. By coordinate transformation, all the results (RTS and GNSS) were obtained in a uniform local BCS, making it convenient for later analysis.

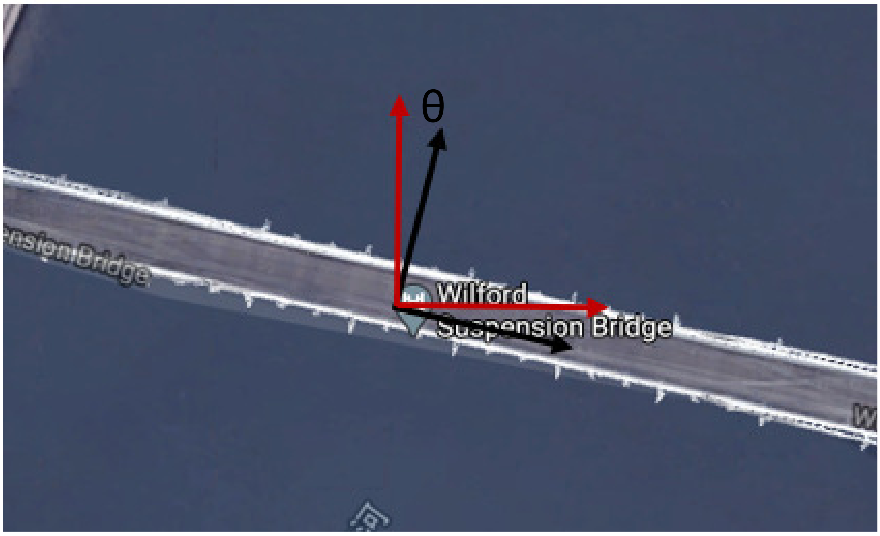

Figure 10. 10 *Plan view of the local GNSS ENU cartesian coordinate system, Northing, and Easting axis (Red) and the bridge cartesian coordinate system, the lateral and longitudinal axis (Black)*

$$\begin{Bmatrix} X \\ Y \\ Z \end{Bmatrix} = \begin{bmatrix} \cos(\theta) & \sin(\theta) & 0 \\ -\sin(\theta) & \cos(\theta) & 0 \\ 0 & 0 & 1 \end{bmatrix} \begin{Bmatrix} x \\ y \\ z \end{Bmatrix} + \begin{Bmatrix} x_0 \\ y_0 \\ z_0 \end{Bmatrix}$$

Equation 10. 1 *Transformation matrix from local ENU to the local BCS. For z components of a small network, the vertical coordinate does not transform*

Where

- $\begin{Bmatrix} x \\ y \\ z \end{Bmatrix}$ is the coordinate from the original coordinate system
- $\begin{Bmatrix} X \\ Y \\ Z \end{Bmatrix}$ is the coordinate after transformation
- $\begin{Bmatrix} x_0 \\ y_0 \\ z_0 \end{Bmatrix}$ is the translation vector to a new point
- ϑ is the clockwise angle for the rotation.

10.3.3 Data analysis

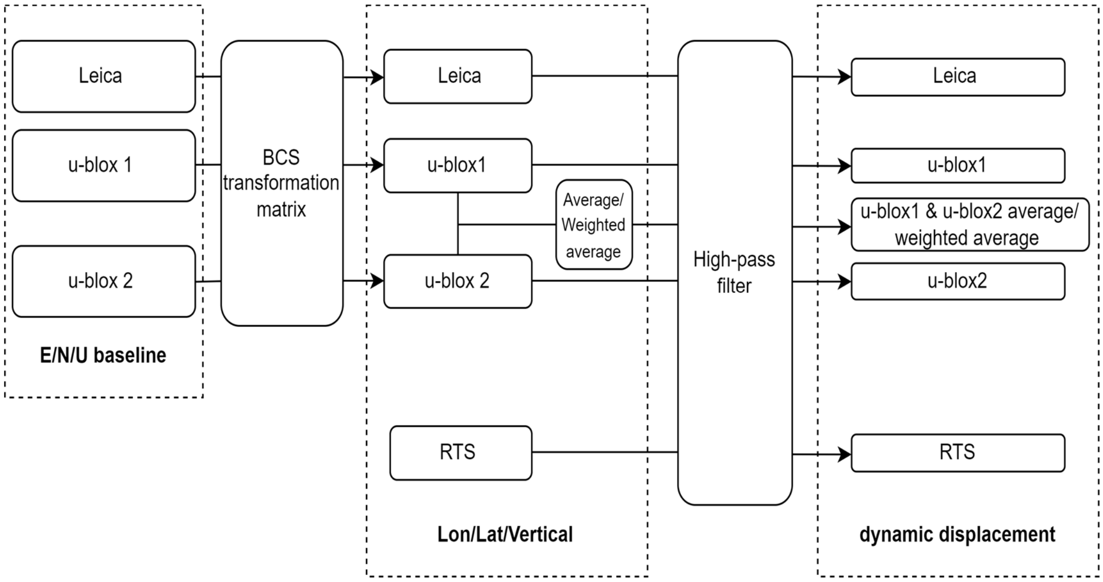

Figure 10. 11 *Flow diagram of the data analysis using high-pass filtering*

Figure 10.11 presents the data analysis procedure using high-pass filter processing. The GNSS solutions are firstly converted to BCS. After BCS coordinate conversion, the average/weighted average process is applied to u-blox1 and u-blox 2 results to assess the averaging impact on accuracy improvement. Spectral analyses are also carried out regarding the original timeseries for modal frequency detection. To extract the dynamic response of the bridge, high-pass filters are applied to original timeseries of Leica, u-blox 1, u-blox 2, average/weighted average combined solution, and RTS to mitigate low frequency errors. The dynamic response obtained from different approach is also compared and analysed later.

The application of high-pass filter would extenuate signals with frequencies lower than the cut-off frequency, leaving only the signals with frequencies larger than the cut-off frequency in the timeseries. Normally, the semi-static displacement would occur with a frequency lower than 0.1Hz (Ioulia et al., 2017). Using a cut-off frequency of 0.1Hz in the high-pass filter would probably also indicate removing the long period deformation, i.e. quasi-static or semi-static displacement. However, it is difficult to separate the semi-static deformation from the multipath biases in the GNSS measurement. Yu et al. (2020) also indicated that when GNSS and accelerometer are used to determine quasi-static displacement, the measurement accuracies are limited to 10 to 20 mm because of multipath signal errors. Therefore, most empirical research regarding a relatively rigid structure used RTS measurement for extraction of the semi-static displacement (Ioulia et al., 2017; Psimoulis., et al., 2016; Ye et al., 2020). The dominant frequency for the semi-static displacement is also very difficult to distinguish from the DFT spectrum due to the dominance of multipath, especially for a relatively rigid short span bridge where the amplitude of the semi-static displacement is in mm-level making it difficult to detect from the multipath signals or even from equipment noise. On the other hand, the dynamic displacement associated with the modal frequency of the bridge (~1.6-1.7 Hz) is not expected to be removed by the high-pass filter using 0.1Hz cut-off frequency. Therefore, only the dynamic deformation of the bridge is focused on.

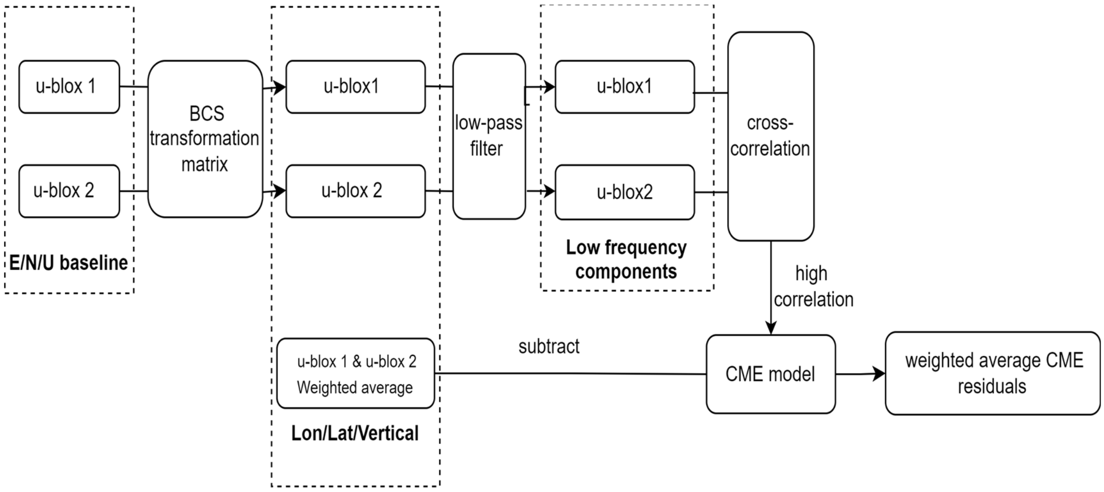

Figure 10. 12 *An alternative approach to remove the low frequency errors such as multipath errors by the CME method*

Figure 10.12 shows an alternative approach to mitigate the low frequency errors by using the spatial correlation between two closely-spaced rover stations instead of simply applying a high-pass filter. This novel approach aims to detect the correlation between the low frequency components and construct a CME model based on them. This approach has been proved useful for SBL roof tests under low multipath conditions. Therefore, it is again devised to test its feasibility for Wilford bridge monitoring. The constructed CME model is subtracted by the weighted average combination of u-blox 1 and u-blox 2 timeseries to obtain the CME filtered solutions which are later compared with the weighted average solution after high-pass filtering to evaluate its effectiveness.

10.4 RTS and GNSS results

The original RTS solutions timeseries in longitudinal, lateral, and vertical axes were plotted for each loading event with the inclusion of 20s of measurement before the excitation and 20s of measurement after the excitation. The equilibrium point was chosen as the first measurement point in the timeseries for each excitation and the timeseries was shifted to origin according to it. For all 12 excitations, it was noticed that some excitations only incurred minimal response from the bridge such as walking, standing, marching activities. The bridge responses from these loadings were too small to be captured from all equipment (GNSS and RTS), while more vibrant and distinguishable responses could be observed by other excitations such as jumping and swinging (corresponding to excitation events 04-09). For excitation 04-09, clear deformation could be detected from the vertical timeseries of RTS, Leica and u-blox. Figure 10.13 shows the original timeseries for u-blox1 for excitation 04-09 in the vertical component.

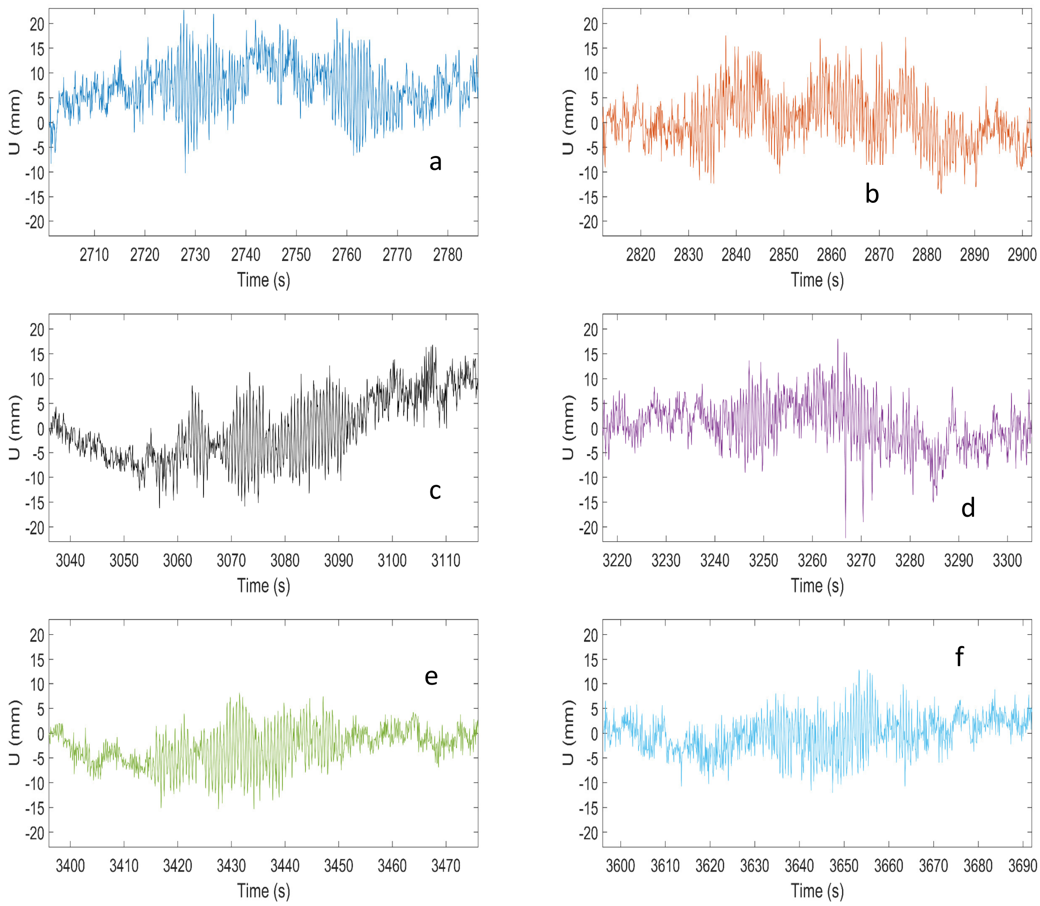

Figure 10. 13 *U-blox1 measurement of bridge vertical displacement for excitation 04-09 with 20s before excitation and 20s after excitation, top row: event 04 (a) and event 05 (b), middle row: event 06 (c) and event 07 (d), bottom row: event 08 (e) and event 09 (f). Clear dynamic motion can be seen within the excitation period.*

To compare the performance of different equipment on the dynamic displacement measurement, timeseries and spectral analyses are plotted for all excitation events using all available measuring equipment (Leica, RTS, and u-blox). In the following analyses, excitation 04 and excitation 05 sample results are shown as examples. In Figure 10.14, the RTS timeseries with equilibrium position at the starting point are plotted for event 04 and event 05 with corresponding DFT spectra. It can be seen from RTS timeseries the dynamic response of the bridge in lateral and vertical direction during excitation with corresponding frequency peak occurring at 1.40 Hz for lateral and 1.68 Hz for vertical component for event 04 and 1.41Hz for lateral and 1.65Hz for vertical components for event 05.

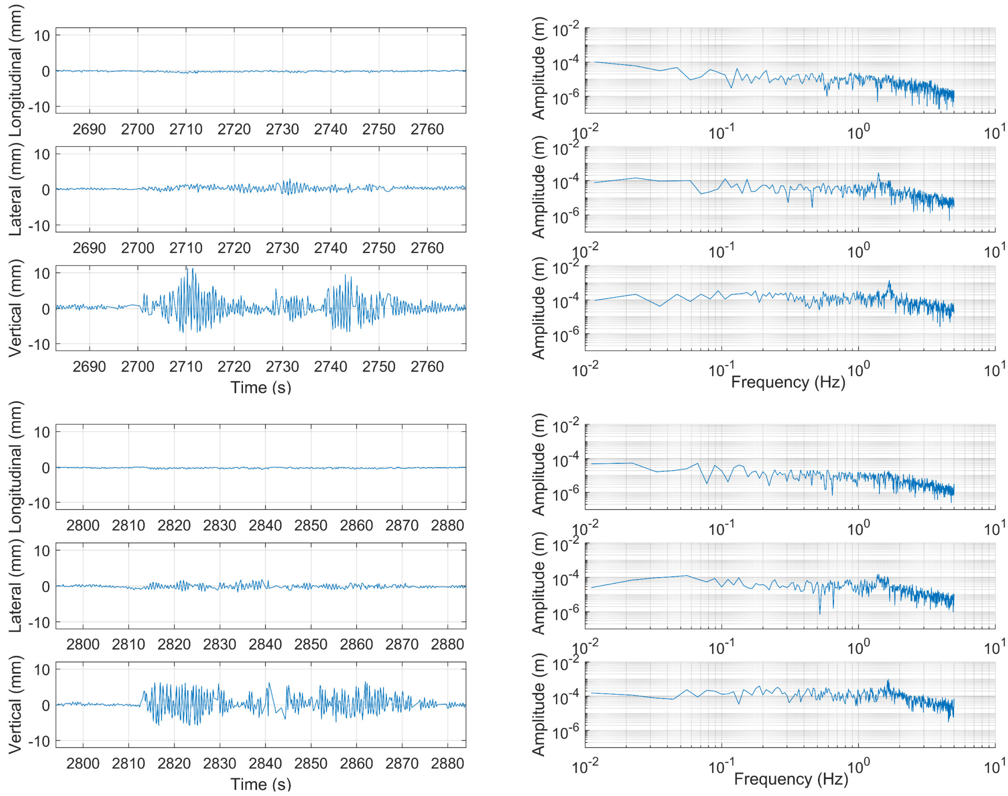

Figure 10. 14 *RTS Lon/Lat/Vertical original timeseries and corresponding DFT spectra for excitation event 04 (top row) and excitation event 05 (bottom row). The RTS timestamp is in UTC with an 18s leap second difference from GNSS time.*

The results from the GNSS solutions are also examined. Similar to RTS solution, the GNSS solution timeseries and spectra of Leica (Figure 10.15) and two u-blox receivers (Figure 10.16& Figure 10.17) are generated for event 04 & event 05 as an example. From Figure 10.15-10.17, it is shown that for longitudinal timeseries, majorly white noise can be detected. However, for lateral and vertical timeseries, a mixture of noise and structural response can be noticed. Due to the vertical loading and excitations on the bridge, the dominant responses are mainly detected from the vertical direction. Comparing Figure 10.14 and Figure 10.15-17, although the midspan of the same bridge is measured, due to different measurement instrument, different timeseries patterns are identified. In Figure 10.14, nearly no long period noise can be identified in RTS timeseries, but on the other hand, Figure 10.15-17 show obvious long period noise. This is also confirmed by the DFT spectra of the timeseries. From the spectra of RTS longitudinal/lateral/vertical solutions, the amplitude is comparatively lower than GNSS results, especially for low-frequency regions. For example, it can be detected in Figure 10.18, the low-frequency amplitude of RTS is at a level of around 10^{-4}m, whereas for GNSS solutions, the amplitude of low-frequency components could reach 10^{-3}m. It is also noticed that the RTS noise in the higher frequency band (>2Hz) is significantly reduced compared to GNSS results (Figure 10.18). The preliminary findings from RTS and GNSS timeseries and spectra show that RTS is more precise and accurate than GNSS due to the overall low noise level. For low-frequency components, RTS is not influenced as much by systematic errors compared to GNSS measurement, where GNSS suffers from majorly multipath induced long-period noise. For higher frequency band, the RTS also shows a decreased noise level compared to GNSS measurement.

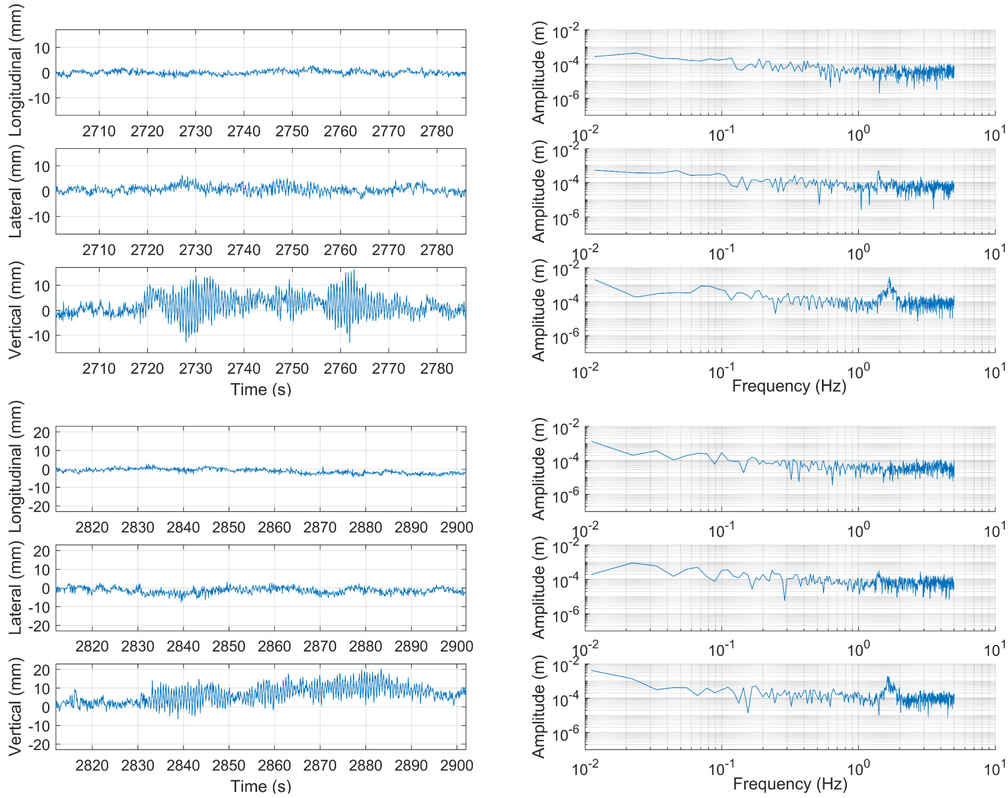

Figure 10. 15 *Leica Lon/Lat/Vertical original timeseries and corresponding DFT spectral analysis for excitation event 04 (top row) and 05 (bottom row)*

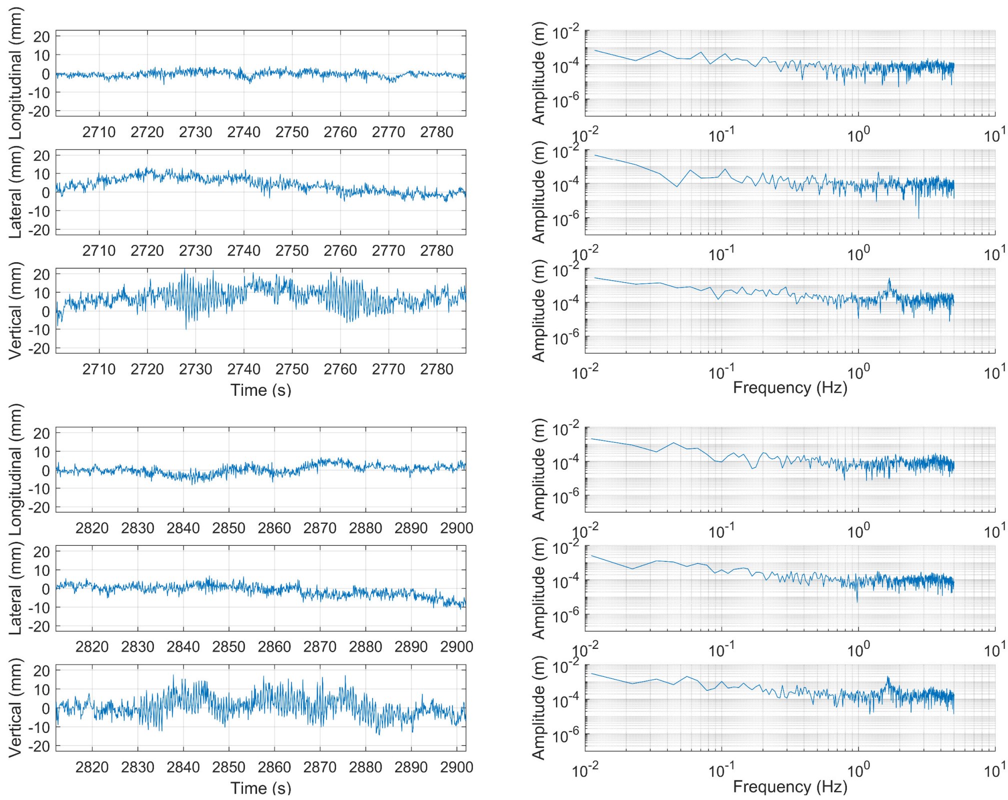

***Figure 10. 16** U-blox1 Lon/Lat/ Vertical original timeseries and corresponding DFT spectral analysis for excitation event 04 (top row) and 05 (bottom row)*

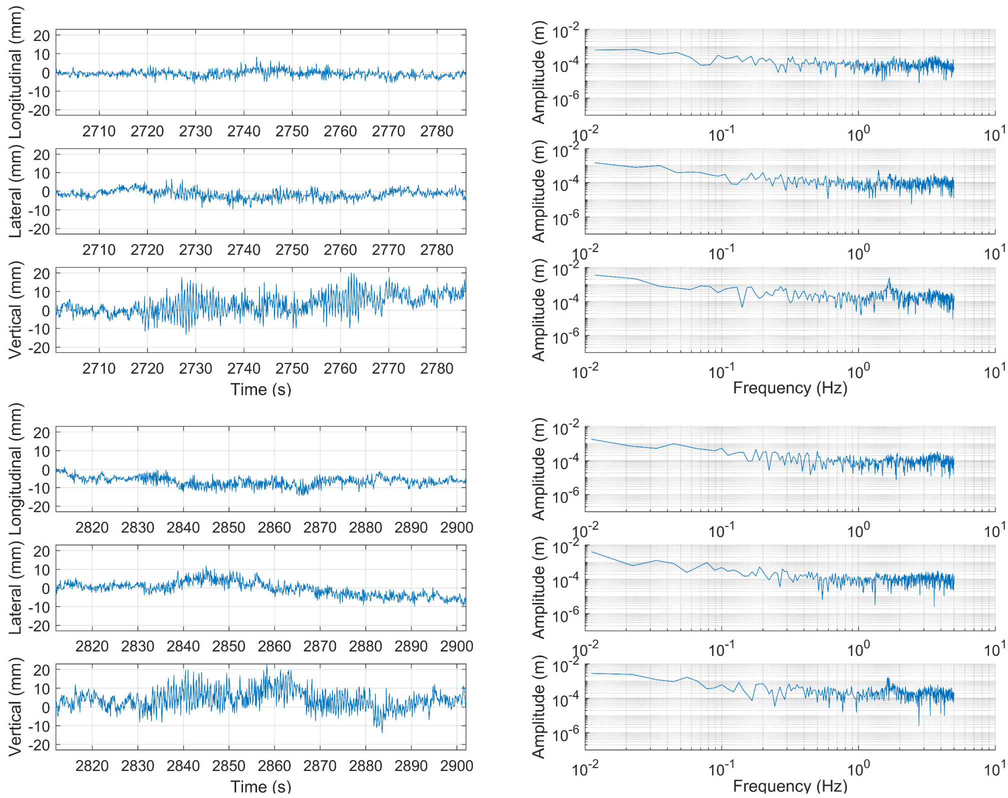

***Figure 10. 17** U-blox2 Lon/Lat/ Vertical original timeseries and corresponding DFT spectral analysis for excitation event 04 (top row) and 05 (bottom row)*

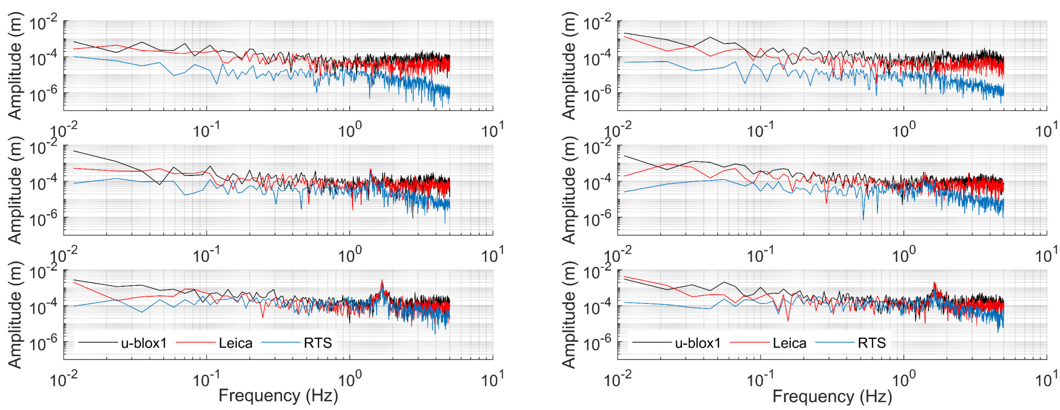

***Figure 10. 18** DFT spectra comparison of Lon/Lat/ Vertical original timeseries between u-blox1, Leica, and RTS for excitation (Left) event 04 and (Right) event 05*

In Figure 10.18, it is compared the spectra of Long/Lat/Vertical components for u-blox1, Leica, and RTS. In general, the RTS spectra have the smallest amplitude, followed by Leica, with the largest amplitude from u-blox1 across the whole frequency domain indicating the decreasing measurement precision from RTS to Leica to u-blox. Large deviations can be found especially in the low-frequency band (< 0.1Hz) between u-blox1, Leica, and RTS. This indicates low-frequency errors vary largely between u-blox1, Leica, and RTS results. For RTS, the low frequency errors usually contain equipment long-term systematic errors if uncalibrated. For GNSS, the low-frequency errors are majorly due to multipath. The difference in the low-frequency component of u-blox and Leica results implies the multipath difference between u-blox rovers (u-blox receiver& patch antenna) and Leica rover (Leica receiver& AS10 antenna). It is shown that the u-blox rovers suffer more from long-period noise (larger amplitude) than Leica receivers due to worse multipath suppression. On the other hand, for frequency range larger than 2Hz, a reduction of noise level could also be seen from u-blox to Leica indicating slightly higher measurement precision can be obtained by geodetic GNSS rovers in comparison to low-cost GNSS rovers.

The frequency analysis for excitation 04 and 05 is conducted for longitudinal/lateral/vertical components of the timeseries. The modal frequencies are detected from frequency analysis by pinpointing the frequency which has the largest corresponding amplitude response (Table 10.3). It is shown that no frequency of significant amplitude is detected with the longitudinal solution analysis for both excitation event 04 and 05. As for the lateral and vertical solution spectral analysis, it is shown that the four equipment would detect very similar peak frequencies, indicating the capability of low-cost equipment in revealing the bridge modal frequency.

Table 10. 3 *Frequencies at peak amplitude from the DFT spectral analysis of Lon/Lat/vertical components of RTS, Leica, U-blox1, U-blox2 for excitation event 04&05(Unit: Hz)*

	Axis	RTS	Leica	U-blox1	U-blox2
Event 04	Longitudinal	N/A	N/A	N/A	N/A
	Lateral	1st 1.40 2nd 1.65-1.70	1st 1.40 2nd 1.74	1st 1.40 2nd 1.69-1.75	1st 1.40 2nd 1.69
	Vertical	1.68	1.68Hz	1.68	1.68
Event 05	Longitudinal	N/A	N/A	N/A	N/A
	Lateral	1.41	1.41	1.38	1.34
	Vertical	1.65	1.63	1.63	1.65

The low-frequency GNSS errors would contaminate the evaluation of dynamic displacement of the bridge. Therefore, a high-pass filter or filtering of the low frequency elements of the timeseries should be implemented for an accurate evaluation of the bridge dynamic deformation. As aforementioned, RTS measurements suffer from a non-constant sampling rate. Prior to applying the high-pass filter, the RTS is firstly synchronised to GNSS measurement. A linear interpolation based on time is implemented to match the GNSS uniform 10Hz sampling rate. The Lon/Lat/Vertical coordinates of RTS non-uniform timestamps were linearly interpolated to the nearest 0.1s which leads to a resultant 10Hz RTS data. The modified RTS timeseries, as well as Leica and u-blox original timeseries, are then subjected to a high-pass filter which is applied to the longitudinal, lateral, and vertical components. The high-pass filter used is a Chebyshev high-pass filter of 8th order with a cut-off frequency of 0.1Hz. It is shown that the long period noise of the original timeseries is mitigated by high-pass filtering and only the high-frequency components including the dynamic response of the bridge above 0.1Hz remains in the timeseries (Figure 10.19, Figure 10.20).

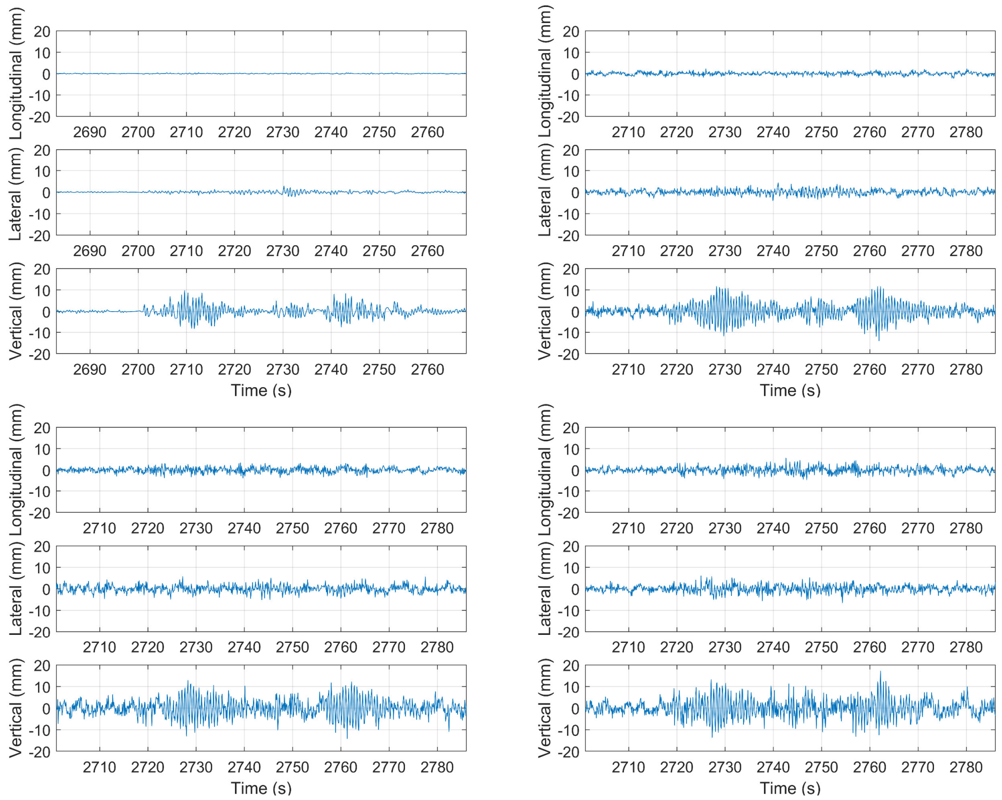

Figure 10. 19 *RTS (top left), Leica (top right), u-blox1 (bottom left), u-blox2(bottom right) Lon/Lat/Vertical timeseries after high-pass filtering for event 04. The RTS timestamp is in UTC time with a 18s leap second difference from GNSS time.*

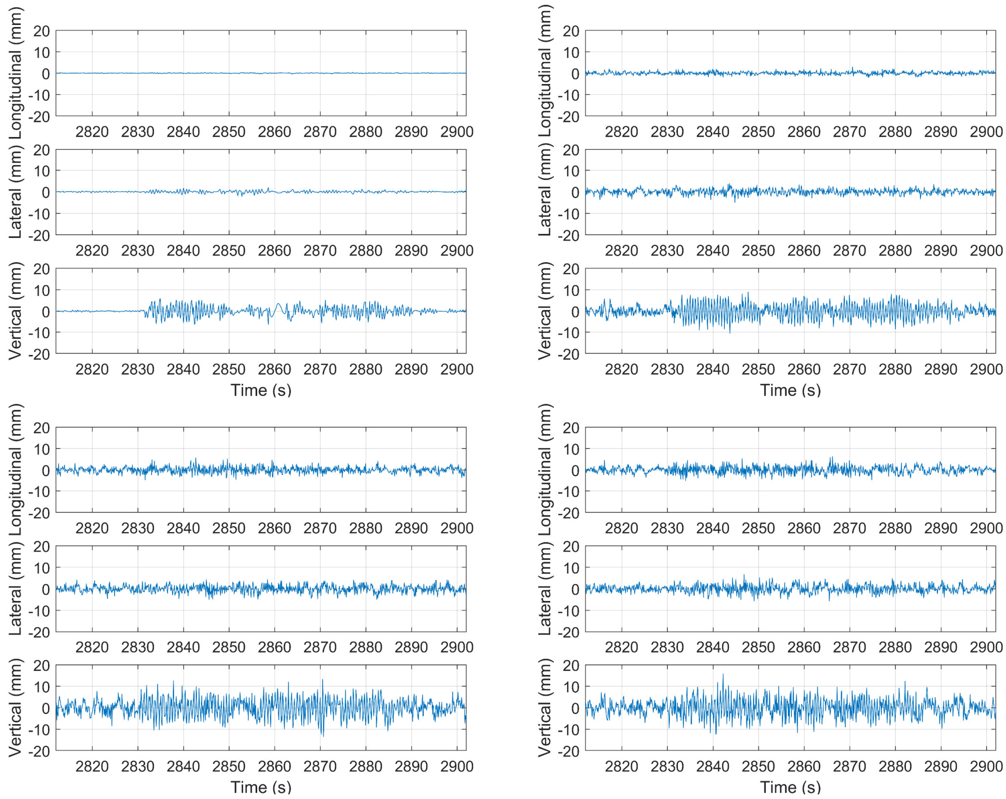

Figure 10. 20 *RTS (top left), Leica (top right), u-blox1 (bottom left), u-blox2(bottom right) Lon/Lat/Vertical timeseries after high-pass filtering for event 05*

10.5 Combined processing between two low-cost solutions

Since a closely-spaced dual low-cost rover system is deployed in the bridge monitoring experiment, further investigations are made to test the possibility of accuracy and precision improvement by combined processing between two low-cost sensors. Two approaches are tested, i) CME filtering, and ii) mean/weighted average combination.

The concept of CME filter, briefly, is to detect the common pattern of errors between different measurements and increase the measurement accuracy/precision by removing the CME. In this case, the low-frequency component of measurement errors between two closely-spaced low-cost stations are assumed spatially correlated and it is expected the performance could be improved with CME filtering. Therefore, the spatial correlation is analysed first between two low-cost receivers' low-frequency components. The correlation analysis is carried out by first applying a low-pass filter to the original Lon/Lat/vertical timeseries. Then the obtained long period noise timeseries from two u-blox are cross-correlated to calculate the correlation coefficient. Shown in Figure 10.21 is the Lon/Lat/Vertical timeseries obtained for two u-blox solutions after Chebyshev low-pass filtering with a cut-off frequency of 0.1Hz and passband ripple of 1dB for excitation event 04 & 05. It can be seen the correlation is poor for event 04, However, for event 05, a strong correlation could be detected for vertical components. The general poor correlation of low-frequency errors (mostly multipath) between the closely-spaced u-blox rovers is probably due to the challenging measurement environment as well as poor multipath suppression capability from patch antennas. The low frequency errors are in general, poorly correlated with the only exception for excitation 05 in the vertical direction (Table 10.4). This indicates the use of CME filtering is generally not feasible.

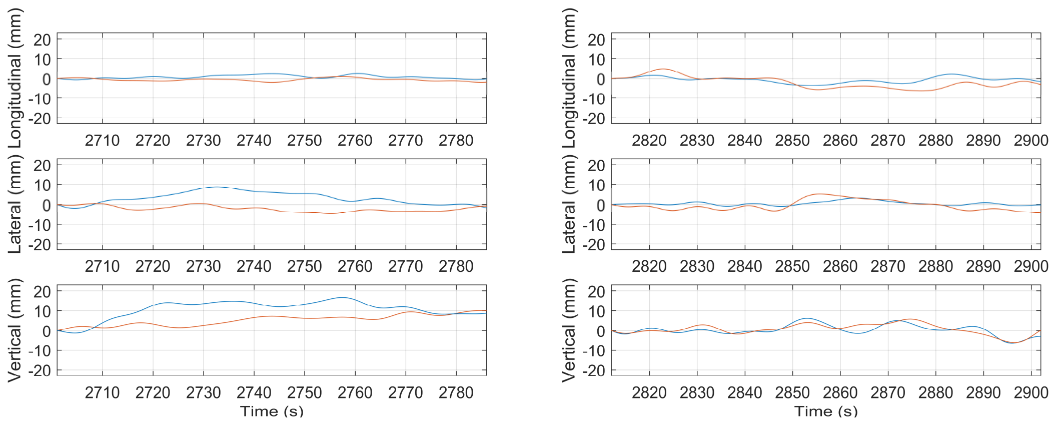

Figure 10. 21 *U-blox1, u-blox2 low-pass filtered Lon/Lat/Vertical timeseries after low-pass filtering, blue indicate u-blox1 and red indicate u-blox2 for (Left) excitation 04, and (Right) excitation 05*

Table 10. 4 *Correlation coefficient for u-blox1 and u-blox2 low-pass filtered result*

Event number	Lateral	Longitudinal	Vertical
01	0.59	-0.28	0.15
02	-0.19	0.48	-0.58
03	0.04	-0.57	-0.12
04	0.01	-0.04	0.33
05	0.74	0.51	0.80
06	-0.67	0.45	0.00
07	-0.69	0.08	-0.72
08	0.68	0.69	-0.43
09	-0.12	0.15	0.03
10	-0.84	0.40	0.06
11	-0.18	0.19	-0.51
12	-0.23	0.79	0.13

The occurrence of a stronger multipath error correlation between low-cost rover stations at excitation 05 is further investigated. It is assumed that the reason may be related to the change of relative geometry between the satellite orbits and receivers leading to a change of multipath phase angle. Therefore, the skyplot before and during excitation 05 is inspected (Appendix D) in Figure S10 and Figure S11. By examining the skyplot before excitation 05 and during excitation 05, it is shown a new GPS satellite G26 starts to appear in the skyplot with a 15-degree elevation angle. The addition of G26 could be a reason consequently affecting the correlation between the low frequency components of the low-cost receivers for excitation 05. The effect of medium to high multipath on the timeseries is believed to be quite complicated and different even for closely-spaced stations, since 1) it includes a combination of multipath errors from separate satellite signal, 2) considering a specific measurement location, the phase and amplitude of multipath is also related to relative geometry of the closely-spaced antennas, 3) the multipath could also be affected the pedestrians passing by. Therefore, the correlation between the closely-spaced stations should be looked further in the future.

To test the efficiency of CME filtering, the measurement from excitation 05 is analysed. The low frequency errors of respective u-blox measurements are obtained by the Chebyshev low-pass filter of original timeseries. CME model is established by using Equation 8.2 and is removed from the original weighted average combined timeseries.

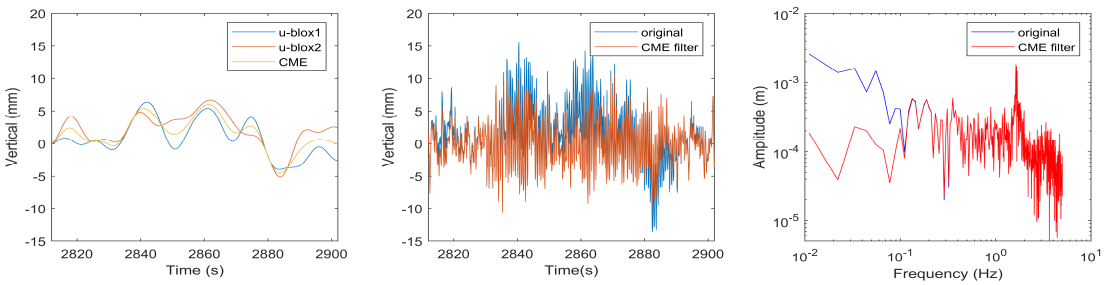

Figure 10. 22 *(Left) u-blox1, u-blox2 low-pass filtered vertical timeseries and simulated low frequency noise model based on CME for excitation 05. (Middle) the weighted average combined original timeseries before and after CME filtering. (Right) spectra of weighted average original timeseries before and after CME filtering*

It is shown in Figure 10.22 (left) the common low frequency errors simulated by CME equation (Equation 8.2) between u-blox1 and u-blox2 low-pass filtered timeseries. The resultant timeseries after CME filtering is alleviated from low-frequency multipath errors in the timeseries (Figure 10.22 (middle)), which is also shown as a huge reduction in amplitude response in the low frequency domain in the DFT spectra (Figure 10.22 (right)). The resultant CME filtered weighted average solutions are later compared with the one using a high-pass filter to assess its effectiveness.

It is also worth noting that in the data processing, due to the application of the low-pass filter, visible time shift is detected, i.e. the filtered timeseries is delayed in time and out of phase from the original timeseries, which would create a problem for CME model construction and later analysis. Therefore, the time shift due to the low-pass filter is compensated and corrected using the zero-phase filtering technique (Figure 10.23).

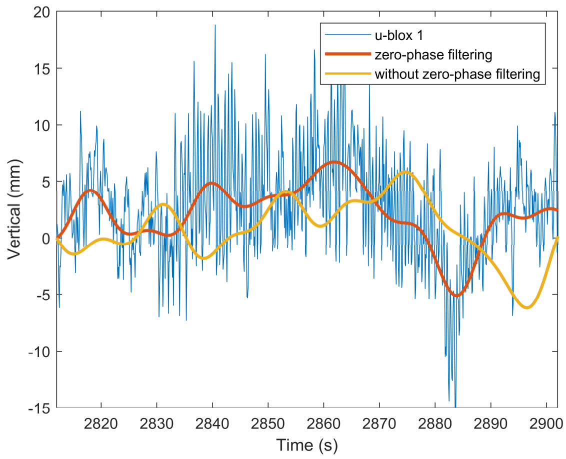

Figure 10. 23 *U-blox1 vertical timeseries for excitation 05, and corresponding low-pass filtered results with and without zero-phase filtering*

Another approach to integrate the two low-cost stations measurement is by average or weighted average. The 'average' is simply averaging of two u-blox longitudinal/lateral/vertical solutions for corresponding epochs (Equation 8.3). And weighted average solutions use weight to represent the contribution of each u-blox timeseries, which is calculated from RTKLIB output for each u-blox receiver for every epoch (Equation 8.4 and Equation 8.5). It is shown in Figure 10.25 and Figure 10.26 that the average and weighted average solutions are almost identical both in the original timeseries and spectra since the weightings used in the weighted average for every epoch are mostly equal to 0.5, or within a range between 0.45-0.55 (Figure 10.24) which is also applicable for all other excitations. Therefore, the weighted average and average are regarded similarly for later analyses. With weighted average combination of u-blox1 and u-blox2 original timeseries, long period noise still exists. And from the DFT spectra, similar modal frequency could be derived with Leica, RTS, and separate u-blox solutions. Figure 10.27 compares the mean/weighted average with separate u-blox solutions in the frequency domain. It is shown that by averaging process, a slight reduction in white noise with frequency larger than 1-2Hz could be noticed, while no significant improvement is detected for the low-frequency component.

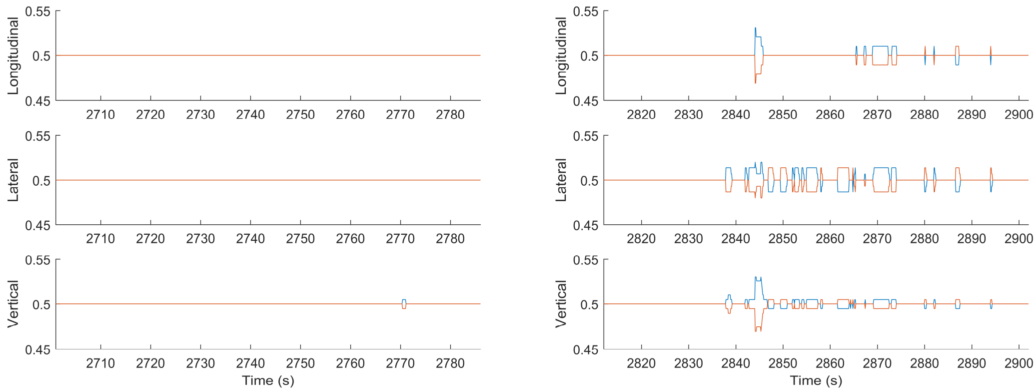

***Figure 10. 24** Lon/Lat/Vertical weighting used for u-blox1 and u-blox2 weighted average combination for (Left) excitation 04 and (Right) excitation 05*

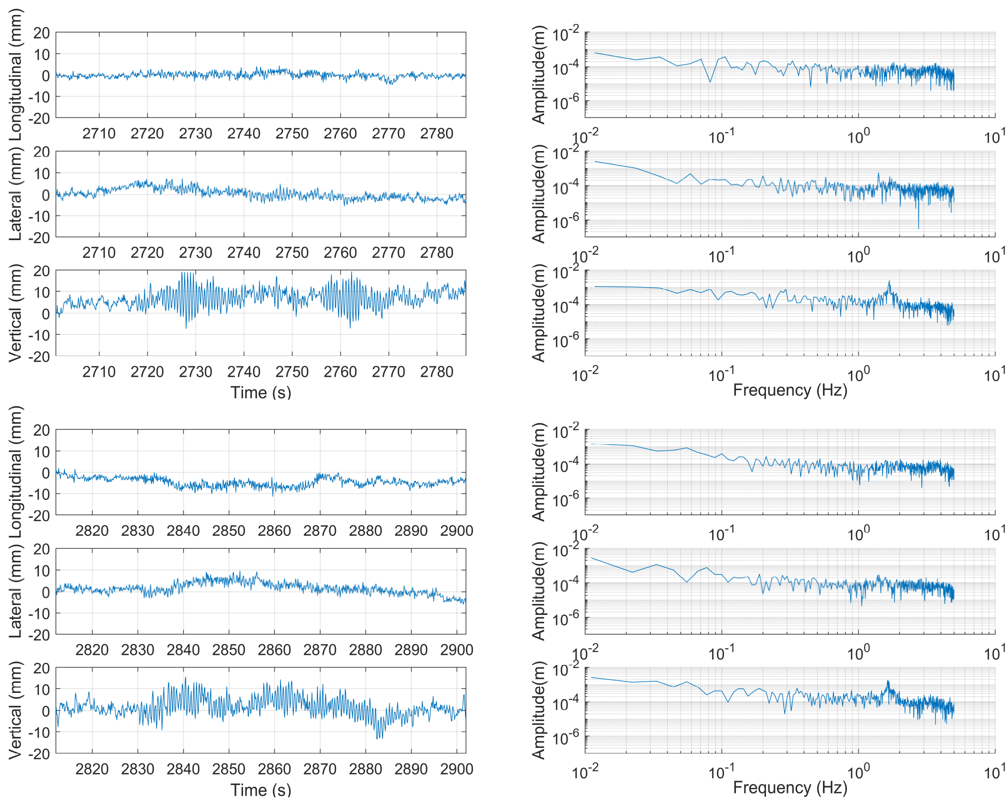

***Figure 10. 25** U-blox1 and u-blox2 averaged Lon/Lat/ Vertical original timeseries and corresponding DFT spectral analysis for excitation event 04 (Top row) &05 (Bottom row)*

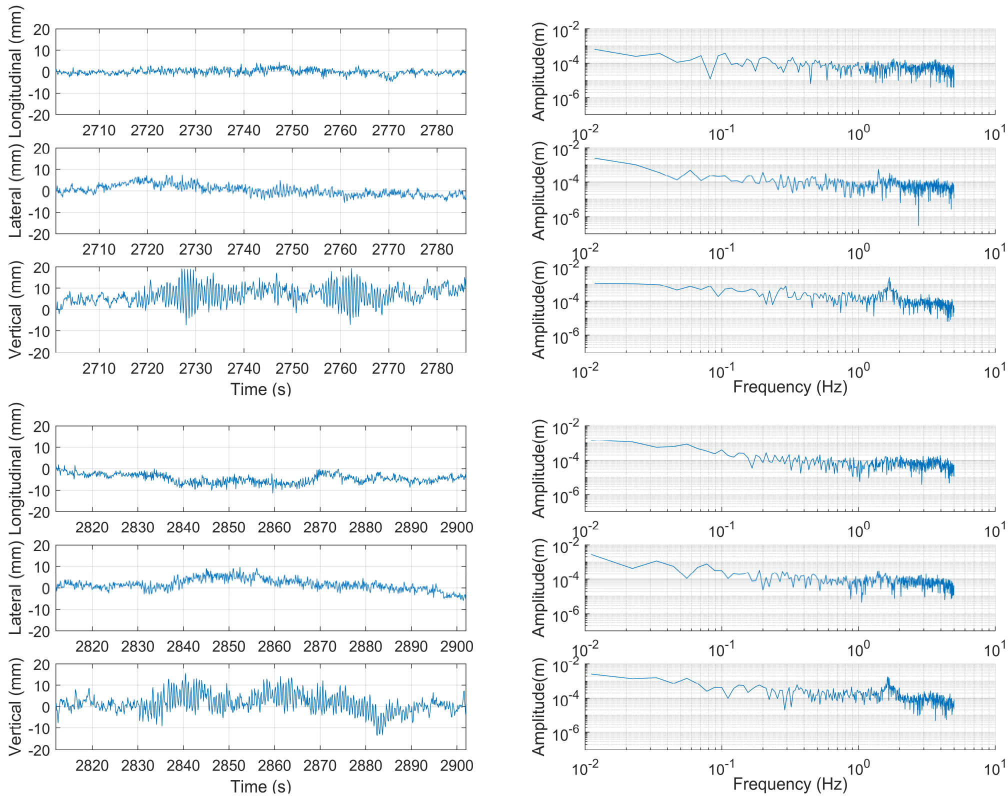

***Figure 10. 26** U-blox1 and u-blox2 weighted average Lon/Lat/ Vertical original timeseries and corresponding DFT spectral analysis for excitation 04 (Top row) & excitation 05 (Bottom row)*

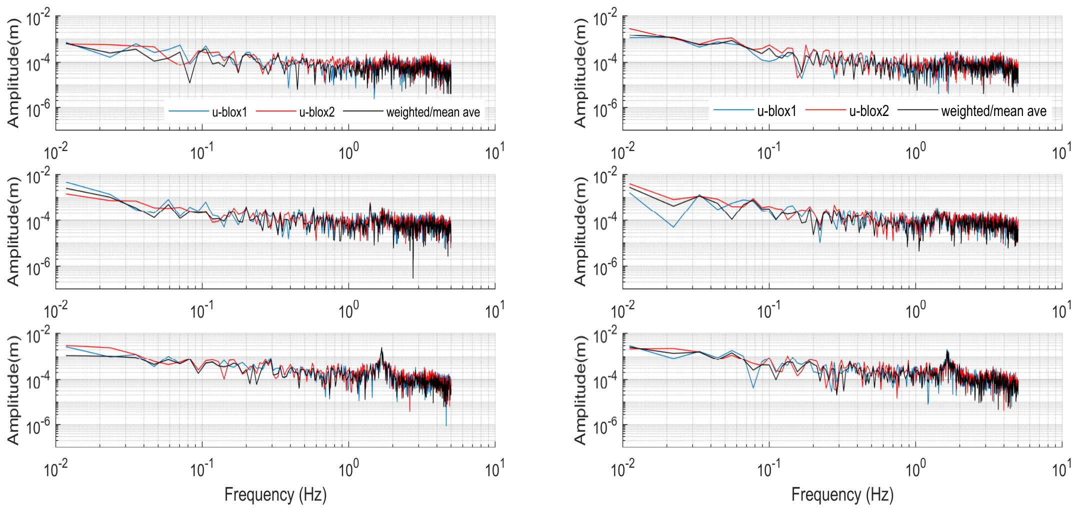

***Figure 10. 27** DFT spectra of the original Lon(top)/Lat(middle)/Vertical(bottom)timeseries for u-blox1, u-blox2, and the mean/weighted average solutions for (Left) excitation 04 & (Right)excitation 05*

To reduce the long period noise of the average combined timeseries, the Chebyshev high-pass filter with the same cut-off frequency and passband ripple is applied for excitation 04 and 05, and the output is shown in Figure 10.28. Comparisons are made between mean/weighted average, Leica, and RTS results both in the high-pass filtered timeseries and frequency domain (Figure 10.29). Compared to Leica and RTS solutions, the mean/weighted average timeseries still show a worse measurement precision as expressed by a higher noise level in periods before and after excitation. From the spectra comparison, it can be seen that Leica still outperforms the average combined solution both in multipath rejection and measurement precision with RTS expressing the lowest noise level across the whole frequency domain compared to GNSS solutions.

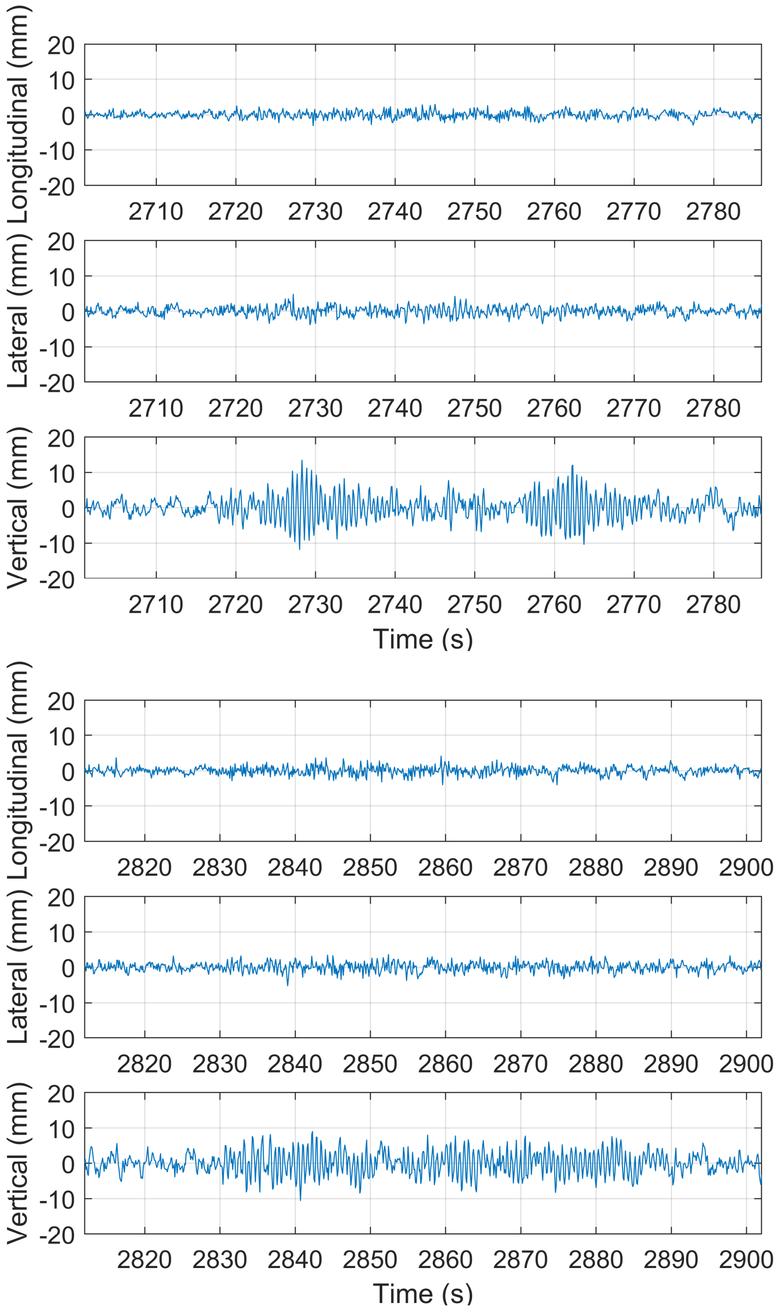

***Figure 10. 28** High-pass filtered mean/weighted average timeseries for excitation event 04 (top) and excitation event 05 (bottom).*

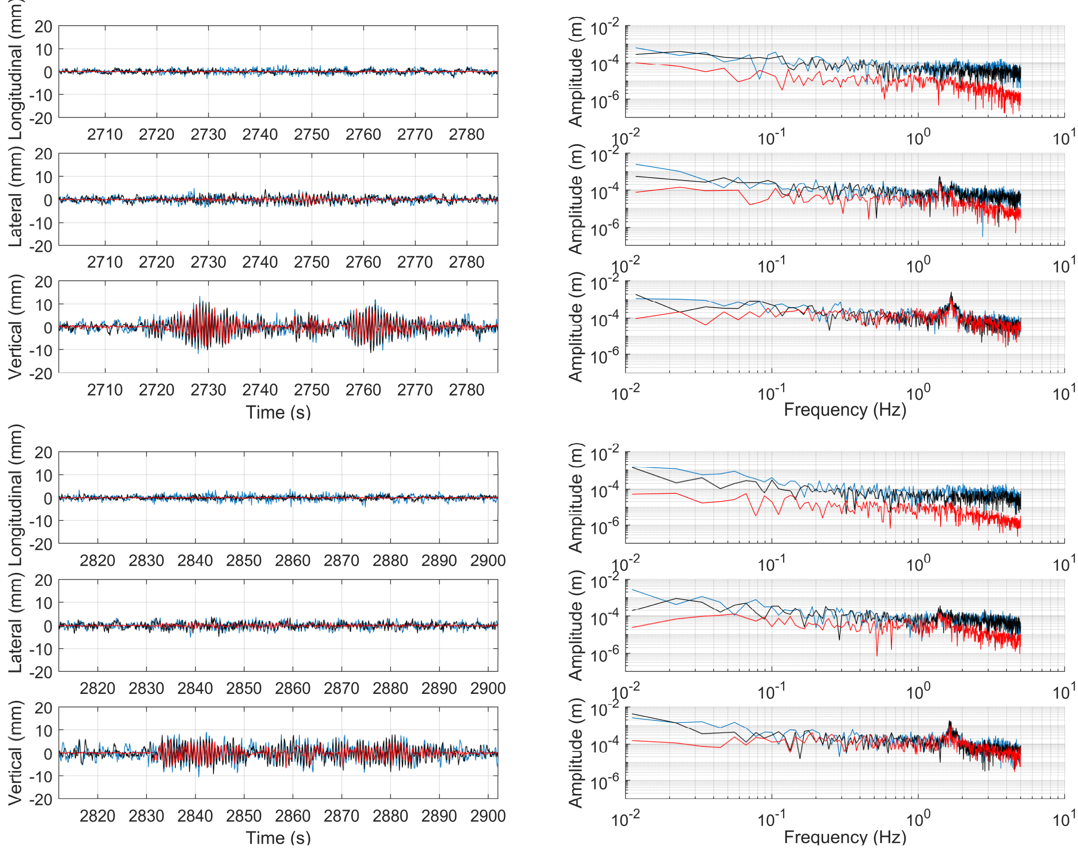

Figure 10. 29 *(Left) high-pass filtered Lon/Lat/Vertical timeseries for RTS (Red), Leica (Black), and average combined u-blox1 and u-blox2 solutions (Blue); (Right) corresponding DFT spectra for excitation 04 (top row) and 05 (bottom row)*

10.6 Accuracy comparison from different measurement results

10.6.1 Methods for visual comparison

To visualise and compare the accuracy of measurement from different equipment, the moving root mean square (MRMS) is used. The RMS is defined by Equation 10.2 and is used as a representation of the magnitude of a set of numbers. In this case, The RMS can be viewed as an indicator of displacement magnitude from the equilibrium point. By creating a moving window, the displacement magnitude can be shown as a function of time. Therefore, by calculation of the MRMS, the pattern of magnitude oscillation in the time domain could be examined.

$$\mathrm{RMS} = \sqrt{\frac{1}{n}\sum_{1}^{n} {x_n}^2}$$

Equation 10. 2 *RMS equation*

Where

- x_n refers to the measurement at current epoch n
- n is the number of elapsing epochs

In the analysis, the MRMS (with 5s moving window) of the high-pass filtered timeseries from Leica, RTS, u-blox1, u-blox2, u-blox1 and u-blox2 mean/weighted average are plotted and compared for both excitation 04 and 05 (Figure 10.30a and Figure 10.30b). The RTS timeseries is in UTC, it is noticed that a time difference of 18s corresponding to current leap seconds is present compared to GPS time. Therefore, RTS is first aligned with GPS time by shifting forward accordingly.

Using RTS measurement as a reference, the relative accuracy with respect to RTS measurement can be calculated by Equation 10.3,

$$\text{Relative accuracy} = \frac{Measurement - Measurement\ of\ RTS}{Measurement\ of\ RTS} = \frac{Measurement}{Measurement\ of\ RTS} - 1$$

Equation 10. 3 *Relative accuracy relative to RTS from other measurements*

Where

- Measurement represents MRMS values from different equipment
- Measurement of RTS represents RTS MRMS result

The relative accuracy denotes the accuracy from other equipment relative to RTS measurement. In Equation 10.3, the measurements in the relative accuracy calculation are represented by the MRMS values. The direct measurement from GNSS and RTS is not used due to the unstable sampling rate of RTS. As aforementioned, the unstable sampling rate of RTS is compensated by linear interpolation. As a result, the adjusted RTS measurement at each epoch is not directly measured but estimated by interpolation of real RTS measurement, which would introduce additional errors. Therefore, MRMS is used in the equation due to the inclusion of multiple measurements in the moving window, instead of the less confident interpolation estimation from a single epoch. The ratio of MRMS (moving window of 5s) for u-blox1, u-blox2, mean/weighted average, and Leica with reference to RTS is calculated and shown in Figure 10.30 c and Figure 10.30 d for excitation event 04 and 05 respectively. The ratio '1' is used as the reference denoting RTS measurement.

10.6.2 Comparison of instruments performances before excitation

The precision and accuracy comparison between different equipment is firstly carried out by analysis of measurement for periods before excitation. It can be seen in Figure 10.30a, when the bridge is under no excitations (no displacement is expected, for example during 2700s-2715s), the RMS of RTS is relatively low (<0.5mm) as compared to GNSS measurements (1-2.5mm), indicating high accuracy of RTS measurement. The RMS of RTS is also quite consistent compared to GNSS indicating its high measurement precision. The performance of u-blox and Leica for the period with no excitation is also assessed and compared. It is shown that higher RMS is detected for u-blox measurement (around 1.5-2.5mm) than Leica (around 1.0-1.6mm) during the period, indicating it is less accurate compared to Leica solutions. The u-blox RMS also shows a less consistent behaviour implying it is also less precise. By averaging, a drop in RMS value could be detected from each separate u-blox solution indicating an accuracy improvement, but Leica is still more accurate.

Similar conclusions could be drawn from Figure 10.30b. The RTS RMS remains consistently low (<0.5mm) before excitation (2800s-2815s). The RMS of Leica is comparatively lower than the RMS of u-blox measurement. Although by averaging, the RMS of each separate u-blox could be reduced, Leica still has better accuracy. Therefore, due to the high precision/accuracy of RTS measurement, it is used as the reference for the relative accuracy calculation.

From Figure 10.30c and Figure 10.30d, for the period before excitation, it is shown that the ratio between GNSS measurement and RTS measurement is largely ranging from 3-15 for excitation 04 and 5-18 for excitation 05. This indicates that the measurement with GNSS has large deviations from RTS in a relative sense for the period with no excitations. It can also be shown that similar to previous findings, the Leica is generally shown better accuracy than u-blox, even though the accuracy can be improved by the average combination of two u-blox solutions.

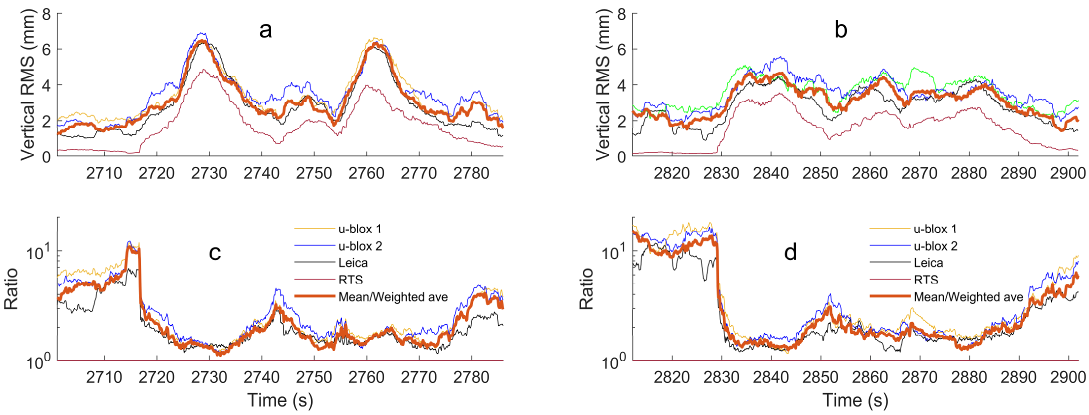

Figure 10. 30 *Moving RMS (5s moving window) for Vertical components of RTS, Leica, u-blox1, u-blox2, mean/weighted average timeseries after high-pass filtering (a) excitation 04 and (b) excitation 05; Ratio calculated using corresponding moving RMS with reference to RTS results (c) excitation 04 and (d) excitation event 05*

10.6.2 Performance comparison during excitation

Apart from the comparison of performance for different equipment before excitation, the performance is also compared during excitations. Regarding excitation 04, in the whole measurement cycle, it can be detected that the RMS of the average solutions is generally lower than separate results or at least similar to the more accurate result between two u-blox rovers. This indicates the overall accuracy improvement by averaging, although the improvement can be unobvious especially during the excitation for both excitation 04 and 05. For example, in Figure 10.30a, the mean/weighted average curve overlaps with u-blox1 at around 2730s and overlaps with u-blox2 at around 2760s. Comparing the mean/weighted average solution to the Leica solution, it can be found that Leica solutions are still generally more accurate. However, there can also be identified periods when the average combined results have lower RMS values (Figure 10.30a around 2730s and around 2750s).

On the other hand, regarding excitation event 05, the mean/weighted average combined timeseries also shows overall accuracy improvement from two separate u-blox receivers across the whole measurement cycle. Similar to findings for excitation

04, the accuracy improvement becomes less visible during excitation. For example, In Figure 10.28b, the mean/weighted average curve overlaps with u-blox2 at around 2830-2840s, with u-blox1 at around 2840s-2850s, and with u-blox2 again at around 2870s-2880s. Comparing mean/weighted average solution to Leica solution, although Leica still shows overall better accuracy, there are also periods when higher accuracy can be obtained from the average combined solution (Figure 10.30b around 2855s-2860s and around 2880s). The findings from Figure 10.28a and Figure 10.28b are also confirmed from observations made from Figure 10.28c and Figure 10.28d.

Regarding the relative accuracy comparison in periods before excitation and during excitation, it can be seen from both Figure 10.28c and Figure 10.28d that the ratio between GNSS and RTS measurement is larger at the beginning (before excitation) and at the end (after excitation) of the timeseries even reaching 15 at some point when there are no loadings applied to the bridge. The reason for that is probably due to little dynamic displacement incurred in periods with no excitations and the measurement only contains background noise. It can be inferred that for periods with no excitations, RTS is much more accurate than GNSS measurement. On the other hand, the ratios drop significantly during excitation regions. This implies that the GNSS measurement accuracy for dynamic displacement detection increases significantly during the excitation period compared to the period out of excitation.

By comparing measurements from different GNSS equipment, observations can also be made from Figure 10.28c and Figure 10.28d that, for the duration before and after excitation, large ratio differences can be detected between $\frac{u\text{−}blox\ 1}{RTS}$, $\frac{u\text{−}blox\ 2}{RTS}$, $\frac{mean/weighted\ average}{RTS}$, and $\frac{Leica}{RTS}$ results indicating their different performances under no excitation. Whereas during excitation, the difference in the ratio is comparatively small, especially when large displacement is to be detected, indicating comparable performance between them when a dynamic displacement is to be measured. This implies that compared to separate u-blox solutions, the accuracy improvement by Leica and mean/weighed average is less effective for periods during excitations than periods with no excitation.

Figure 10.30 only gives a preliminary indication of the performance of different equipment; the accuracy and precision are quantified in the next part. From Figure 10.30, it can be derived that, 1) with reference to RTS, the GNSS measurements are more accurate during the excitation compared to the period out of the excitation 2) The accuracy from different GNSS solutions is similar and comparable when the bridge is under dynamic loading, whereas different when under no excitations.

10.6.3 Amplitude, frequency, noise level determination, and accuracy evaluation

The amplitude of the displacement measured by different equipment is also evaluated for each excitation. The amplitude refers to the maximum value of displacement corresponding to the equilibrium position of the bridge. In the displacement calculation, it is first identified the period during excitation when the largest displacement occurs in RTS measurement. Then the maximum displacement is evaluated with the same period for other measurements. The amplitude derived is shown in Table 10.5.

It is expected that the best estimation can be derived by using RTS measurement due to its high precision and accuracy. It is shown in Table 10.5 that, generally the amplitude determined from the Leica rover is in closer proximity to the RTS compared to separate u-blox results with maximum deviation up to 2.7mm for excitation 05. As for u-blox solutions for excitation 05, excitation 06, and excitation 07, large deviations can be observed in u-blox1 and u-blox2 solutions reaching even up to 6mm difference, indicating high uncertainty of low-cost measurement. The disagreement between u-blox1 and u-blox2 results could be due to the reason identified in 10.3.1, where it is seen frequent vibrations of satellite numbers in NSAT timeseries for u-blox results, leading to potentially large uncertainty in solution calculation and amplitude determination. It is shown in Figure 10.31, the amplitude difference between u-blox1 and u-blox2 in Table 10.5 is due to some small jumps in the timeseries (for example, small spikes are shown around 2840s for u-blox1 vertical timeseries, and at around 3266s for u-blox2). It is also shown that the occurrence of these small spikes may be related to the drop of satellite numbers and would eventually affect the accuracy of amplitude determination. However, the reason for the large amplitude difference for excitation 06 is still unclear, where the amplitude determined from u-blox1 is even smaller than RTS measurement, this abnormal behaviour for u-blox1 should be further investigated in the future. Table 10.5 also demonstrates the little effect of average combined solution in accuracy improvement of amplitude derivation, nevertheless, regarding the whole timeseries, the average solution would generally improve the accuracy from separate results (Figure 10.30), this indicates its potential to achieve better accuracy with reduced noise level (Table 10.6) for dynamic displacement monitoring of the bridge.

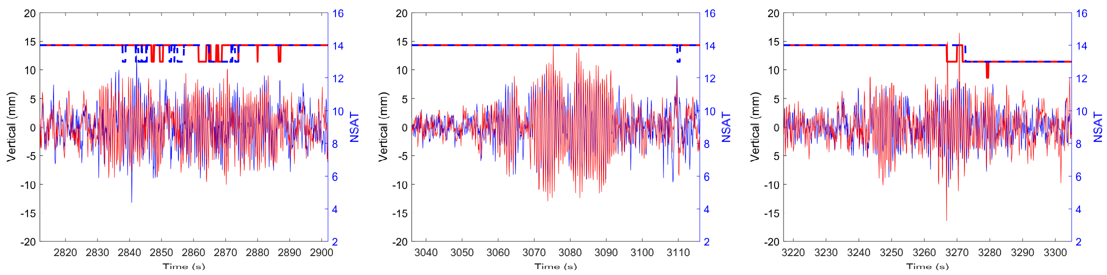

Figure 10. 31 *Occurrence of unexpected spikes (uncertainties) in correlation to satellite number drop, u-blox1 Vertical and NSAT timeseries (Blue) and u-blox2 Vertical and NSAT timeseries (Red) for (Left) excitation 05, (Middle) excitation 06, and (Right) excitation 07, where large amplitude deviation between u-blox1 and u-blox2 is identified*

Table 10. 5 *Displacement amplitude determined from high-pass filtered timeseries with respect to equilibrium point for Excitation 04 -09 (Unit: mm) and from CME filtered mean/weighted average timeseries for excitation 05*

	RTS	Leica	U-blox1	U-blox2	Mean/weighted average	CME filter
Excitation 04	9.8	11.4	13.8	13.4	13.5	
Excitation 05	6.3	8.9	8.8	13.2	10.5	10.6
Excitation 06	12.5	14.5	9.5	13.8	14.5	
Excitation 07	7.4	7.9	16.5	10.5	12.1	
Excitation 08	10.0	10.0	10.2	11.0	10.6	
Excitation 09	8.8	9.1	10.3	13.0	10.4	

Table 10. 6 *The mean μ and STD σ for the high-pass filtered solution of the 20s before excitation for excitation 04-09 (Unit: mm) and for CME filtered weighted average combined solution of 20s before excitation for excitation 05.*

Unit(mm)		RTS	Leica	U-blox1	U-blox2	Mean/weighted average	CME filter
Excitation 04	μ	0	0	0	0	0	
	σ	0.3	1.4	2.3	2.1	1.8	
Excitation 05	μ	0	0	0	0	0	0
	σ	0.2	1.8	2.7	2.6	2.2	2.3
Excitation 06	μ	0	0	0	0	0	
	σ	0.1	1.3	1.4	1.5	1.2	
Excitation 07	μ	0	0	0	0	0	
	σ	0.8	1.6	2.2	1.7	1.7	
Excitation 08	μ	0	0	0	0	0	
	σ	0.3	1.2	1.2	1.1	1.0	
Excitation 09	μ	0	0	0	0	0	
	σ	0.1	1.3	1.7	1.8	1.3	

Table 10. 7 *Frequency detected from spectral analysis from each excitation 04-09*

	Axis	RTS	Leica	U-blox1	U-blox2
Event 04	Longitudinal	N/A	N/A	N/A	N/A
	Lateral	1st 1.40 2nd 1.65-1.70	1st 1.40 2nd 1.74	1st 1.40 2nd 1.69-1.75	1st 1.40 2nd 1.69
	Vertical	1.68	1.68Hz	1.68	1.68
Event 05	Longitudinal	N/A	N/A	N/A	N/A
	Lateral	1.41	1.41	1.38	1.34
	Vertical	1.65	1.63	1.63	1.63
Event 06	Longitudinal	N/A	N/A	N/A	N/A
	Lateral	1.436/1.685	1.411/2.846	1.685	N/A
	Vertical	1.685	1.673/2.846	1.685/2.846	1.685/2.846
Event 07	Longitudinal	N/A	N/A	N/A	N/A
	Lateral	1.40	1.40	1.40	1.40
	Vertical	1.66	1.65	1.65	1.65
Event 08	Longitudinal	N/A	N/A	N/A	N/A
	Lateral	1.67	1.67	1.67	1.41/2.86/3.35
	Vertical	1.67	1.67	1.67	1.67
Event 09	Longitudinal	N/A	N/A	N/A	N/A
	Lateral	0.8012/1.39	1.39	1.39/3.205	1.42
	Vertical	1.61	1.60	1.61	1.61

The parameters (mean (μ) and STD (σ)) to reflect the noise level of measurements from different equipment are also calculated in Table 10.6 based on a 20s-period before excitation using the high-pass filtered results. By assuming a normal distribution of the background noise before excitation, the noise levels are estimated accordingly with a 99.7% confidence level, which corresponds to an interval within $\mu \pm 3\sigma$. It is assumed that the external and internal noise before excitation and during excitation is similar. Therefore, the noise level can be determined for RTS, Leica, u-blox 1, u-blox 2, and the mean/weighted averaged solution, respectively for each excitation. It is shown in Table 10.6, the noise level from mean/weighted average combined results are effectively reduced from separate u-blox solutions for each excitation 04-09. Moreover, a similar noise level between CME filtered and high-pass filtered average combined results can be seen from excitation 05.

The modal frequencies derived from the DFT spectra are also concluded for excitation 04-09 (Table 10.7). By examining the frequency obtained for different excitations using different equipment, although the modal frequencies derived from swinging activity have an offset within 0.1Hz from jumping events, very similar modal frequency could also be revealed from low-cost GNSS receivers in comparison to high-grade geodetic GNSS and RTS equipment.

The measurement difference between different equipment is calculated by root mean square difference (RMSD) between different timeseries, using Equation 10.4.

$$RMSD = \sqrt{\frac{\sum_{t=1}^{n}(x_{1,t} - x_{2,t})^2}{n}}$$

Equation 10. 4 *RMSD equation*

Where

- n is the number of epochs,
- t represents the current epoch
- $x_{1,t}$ denotes the measurement of one equipment at the current epoch
- $x_{2,t}$ denotes the measurement of the other equipment at the same epoch.

By using Equation 10.4, the difference between two different measurements can be evaluated. RMSD values from u-blox1, u-blox2, mean/weighted average are calculated correspondingly with respect to the Leica solution. The RTS measurement is not used in the evaluation mainly due to the unstable RTS sampling frequencies. As a result of linear interpolation of RTS measurement to synchronise with GNSS measurement, it is perceived that the time interpolation of measurement could not reflect true RTS measurement at each interpolated timestamp. When calculating RMSD, the inaccurate estimation in RTS measurement would further degrade the results making it less valid. Therefore, the Leica measurement with a constant sampling rate is used as the reference. In the calculation of RMSD, the 20s before excitation and period during excitation are adopted, the 20s after excitation is not considered due to potential post-excitation related movement.

Table 10.8 shows the RMSD values for u-blox1, u-blox2, and mean/weighted average compared to Leica results. It can be seen from Table 10.8, by using mean/weighted average results, the difference from Leica results is further reduced when compared to separate low-cost solutions, this indicates the overall accuracy improvement by mean/weighted average processing. It is also shown that the maximum RMSD of u-blox to Leica is around 3mm with RMSD generally larger during excitation compared to period without excitations.

Finally, the RMSD of the CME filter for excitation 05 is also calculated with reference to Leica results, it is shown that for mean/weighted average solutions, larger measurement deviation from Leica solution is detected by CME filter (for example 2.7 for before excitation and 2.9 for after excitation) compared to high-pass filter (for example 2.4 for before excitation and 2.4 for after excitation). This implies that CME filtered results are less accurate than high-pass filtered results both for the period before excitation and during excitation for mean/weighted average solutions. However, when compared to separate high-pass filtered u-blox results, an improvement can be detected from the CME filter with the mean/weighted average results.

Table 10. 8 *RMSD value (mm) for u-blox1, u-blox2, Mean/weighted average with reference to Leica results for periods 20s before excitation and period during excitation*

	u-blox1		u-blox2		Mean/weighted average		Mean/weighted average CME	
Excitation	before	during	before	during	before	during	before	during
04	2.2	2.4	2.2	2.9	1.9	2.1		
05	3.1	2.9	2.5	3.2	2.4	2.4	2.7	2.9
06	1.8	2.6	1.6	2.3	1.5	2.0		
07	2.2	3.0	1.9	2.6	1.8	2.4		
08	1.4	1.7	1.2	1.5	1.2	1.4		
09	1.9	2.5	2.1	2.7	1.6	2.2		

10.7 Comparison of deformation monitoring results; GPS-only and GPS+GLONASS solutions

The previous analyses and results are all based on GPS+GLONASS timeseries. Since both GPS and GPS+GLONASS timeseries during excitation events are not disturbed by the occurrence of cycle slips, comparisons are made between the final solutions from GPS only and GPS+GLONASS timeseries to assess the impact of multi-constellation for deformation monitoring. The comparison of GPS-only and GPS+GLONASS solutions are shown in Figure 10.32, Figure 10.33, and Figure 10.34 for u-blox1, u-blox2, and Leica solutions respectively, in forms of high-pass filtered result, MRMS and NSAT/GDOP timeseries. It is shown that from both RMS and high-pass filtered results, by incorporating GLONASS constellation, a general improvement in accuracy can be detected with a decrease of GDOP value. It could also be noted that generally, the accuracy improvement by the inclusion of GLONASS is comparatively more significant for low-cost u-blox measurement than geodetic measurement.

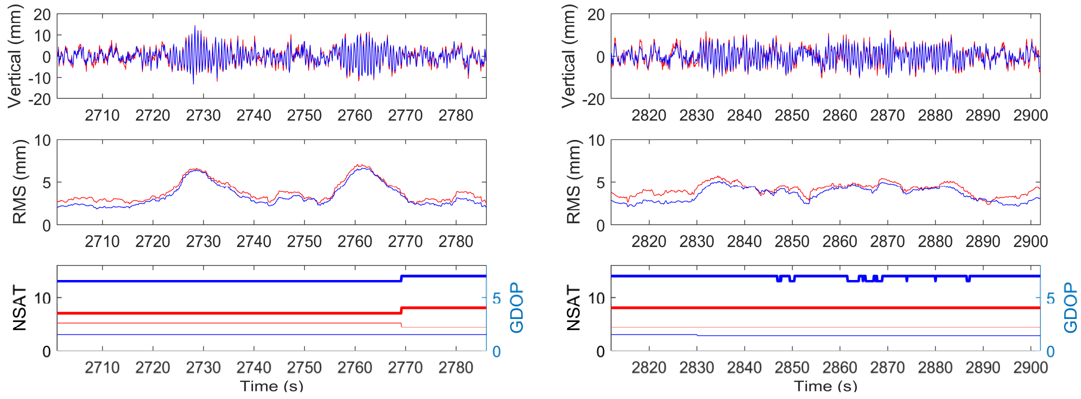

***Figure 10. 32 Top row**: u-blox1 GPS-only(red) and GPS+GLONASS (blue) high-pass filtered timeseries for (left) excitation 04 and (right) excitation 05. **Middle row:** MRMS with moving window of 5 seconds of high-pass filtered u-blox1 GPS-only (red) and GPS+GLONASS (blue) timeseries for (left) excitation 04 and (right) excitation 05. **Bottom row**: (thick line) number of valid satellites (NSAT), and (thin line) GDOP timeseries observed by u-blox1, with GPS-only (red) and GPS+GLONASS (blue).*

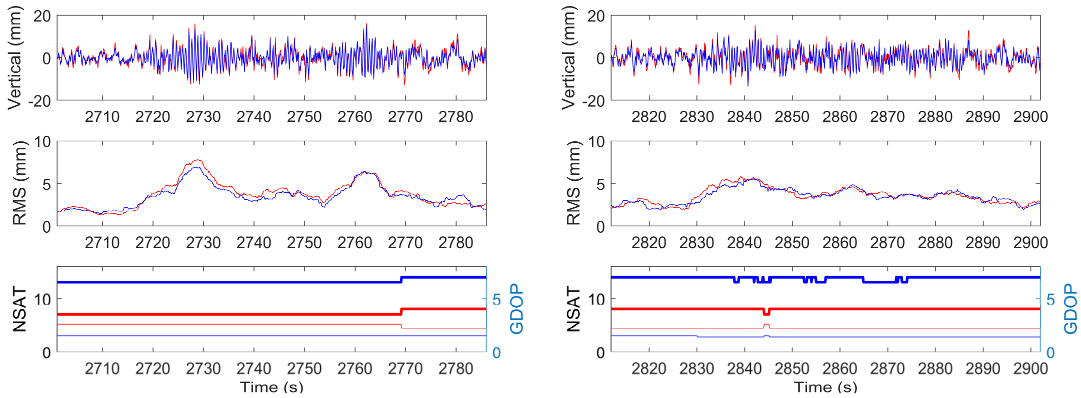

***Figure 10. 33 Top row**: u-blox2 GPS-only(red) and GPS+GLONASS (blue) high-pass filtered timeseries for (left) excitation 04 and (right) excitation 05. **Middle row:** MRMS with moving window of 5 seconds of high-pass filtered u-blox2 GPS-only (red) and GPS+GLONASS (blue) timeseries for (left) excitation 04 and (right) excitation 05. **Bottom row**: (thick line) number of valid satellites (NSAT), and (thin line) GDOP timeseries observed by u-blox2, with GPS-only (red) and GPS+GLONASS (blue).*

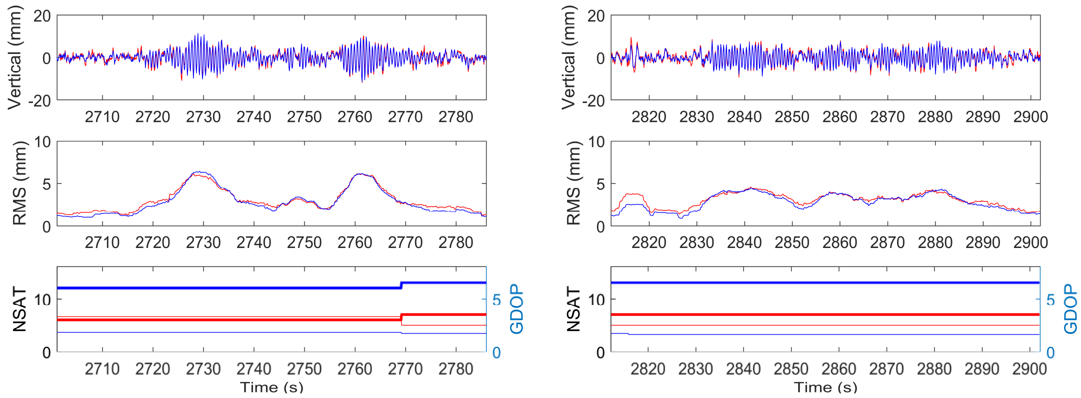

***Figure 10. 34 Top row**: Leica GPS-only(red) and GPS+GLONASS (blue) high-pass filtered timeseries for (left) excitation 04 and (right) excitation 05. **Middle row:** MRMS with moving window of 5 seconds of high-pass filtered Lecia GPS-only (red) and GPS+GLONASS (blue) timeseries for (left) excitation 04 and (right) excitation 05. **Bottom row**: (thick line)*

number of valid satellites (NSAT), and (thin line) GDOP timeseries observed by Leica, with GPS-only (red) and GPS+GLONASS (blue).

10.8 Discussion and Summary

In this chapter, the feasibility of using low-cost GNSS receivers in measuring the dynamic deformation of a rigid bridge is tested in comparison to geodetic GNSS receivers and high precision RTS measurement. Approaches of combining the results from two closely-spaced low-cost GNSS rovers are also attempted to obtain a more accurate and precise result.

The experiment uses four different sensors (1* Leica rover, 2*u-blox rovers, and 1*RTS target) deployed at midspan of the bridge to measure displacement due to different human loading. The RTS measurement of the target is expected to have the most accurate and precise results in comparison to GNSS results and is therefore chosen as the reference. It is claimed that the RTS model (MS 60) adopted in the experiment has a distance accuracy of 1mm + 1.5ppm and angular accuracy of 1" (Leica Geosystem, 2020). For GNSS measurement, the Leica GS10 used is allegedly to have an accuracy of 8 mm + 1 ppm horizontally and 15 mm + 1 ppm vertically (Leica Geosystem, 2012).

During the experiment, due to RTS monitoring with only one face, the measurement error of RTS includes the mechanical imperfection within the equipment, such as line of sight error, tilting axis error, vertical collimation error, and compensator index error. For GNSS solutions, due to signal reflection and diffraction from surrounding obstruction, the multipath would remain the major source of error for a SBL DD processing. Other noise from the measuring equipment such as receivers' internal noise and antennas PCV would also be reflected in the solution timeseries. To mitigate multipath and PCV error, it is assumed that they are noise normally of low frequencies since their variations are related to gradual change in the relative geometry of observed satellite to receivers. Hence, the original timeseries from different sensors (RTS, Leica, two u-blox receivers) are filtered by the same Chebyshev high-pass filter to remove any long period noise. The resultant filtered data should be composed of high-frequency dynamic responses from the bridge under imposed load and receiver noise. The DFT spectral analyses are also conducted. From the spectra, it shows that a similar modal frequency could be derived from all measuring devices regarding latitude and vertical timeseries for jumping and swinging excitations. Comparing DFT spectra of the original timeseries, it is shown that across the frequency domain, the spectra from the two u-blox receivers generally have the largest amplitude, followed by the Leica spectrum, with the smallest amplitude from RTS. This indicates the coloured noise and white noise level gradually decrease from low-cost rover to geodetic rover. And least impact of noise can be shown in RTS measurement.

The approaches of accuracy and precision improvement by taking advantage of the two closely-spaced low-cost stations are also tested. Similar to the SBL roof test, it is first devised to remove the spatial correlated noise pattern between two u-blox solutions by CME filter. However, further analysis shows that the low-frequency pattern of closely-spaced u-blox rovers is not generally correlated which indicates the CME filter is not feasible for general use. Nevertheless, for excitation 05, a strong correlation is still detected for the low-frequency vertical component of the two closely-spaced rover stations. Therefore, CME filtering is applied only to excitation 05 to test the effectiveness of this method. In the study, the CME model is created from the low frequency components of the two u-blox GNSS timeseries using a Chebyshev low-pass filter. It is shown that without zero-phase filtering, the low-pass filtered timeseries would be delayed in phase compared to original timeseries. The phase shift of the low-pass filter can be adjusted by zero-phase filtering. It is found that CME filtering has the potential to remove the low-frequency errors in the timeseries. Besides the CME filtering approach, it is also attempted to combine the two u-blox original data by mean and weighted average. Due to the nearly equal weighting of the coefficients, it is found that the mean and weighted average results are nearly the same. Spectral analysis and high-pass filter are also applied and conducted to the average and weighted average solutions. It is shown that with average and weighted average, the high-frequency region related to white noise tends to be reduced in comparison to each separate solution.

To investigate the feasibility of deformation monitoring with low-cost GNSS rovers, the performance of different sensors (RTS, Leica, 2*u-blox) in displacement monitoring is compared both for the period before excitation and after excitation. The MRMS of high-pass filtered solution for each equipment and the average of two u-box solutions are plotted. It is shown that RTS would generally have the best accuracy and precision among all solutions, followed by Leica solution and least accuracy and precision from u-blox. A general trend of increased accuracy could be detected with the mean/weighted average from each separate low-cost result, which could even reach better accuracies than Leica during some periods. However, for periods within excitations, the effect of accuracy improvement by average is not so obvious. The relative accuracy between different equipment with RTS is calculated as a ratio and plotted in the timeseries. It is concluded that with RTS measurement as the reference, the GNSS solutions are more accurate in reflecting the real displacement of the bridge during the excitation period compared to periods without excitations. Furthermore, similar and comparable performances between low-cost and survey-grade GNSS solutions can be derived when the bridge is under dynamic deformation.

The amplitude during the excitation period is also evaluated and determined with reference to RTS. It is found that compared to u-blox results, the Leica results are more accurate. Large deviations can be detected between the two u-blox receiver solutions during some excitation events, which could be due to variations in the number of satellites used for coordinate computation and no obvious improvement in amplitude determination could be detected from the averaging process.

To quantify the noise level for measurement from each equipment, it is assumed constant measurement noise level (internal receiver noise and antenna noise) during excitation and without excitation. The 3-sigma rule is adopted with a 99.7% confidence level based on the normal distribution for the non-excitation period. It can be inferred, although u-blox solutions show an overall higher noise level as compared to RTS and Leica for both separate and average solutions, a lower STD could be obtained with the average process than from separate low-cost results. The measurement differences between low-cost u-blox receivers are also quantified based on RMSE with respect to Leica measurements, it is shown that the overall measurement difference between u-blox and Leica is no more than ~3mm both before excitation and during excitation.

In conclusion, from the Wilford bridge trial, it is verified the capability of using low-cost receivers in measuring bridge centimetre level deformation. The amplitude of bridge deformation due to excitations are all less than 1.5 cm. It is shown that with reference to RTS solutions, the amplitude could be detected with a maximum deviation of 2.7mm from the geodetic GNSS rover and with a maximum deviation of 9.1mm from the low-cost rover. However, it is worth mentioning that the maximum 9.1mm is believed to be caused by the signal tracking instability of the u-blox receiver, where GPS+GLONASS NSAT frequently oscillates in the timeseries. The difference is normally up to 4mm if the effect of NSAT vibration on the amplitude determination is ignored. It is also shown from the RMSD calculation (Table 10.8) that, although the u-blox rover is less accurate than Leica, the overall measurement difference in between them is not large, within a range between 1-3mm even during excitations. The difference could be further reduced by average processing between two closely-spaced low-cost solutions to a maximum of 2.5mm. By examining all excitation events, similar modal frequencies are derived from the DFT spectra using different measuring instruments.

Chapter 11 Conclusion and outlook

11.1 Conclusions

The study aims to assess the feasibility of low-cost receivers in deformation monitoring and evaluate the best achievable accuracy and precisions through experiment design and data analysis. To achieve this goal, the performance of low-cost receivers was evaluated in different experiment configurations. Several roof tests (ZBL, SBL static, SBL kinematic) were conducted prior to the practical fieldwork measurement (Wilford bridge trial) and approaches were devised to improve the low-cost measurement precision by incorporation of another low-cost receiver in the nearfield. The roof tests were divided into three sub-experiments, 1) a preliminary ZBL test for receiver internal noise evaluation, 2) a SBL test with static rovers to assess and mitigate the systematic noise in a practical monitoring configuration, 3) a SBL experiment with a rover moving in a pre-designed trajectory and frequency to analyse the precision of GNSS rover in dynamic displacement monitoring. In the 2nd and 3rd lab test, another low-cost GNSS station consisted of the same model of equipment (patch antenna & u-blox receiver) was configured in close-vicinity for possible precision enhancement by combined processing between the two low-cost rover measurements. Finally, a bridge monitoring fieldwork was carried out on a short-span suspension bridge, in which two closely-spaced low-cost GNSS rovers, geodetic GNSS rover and RTS were deployed. The performance of the low-cost GNSS receivers in monitoring the same displacement in midspan of the bridge was assessed against measurements from other geodetic instruments.

11.1.1 Zero-baseline

The ZBL solutions are regarded as a measurement of the receiver internal noise plus the DOP effect imposed on the solutions from constellation-receiver relative geometries. Based on the ZBL experiment, it is concluded that for E components, the noise levels are at 0.3-0.4 mm and 0.5-0.6mm for geodetic GNSS receiver and low-cost GNSS receivers respectively. In comparison to E components, slightly worse precision can be detected from N with 0.4-0.6mm and 0.7-1mm for geodetic and low-cost GNSS solutions, respectively. For Up components, the precision degrades further from E/N components, with precision in the range of 1-2mm for the geodetic receiver, and 2-3mm for the low-cost receiver.

Based on ZBL data analysis, it is also shown that the measurement noise is influenced by many factors, such as different grades of receivers, different grades of antennas, different multi-constellation, etc. It can be computed that irrespective of the antenna used, the difference between precision of low-cost grade and geodetic grade GNSS receiver is normally around 0.2-0.3mm for E, 0.3-0.5mm for N, and around 1mm for Up. By adopting the patch antenna in ZBL, the precision of solutions tends to be worse than when the geodetic antenna is used. The difference is small for E/N components with only up to 0.2mm difference, but for Up components, a distinguishable difference at around 0.7-0.8 mm can be found. ZBL results are also affected by different constellations. An improved measurement precision can be detected with GPS+Galileo compared to GPS-only solution, indicating the benefit of inclusion of multi-constellation in obtaining more precise results. By the addition of

GLONASS constellations, a slight improvement of precision can be generally detected with geodetic measurement. However, regarding low-cost receiver measurement, the precision degrades due to the frequent occurrence of cycle slips and data losses in the timeseries, indicating the incompatibility of the low-cost receiver in processing GLONASS observations. It is noticed that the precision improvement by the inclusion of other different constellations is usually small with only up to 0.2mm precision improvement. This indicates the limited efficiency of multi-constellation on precision improvement which is probably due to the overall low noise level in the measurement residuals diluting the effect of multi-GNSS on the solution. The impact of satellite-receiver relative geometry (DOP) on the precision of measurement is also examined. A positive correlation is seen between the STD of measurement residuals and corresponding DOP values for each epoch.

In summary, the findings from ZBL tests are in close agreement with results from Andrei et al.(2011) using u-blox LEA 6T and in a similar level of magnitude with Msaewe et al. (2017) using Leica measurement. This further confirms and verifies our ZBL experimental result adopting the low-cost receiver as well as the Leica receiver.

11.1.2 SBL static test

The analysis of the system noise within a SBL setup is carried out with different base station options. It is concluded the base station receiver grade has negligible impact on the rover solutions, while on the other hand, a better base station antenna generally leads to noticeable precision improvement. Compared with patch base antenna, the solutions obtained using geodetic base station antenna generally result in E/N precision improvement of up to 1mm, and Up components of more than 1mm.

The precisions of the low-cost rovers in the SBL static test are evaluated under relatively low multipath conditions. It is shown that generally, without any filtering carried out to the original timeseries, a precision of 3-4mm for Easting component, 5-6mm for Northing component, and around 10mm for Up component can be derived for GPS-only solution when both rover and base adopt low-cost GNSS equipment (low-cost receiver and patch antenna). Precision improvement is seen with multi-GNSS solutions. More precise results can be obtained by including Galileo constellation with further precision improvement by the inclusion of GLONASS constellation observation. However, the trade-off is that the percentage of data loss due to float solutions also increases by incorporation of different constellations, a visible decrease of data availability could be detected especially when GLONASS is included.

To mitigate the low frequency errors within the original timeseries such as multipath, PCV, etc, a novel CME filtering approach is proposed. The CME filtered residuals are compared with results adopting SDF which is conventionally used for multipath mitigation. It is concluded that, by applying the CME filter, the precision could be improved from the initial timeseries. Depending on the constellation used, the CME will result in the Easting precision ranging from 1-2mm, Northing precision ranging from 1.5-3mm, and Up precision ranging from 3-5mm. Similar to the original timeseries, the CME filtered results are also shown to be improved with multi-constellation, with GPS+GLONASS+Galileo CME showing the most precise results, followed by GPS+Galileo and GPS only CME residuals.

The original timeseries are also subjected to SDF as a comparison to the CME filtering. The E/N/Up precisions are obtained by calculation of the STDs of E/N/Up SDF residuals respectively. The SDF results show a precision around 1mm for Easting, 1-2mm for Northing, and 2-3mm for Up component. Comparing CME and SDF method, it can be seen that by multi-GNSS CME, for example (GPS+GLONASS+Galileo), comparable or slightly worse precision could be achieved compared to SDF residuals for E/N components. Whereas for the Up component, significant better precision is achieved by SDF. Finally, a combination of CME filter and SDF is applied to original timeseries leading to a further precision improvement with precision below 1mm for E/N components, and 1-2mm for Up component. Besides SDF and CME filtering approach, it is also confirmed that enhanced precision could be achieved by average/weighted average combination in comparison to the solutions derived from separate low-cost receiver.

The SBL static from this study are compared to research from Lu et al.(2019), Andrei et al. (2011) and Garrido-Carretero et al.(2019) adopting low-cost u-blox receivers. It is found that the baseline solution could reach an positioning precision of centimetre level: ~5mm for horizontal precision and ~10mm for Up precision (Andrei et al., 2011), ±5.5 mm for the horizontal and ±11 mm for heights (Garrido-Carretero et al.,2019), and 0.5cm-1cm in the static scenario (Lu et al., 2019), which is in accordance with our SBL solution before low-frequency error mitigation.

11.1.3 SBL kinematic test

In the SBL kinematic test, the precision of dynamic displacement monitoring of a designed circular motion is assessed by low-cost and geodetic GNSS rovers. The performance of frequency analysis from both low-cost and geodetic measurements is also evaluated. Firstly, it is confirmed again the base station receiver grade has a negligible effect on the precision of the results.

A similar level of precisions could be detected for test with different rotation radii, and no significant correlation is found between the precision and rotation amplitude. It is summarised that the precision of geodetic GNSS rover in dynamic motion measurement when the base station adopts geodetic antenna is around 2-3 mm for E, 3-4 mm for N, and 4-5mm for Up for GPS-only solutions. A precision improvement of around 1mm is noticed if the GPS+Galileo solution is considered. Regarding GPS-only solutions obtained with the low-cost rover and the geodetic base antenna, a precision of around 4mm in E, 6-7mm for N, and up to 10mm for Up can be found. The precision again improves with GPS+Galileo observations, with a precision improvement of up to 1mm for E, 2mm for N, and 3 mm for Up.

The results are also analysed with patch base antenna. By comparing the solutions from different grades of base antenna, it is shown that for E/N, precision using patch base antenna is usually degraded from solutions obtained using the geodetic base antenna. However, for Up component, better precision could sometimes be detected when the patch antenna is used in the base which may be caused by uncalibrated antenna parameters.

In SBL kinematic test, a closely-spaced dual low-cost rover system is adopted. It is shown that by averaging of the two low-cost measurements, improved precision is achievable. Two data filtering techniques are also considered. On one hand, the CME filtering is fulfilled by simulating and differentiating a similar pattern of low frequency noise between the two close-by receivers. On the other hand, a high-pass filter is adopted to mitigate any noise below a certain cut-off frequency. Although the CME filter and high-pass filter both aim to mitigate low-frequency noise in the results with precision improvement detected by both approaches, a better precision is achieved with high-pass filter. Furthermore, the precision improvement from average processing is not confined only to the original timeseries. Solutions obtained by applying CME filtering and high-pass filtering to the averaged original timeseries, also exhibit improved precision from each separate low-cost solution subjected to CME filtering and high-pass filtering.

The kinematic experiment results are compared and verified by low-cost u-blox dynamic experiment results from Cina and Piras (2015), Biagi et al. (2016), and Lu et al. (2019). An accuracy of around sub-centimetre level for horizontal component and centimetre level for vertical component can be obtained (Cina and Piras, 2015; Biagi et al., 2016). Lu et al. (2019) also claimed that the accuracy in their dynamic scenario could reach 1 cm and 2cm in the horizontal and vertical direction respectively, with 6-8mm precision in horizontal and ~13mm precision in Up for GPS only solutions. By comparison, our low-cost u-blox kinematic rover results are in close agreement with empirical dynamic displacement results, and it is also concluded from our kinematic tests that, sub-centimetre precision could be derived for horizontal components and ~1-2cm level precision could be obtained with vertical component.

11.1.4 Bridge trial

To achieve the aim of this study, the low-cost GNSS equipment is employed on a real monitoring scenario to monitor a suspension bridge under purposely imposed loads. The measurement with respect to the same displacement is acquired by different measuring equipment (low-cost GNSS rover, geodetic GNSS rover, terrestrial RTS). The performance of the low-cost GNSS sensors in bridge deformation monitoring is assessed and compared against RTS and survey-grade GNSS instrument. From DFT spectra, the same modal frequency could be derived from low-cost GNSS measurement compared to geodetic solutions (survey-grade GNSS and RTS). By comparing the spectra of the original timeseries, it is observed that the low-cost GNSS measurement tends to have the highest amplitude followed by geodetic GNSS and RTS measurement, both in the low-frequency band (<0.1Hz) and high-frequency band (> 2Hz). The occurrence of a higher amplitude low-frequency noise in GNSS measurement is probably due to the evident multipath impact. Furthermore, due to poor multipath rejection capability from low-cost receiver and patch antenna, a higher amplitude of low-frequency error is observed in the low-cost GNSS spectrum than the geodetic GNSS spectrum.

Apart from frequency analysis, the displacement amplitude determined with GNSS measurement is also compared with that using RTS. It can be seen that the accuracy of geodetic GNSS measurement in amplitude determination can be up to 2.7 mm with the reference to the RTS measurement, while the accuracy from low-cost GNSS solutions could reach a maximum of 9mm. Although the large deviation of the displacement may be related to the processing noise and instability caused by NSAT variations.

Similar to the SBL test, a dual closely-spaced low-cost rover system configuration is employed to take advantage of the spatial correlation between them. CME filtering is conceived for potential improvement by mitigating the partly common low-frequency errors. This approach is however proved only applicable for one excitation scenario, indicating it cannot be generalised. To assess the efficiency of CME filtering, it is applied to the mean/weighted average solution for the eligible excitation. The accuracy and precision are shown to be improved immensely from the original unfiltered data which is even be better than the separate low-cost high-pass filtered results.

The mean and weighted average processing between close-by low-cost stations are also attempted, it is concluded that a general accuracy improvement from each separate low-cost result could be noticed particularly before and after excitation with less obvious improvement during excitations. The mean and weighted average is identical due to the similar weighting used in the calculation. Although no obvious improvement in amplitude determination is detected with average processing, a decrease in the background noise level can be observed from separate low-cost solutions, reaching comparable noise level with geodetic solutions.

To conclude, based on analysis of a practical deformation monitoring case study, the low-cost GNSS receivers could achieve a comparable performance compared to single frequency geodetic grade receivers, where the measurement difference is no more than ~3mm. If an additional low-cost station is also set up in the vicinity, by analysing the averaged solution between them, similar noise level, modal frequency, and reduced measurement difference (~1.2mm-2.5mm) could be obtained compared to geodetic GNSS rovers. This indicates the high potential of low-cost receiver for centimetre level dynamic displacement detection under certain conditions, such as 1) SBL with a good sky view, 2) multi-GNSS, 3) closely-spaced dual low-cost rover, 4) appropriate filtering technique, 5) postprocessing.

The results from the frequency analysis of the Wilford bridge trial are also compared with empirical research regarding the same bridge. The modal frequencies derived from the low-cost GNSS measurement in this study (~1.68Hz) are in correspondence with previous studies where similar modal frequencies of around 1.68 - 1.74 Hz were reported (Meng et al., 2007; Meo et al., 2006; Yu et al., 2014; Ioulia et al., 2018, Psimoulis et al., 2016).

11.1.5 Summary

The low-cost receiver used in this study is u-blox M8T, representing the popularly tested low-cost GNSS receivers at the time of experiment (Dabove and Pietra, 2019; Gill et al., 2017; Realini et al., 2017) and the GNSS processing software is an open-source software frequently used in company with low-cost receivers (Wisniewski et al., 2013; Takasu and Yasuda, 2009; Liu and Li, 2017). Apart from conclusions drawn from the individual case of using the specific hardware and software, it shows that with the current available modern low-cost receivers, the ZBL and SBL results could be comparable with single-frequency geodetic receiver. The ZBL results show E /N precisions are within 1mm and around 2-3 mm for U. For the SBL test, precision of sub-centimetre for E/N and centimetre level for Up could be obtained, with the SBL static test showing slightly better precision than SBL dynamic test. The SBL results are also improved significantly after adopting various approaches (e.g. CME, SDF, and average combination). Moreover, a dominant frequency of ~0.362 Hz could be accurately determined from SBL dynamic test. From the bridge trial analysis, it is concluded that the performance between u-blox and Leica in dynamic displacement monitoring are comparable in terms of modal frequency determination, accuracy, and measurement difference. Considering measurement background noise, the low-cost GNSS sensor is suitable for centimetre level displacement detection with 95% or above confidence. The dominant frequency derivation for both SBL kinematic tests (~0.362Hz) and bridge fieldwork (~1.68Hz) indicates the applicability of low-cost GNSS receiver in monitoring most engineering structures (rigid or flexible) and for both long period and short period displacements.

11.2 Potential improvement and outlook for future research

This study pioneers by assessing the performance of the low-cost GNSS receiver in monitoring the displacement of civil engineering structures. Empirical research with geodetic monitoring using low-cost GNSS equipment usually focuses on geohazard monitoring such as landslide monitoring, earthquake monitoring, etc. From these studies, it is concluded that centimetre level accuracy can be achieved by low-cost GNSS receivers. On the other hand, in this study, it is proven that the low-cost GNSS receivers could also be applied to monitoring civil engineering infrastructures, where displacement response from the bridge is continuously measured. It is shown that regarding dynamic response monitoring of the bridge, with reference to conventional RTS solution, a maximum of 8mm deviation in amplitude can be derived from a dual low-cost rover system with a noise level of ~4mm indicating its potential for displacement detection within centimetre level accuracy.

There are also issues not accounted for and need further investigation. For example, in this study, a specific u-blox model (u-blox M8T) is used. There are also other low-cost GNSS receiver models on the market. However, according to literature review, the mainstream low-cost receivers tested were u-blox receivers (Biagi et al., 2016; Cina and Piras, 2015; Caldera et al., 2016), although different u-blox models were adopted. Biagi et al. (2016) used u-blox NEO-7P receivers and antenna in their study and achieved an accuracy around 5 mm for horizontal components and 13mm for vertical component in a SBL of 130m. Cina and Piras (2015) employed the low-cost u-blox EVK-5T receiver and a geodetic external antenna as the rover with a VRS base station within 1km baseline length. It was found that the positional accuracy could be on a sub-cm level. The accuracy by u-blox NEO-M8P with Trimble external antenna was reported to be 4 and 8 mm for the horizontal and vertical component in RTK and 2mm (horizontal) and 5mm (vertical) for post-processing mode (Hamza et al., 2020). On the other hand, Garrido-Carretero et al. (2019) found the RTK accuracy by using NEO-M8P with a patch antenna could reach 5.5 mm for the horizontal component and 11 mm for the vertical component for a 350m SBL. Lu et al. (2019) adopted U-blox-M8P receivers in a SBL and the accuracy reached 0.5 and 1 cm in a static scenario, and 1 and 2 cm on a dynamic platform.

From the previous studies employing different models of low-cost u-blox receivers, a slightly different accuracy level could be noticed due to the different design and quality of receivers' architecture, different baseline length, or use of an external antenna. But overall, it could be shown that the accuracies of the u-blox receivers are comparable reaching sub-centimetre level accuracy in a SBL scenario. The choice of different u-blox models probably could influence the accuracy of the result by a small margin, whereas, can be regarded insignificant compared to the choice of the baseline length, use of external antenna etc, as it is also found that the receiver grade would not have a significant impact on the carrier phase performance (Takasu and Yasuda, 2008). For receivers other than u-blox, not much research has been carried out, more experiments regarding GNSS receivers manufactured by other companies are recommended to test and evaluate their performance in the future.

In this paper, the dynamic displacement of a relatively rigid structure was monitored. From the bridge monitoring, the modal frequency of the rigid structures was also verified based on other measuring instruments as well as from empirical studies. However, for long-span bridges or high-rise building or towers with modal frequency less than 1Hz, the low-cost monitoring feasibility is not tested. Where the modal frequency of the long span bridge could range from 0.1Hz to 0.5Hz (Nakamura, 2000; Celebi and Sanli, 2002; Tamura et al., 2002). Therefore, further research could be conducted to assess whether low modal frequency could be identified from the monitoring of long-span bridges or high-rise buildings.

Another improvement of the results could be the inclusion of BDS, the BeiDou Navigation System. BDS is a fast-developing navigation system with global coverage. With the fast development of the BDS in the past decades, BDS measurement could also be made in conjunction with other constellation observations to enhance measurement accuracy. However, the experiment was conducted in 2018-2019, which put a limitation on the number of BeiDou satellites to be observed during that time in the UK. Xi et al. (2018) found that the integration of BDS with GPS could improve the precision of the results by 20%-30% compared to GPS-only results. And based on the real GPS and BDS measurements collected, the combined GPS and BDS results seemed to be much more promising and reliable with lower background noise and higher availability. Therefore, a further recommendation could be to include the BDS observation for the bridge monitoring in the future and examine the accuracy/availability improvement.

One of the other improvements that could be done is to pre-calibrate the rover antenna, the parameters of the patch antenna used in this study are not calibrated, parameters such as PCV and PCO are not defined and taken into consideration for GNSS solution computation. To account for PCV and PCO errors when different antennas are used for rover and base station, a separate test is required to calibrate the antenna used in the experiment by PCV and PCO modelling. According to Hamza (2021), the low-cost calibrated antenna is now emerging in the market. The calibrated antenna parameters would probably improve the precision making it more comparable to geodetic measurement, which will need to be further researched.

According to Jo et al. (2013), the more sensors used in the monitoring, the better precision would be achieved. However, in all SBL tests carried out in the current study, only two low-cost stations in close range are used. Further analysis is required to evaluate possible precision improvement by adopting an array of closely-spaced low-cost stations. Moreover, deploying a cluster of low-cost GNSS rovers could also be beneficial for verification and assurance of the low-cost results by introducing redundant measurement, particularly when one or multiple low-cost stations fail to function within the low-cost monitoring system.

Another improvement that can be made to the experiment is to examine the impact of different grades of rover antennas on the precision of the solution. Better performance is expected with geodetic grade antenna due to its sophisticated design for multipath suppression. A possible high correlation between residuals of adjacent low-cost stations might also be expected after suppressing the multipath signals by antenna hardware design. On the other hand, the price difference between geodetic and patch antenna is much lower compared to the difference between geodetic receivers and low-cost receivers. Therefore, further research could be carried out to test performance improvement by switching rover antenna grade and evaluations could be made by weighing between the benefit of using a geodetic antenna and the trade-off of an increased budget.

Further improvement and future studies can also be made,

1. to evaluate the multi-constellation impact on the performance of low-cost GNSS deformation monitoring applications.
2. to investigate accuracy enhancing approaches by the inclusion of relative geometry and spatial correlation between the closely-aligned patch antennas in CME filtering and use it in real-time applications.
3. to evaluate the possible relationship between the precision and the increasing displacement amplitude to be monitored. This could be accomplished in the SBL kinematic test, where tests for more rotation radii could be conducted.

The prospect of the study is to acquire accurate and reliable real-time displacement of the monitoring structure with a low-cost monitoring system consisted of clusters of low-cost stations and put it into automation, which could be achieved by several critical steps (Meng et al., 2019); 1) in-situ sensor deployment, 2) acquisition and transmission of GNSS observations, 3) GNSS data processing, 4) structure evaluation and notification, 5) data and output management. As for the artificial intelligence (AI) in deformation application, Nsbuga et al. (2021) used an artificial neural network to predict the displacement of a tunnel, by using the overburden factor, the stress reduction factor, and the soil modulus elasticity as input and displacements of the tunnel crest over time as output to train the data. For the bridge deformation monitoring, traffic on the bridge and other loading parameters (wind, etc) could also be used as the input, and deformation of the bridge as the output to train the data. But the loading on the bridge is not always predictable and varies drastically in case of a rare occasion (e.g. thunderstorm or earthquake, etc.) which would directly impact the deformation monitoring of the bridge. Therefore, AI could be used for monitoring the bridge theoretically providing sufficient training data but may not be as accurate as the in-situ measurement of displacement in case of unforeseen circumstances and it would be less accurate for AI to predict the bridge displacement epoch by epoch compared to the in-situ onsite measurement.

To achieve the ultimate goal, RTK mode with a pre-established CORS network should be used to reduce the cost of large-scale SHM applications and the spatial correlation between the array of low-cost stations should be utilised. However, a lot of problems still need to be considered for the NRTK solutions with low-cost receiver/antenna, such as the ambiguity resolution is problematic over longer baselines and quick TTFF is also required due to the occurrence of cycle slips, indicating the necessity and advantage of using a dual-frequency receiver in RTK applications. Recently, new models of multi-GNSS low-cost GNSS receivers are manufactured with dual-frequency capability which is a useful feature to achieve reliable RTK deformation monitoring. Therefore, future studies could be carried out with the low-cost multi-frequency receiver in real-time applications under practical measurement conditions to assess its feasibility and performance. The accuracy improvement from sensor fusion between low-cost GNSS and other low-cost measuring unit could also be further investigated.

.

References

Alkan, R. M., & Saka, M. H. (2009). A performance analysis of low-cost GPS receivers in kinematic applications. *The Journal of Navigation*, *62*(4), 687.

Andrei, C. O., Vermeer, M., Kuusniemi, H., & Koivula, H. (2011). Evaluation of absolute and relative carrier phase positioning using observations from navigation-grade u-blox 6T receiver. In *Proc. 3rd Int. Colloquium on Scientific and Fundamental Aspects of the Galileo Programme, Copenhagen, Denmark* (Vol. 31).

Angeli, M. G., Pasuto, A., & Silvano, S. (2000). A critical review of landslide monitoring experiences. *Engineering Geology*, *55*(3), 133-147.

Ashkenazi, V., & Roberts, G. W. (1997). Experimental monitoring of the Humber Bridge using GPS. In *Proceedings of the institution of civil engineers-civil engineering* (Vol. 120, No. 4, pp. 177-182). Thomas Telford-ICE Virtual Library.

Axelrad, P., Comp, C. J., & Macdoran, P. F. (1996). SNR-based multipath error correction for GPS differential phase. *IEEE Transactions on Aerospace and Electronic Systems*, *32*(2), 650-660.

Bellone, T., Dabove, P., Manzino, A. M., & Taglioretti, C. (2016). Real-time monitoring for fast deformations using GNSS low-cost receivers. *Geomatics, natural hazards and risk*, *7*(2), 458-470.

Benoit, L., Briole, P., Martin, O., Thom, C., Malet, J. P., & Ulrich, P. (2015). Monitoring landslide displacements with the Geocube wireless network of low-cost GPS. *Engineering Geology*, *195*, 111-121.

Biagi, L., Grec, F. C., & Negretti, M. (2016). Low-cost GNSS receivers for local monitoring: Experimental simulation, and analysis of displacements. *Sensors*, *16*(12), 2140.

Bidikar, B., Chapa, B. P., Kumar, M. V., & Rao, G. S. (2020). GPS Signal Multipath Error Mitigation Technique. In *Satellites Missions and Technologies for Geosciences*. IntechOpen

Bilich, A., Axelrad, P., & Larson, K. M. (2007). Scientific utility of the signal-to-noise ratio (SNR) reported by geodetic GPS receivers. In *Proc. ION GNSS* (pp. 26-28).

Braasch, M. S. (1996). GPS multipath model validation. In *Proceedings of Position, Location and Navigation Symposium-PLANS'96* (pp. 672-678). IEEE.

Braasch, M. S., & Van Dierendonck, A. J. (1999). GPS receiver architectures and measurements. *Proceedings of the IEEE*, *87*(1), 48-64.

Brown, N., Troyer, L., Zelzer, O., & Van Cranenbroek, J. (2006). Advances in RTK and Post Processed Monitoring with SingleFrequency GPS. *Positioning*, *1*(10).

Brownjohn, J. M. (2007). Structural health monitoring of civil infrastructure. *Philosophical Transactions of the Royal Society A: Mathematical, Physical and Engineering Sciences*, *365*(1851), 589-622.

Cai, Y., Cheng, P., Meng, X., Tang, W., & Shi, C. (2011, June). Using network RTK corrections and low-cost GPS receiver for precise mass market positioning and navigation applications. In *2011 IEEE Intelligent Vehicles Symposium (IV)* (pp. 345-349). IEEE.

Caldera, S., Realini, E., & Yoshida, D. (2015). Geodetic monitoring experiment by low-cost GNSS receivers and goGPS positioning engine.

Caldera, S., Realini, E., Barzaghi, R., Reguzzoni, M., & Sansò, F. (2016). Experimental study on low-cost satellite-based geodetic monitoring over short baselines. *Journal of Surveying Engineering*, *142*(3), 04015016.

Celebi, M., & Sanli, A. (2002). GPS in pioneering dynamic monitoring of long-period structures. *Earthquake Spectra*, *18*(1), 47-61.

Chan, W. S., Xu, Y. L., Ding, X. L., & Dai, W. J. (2006). An integrated GPS–accelerometer data processing technique for structural deformation monitoring. *Journal of Geodesy*, *80*(12), 705-719.

Chang, X. W., Yang, X., & Zhou, T. (2005). MLAMBDA: a modified LAMBDA method for integer least-squares estimation. *Journal of Geodesy*, *79*(9), 552-565.

Choi, K., Bilich, A., Larson, K. M., & Axelrad, P. (2004). Modified sidereal filtering: Implications for high-rate GPS positioning. *Geophysical research letters*, *31*(22).

Cina, A., & Piras, M. (2015). Performance of low-cost GNSS receiver for landslides monitoring: test and results. *Geomatics, Natural Hazards and Risk*, *6*(5-7), 497-514.

Cosser, E., Roberts, G. W., Meng, X., & Dodson, A. H. (2003, May). The comparison of single frequency and dual frequency GPS for bridge deflection and vibration monitoring. In *Proc of the Deformation Measurements and Analysis, 11th International Symposium on Deformation Measurements, International Federation of Surveyors (FIG)*.

Dabove, P., & Manzino, A. M. (2014). GPS & GLONASS mass-market receivers: positioning performances and peculiarities. *Sensors*, *14*(12), 22159-22179.

Dabove, P., & Di Pietra, V. (2019). Towards high accuracy GNSS real-time positioning with smartphones. *Advances in Space Research*, *63*(1), 94-102.

Dawidowicz, K. (2011). Comparison of using relative and absolute PCV corrections in short baseline GNSS observation processing. *Artificial Satellites*, *46*(1), 19-31.

Eissfeller, B., Ameres, G., Kropp, V., & Sanroma, D. (2007). Performance of GPS, GLONASS and Galileo. In *Photogrammetric Week* (Vol. 7, pp. 185-199).

EL-Hattab, A. I. (2013). Influence of GPS antenna phase center variation on precise positioning. *NRIAG Journal of Astronomy and Geophysics*, *2*(2), 272-277.

Erol, S., Erol, B., & Ayan, T. (2004, July). A general review of the deformation monitoring techniques and a case study: analysing deformations using GPS/levelling. In *XXth ISPRS Congress* (Vol. 7, No. 5, p. 12).

Everett T (2018a) Updated guide to the RTKLIB configuration file, available from https://rtklibexplorer.wordpress.com/2018/11/27/updated-guide-to-the-rtklib-configuration-file/ accessed on 06/05/2021

Everett T (2018b) Glonass Ambiguity Resolution with RTKLIB Revisited, available from https://rtklibexplorer.wordpress.com/2018/06/14/glonass-ambiguity-resolution-with-rtklib-revisited/ accessed on 06/05/2021

Everett T (2020) Demo5 b33c binaries, available from http://rtkexplorer.com/downloads/rtklib-code/ accessed on 06/05/2021

Farrar, C. R., & Worden, K. (2007). An introduction to structural health monitoring. *Philosophical Transactions of the Royal Society A: Mathematical, Physical and Engineering Sciences*, *365*(1851), 303-315.

Garrido-Carretero, M. S., Borque-Arancón, M. J., Ruiz-Armenteros, A. M., Moreno-Guerrero, R., & Gil-Cruz, A. J. (2019). Low-cost GNSS receiver in RTK positioning under the standard ISO-17123-8: A feasible option in geomatics. *Measurement*, *137*, 168-178.

Ge, L., Han, S., & Rizos, C. (2000). Multipath mitigation of continuous GPS measurements using an adaptive filter. *GPS solutions*, *4*(2), 19-30.

Gili, J. A., Corominas, J., & Rius, J. (2000). Using Global Positioning System techniques in landslide monitoring. *Engineering geology*, *55*(3), 167-192.

Gill, M., Bisnath, S., Aggrey, J., & Seepersad, G. (2017). Precise point positioning (PPP) using low-cost and ultra-low-cost GNSS receivers. In *Proceedings of the 30th International Technical Meeting of The Satellite Division of The Institute of Navigation (ION GNSS+ 2017)* (pp. 226-236).

Glabsch, J., Heunecke, O., & Schuhbäck, S. (2009). Monitoring the Hornbergl landslide using a recently developed low cost GNSS sensor network.

GSP (2020). Kalibrasi GNSS. Retrieved from http://www.jasasurveypemetaan.com/kalibrasi-receiver-gps-gnss/

Guo, J., Li, X., Li, Z., Hu, L., Yang, G., Zhao, C., ... & Ge, M. (2018). Multi-GNSS precise point positioning for precision agriculture. *Precision agriculture*, *19*(5), 895-911.

Habboub, M., Psimoulis, P. A., Bingley, R., & Rothacher, M. (2020). A multiple algorithm approach to the analysis of GNSS coordinate timeseries for detecting geohazards and anomalies. *Journal of Geophysical Research: Solid Earth*, *125*(2), e2019JB018104

Hamza, V., Stopar, B., & Sterle, O. (2021). Testing the Performance of Multi-Frequency Low-Cost GNSS Receivers and Antennas. *Sensors*, *21*(6), 2029.

Hamza, V., Stopar, B., Ambrožič, T., Turk, G., & Sterle, O. (2020). Testing Multi-Frequency Low-Cost GNSS Receivers for Geodetic Monitoring Purposes. *Sensors*, *20*(16), 4375.

Hannon, B., Sergeant, P., & Dupré, L. (2016). Time-and spatial-harmonic content in synchronous electrical machines. *IEEE Transactions on Magnetics*, *53*(3), 1-11.

Henkel, P., & Iafrancesco, M. (2014). Tightly coupled position and attitude determination with two low-cost GNSS receivers. In *2014 11th International Symposium on Wireless Communications Systems (ISWCS)* (pp. 895-900). IEEE.

Heunecke, O., Glabsch, J., & Schuhbäck, S. (2011). Landslide monitoring using low cost GNSS equipment n experiences from two alpine testing sites. *Journal of civil engineering and architecture*, *5*(8).

Hyzak, M., Leach, M., & Duff, K. (1997, May). Practical application of GPS to bridge deformation monitoring. In *Proceedings of Permanent Committee Meeting and Symposium, International Federation of Surveyor (FIG)* (pp. 11-16).

Peppa, I., Psimoulis, P., & Meng, X. (2018). Using the signal-to-noise ratio of GPS records to detect motion of structures. *Structural control and health monitoring*, *25*(2), e2080.

Jackson, J., Saborio, R., Ghazanfar, S. A., Gebre-Egziabher, D., & Davis, B. (2018). Evaluation of low-cost, centimeter-level accuracy OEM GNSS receivers.

Janssen, V., Roberts, C., Rizos, C., & Abidin, H. Z. (2002). Low-cost GPS-based volcano deformation monitoring at Mt. Papandayan, Indonesia. *Journal of volcanology and geothermal research*, *115*(1-2), 139-151.

Jo, H., Sim, S. H., Tatkowski, A., Spencer Jr, B. F., & Nelson, M. E. (2013). Feasibility of displacement monitoring using low-cost GPS receivers. *Structural Control and Health Monitoring*, *20*(9), 1240-1254.

Joseph, A., & Petovello, M. (2010). Measuring GNSS signal strength. *Inside GNSS*, *5*(8), 20-25.

Kalkan, Y. (2014). Geodetic deformation monitoring of Ataturk Dam in Turkey. *Arabian journal of geosciences*, *7*(1), 397-405.

Kkddkkdd. (2017). ECEF ENU Longitude Latitude relationship in right-hand rule. Retrieved from https://commons.wikimedia.org/wiki/File:ECEF_ENU_Longitude_Latitude_right-hand-rule.svg

Knight, P. J., Bird, C. O., Sinclair, A., & Plater, A. J. (2020). A low-cost GNSS buoy platform for measuring coastal sea levels. *Ocean Engineering*, *203*, 107198.

Kubo, N., Kobayashi, K., Hsu, L. T., & Amai, O. (2017). Multipath mitigation technique under strong multipath environment using multiple antennas.

Langley, R. B. (1997). GPS receiver system noise. *GPS world*, *8*(6), 40-45.

Langley, R. B. (1999). Dilution of precision. *GPS world*, *10*(5), 52-59.

Lau, L., & Cross, P. (2007). Investigations into phase multipath mitigation techniques for high precision positioning in difficult environments. *The Journal of Navigation*, *60*(3), 457-482.
Leica Geosystems AG. (2012). Leica Viva GNSS GS10 receiver Datasheet [online] Heerbrugg, Switzerland Retrieved November, 2019, from https://w3.leicageosystems.com/downloads123/zz/gpsgis/viva%20gnss/brochures-datasheet/leica_viva_gnss_gs10_receiver_ds_en.pdf
Leica Geosystems AG. (2020). Leica Nova MS60 Data sheet [online] Heerbrugg, Switzerland Retrieved November, 2020, from https://leica-geosystems.com/-/media/files/leicageosystems/products/datasheets/leica_nova_ms60_ds.ashx?la=en&hash=AB5679E327538292C23BD76C0CCF3B52
Lennen, G. R. (1996). *U.S. Patent No. 5,537,121*. Washington, DC: U.S. Patent and Trademark Office.
Lovse, J. W., Teskey, W. F., Lachapelle, G., & Cannon, M. E. (1995). Dynamic deformation monitoring of tall structure using GPS technology. *Journal of surveying engineering*, *121*(1), 35-40.
LSPO (n.d.) Sampling Theorem and Frequency Spectrum Aliasing. Retrieved from https://storm.uni-mb.si/CoLoS/applets/aliasing/index.html
Liu, T., & Li, B. (2017). Single-frequency BDS/GPS RTK with low-cost U-blox receivers. In *2017 Forum on Cooperative Positioning and Service (CPGPS)* (pp. 232-238). IEEE.
Lu, L., Ma, L., Wu, T., & Chen, X. (2019). Performance analysis of positioning solution using low-cost single-frequency u-blox receiver based on baseline length constraint. *Sensors*, *19*(19), 4352.
Mader, G. L. (1999). GPS antenna calibration at the National Geodetic Survey. *GPS solutions*, *3*(1), 50-58.
Manzini, N., Orcesi, A., Thom, C., Brossault, M. A., Botton, S., Ortiz, M., & Dumoulin, J. (2020). Performance analysis of low-cost GNSS stations for structural health monitoring of civil engineering structures. *Structure and Infrastructure Engineering*, 1-17.
Manzino, A. M., Dabove, P., & Gogoi, N. (2018). Assessment of positioning performances in Italy from GPS, BDS and GLONASS constellations. *Geodesy and Geodynamics*, *9*(6), 439-448.
Medina, D., Heßelbarth, A., Büscher, R., Ziebold, R., & García, J. (2018). On the Kalman filtering formulation for RTK joint positioning and attitude quaternion determination. In *2018 IEEE/ION Position, Location and Navigation Symposium (PLANS)* (pp. 597-604). IEEE.
Meng, X., Dodson, A. H., & Roberts, G. W. (2007). Detecting bridge dynamics with GPS and triaxial accelerometers. *Engineering Structures*, *29*(11), 3178-3184.
Meng, X., Roberts, S., Cui, Y., Gao, Y., Chen, Q., Xu, C., ... & Bhatia, P. (2018). Required navigation performance for connected and autonomous vehicles: where are we now and where are we going?. *Transportation planning and technology*, *41*(1), 104-118.
Meng, X., Nguyen, D. T., Owen, J. S., Xie, Y., Psimoulis, P., & Ye, G. (2019). Application of GeoSHM system in monitoring extreme wind events at the forth Road Bridge. *Remote Sensing*, *11*(23), 2799.
Meo, M., Zumpano, G., Meng, X., Cosser, E., Roberts, G., & Dodson, A. (2006). Measurements of dynamic properties of a medium span suspension bridge by using the wavelet transforms. *Mechanical systems and signal processing*, *20*(5), 1112-1133.
Misra, P. N. (1996). Innovation: The Role of the Clock in a GPS Receiver. *GPS world*, *7*(4), 60-67.

Msaewe, H. A., Hancock, C. M., Psimoulis, P. A., Roberts, G. W., Bonenberg, L., & de Ligt, H. (2017). Investigating multi-GNSS performance in the UK and China based on a zero-baseline measurement approach. *Measurement*, *102*, 186-199.

Msaewe, H. A., Psimoulis, P. A., Hancock, C. M., Roberts, G. W., & Bonenberg, L. (2021). Monitoring the response of Severn Suspension Bridge in the United Kingdom using multi-GNSS measurements. *Structural Control and Health Monitoring*, *28*(11), e2830.

Nakamura, S. I. (2000). GPS measurement of wind-induced suspension bridge girder displacements. *Journal of structural Engineering*, *126*(12), 1413-1419.

Navipedia. (2014a). Digital Signal Processing. Retrieved 10:52, June 23, 2018 from http://www.navipedia.net/index.php?title=Digital_Signal_Processing&oldid=13216

Navipedia. (2014b). Frequency Lock Loop (FLL) Retrieved 10/05/2021 from https://gssc.esa.int/navipedia/index.php/Frequency_Lock_Loop_(FLL)

Navipedia. (2014c). Delay Lock Loop (DLL) Retrieved 10/05/2021 from https://gssc.esa.int/navipedia/index.php/Delay_Lock_Loop_(DLL)

Navipedia. (2014d). Phase Lock Loop (PLL) Retrieved 10/05/2021 from https://gssc.esa.int/navipedia/index.php/Phase_Lock_Loop_(PLL)

Chernov, N. (2021). Circle Fit (Pratt method) (https://www.mathworks.com/matlabcentral/fileexchange/22643-circle-fit-pratt-method), MATLAB Central File Exchange. Retrieved May 6, 2021.

Nikolaidis, R. (2002). *Observation of geodetic and seismic deformation with the Global Positioning System*. University of California, San Diego.

Nie, Z., Liu, F., & Gao, Y. (2020). Real-time precise point positioning with a low-cost dual-frequency GNSS device. *Gps Solutions*, *24*(1), 1-11.

Notti, D., Cina, A., Manzino, A., Colombo, A., Bendea, I. H., Mollo, P., & Giordan, D. (2020). Low-cost GNSS solution for continuous monitoring of slope instabilities applied to Madonna Del Sasso Sanctuary (NW Italy). *Sensors*, *20*(1), 289.

Nsubuga, S., Tsakiri, M., & Georgiannou, V. (2021). A smart decision tool for the prediction of tunnel crown displacements. *Applied Geomatics*, *13*(1), 77-91.

Odolinski, R., & Teunissen, P. J. (2016). Single-frequency, dual-GNSS versus dual-frequency, single-GNSS: a low-cost and high-grade receivers GPS-BDS RTK analysis. *Journal of geodesy*, *90*(11), 1255-1278.

Odolinski, R., & Teunissen, P. J. G. (2017a). Innovation: Low-cost single-frequency positioning approach. GPS World,[Online]. https://www. gpsworld. com/innovation-low-cost-single-frequency-positioningapproach-with-gps-bds-rtk/.[Accessed: 02 December 2018].

Odolinski, R., & Teunissen, P. J. (2017b). Low-cost, high-precision, single-frequency GPS–BDS RTK positioning. *GPS solutions*, *21*(3), 1315-1330.

Odolinski, R., & Teunissen, P. J. (2019). An assessment of smartphone and low-cost multi-GNSS single-frequency RTK positioning for low, medium and high ionospheric disturbance periods. *Journal of Geodesy*, *93*(5), 701-722.

Othman, Z., Wan, A. W., & Anuar, A. (2011). Evaluating the performance of GPS survey methods for landslide monitoring at hillside residential area: static vs rapid static. In *2011 IEEE 7th International Colloquium on Signal Processing and its Applications* (pp. 453-459). IEEE.

Pepe, M. (2018). CORS architecture and evaluation of positioning by low-cost GNSS receiver. *Geodesy and Cartography*, *44*(2), 36-44.

Poluzzi, L., Tavasci, L., Corsini, F., Barbarella, M., & Gandolfi, S. (2019). Low-cost GNSS sensors for monitoring applications. *Applied Geomatics*, 1-10.

Pesyna, K. M., Heath, R. W., & Humphreys, T. E. (2014). Centimeter positioning with a smartphone-quality GNSS antenna. In *Proceedings of the 27th*

International Technical Meeting of the Satellite Division of The Institute of Navigation (ION GNSS+ 2014) (pp. 1568-1577).
Chang, P. C., Flatau, A., & Liu, S. C. (2003). Health monitoring of civil infrastructure. *Structural health monitoring*, *2*(3), 257-267.
Seibold. P. (2021). Sine fitting (https://www.mathworks.com/matlabcentral/fileexchange/66793-sine-fitting), MATLAB Central File Exchange. Retrieved May 6, 2021.
Pratt, V. (1987). Direct least-squares fitting of algebraic surfaces. *ACM SIGGRAPH computer graphics*, *21*(4), 145-152.
Psimoulis, P. A., & Stiros, S. C. (2007). Measurement of deflections and of oscillation frequencies of engineering structures using Robotic Theodolites (RTS). *Engineering Structures*, *29*(12), 3312-3324.
Psimoulis, P., Pytharouli, S., Karambalis, D., & Stiros, S. (2008). Potential of Global Positioning System (GPS) to measure frequencies of oscillations of engineering structures. *Journal of Sound and Vibration*, *318*(3), 606-623.
Psimoulis, P., Peppa, I., Bonenberg, L., Ince, S., & Meng, X. (2016). Combination of GPS and RTS measurements for the monitoring of semi-static and dynamic motion of pedestrian bridge.
Quan, Y., Lau, L., Roberts, G. W., & Meng, X. (2016). Measurement signal quality assessment on all available and new signals of multi-GNSS (GPS, GLONASS, Galileo, BDS, and QZSS) with real data. *The Journal of Navigation*, *69*(2), 313-334.
Rademakers, E., De Bakker, P., Tiberius, C., Janssen, K., Kleihorst, R., & El Ghouti, N. (2016, May). Obtaining real-time sub-meter accuracy using a low cost GNSS device. In *2016 European Navigation Conference (ENC)* (pp. 1-8). IEEE.
Ray, J. K., & Cannon, M. E. (1999). Characterization of GPS carrier phase multipath. In *Proceedings of the 1999 National Technical Meeting of the Institute of Navigation* (pp. 343-352).
Ray, J. K., Cannon, M. E., & Fenton, P. (2001). GPS code and carrier multipath mitigation using a multiantenna system. *IEEE Transactions on Aerospace and Electronic Systems*, *37*(1), 183-195.
Realini, E., & Reguzzoni, M. (2013). goGPS: open source software for enhancing the accuracy of low-cost receivers by single-frequency relative kinematic positioning. *Measurement Science and technology*, *24*(11), 115010.
Realini, E., Caldera, S., Pertusini, L., & Sampietro, D. (2017). Precise GNSS positioning using smart devices. *Sensors*, *17*(10), 2434.
Rothacher, M., Schaer, S., Mervart, L., & Beutler, G. (1995). Determination of antenna phase center variations using GPS data. In *IGS Workshop Proceedings: Special Topics and New Directions* (pp. 205-220). Germany: GeoForschungsZentrum Potsdam.
Roberts, G. W., Cosser, E., Meng, X., & Dodson, A. (2004). High frequency deflection monitoring of bridges by GPS. *Journal of Global Positioning Systems*, *3*(1-2), 226-231.
Roberts, G. W., Tang, X., & He, X. (2018). Accuracy analysis of GPS/BDS relative positioning using zero-baseline measurements. *The Journal of Global Positioning Systems*, *16*(1), 1-8.
Satirapod, C., & Rizos, C. (2005). Multipath mitigation by wavelet analysis for GPS base station applications. *Survey Review*, *38*(295), 2-10.
Savvaidis, P. D. (2003). Existing landslide monitoring systems and techniques. *From Stars to Earth and Culture*, 242-258.
Schmid, R., Rothacher, M., Thaller, D., & Steigenberger, P. (2005). Absolute phase center corrections of satellite and receiver antennas. *GPS solutions*, *9*(4), 283-293.
Schmid, R., Steigenberger, P., Gendt, G., Ge, M., & Rothacher, M. (2007). Generation of a consistent absolute phase-center correction model for GPS receiver and satellite antennas. *Journal of Geodesy*, *81*(12), 781-798.

Shen, N., Chen, L., Liu, J., Wang, L., Tao, T., Wu, D., & Chen, R. (2019). A review of global navigation satellite system (GNSS)-based dynamic monitoring technologies for structural health monitoring. *Remote* Sensing, 11(9), 1001.

Sioulis, A., Tsakiri, M., & Stathas, D. (2015). Evaluation of low-cost, high sensitivity GNSS receivers based on the ISO RTK standards. *Int. J. Geomat. Geosci.*, (2), 1597-1606.

Skoglund, M., Petig, T., Vedder, B., Eriksson, H., & Schiller, E. M. (2016). Static and dynamic performance evaluation of low-cost RTK GPS receivers. In *2016 IEEE Intelligent Vehicles Symposium (IV)* (pp. 16-19). IEEE.

Stempfhuber, W., & Buchholz, M. (2011). A precise, low-cost RTK GNSS system for UAV applications. *Proc. of Unmanned Aerial Vehicle in Geomatics, ISPRS*.

Takasu, T., & Yasuda, A. (2008). Evaluation of RTK-GPS performance with low-cost single-frequency GPS receivers. In *Proceedings of international symposium on GPS/GNSS* (pp. 852-861).

Takasu, T., & Yasuda, A. (2009). Development of the low-cost RTK-GPS receiver with an open source program package RTKLIB. In *International symposium on GPS/GNSS* (Vol. 1). International Convention Center Jeju Korea.

Takasu, T. (2013). RTKLIB ver. 2.4. 2 Manual. *RTKLIB: An Open Source Program Package for GNSS Positioning*, 29-49.

Tamura, Y., Matsui, M., Pagnini, L. C., Ishibashi, R., & Yoshida, A. (2002). Measurement of wind-induced response of buildings using RTK-GPS. *Journal of Wind Engineering and Industrial Aerodynamics*, *90*(12-15), 1783-1793.

Teunissen, P.J.G. (1995) The least-squares ambiguity decorrelation adjustment: a method for fast GPS integer ambiguity estimation. *Journal of Geodesy* **70,** 65–82

U-blox AG. (2020), NEO/LEA-M8T u-blox M8 concurrent GNSS timing modules Data sheet[online] Retrieved November 2020, from https://www.u-blox.com/sites/default/files/NEO-LEA-M8T-FW3_DataSheet_%28UBX-15025193%29.pdf

Uren, J., & Price, W. F. (1994). Deformation Monitoring. In *Surveying for Engineers* (pp. 554-571). Palgrave, London.

Vagle, N., Broumandan, A., Jafarnia-Jahromi, A., & Lachapelle, G. (2016). Performance analysis of GNSS multipath mitigation using antenna arrays. *The Journal of Global Positioning Systems*, *14*(1), 1-15.

Van Sickle, J. (2008). *GPS for land surveyors*. Crc Press.

Verhagen, S., Odijk, D., Teunissen, P. J., & Huisman, L. (2010, December). Performance improvement with low-cost multi-GNSS receivers. In *2010 5th ESA workshop on satellite navigation technologies and European workshop on GNSS signals and signal processing (NAVITEC)* (pp. 1-8). IEEE.

Wakileh, G. J. (2003). Harmonics in rotating machines. *Electric Power Systems Research*, *66*(1), 31-37.

Wang, G. (2011). GPS landslide monitoring: single base vs. network solutions—a case study based on the Puerto Rico and Virgin Islands permanent GPS network. *Journal of Geodetic Science*, *1*(3), 191-203.

Wang, G., & Soler, T. (2012). OPUS for horizontal subcentimeter-accuracy landslide monitoring: Case study in the Puerto Rico and Virgin Islands region. *Journal of Surveying Engineering*, *138*(3), 143-153.

Wang, G. Q. (2013). Millimeter-accuracy GPS landslide monitoring using Precise Point Positioning with Single Receiver Phase Ambiguity (PPP-SRPA) resolution: a case study in Puerto Rico. *Journal of geodetic science*, *3*(1), 22-31.

Wanninger, L. (2012). Carrier-phase inter-frequency biases of GLONASS receivers. *Journal of Geodesy*, *86*(2), 139-148.

Weill, L. R. (1997). Conquering mutlipath: The GPS accuracy battle. *GPS world*, *4*, 59-66.

Weston, N. D., & Schwieger, V. (2014). *Cost effective GNSS positioning techniques*. FIG.

Wilkinson, M. W., McCaffrey, K. J., Jones, R. R., Roberts, G. P., Holdsworth, R. E., Gregory, L. C., ... & Iezzi, F. (2017). Near-field fault slip of the 2016 Vettore Mw 6.6 earthquake (Central Italy) measured using low-cost GNSS. *Scientific Reports*, *7*(1), 1-7.

Wiśniewski, B., Bruniecki, K., & Moszyński, M. (2013). Evaluation of RTKLIB's Positioning Accuracy Usingn low-cost GNSS Receiver and ASG-EUPOS. *TransNav: International Journal on Marine Navigation and Safety of Sea Transportation*, *7*(1), 79-85.

Wouters, M. J., & Marais, E. L. (2019). Using Low-cost Receivers for Multi-GNSS Time Transfer. In *2019 Joint Conference of the IEEE International Frequency Control Symposium and European Frequency and Time Forum (EFTF/IFC)* (pp. 1-5). IEEE.

Xi, R., Jiang, W., Meng, X., Chen, H., & Chen, Q. (2018). Bridge monitoring using BDS-RTK and GPS-RTK techniques. *Measurement*, *120*, 128-139.

Xue, C., Psimoulis, P., Zhang, Q., & Meng, X. (2021). Analysis of the performance of closely-spaced low-cost multi-GNSS receivers. *Applied Geomatics*, *13*(3), 415-435.

Yi, T., Li, H., & Gu, M. (2010). Recent research and applications of GPS based technology for bridge health monitoring. *Science China Technological Sciences*, *53*(10), 2597-2610.

Yi, T. H., Li, H. N., & Gu, M. (2011). A new method for optimal selection of sensor location on a high-rise building using simplified finite element model. *Structural Engineering and Mechanics*, *37*(6), 671-684.

Yi, T. H., Li, H. N., & Gu, M. (2013a). Experimental assessment of high-rate GPS receivers for deformation monitoring of bridge. *Measurement*, *46*(1), 420-432.

Yi, T. H., Li, H. N., & Gu, M. (2013b). Recent research and applications of GPS-based monitoring technology for high-rise structures. *Structural Control and Health Monitoring*, *20*(5), 649-670.

Yu, J., Meng, X., Shao, X., Yan, B., & Yang, L. (2014). Identification of dynamic displacements and modal frequencies of a medium-span suspension bridge using multimode GNSS processing. *Engineering Structures*, *81*, 432-443.

Yu, J., Fang, Z., Meng, X., Xie, Y., & Fan, Q. (2020). Measurement of quasi-static and dynamic displacements of footbridges using the composite instrument of a smartstation and an accelerometer: case studies. *Remote Sensing*, *12*(16), 2635.

Zhang, L., & Schwieger, V. (2013). Investigation regarding different antennas combined with low-Cost GPS receivers. In *FIG Working Week*.

Zhang, L. & Schwieger, V. (2016). Improving the Quality of Low-Cost GPS Receiver Data for Monitoring Using Spatial Correlations. Journal of Applied Geodesy, 10(2), 119-129.

Zhang, Q., Ma, C., Meng, X., Xie, Y., Psimoulis, P., Wu, L., ... & Dai, X. (2019). Galileo augmenting GPS single-frequency single-epoch precise positioning with baseline constrain for bridge dynamic monitoring. *Remote Sensing*, *11*(4), 438.

Zhou, G.-D., Yi, T.-H., Chen, B. & Chen, X. (2018). Modeling Deformation Induced by Thermal Loading Using Long-Term Bridge Monitoring Data. *Journal of Performance of Constructed Facilities,* 32**,** 04018011.

Appendix A

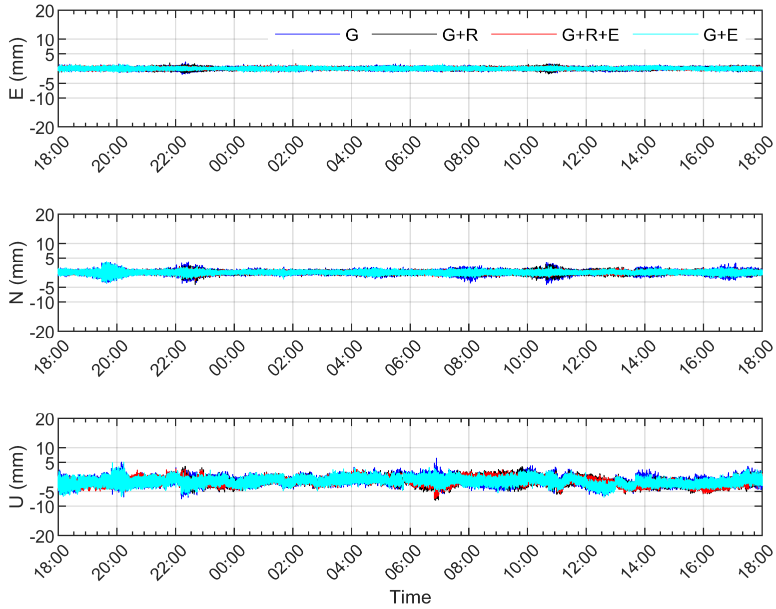

Figure S 1 *E/N/U coordinate timeseries of case E. ZBL measurements for the four available solutions: G: GPS-only, G+R: GPS+GLONASS, G+R+E: GPS+GLONASS+Galileo, and G+E: GPS+Galileo*

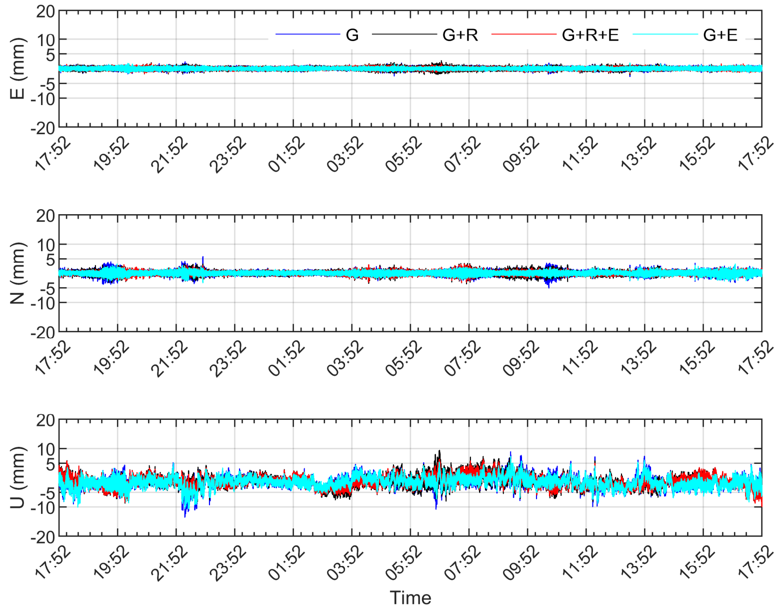

Figure S 2 *E/N/U coordinate timeseries of case B. ZBL measurements for the four available solutions: G: GPS-only, G+R: GPS+GLONASS, G+R+E: GPS+GLONASS+Galileo, and G+E: GPS+Galileo*

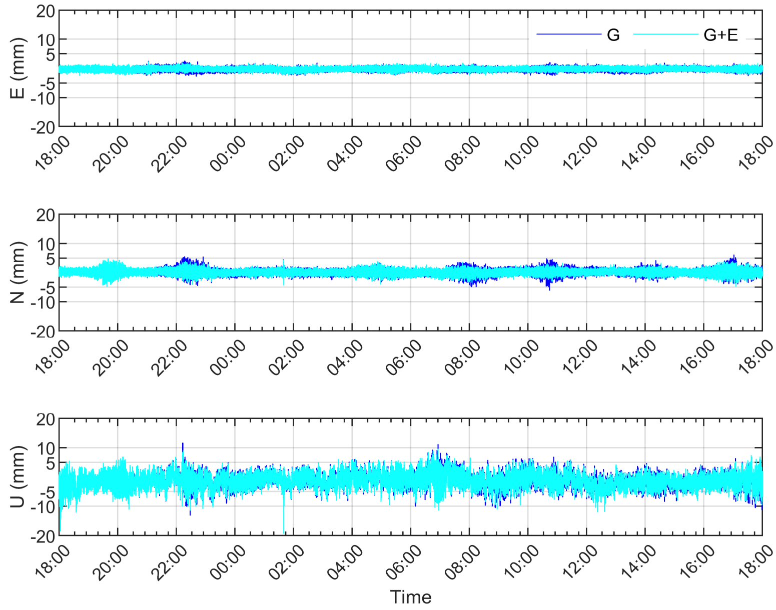

Figure S 3 *E/N/U coordinate timeseries of case F. ZBL measurements for the four available solutions: G: GPS-only, G+R: GPS+GLONASS, G+R+E: GPS+GLONASS+Galileo, and G+E: GPS+Galileo*

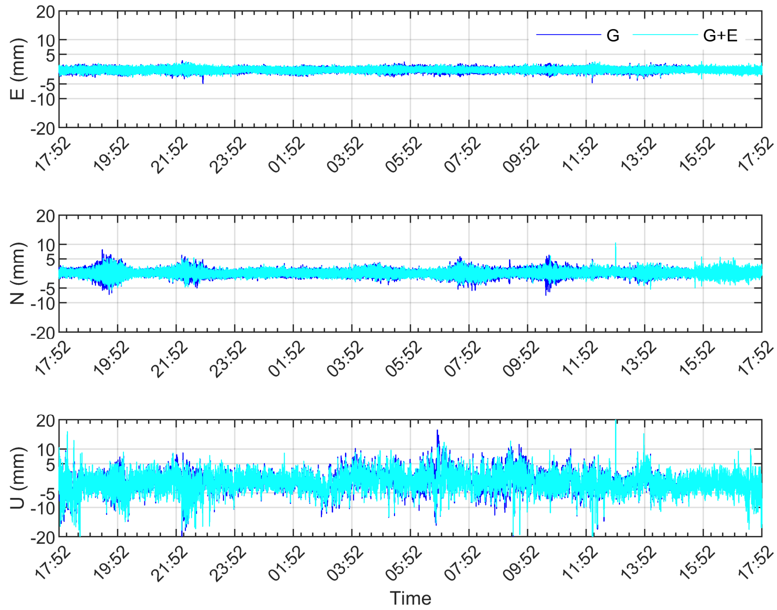

Figure S 4 *E/N/U coordinate timeseries of case C. ZBL measurements for the four available solutions: G: GPS-only, G+R: GPS+GLONASS, G+R+E: GPS+GLONASS+Galileo, and G+E: GPS+Galileo*

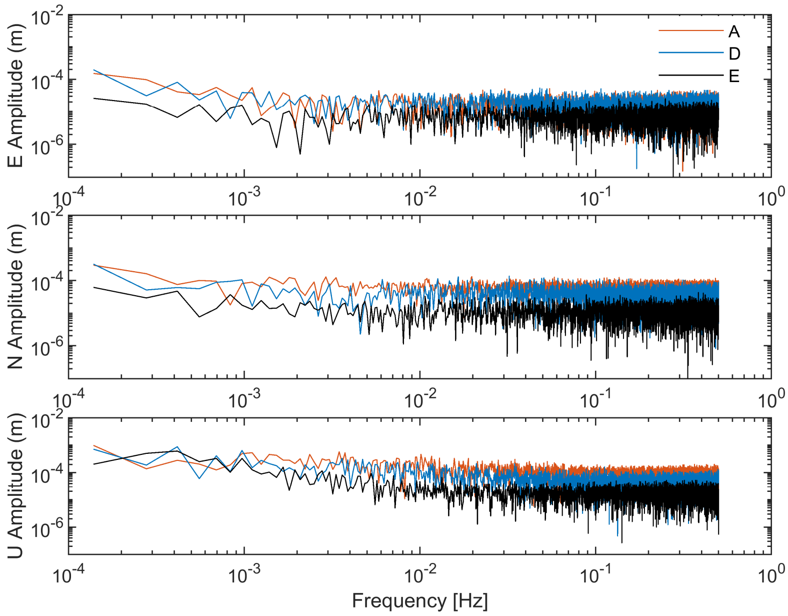

Figure S 5 *Spectra of E/N/U components for the solutions of the cases A, D, and E using GPS+GLONASS constellation.*

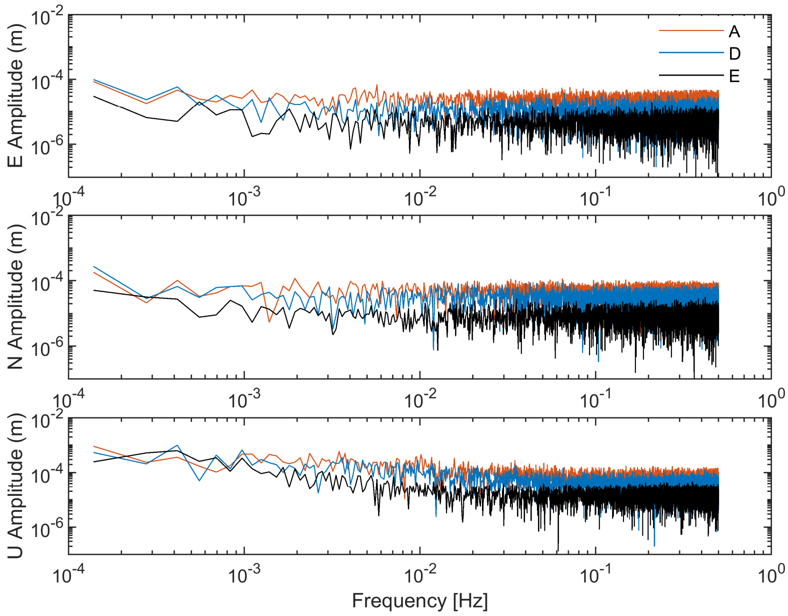

Figure S 6 *Spectra of E/N/U components for the solutions of the cases A, D, and E using GPS+GLONASS+Galileo constellation.*

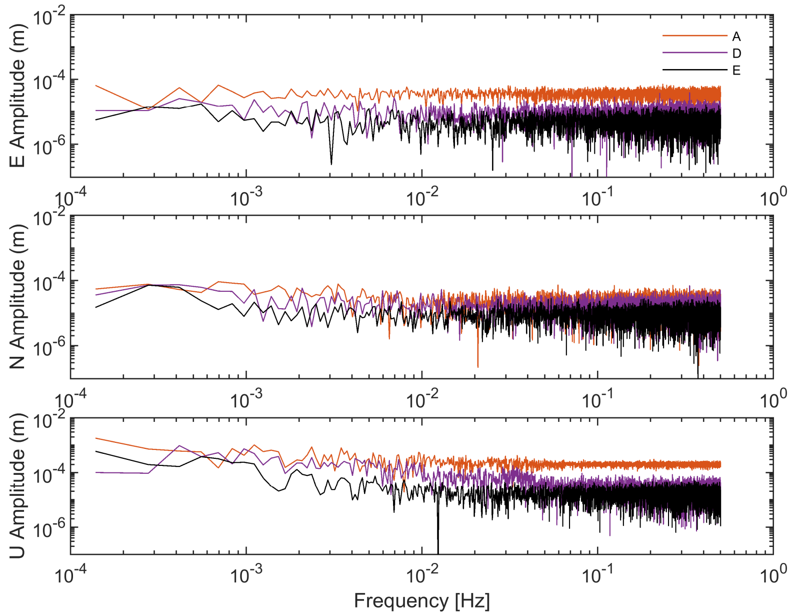

Figure S 7 *Spectra of E/N/U components for the solutions of the cases A, D, and E using GPS+Galileo constellation.*

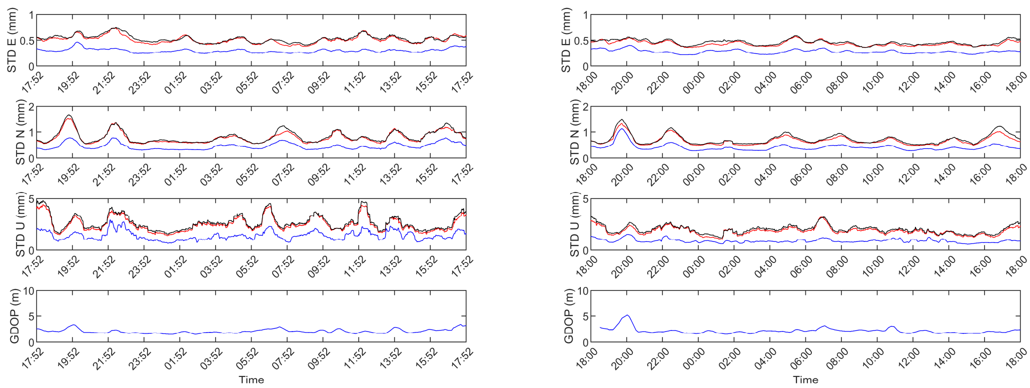

Figure S 8 *The MSTD timeseries for E/N/U and the GDOP moving average timeseries for the GPS+Galileo measurements using (Left) the patch antenna and (Right) the geodetic antenna, having as base-rover; both Leica receivers (blue line), both u-blox receivers (red line) and Leica and u-blox receiver (black line).*

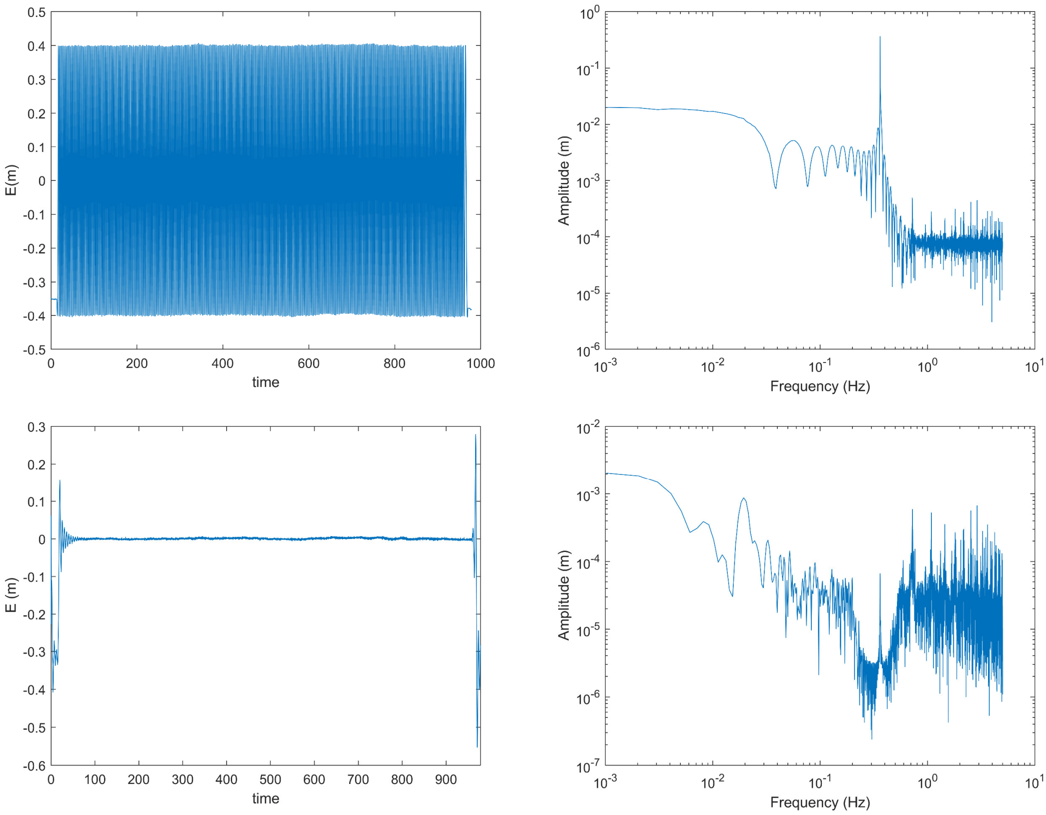

Figure S 9 *(Top left) original timeseries for Eastings when using Leica rover and Leica base; (Top right) corresponding DFT spectral analysis; (Bottom left) band-stop filtered timeseries; (Bottom right) DFT spectral analysis with respect to 500s to 900s of the band-stop filtered timeseries*

Appendix B

Kalman filter Algorithm

In RTKLIB (Takasu, 2013), an EKF (Extended Kalman Filtering) is used to obtain the kinematic mode final solution. Similar to derivation in Kalman filtering, with a change of notations.

The EKF is formulated as follows; by using EKF, the state vector and its covariance matrix can be estimated with Equation S1,

$$\hat{x}_k(+) = \hat{x}_k(-) + \mathrm{K_k}(\mathrm{y_k} - \mathrm{h}(\hat{x}_k(-)))$$

$$\mathrm{P_k}(+) = \left(\mathrm{I} - \mathrm{K_k} H\left(\hat{x}_k(-)\right)\right) * \mathrm{P_k}(-)$$

$$K_k = \mathrm{P_k}(-) H\left(\hat{x}_k(-)\right)^T \left(H\left(\hat{x}_k(-)\right)\mathrm{P_k}(-) H\left(\hat{x}_k(-)\right)^T + R_k\right)^{-1}$$

Equation S 1 *Estimation of the state vector and covariance matrix with measurement vector*

Where

- $\hat{x}_k$ denotes the estimated state vector at epoch t_k,
- $\mathrm{P_k}$ denotes its covariance matrix, with (-) and (+) indicate before and after update of the EKF,
- $\mathrm{y_k}$ is the measurement vector at t_k,
- h(x) is the measurement model vector,
- H(x) is the matrix of partial derivatives
- R_k stands for the covariance matrix of measurement errors

By assumption of the linear system model, the time update of the state vector and covariance matrix can be formed with Equation S2, where the state vector and covariance matrix of epoch t_{k+1} could be predicted.

$$\hat{x}_{k+1}(-) = \mathrm{F_k}^{\mathrm{k+1}} \hat{x}_k(+) \qquad \mathrm{P_{k+1}}(-) = \mathrm{F_k}^{\mathrm{k+1}} \mathrm{P_k}(+) {\mathrm{F_k}^{\mathrm{k+1}}}^T + \mathrm{Q_k}^{\mathrm{k+1}}$$

Equation S 2 *Time update state vector and its covariance matrix*

Where

- $\mathrm{F_k}^{\mathrm{k+1}}$ is the transition matrix from t_k to t_{k+1}
- $\mathrm{Q_k}^{\mathrm{k+1}}$ is the covariance matrix of the system noise from t_k to t_{k+1}

In the DD SBL using triple frequency GPS/GLONASS observations, the unknown vector x is defined as

$$x = ({r_r}^T, {v_r}^T, {B_1}^T, {B_2}^T, {B_5}^T)^T$$

Equation S 3 *State vector definition in DD for short baseline*

Where

- r_r is the estimated receiver position,
- v_r is the velocity estimation,

- B_i is the L_i frequency between-receiver SD carrier phase biases in unit of cycles.

The measurement vector y is also defined with DD carrier phase and code pseudorange as follows.

$$y = ({\Phi_1}^T, {\Phi_2}^T, {\Phi_5}^T, {P_1}^T, {P_2}^T, {P_5}^T)^T$$

Equation S 4 *Definition of measurement vector in DD for SBL*

Where

- Φ_i is the L_i frequency DD carrier phase measurement
- P_i is the L_i frequency DD code phase measurement

Using Equation S1 and Equation S2, the EKF could be updated with measurement and with time. The detailed equations and matrices for measurement update of EKF could be found in the RTKLIB manual page 164 for a triple frequency scenario, with detailed expression measurement model vector h(x), the matrix of partial derivatives H(x), and the covariance matrix of measurement errors R. For time update of EKF, considering receiver dynamics and kinematic processing mode, the transition matrix in system equation can be formed by,

$$F_k^{k+1} = \begin{matrix} I_{3*3} & I_{3*3} * \tau_r & 0 \\ 0 & I_{3*3} & 0 \\ 0 & 0 & I_{(3m-3)*(3m-3)} \end{matrix}$$

Equation S 5 *Formation of transition matrix in the system equation considering receiver dynamics*

And the covariance matrix of the system noise can be formed as

$$Q_k^{k+1} = \begin{matrix} 0_{3*3} & 0 & 0 \\ 0 & Q_v & 0 \\ 0 & 0 & 0_{(3m-3)*(3m-3)} \end{matrix}$$

Equation S 6 *Formation of the covariance matrix of system noise considering receiver dynamics*

Where

- $Q_v = {E_r}^T diag({\sigma_{ve}}^2\tau_r, {\sigma_{vn}}^2\tau_r, {\sigma_{vu}}^2\tau_r)E_r$
- E_r is the coordinates rotation matrix from ECEF to the local coordinates at the receiver position
- τ_r is the GPS/GNSS receiver sampling interval,
- σ_{ve}, σ_{vn}, σ_{vu} are STDs of east, north, and up components of the rover velocity system noise

With kinematic processing mode, if the receiver dynamics are not taken into consideration, the transition matrix and covariance matrix of the system noise changes to

$$F_k^{k+1} = \begin{matrix} I_{3*3} & 0 & 0 \\ 0 & I_{3*3} & 0 \\ 0 & 0 & I_{(3m-3)*(3m-3)} \end{matrix} \quad \text{and} \quad Q_k^{k+1} = \begin{matrix} \infty_{3*3} & 0 & 0 \\ 0 & 0 & 0 \\ 0 & 0 & 0_{(3m-3)*(3m-3)} \end{matrix}$$

Equation S 7 *Formation of transition matrix in the system equation and covariance matrix of system noise without considering receiver dynamics*

As can be seen in Equation S7, an infinite process noise is added to the variance of receiver position to reset the receiver position state to the initial estimated position every epoch to avoid instability in computation where the initial guess of the position is obtained by single point positioning process. If a cycle slip is detected in the measurement data, the state of the corresponding SD carrier-phase bias is also reset to the initial value. RTKLIB detects the cycle-slips by LLI (loss of lock indicator) in the input measurement data and geometry-free LC (linear combination) phase jumps if the dual-frequency measurements are available.

Integer ambiguity resolution

The integer ambiguity resolution can be solved into integer values once the estimated states are obtained in the EKF measurement update to improve the accuracy and convergence time. Recall the formation of DD state vectors for short baseline also includes SD carrier phase biases. Therefore, firstly, the estimated state and covariance matrix are transformed to DD form by

$$\hat{x}'_{\mathrm{k}} = \mathrm{G}\hat{x}_k(+) = (\hat{r}_r^{\,T}, \hat{v}_r^{\,T}, \hat{N}^T)^T$$

$$P'_k = GP_k(+)G^T = \begin{matrix} Q_R & Q_{NR} \\ Q_{RN} & Q_N \end{matrix}$$

Equation S 8 *Transformation of the state vector and covariance matrix from SD to DD*

Where

- G is the SD to DD transformation matrix and $\mathrm{G} = \begin{matrix} I_{6*6} & 0 & 0 & 0 \\ 0 & D & 0 & 0 \\ 0 & 0 & D & 0 \\ 0 & 0 & 0 & D \end{matrix}$, where D is expressed as $\mathrm{D} = \begin{matrix} 1 & -1 & 0 & \dots & 0 \\ 1 & 0 & -1 & \dots & 0 \\ \vdots & \vdots & \vdots & \ddots & \vdots \\ 1 & 0 & 0 & \dots & -1 \end{matrix}$

The transformation is conducted to transform the SD carrier phase bias to DD carrier form to obtain float ambiguities estimate $\hat{N}$ and their covariance matrix Q_N, by solving an integer least square (ILS) problem, the integer vector can be obtained by solving Equation S9,

$$\mathrm{N} = \mathrm{argmin}\,(((\mathrm{N} - \hat{N})^{\mathrm{T}} Q_N^{-1} (\mathrm{N} - \hat{N}))$$

Equation S 9 *Formation of integer least square to calculate integer ambiguity where N should be solved as integers.*

The RTKLIB employs LAMBDA and MLAMBDA to search efficiently by shrinking the integer search space based on combinations of linear transformations, in the transformation search space, an efficient tree-search algorithm is also adopted. A more detailed description of LAMBDA and MLAMBDA could be found in the paper published by Teunissen (1995) and Chang et. al (2005). A reliability check of the integer ambiguity resolution is conducted as a validation process in RTKLIB by ratio test, where the ratio is calculated by Equation S10, namely the weighted sum of squared residuals of second-best solution with integer ambiguity N2 over that with the best solution with integer ambiguity N1. And a R threshold is established and set to a fixed value to validate the resolution

$$\mathrm{R} = \frac{(N2 - \widehat{N})^T {Q_N}^{-1}(N2 - \widehat{N})}{(N1 - \widehat{N})^T {Q_N}^{-1}(N1 - \widehat{N})} > \mathrm{R}_{\mathrm{threshold}}$$

Equation S 10 *Ratio validation test for integer ambiguity resolution*

After validation, the fixed solution (r_r, v_r) can be obtained by Equation S11, and if the validation failed to comply with the minimum R threshold, the float solution is used

$$\begin{matrix} r_r \\ v_r \end{matrix} = \begin{matrix} \widehat{r_r} \\ \widehat{v_r} \end{matrix} - Q_{RN} {Q_N}^{-1}(\widehat{N} - N1)$$

Equation S 11 *Fixed solution calculation after the ambiguity is fixed*

.

Appendix C

The settings below show a general example for processing data for the rotation test.

```
# rtkpost options (2020/05/21 13:07:59, v.demo5 b33c)
pos1-posmode       =kinematic  # (0:single,1:dgps,2:kinematic,3:static,4:static-start,5:movingbase,6:fixed,7:ppp-kine,8:ppp-static,9:ppp-fixed)
pos1-frequency     =l1         # (1:l1,2:l1+l2,3:l1+l2+l5,4:l1+l2+l5+l6)
pos1-soltype       =combined   # (0:forward,1:backward,2:combined)
pos1-elmask        =15         # (deg)
pos1-snrmask_r     =off        # (0:off,1:on)
pos1-snrmask_b     =off        # (0:off,1:on)
pos1-snrmask_L1    =0,0,0,0,0,0,0,0,0
pos1-snrmask_L2    =0,0,0,0,0,0,0,0,0
pos1-snrmask_L5    =0,0,0,0,0,0,0,0,0
pos1-dynamics      =on         # (0:off,1:on)
pos1-tidecorr      =off        # (0:off,1:on,2:otl)
pos1-ionoopt       =brdc       # (0:off,1:brdc,2:sbas,3:dual-freq,4:est-stec,5:ionex-tec,6:qzs-brdc,7:qzs-lex,8:stec)
pos1-tropopt       =saas       # (0:off,1:saas,2:sbas,3:est-ztd,4:est-ztdgrad,5:ztd)
pos1-sateph        =brdc       # (0:brdc,1:precise,2:brdc+sbas,3:brdc+ssrapc,4:brdc+ssrcom)
pos1-posopt1       =off        # (0:off,1:on)
pos1-posopt2       =off        # (0:off,1:on)
pos1-posopt3       =off        # (0:off,1:on,2:precise)
pos1-posopt4       =off        # (0:off,1:on)
pos1-posopt5       =on         # (0:off,1:on)
pos1-posopt6       =off        # (0:off,1:on)
pos1-exclsats      =           # (prn ...)
pos1-navsys        =1          # (1:gps+2:sbas+4:glo+8:gal+16:qzs+32:comp)
pos2-armode        =continuous # (0:off,1:continuous,2:instantaneous,3:fix-and-hold)
pos2-gloarmode     =fix-and-hold # (0:off,1:on,2:autocal,3:fix-and-hold)
pos2-bdsarmode     =off        # (0:off,1:on)
pos2-arfilter      =on         # (0:off,1:on)
pos2-arthres       =3
pos2-arthres1      =0.1
pos2-arthres2      =0
pos2-arthres3      =1e-09
pos2-arthres4      =1e-05
pos2-varholdamb    =0.1        # (cyc^2)
pos2-gainholdamb   =0.01
pos2-arlockcnt     =0
pos2-minfixsats    =4
pos2-minholdsats   =5
pos2-mindropsats   =10
pos2-rcvstds       =off        # (0:off,1:on)
pos2-arelmask      =15         # (deg)
pos2-arminfix      =20
pos2-armaxiter     =1
pos2-elmaskhold    =15         # (deg)
pos2-aroutcnt      =20
pos2-maxage        =30         # (s)
```

```
pos2-syncsol       =off        # (0:off,1:on)
pos2-slipthres     =0.05       # (m)
pos2-rejionno      =1000       # (m)
pos2-rejgdop       =30
pos2-niter         =1
pos2-baselen       =0          # (m)
pos2-basesig       =0          # (m)
out-solformat      =enu        # (0:llh,1:xyz,2:enu,3:nmea)
out-outhead        =on         # (0:off,1:on)
out-outopt         =on         # (0:off,1:on)
out-outvel         =off        # (0:off,1:on)
out-timesys        =gpst       # (0:gpst,1:utc,2:jst)
out-timeform       =hms        # (0:tow,1:hms)
out-timendec       =3
out-degform        =deg        # (0:deg,1:dms)
out-fieldsep       =
out-outsingle      =off        # (0:off,1:on)
out-maxsolstd      =0          # (m)
out-height         =ellipsoidal # (0:ellipsoidal,1:geodetic)
out-geoid          =internal   # (0:internal,1:egm96,2:egm08_2.5,3:egm08_1,4:gsi2000)
out-solstatic      =all        # (0:all,1:single)
out-nmeaintv1      =0          # (s)
out-nmeaintv2      =0          # (s)
out-outstat        =residual   # (0:off,1:state,2:residual)
stats-weightmode   =elevation  # (0:elevation,1:snr)
stats-eratio1      =400
stats-eratio2      =300
stats-eratio5      =300
stats-errphase     =0.003      # (m)
stats-errphaseel   =0.003      # (m)
stats-errphasebl   =0          # (m/10km)
stats-errdoppler   =1          # (Hz)
stats-snrmax       =52         # (dB.Hz)
stats-stdbias      =30         # (m)
stats-stdiono      =0.03       # (m)
stats-stdtrop      =0.3        # (m)
stats-prnaccelh    =3          # (m/s^2)
stats-prnaccelv    =1          # (m/s^2)
stats-prnbias      =0.0001     # (m)
stats-prniono      =0.001      # (m)
stats-prntrop      =0.0001     # (m)
stats-prnpos       =0          # (m)
stats-clkstab      =5e-12      # (s/s)
ant1-postype       =llh        # (0:llh,1:xyz,2:single,3:posfile,4:rinexhead,5:rtcm,6:raw)
ant1-pos1          =90         # (deg|m)
ant1-pos2          =0          # (deg|m)
ant1-pos3          =-6335367.6285 # (m|m)
ant1-anttype       =
ant1-antdele       =0          # (m)
ant1-antdeln       =0          # (m)
ant1-antdelu       =0          # (m)
```

```
ant2-postype      =single     # (0:llh,1:xyz,2:single,3:posfile,4:rinexhead,5:rtcm,6:raw)
ant2-pos1         =0          # (deg|m)
ant2-pos2         =0          # (deg|m)
ant2-pos3         =0          # (m|m)
ant2-anttype      =
ant2-antdele      =0          # (m)
ant2-antdeln      =0          # (m)
ant2-antdelu      =0          # (m)
ant2-maxaveep     =1
ant2-initrst      =on         # (0:off,1:on)
misc-timeinterp   =on         # (0:off,1:on)
misc-sbasatsel    =0          # (0:all)
misc-rnxopt1      =
misc-rnxopt2      =
misc-pppopt       =
file-satantfile   =
file-rcvantfile   =
file-staposfile   =
file-geoidfile    =
file-ionofile     =
file-dcbfile      =
file-eopfile      =
file-blqfile      =
file-tempdir      =
file-geexefile    =
file-solstatfile  =
file-tracefile    =
```

Appendix D

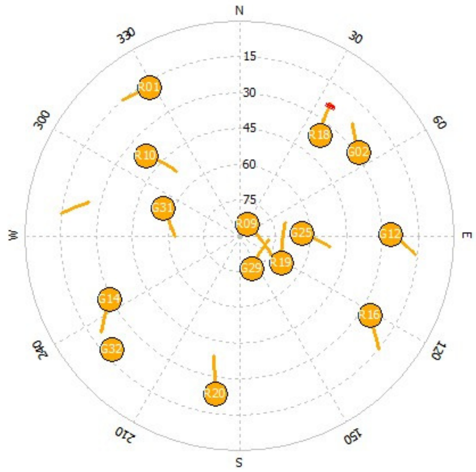

Figure S 10 *Skyplot before excitation event 05*

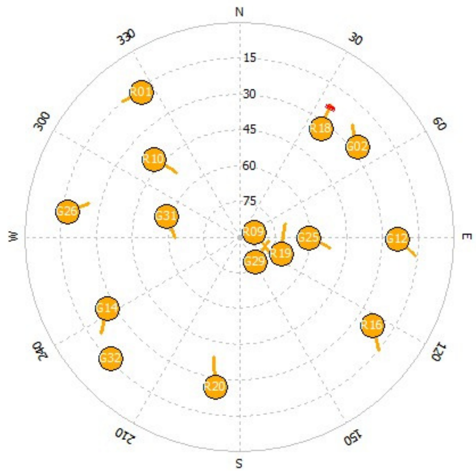

Figure S 11 *Skyplot during excitation event 05, G26 is joining into the skyplot*

Appendix E

$$\sigma_{th} = \frac{\lambda}{2\pi}\sqrt{\frac{B_n}{C/N_0}(1 + \frac{1}{2TC/N_0})}$$

where:

- λ is wavelength of the carrier signal [m].
- B_n is the loop bandwidth [Hz].
- C/N_0 is the carrier to noise ratio [Hz].
- T is the integration time [s].

Figure S 12 *The PLL thermal noise jitter (Navipedia, 2014d)*

$$\sigma_{th} = \frac{1}{T_c}\sqrt{\frac{B_n \int_{-B_{fe}/2}^{B_{fe}/2} S_s(f) sin^2(\pi f \delta T_c) df}{(2\pi)^2 C/N_0 [\int_{-B_{fe}/2}^{B_{fe}/2} f S_s(f) sin(\pi f \delta T_c) df]^2}} \times \sqrt{1 + \frac{\int_{-B_{fe}/2}^{B_{fe}/2} S_s(f) cos^2(\pi f \delta T_c) df}{TC/N_0 [\int_{-B_{fe}/2}^{B_{fe}/2} S_s(f) cos(\pi f \delta T_c) df]^2}}$$

where:

- T_c is the chip period [s].
- R_c is the chipping rate [chip/s].
- B_{fe} is the double sided front-end bandwidth [Hz].
- B_n is the loop noise bandwidth [Hz].
- $S_s(f)$ is the power spectral density of the signal, normalized to unit area over infinite bandwidth.
- δ is the Early-Late spacing.

Figure S 13 *The DLL thermal noise jitter (Navipedia, 2014c)*

$$\sigma_{th} = \frac{\lambda}{2\pi T}\sqrt{\frac{4FB_n}{C/N_0}(1 + \frac{1}{TC/N_0})}$$

where:

- λ is the wavelength of the carrier signal [m].
- B_n is the loop bandwidth [Hz].
- C/N_0 is the carrier-to-noise ratio [dB-Hz].
- T is the integration time [s].
- F = 1, at high carrier to noise ration; F = 2, otherwise.

Figure S 14 *The FLL thermal noise jitter (Navipedia, 2014b)*

Appendix F

```
# rtkpost options (2021/05/11 19:11:37, v.demo5 b33c)

pos1-posmode       =kinematic  # (0:single,1:dgps,2:kinematic,3:static,4:static-start,5:movingbase,6:fixed,7:ppp-kine,8:ppp-static,9:ppp-fixed)
pos1-frequency     =l1         # (1:l1,2:l1+l2,3:l1+l2+l5,4:l1+l2+l5+l6)
pos1-soltype       =forward    # (0:forward,1:backward,2:combined)
pos1-elmask        =15         # (deg)
pos1-snrmask_r     =off        # (0:off,1:on)
pos1-snrmask_b     =off        # (0:off,1:on)
pos1-snrmask_L1    =35,35,35,35,35,35,35,35,35
pos1-snrmask_L2    =0,0,0,0,0,0,0,0,0
pos1-snrmask_L5    =0,0,0,0,0,0,0,0,0
pos1-dynamics      =on         # (0:off,1:on)
pos1-tidecorr      =off        # (0:off,1:on,2:otl)
pos1-ionoopt       =brdc       # (0:off,1:brdc,2:sbas,3:dual-freq,4:est-stec,5:ionex-tec,6:qzs-brdc,7:qzs-lex,8:stec)
pos1-tropopt       =saas       # (0:off,1:saas,2:sbas,3:est-ztd,4:est-ztdgrad,5:ztd)
pos1-sateph        =brdc       # (0:brdc,1:precise,2:brdc+sbas,3:brdc+ssrapc,4:brdc+ssrcom)
pos1-posopt1       =off        # (0:off,1:on)
pos1-posopt2       =off        # (0:off,1:on)
pos1-posopt3       =off        # (0:off,1:on,2:precise)
pos1-posopt4       =off        # (0:off,1:on)
pos1-posopt5       =on         # (0:off,1:on)
pos1-posopt6       =off        # (0:off,1:on)
pos1-exclsats      =           # (prn ...)
pos1-navsys        =5          # (1:gps+2:sbas+4:glo+8:gal+16:qzs+32:comp)
pos2-armode        =continuous # (0:off,1:continuous,2:instantaneous,3:fix-and-hold)
pos2-gloarmode     =autocal    # (0:off,1:on,2:autocal,3:fix-and-hold)
pos2-bdsarmode     =off        # (0:off,1:on)
pos2-arfilter      =on         # (0:off,1:on)
pos2-arthres       =1
pos2-arthres1      =0.01
pos2-arthres2      =-0.055
pos2-arthres3      =1e-09
pos2-arthres4      =1e-05
pos2-varholdamb    =0.01       # (cyc^2)
pos2-gainholdamb   =0.01
pos2-arlockcnt     =5
pos2-minfixsats    =4
pos2-minholdsats   =5
pos2-mindropsats   =7
pos2-rcvstds       =off        # (0:off,1:on)
pos2-arelmask      =15         # (deg)
pos2-arminfix      =0
pos2-armaxiter     =1
pos2-elmaskhold    =15         # (deg)
pos2-aroutcnt      =1
pos2-maxage        =1          # (s)
pos2-syncsol       =off        # (0:off,1:on)
```

```
pos2-slipthres     =0.01       # (m)
pos2-rejionno      =1000       # (m)
pos2-rejgdop       =30
pos2-niter         =1
pos2-baselen       =0          # (m)
pos2-basesig       =0          # (m)
out-solformat      =enu        # (0:llh,1:xyz,2:enu,3:nmea)
out-outhead        =on         # (0:off,1:on)
out-outopt         =on         # (0:off,1:on)
out-outvel         =off        # (0:off,1:on)
out-timesys        =gpst       # (0:gpst,1:utc,2:jst)
out-timeform       =hms        # (0:tow,1:hms)
out-timendec       =3
out-degform        =deg        # (0:deg,1:dms)
out-fieldsep       =
out-outsingle      =off        # (0:off,1:on)
out-maxsolstd      =0          # (m)
out-height         =ellipsoidal # (0:ellipsoidal,1:geodetic)
out-geoid          =internal   # (0:internal,1:egm96,2:egm08_2.5,3:egm08_1,4:gsi2000)
out-solstatic      =all        # (0:all,1:single)
out-nmeaintv1      =0          # (s)
out-nmeaintv2      =0          # (s)
out-outstat        =residual   # (0:off,1:state,2:residual)
stats-weightmode   =elevation  # (0:elevation,1:snr)
stats-eratio1      =400
stats-eratio2      =300
stats-eratio5      =300
stats-errphase     =0.003      # (m)
stats-errphaseel   =0.003      # (m)
stats-errphasebl   =0          # (m/10km)
stats-errdoppler   =1          # (Hz)
stats-snrmax       =52         # (dB.Hz)
stats-stdbias      =30         # (m)
stats-stdiono      =0.03       # (m)
stats-stdtrop      =0.3        # (m)
stats-prnaccelh    =3          # (m/s^2)
stats-prnaccelv    =1          # (m/s^2)
stats-prnbias      =0.0001     # (m)
stats-prniono      =0.001      # (m)
stats-prntrop      =0.0001     # (m)
stats-prnpos       =0          # (m)
stats-clkstab      =5e-12      # (s/s)
ant1-postype       =llh        # (0:llh,1:xyz,2:single,3:posfile,4:rinexhead,5:rtcm,6:raw)
ant1-pos1          =90         # (deg|m)
ant1-pos2          =0          # (deg|m)
ant1-pos3          =-6335367.6285 # (m|m)
ant1-anttype       =
ant1-antdele       =0          # (m)
ant1-antdeln       =0          # (m)
ant1-antdelu       =0          # (m)
ant2-postype       =single     # (0:llh,1:xyz,2:single,3:posfile,4:rinexhead,5:rtcm,6:raw)
```

```
ant2-pos1        =0        # (deg|m)
ant2-pos2        =0        # (deg|m)
ant2-pos3        =0        # (m|m)
ant2-anttype     =
ant2-antdele     =0        # (m)
ant2-antdeln     =0        # (m)
ant2-antdelu     =0        # (m)
ant2-maxaveep    =1
ant2-initrst     =on       # (0:off,1:on)
misc-timeinterp  =on       # (0:off,1:on)
misc-sbasatsel   =0        # (0:all)
misc-rnxopt1     =
misc-rnxopt2     =
misc-pppopt      =
file-satantfile  =
file-rcvantfile  =
file-staposfile  =
file-geoidfile   =
file-ionofile    =
file-dcbfile     =
file-eopfile     =
file-blqfile     =
file-tempdir     =
file-geexefile   =
file-solstatfile =
file-tracefile   =
```